NORTHWESTERN UNIVERSITY

In Situ Morphology, Formation, and Dynamics of Heterogeneous Soft Matter Systems Elucidated via Liquid Phase Transmission Electron Microscopy

A DISSERTATION

SUBMITTED TO THE GRADUATE SCHOOL
IN PARTIAL FULFILLMENT OF THE REQUIREMENTS

for the degree

DOCTOR OF PHILOSOPHY

Materials Science and Engineering

By

Maria Anastasia Vratsanos

EVANSTON, ILLINOIS

September 2023

Abstract

Herein, we present an overview of our studies of the morphology, dynamics, and formation of heterogeneous soft matter systems *via* the emerging technique of liquid phase transmission electron microscopy (LPTEM). This particular subset of materials, more commonly referred to as emulsions, is tremendously commercially and biologically relevant, encompassing applications in food science, commodity materials, and biology. Emulsions operate on the principle of sequestering incompatible phases via a mutually compatible interface, typically an amphiphilic molecule known as a surfactant. It is precisely because of this phase separation that these materials are interesting, but it is also what makes them especially challenging to characterize. Indirect methods (such as scattering) require assumptions about overall material properties, morphology, and population distributions, which are immensely complicated by the multiphasic nature, while conventional imaging techniques have historically required sample fixation to attain the necessary spatial resolution, thereby eliminating the dynamic aspect of these materials. We have shown LPTEM to be an effective way to image these materials in their native, solvated state at unprecedented spatiotemporal resolution. Using this technique, we have examined their morphology, quantified their formation and destabilization, analyzed their motion, utilized them as reaction loci, and observed their stimuli response. We contend that this class of materials is uniquely suited for continued study via this technique not only due to their utility as materials but also because of their tunable contrast, mobility, and stability. Emulsions have the additional benefit of well-defined, modular droplet sizes, which may range from a few nanometers to over a micron. The LPTEM field has consistently encountered issues of spatial confinement which hinder and interfere with *in situ* reactions and processes. However, if reactants are contained in an emulsion droplet, the degree of confinement is known and controllable. We are confident that further

inquiries into such materials will yield insight into more complex processes, such as emulsion polymerization, higher order interface reorganization, and organogel formation. Further, we anticipate that emulsions will be used as *in situ* microreactors to counteract the artifacts of confinement in LPTEM and control reactions during observation.

Acknowledgements

There are many folks without whom I would not be writing this document, and to thank them all would take far too many pages, so I'll do my best to be selective.

To my advisor, **Professor Nathan Gianneschi**, I owe a great many things, but for the purposes of brevity, we'll stick to the best ones. I wouldn't be at Northwestern today without Nathan, and he's worked with me every step of the way to create a thesis that I'm proud of, despite more than a few challenges along the way. I have grown as a scholar, a researcher, and a human being during my five years in Evanston, and I am so grateful to Nathan for helping me do so.

I would also like to thank the members of my committee**, Professors Vinayak Dravid, Erik Luijten**, and **Joe Patterson**, for their insightful commentary and fruitful discussion.

All students understand how important it is to have good mentors. I've been fortunate to have many throughout my research career, but I'd like to highlight **Dr. Mollie Touve**, who taught me everything I know about liquid cell and showed me just how cool a thesis project like this could be, and **Dr. Karthik Gnanasekaran**, for showing me how to properly do said project. I am also incredibly grateful to my pre-grad school mentors for encouraging my graduate school aspirations and teaching me what it means to do real research: **Professor Gary Wnek** and **Dr. Anne Walker**, **Professor George Pins** and **Dr. Meg Chrobak**, **Professor Christopher Williams** and **Dr. Nick Chartrain,** and **Dr. John Zielinski**.

I've been lucky to have many wonderful collaborators during this thesis. **Professor Brent Sumerlin** and his student **Megan Lott**, as well as **Professor Lauren Zarzar** have been particularly enlightening as Nathan and I delved into this new-to-us field of materials. Our colleagues in Bologna, **Professor Francesco Zerbetto** and **Dr. Evangelos Bakalis**, have also been

instrumental in understanding the complex physics inside the liquid cell, and I am very grateful for our fruitful collaborations.

Thanks to everyone in the Gianneschi group with whom I've had the good fortune of overlapping. **Dr. Matt Thompson**, thanks for letting me constantly come to you with non-chemistry related anxieties. **Brittney Williams** and **Chris Sharpe**, thanks for always being down for a procrastination coffee run.

I met many wonderful people during my time at Northwestern, but thank you especially to **Dalton Cox, Matt Sweers**, and **Jennie Glerum** for your companionship, camaraderie, and counsel. I'm especially grateful for our shared love of cats and craft beer. Thanks also **Sam Wong, Kendall Sullivan, and Louie Fisher** for being the best people to hang out on a boat with.

I'd like to thank my family. My parents, **Dr. Menas Vratsanos** and **Dr. Lori Anderson**, were my first teachers and mentors, and molded me into the scientist I am today. I am forever grateful to them for instilling in me a love of learning and a commitment to education. Thanks also to my brother, **Alex Vratsanos**, for unending support and encouragement.

Finally, to my guys, **Adam Thompson** and **Steve Holt**. Their contributions could fill an entire book, but we'll keep it brief. Thanks to Steve Holt for being the most excellent cat and providing endless comfort and entertainment. Adam, thank you for being my person on both the good days and the bad. Thank you for literally everything. I love you.

Research Support:

The work discussed here was facilitated by an NSF Graduate Research Fellowship (DGE-1842165) and a Dr. John N. Nicholson fellowship from Northwestern University. Additional support includes government funding through the Army Research Office (W911NF-17-1-0326,

W911NF-18-1-0359, MURI W911NF-15-1-0568, W911NF-18-1-0414) and the National Science Foundation (CHE-MSN 1905270). This work made use of the EPIC facility within Northwestern University's NUANCE facility, which receives support from the Soft and Hybrid Nanotechnology Experimental (SHyNE) Resource (NSF ECCS-202563), the International Institute for Nanomaterials (NIH-S10OD026871), and the Materials Research Science and Engineering Centers (NSF DMR-1720139).

Dedication

To my family, both the one I started with and the one I found along the way.

Table of Contents

List of Figures

List of Tables

Chapter 1 Introduction: An Overview of Structural Characterization of Emulsions

Mixed phase heterogeneous soft materials, such as emulsions, dispersions, *etc*., are ubiquitous in both natural and synthetic systems. On a fundamental level, such systems exist to compatibilize incompatible liquid components with a mutually compatible interface. In biology, an example of such phase separation is the digestion of consumed fats and lipids, which is facilitated through bile salt surfactants that allow for high surface area fat droplets to travel through the aqueous digestive tract.[1] Synthetic applications include dispersing pigments in paints and coatings, commodity plastics, and a wealth of culinary sauces and condiments.[2] Despite their immense and sweeping utility, the study of the structures of such materials has remained difficult. Being comprised of two immiscible liquids and an interface, emulsions present a challenge for many conventional structural characterization techniques that rely on understanding a sample's solvent parameters, simply because there are now two such materials for which one must account. Further, emulsions may have either oil-in-water (o/w) or water-in-oil (w/o) formulation, various interfacial stabilizers, and increasingly complex morphologies, which means that sample preparation must account for each of these respective features. Additionally, emulsions are thermodynamically unstable, and are thus intrinsically dynamic in nature, and may exhibit morphological changes over the timescale of observation. Generally, the researcher must decide *a priori* whether their interest lies in probing the morphology at a given time, or the change in such, as it is typically not feasible to do both simultaneously. To effectively examine morphology, it is often necessary to preserve it somehow (*e.g.*, chemical or cryogenic fixation) in order to prepare the sample for direct observation. However, this precludes study of the transitions of such materials, and is difficult to accomplish without perturbing the material from its native state.

There is also significant interest in characterizing these materials' instabilities over time, and the rates at which and mechanisms by which they occur, as this is the driving force in determining an emulsion's longevity.[3] Such studies typically utilize indirect methods, which are often more amenable to *in situ* experiments and allow repeated measurements of the same sample over time. However, such results are predicated on choosing appropriate models through which to interpret results, which can be quite complex. Additionally, these results are reflective of the majority process, and may not accurately reflect statistically rarer events, which usually get lost in the noise of averaging. Thus, it is common to use a variety of techniques in order to get a complete view of the material.[4] Here, we will survey the techniques commonly used to study this class of materials and discuss shortcomings and opportunities, particularly regarding emerging microscopy techniques. We posit that *in situ* microscopy technologies like liquid phase transmission electron microscopy (LPTEM) are uniquely able to characterize such materials with respect to both morphology and dynamics.[5,6]

While there are numerous techniques used to characterize emulsions, we will focus predominantly on techniques related to evaluation of droplet size, morphology, and evolution here, as these are the most common ways to glean mechanistic information.[7] Most of these characterization techniques can be classified as either direct or indirect. Indirect characterization refers to a method which gives population information about a material in a roundabout way, often by measuring the response of an imparted stimulus to the material (*e.g.,* light scattered by the sample). Direct observation, on the other hand, is typically achieved *via* microscopy, often utilizing advanced instrumentation like electron microscopes to achieve greater resolution. Each set of techniques yields different information about the material in question, and such results are complementary and help to paint a holistic picture of the sample. [8]

1.1. Indirect Characterization

When considering dynamic materials, one of the most common characterization approaches is to get population statistics over time via scattering techniques. Such techniques are effective at establishing an aggregate picture of the system as a whole, and samples are often able to be analyzed *in situ,* where the environment may be modulated during study. Results of such studies rely on interpretation of averaged data through the lens of a chosen model. If the model is not carefully chosen, or if the assumptions upon which the model relies are not accurate, such results may be misleading or erroneous.

Collectively, scattering techniques function by focusing an energy source through a sample with a downstream detector that collects the transmitted energy to quantify how it has been altered by its interaction with the sample.[7–9] Typical sources of energy include photons, X-rays, and neutrons, which each interact with different components of a sample, and hence, yield different structural information about the material. For example, light scattering (e.g., dynamic light scattering or nanoparticle tracing analysis) details material behavior on length scales greater than the nanometer, such as the hydrodynamic radius of droplets, while x-ray techniques give information about the electronic structure present on smaller length scales.[10,11] One significant advantage of these techniques is that typically permit the *in situ* variation of sample environment during measurement, such as by heating or pH alteration[11]. Additionally, these techniques can be non-destructive, allowing for sample recovery in some cases. These methods face the challenge of determining a real space structure from reciprocal space scattering patterns.

1.1.1. Photon Scattering

Dynamic light scattering, sometimes referred to as photon correlation spectroscopy, impinges monochromatic light waves onto a sample-containing cuvette.[10] In the cuvette, particles

are undergoing Brownian motion as a result of thermal fluctuations in the surrounding fluids. Such fluctuations interferes with the transmission of the incident light, giving rise to a phenomenon known as Rayleigh scattering.[9] Quantification of the intensity over time gives rise to information regarding the molecular weight and radius of gyration of the material, while analysis of the variation in intensity yields the hydrodynamic radius of the material.[10] Mathematically, the models used to interpret the fluctuations rely upon the assumption of a spherical morphology, and results for non-spherical particles will be inaccurate. DLS generates a distribution of results based upon the aggregate results of several scans of the sample, which gives rise to a distribution of the parameter of interest. Distributions give an illuminating picture of population dispersity and will reflect variation in the population. However, such distributions may also be skewed by the nature of statistics, as the averages taken are not robust with respect to outliers – thus, larger particles and aggregates are typically over-represented and may appear to be a larger portion of the population than is accurate.[9] DLS is straightforward, quick to run, and can be used to analyze many samples in a short period of time. The subsequent data analysis is also relatively simple. Such simplicity can be useful when evaluating dynamic materials, as it is possible to characterize their size evolution with reasonably high temporal resolution (scans every few minutes). DLS is typically the most common way to measure emulsion size distribution, both with respect to formulation (**Figure 1.1A**) and changes in time (**Figure 1.1B**).[2,12] However, in emulsions with complex or non-spherical morphologies (*e.g.,* cylindrical or bicontinuous), DLS will not yield accurate information, as the models are no longer appropriate.

Nanoparticle tracking analysis (NTA) is another comparable technique which relies on following the motion of nanoparticles to discern their diffusivity and thus glean particle size information.[13] NTA is more robust with respect to outliers and contaminants, but also requires

more user expertise (particularly regarding sample parameters) and more time to collect equivalent data. Some instruments are also equipped with temperature modulation, allowing materials that exist at temperatures other than ambient or thermal transitions to be studied. Such techniques are often quite amenable to a variety of solvents as well, with the caveat that the properties of these solvents must be known and accounted for when processing the data.[10] Thus, assumptions for dispersed phase systems may not be wholly accurate. Further, conclusions drawn based on the rates of change of droplet size may be incorrect depending on the models used to fit the data. With a mixed-phase material, assumptions must be made about the overall refractive index of the dispersion, as well as of the form of the size distribution.[7]

DLS and NTA both yield size distributions of emulsion droplets and can be performed with reasonably high temporal resolution, from which one can extract a droplet growth rates. If r^3 is linear in time, it is typically taken to be an indication of Ostwald ripening, but does not necessarily mean that coalescence or flocculation is not also occurring.[14] Formed flocs will rapidly outpace the limit of detection on most instrumentation, and coalescence events may be sufficiently infrequent so as to get lost in the distribution.[15–17] Samples must be dilute (typically, 1% or less) in order for results to be accurate, which precludes many commercial materials from being characterized this way.[18]

Multiple light scattering may also be used to generate a measure of stability in time by evaluating turbidity, which is directly related to demulsification rates.[19] Static light scattering gives more nuanced information about molecular weight and concentration, and has subsequently been used to analyze coarsening rates in time to determine the crossover point between Ostwald ripening and coalescence (**Figure 1.1C** and **D**).[12]

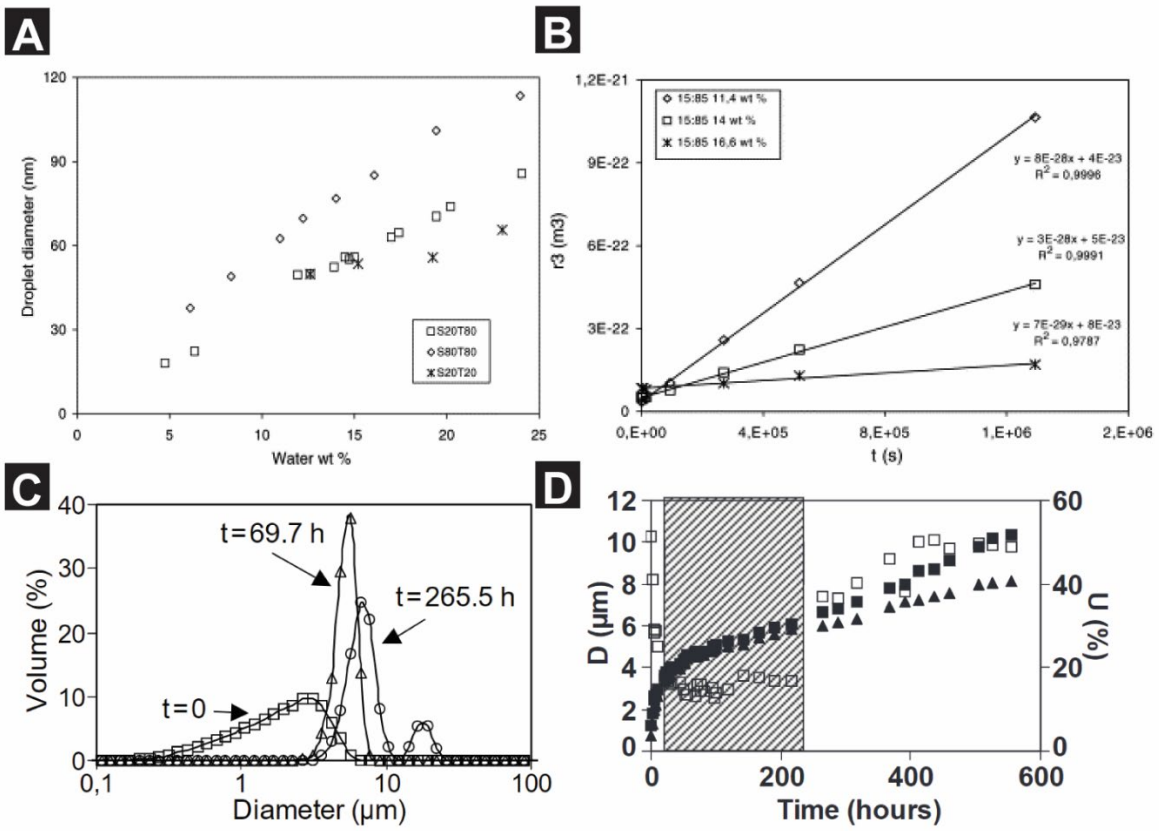

Figure 1.1 Photon scattering methods used to characterize emulsions
(A) Size distribution as a function of water content across three surfactants, establishing design parameters through formulation[14] (B) Nanoemulsion size over time as a function of formulation, indicating stability[14] (C) Size distribution over time of an octane in water emulsion stabilized by SDS[12] (D) Time evolution of dispersity of the aforementioned emulsions, which is used to infer predominant methods of ripening [12]

1.1.2. X-Ray Scattering

X-ray scattering is the result of interaction with molecular electrons and contrast is generated by variations in electron density through the molecule. Here, the degree of scattering is inversely proportional to real space length scale, and falls into two main regimes: wide angle for atomic scale study and small angle for nanometer features and longer.[20] For the purposes of this work, we will primarily consider small angle x-ray scattering (SAXS), as it is the more relevant length scale for emulsion morphology. In SAXS, elastically scattered X-rays are collected, and solvent background is subtracted to generate a scattering signal from the solvated material, giving detail to a spatial resolution of nanometers. These scattering patterns must be fitted to a structure

function. While software does permit automated assignment of the form factor, much of the onus is on the researcher to correctly interpret and assign the fitting parameters, making it a difficult and nuanced process. Many studied emulsions are assumed to be spherical droplets, but differences in structure as a function of formulation or concentration may be elucidated (**Figure 1.2A**, **Figure 1.2B**).[21,22] In more complex cases, real space reconstruction is challenging with SAXS data and is often facilitated by coherent SAXS.[23] Excellent *in situ* SAXS studies have been undertaken to probe the evolution of emulsion polymerizations in time, which have indicated structural evolution in time (**Figure 1.2C**).[24,25] However, these studies still employ direct observation to confirm morphology.

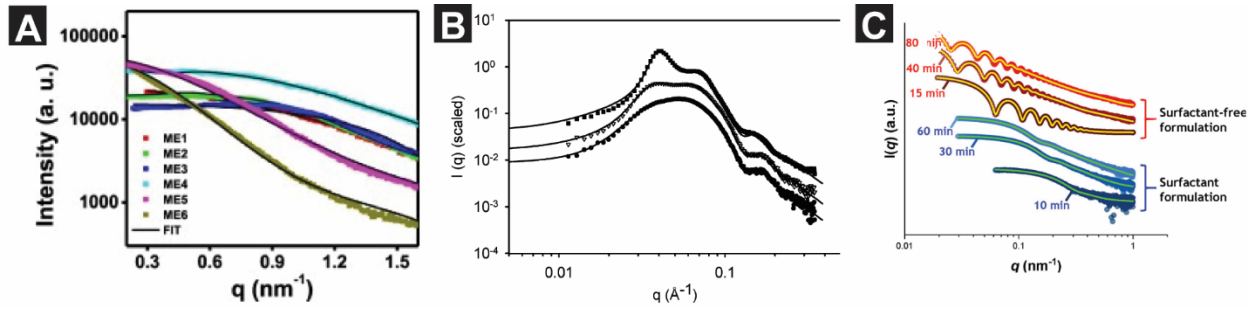

Figure 1.2 SAXS data of emulsions

(A) SAXS traces and fits for emulsions as a function of surfactant. Here, ME1-ME6 are the same formulations with varied surfactants, with variations in form factors present[21] (B) SAXS data at a fixed level of surfactant coverage as a function of volume fraction of the dispersed phase[22] (C) Time resolved SAXS data of an aqueous emulsion polymerization with and without surfactants present shows evolution of structures over time[24]

1.1.3. Neutron Scattering

Unlike SAXS, contrast in small angle neutron scattering (SANS) arises from the interaction of the incident beam with the nuclei of the studied material. Thus, SANS operates in a different q-range than SAXS, and as such, is able to probe other features.[26,27] For many of the systems discussed, the combination of SAXS and SANS is necessary for mechanism corroboration, given that the structure and interactions are fundamentally mixed in the available q-range.[28] Additionally,

kinetic studies are typically less feasible in SANS than SAXS due to limitations of flux.[11] Thus, it is common to see SANS used in combination with a variety of other techniques, including SAXS, DLS, and MD.[27,29,30]

SANS can be used to evaluate interfacial thickness and amount of adsorbed surfactant utilizing contrast matching with hydrogenated and deuterated species.[31] Under appropriate dilution, radii of gyration of dispersed moieties may also be obtained. These two pieces of information, in combination, can indicate the volume fraction of surfactant in the interfacial layer by using a geometric consideration of radius, interfacial thickness and quantity of adsorbed surfactant, and such information is crucial in understanding emulsion stability.[31] SANS can be used for *in situ* variable temperature experiments to probe morphological transformations, such as phase inversion (**Figure 1.3A**).[29] It can also investigate slight structural changes a function of surfactant concentration, and can identify regions based on contrast matching (**Figure 1.3B**).[32] Again, SANS is commonly used in tandem with other techniques like SAXS, given the difference in accessible q-regions (**Figure 1.3C**).[30] Due to logistical constraints, SANS is less commonly used than SAXS.

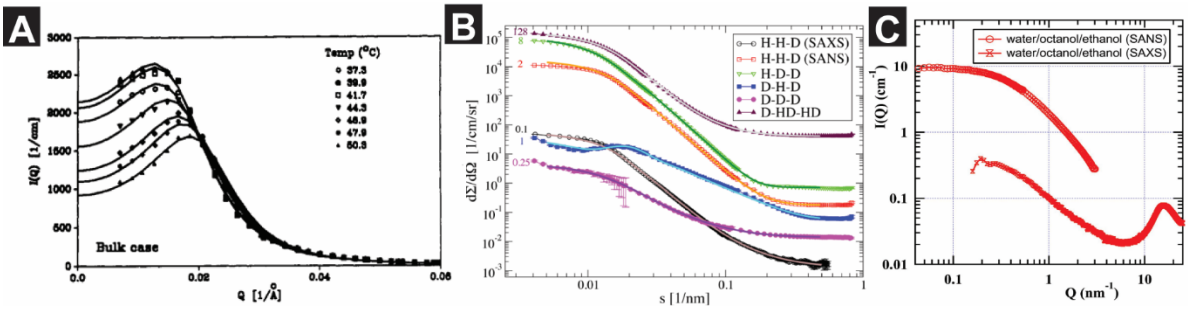

Figure 1.3 SANS data for mixed phase systems
(A) Variable temperature SANS to probe structural evolution of bicontinuous microemulsion as it experiences phase inversion from water-in-decane to decane-in-water [29] (B) SANS traces for emulsions as a function of DMPC concentration, with a SAXS trace included for comparison[32] (C) Comparison of SAXS and SANS traces for detergentless ouzo-type emulsions of octanol in water and ethanol[30]

1.2. *In silico*

In silico simulations are a powerful tool that can model and depict structures and dynamics of molecules, interfaces, and self-assembly processes.[33,34] Such simulations are useful methods to visualize processes on a molecular or atomistic length scale and at extremely high temporal resolution. In the case of emulsions, such a close view can necessitate an assumption of a planar interface.[35] While this assumption is often accurate to a first approximation, the nuances of more complex morphology and behaviors may not be accurately represented in this view. Additionally, some processes are also necessarily disallowed in order for the simulation to run properly, such as nanobubble formation, which can significantly impact emulsion behavior.[33]

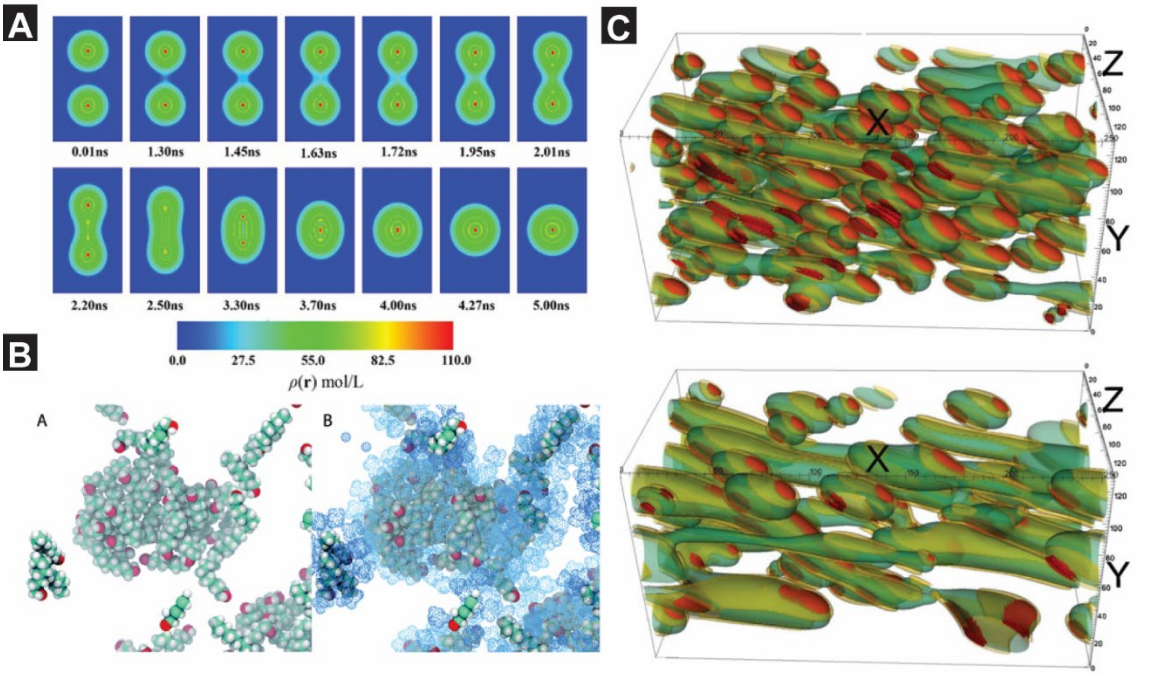

Figure 1.4 Simulations of emulsion dynamics and formation.
(A) Time-dependent density functional study of nanodroplet coalescence in time[36] (B) Molecular dynamics following the formation of surfactant-free micelles from ternary solutions[37] (C) Morphology of emulsions under shear as a function of surfactant strength – high surfactant strength (top) and low surfactant strength (bottom)

Time-dependent density functional theory has been used to simulate the intermediates present in the process of nanodroplet coalescence and has shown the emergence of a "peanut"

structure during the bridging of individual droplets, and the subsequent drainage into a singular spherical droplet (**Figure 1.4A**).[36] In the case of these nanodroplets, the time scale is on the order of nanoseconds, which precludes study by nearly any other physical mechanism.

Molecular dynamics (MD) have been utilized extensively by Schöttl to predict and describe the behavior in spontaneously emulsifying ternary systems. [37–39] Here, MD has been used to generate simulated scattering traces across different contrast variations, which are then compared to experimental SAXS data for validation. While the scattering corroborates the validity of the simulations, the results from the MD experiments are able to give the most detailed structural information about the studied ultra-flexible microemulsions. These experiments have followed the emergence of oil-rich clusters which then evolve into micron scale droplets which are comprised of a percolated bicontinuous network (**Figure 1.4B**).[39]

Direct numerical simulation can also be used and has modeled the effects of shear in emulsions as a function of surfactant strength, which necessarily dictates the properties of the interface.[40] Here, lattice Boltzmann simulations were used to circumvent the challenge of experimentally evaluating the dynamics of surfactant interfaces under variable conditions. Such lattices were able to examine the effects of changing volume fraction of the dispersed phase and the ionic strength of the surfactant (**Figure 1.4C**).

Like modeling, one can theoretically derive estimations of emulsion properties from calculations based on constitutive equations. Such approaches can give information about ‘unmeasurable’ details and provide insight prior to synthesis, but again are dependent on assumptions and may not accurately reflect the breadth of conditions present in reality.[41]

Overall, *in silico* experiments are excellent ways to narrow in on phenomena which are too rapid or too small to observe physically, but are well complemented by the scattering techniques previously discussed, and can give helpful context for the interpretation of such. [37] Limitations of such approaches include the computational intensity of many of these simulations, especially at large spatial and temporal scales. While coarse grained models may be used in order to more efficiently simulate larger systems, these are often difficult to reconcile across length scales. Regardless, all simulations require the input of some boundary conditions and parameters, necessitating *a priori* assumptions. Perhaps the biggest barrier in applying these methods is that the researcher typically sets out to observe a given process or phenomenon, so it is difficult to ascertain how often such events truly occur in the actual sample, or if other phenomena are simultaneously occurring.

1.3. Direct Observation

Direct observation of a material removes much of the ambiguity in structural assignment, but is often more experimentally complex. The material must be prepared in a manner suited to the observation technique (dyed, vitrified, *etc*.). Additionally, imaging a material gives information about a subset of the sample population – statistics of size distribution and the like are limited to what is in the field of view, and may thus not be representative of the whole. Some techniques may also result in experimental artifacts, such as alteration of structure and size when drying samples for conventional electron microscopy.

1.3.1. Optical and Fluorescence Microscopy

Optical microscopy has long been the only approach for seeing the structure of emulsions, given their structural dependance on hydration and the wide range of sample compatibility. However, this approach is inherently limited by the resolution granted by the wavelengths of

visible light. Auxiliary techniques such as polarization and fluorescence may be used to improve spatial resolution and highlight features of interest, but have their respective restrictions: polarization showcases only birefringent features, and fluorescence requires the addition of an appropriate tag or dye, which then incurs assumptions about which phase is localizing the tag.[42] Leveraging these fluorescent moieties, many techniques also utilize averaging or frequency dependent responses (e.g., fluorescence resonance energy transfer (FRET) or stimulated emission depletion microscopy (STED)), which means that the time scale of observable processes is also inherently temporally limited by the nature of detection—that is, if collection of sufficient signal to form an image requires 1 minute of data collection, many dynamic phenomena will be invisible by these methods.[34] W/o emulsions in particular are especially constrained to optical microscopy due to sample preparation constraints for other higher resolution alternatives like electron microscopy, which will be discussed in more detail in the next section.

In its simplest form, optical microscopy uses a series of glass lenses to magnify a sample located below it. Because this is conducted in open air, the sample may be fluid or fixed, and simple strategies like employment of a coverslip can be used to prevent evaporation and other sample altering processes. For this reason, it is typically the easiest and most straightforward way to probe emulsion morphology, and doing so can generate images with reasonable resolution (**Figure 1.5A**).[43] Here, the assignment of phases is reliant on differentiation by refractive index and *a priori* knowledge of which phase was dispersed. These capabilities can be augmented by the use of fluorescence capabilities, such as by utilizing a dye with selective solubility. For example, Nile Red is a lipophilic dye which localizes to the hexane in the o/o/w dispersion below, making the droplets fluoresce red when illuminated with a higher energy light source and confirming the previous assignments of phases (**Figure 1.5B**).[43] Polarized light microscopy takes the approach of

illuminating the sample with polarized, or directional, light in order to interact with the birefringent and anisotropic features in a sample, which can be useful when the oily domains in the dispersed phase have crystallized, such as in many food emulsions like whipping cream (**Figure 1.5C**).[42,44]

Turbid emulsions can pose a significant challenge for the aforementioned techniques, given their strong scattering of visible light, which may be the result of either a high volume fraction of the dispersed phase or the presence of large droplets. In such cases, single molecule localization microscopy can circumvent this by utilizing fluorescent interfacial labels. Here, the transient illumination of these tags allows superior resolution as a result of their increased separation from the background, which yields a surpassing of the diffraction limit in super-resolution microscopy (**Figure 1.5D**).[45] These techniques can also yield a topographical picture of such systems with sufficient signal and resolution. For example, a series of images may be taken at varying focal planes to generate a sequence of micrographs throughout the depth of the sample in order to interrogate the network structure of the emulsion (**Figure 1.5E**).[45]

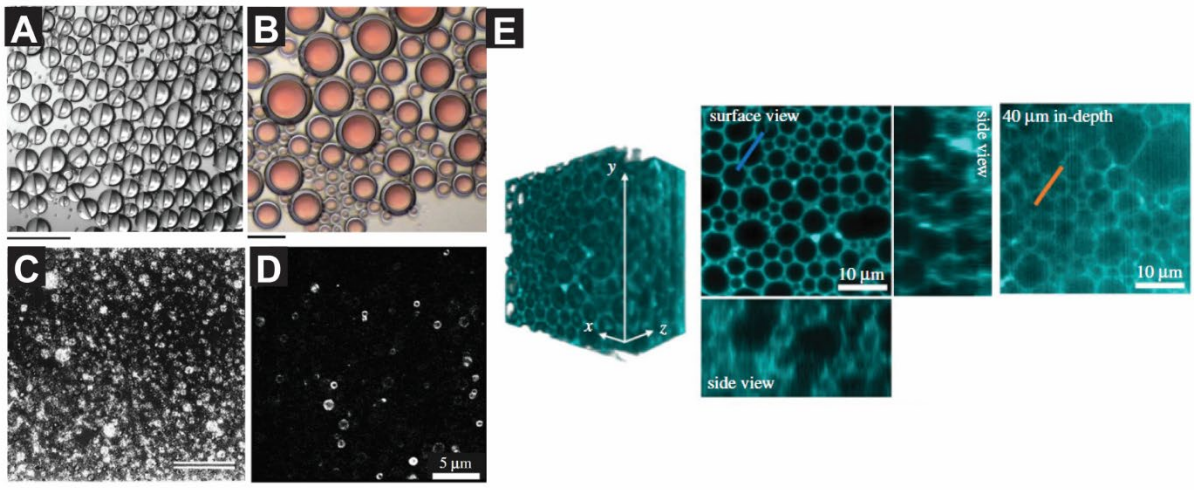

Figure 1.5 An overview of optical and fluorescence micrographs of typical food emulsions.
(A) Optical microscopy of Janus droplets in a triphasic emulsion of ethyl nonafluorobutyl ether and dichlorobenzene in water. Scale bar is 200µm[43] (B) Fluorescence microscopy of another triphasic emulsion with core-shell droplets of hexane in perfluorohexane in water. Nile Red selectively solubilizes in the hexane phase. Scale bar is 100µm[43] (C) Whipping cream in the polarizing microscope, where the crystallized milkfat exhibits birefringence shows as a lighter

phase. Scale bar = 5μm[42] (D) Super-resolution micrograph of rapeseed oil in water, where SDS and phosvitin were used as surfactants. Phosvitin was conjugated with Alexa Fluor647 for the STORM measurements[45] (E) Three dimensional rendering of model food emulsion generated by z-stack of confocal images detecting Nile Blue tag[45]

1.3.2. Scanning Electron Microscopy

Scanning electron microscopy (SEM) is a form of low voltage electron microscopy, where electrons are used to illuminate the sample, rather than photons.[46] Given the relative wavelength of electrons with respect to photons, it is physically possible to achieve significantly greater resolution, and has thus enabled the visualization of nanoscale materials and features. An electron source is passed through magnetic lenses prior to reaching the sample, which require the column of the microscope to be under extremely high vacuum conditions.[47] Thus, samples inserted into the microscope must be dry, fixed, or sealed to prevent evaporation and column contamination. These instruments typically operate at an accelerating voltage of 30kV (compared to >80kV for most TEMs) and relies on a scanning probe approach to generate topological images of a sample surface at (typically) lower magnifications. Images are most commonly generated by the collection of secondary electrons which are emitted by the sample upon application of the electron probe. In order to produce such electrons, the specimen needs to be conductive, which may be achieved by applying an appropriate coating.[48]

Environmental SEM (ESEM) is a specialized approach, whereby applying sufficient vapor pressure in the sample chamber, the material remains in the liquid phase. [42,49] Such setups rely on specialized gaseous secondary electron detectors in order to acquire signal. These are typically operating under environments of water vapor, which is not sufficient to prevent evaporation of alternate solvents, so it is primarily useful for imaging of o/w emulsions (**Figure 1.6A**). Samples are typically cooled under reduced pressure before filling with vapor.[49] Matthews *et al.* were able to image a variety of o/w emulsions via ESEM using the protocol outlined above (**Figure 1.6B**).

The w/o emulsions they prepared were not sufficiently stable for imaging, and demulsification is evident (**Figure 1.6C**).[49]

The low temperature required for study (2°C) may also preclude the use of many organic phases of interest, as this is below the melting point for many alkanes and oils, and would thus cause the solidification and structural alteration of such materials. The partitioning of the instrument which is required to maintain pressure also precludes the application of external stimuli, such as heating or flow. Thus, ESEM is useful for imaging the demulsification of a prepared material, but is not able to image processes induced by addition of external perturbations. Additionally, the image exposures for this study ranged from 1 to 26 seconds per image, as dictated by limitations of signal. This is sufficient to evaluate morphological evolution in time, but is too slow to image individual dynamic events, such as coalescence or flocculation.

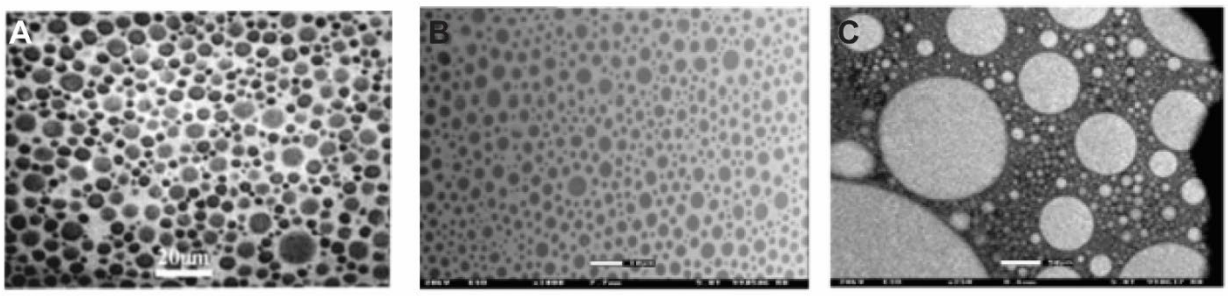

Figure 1.6 Emulsions imaged by Environmental SEM (ESEM)
(A**)** Vegetable oil in water via ESEM[50] (B) Diheptyl phthalate in water and (C) water-in-deheptyl phthalate emulsions imaged via ESEM, with scale bars of 10 and 50 μm, respectively [49]

1.3.3. Atomic Force Microscopy

Atomic force microscopy (AFM) has been employed in the study of emulsion morphology and structure in a manner similar to conventional TEM, where dispersions of interest are diluted and deposited onto a substrate (here, mica or another AFM surface) before applying a probe in tapping mode.[51] There are many published reports of such studies, and some are in agreement with

correlative studies (such as TEM, SAXS, or DLS), but many are plagued by discrepancies in droplet size.[52,53] This is unsurprising in that the dehydration of such materials is known to yield structural alteration, just as in TEM. AFM is beneficial in that it is able to give topological information in a third dimension, which eludes most other methods of observation. Emulsions must be significantly diluted (typically, 100-1000x) in order to study by AFM so that a dense droplet population does not confound the results (**Figure 1.7A**).

Some AFMs are equipped with liquid or solution cells, where the cantilevers are able to probe hydrated materials. This is referred to as solution-state or liquid phase AFM and can give excellent resolution (on the order of 5 nanometers) in liquid and has successfully been used to image self-assembly processes (**Figure 1.7B**).[52] However, this technique relies on fixation to and interaction with substrate. Emulsion droplets must be anchored to the substrate prior to study so that they are not displaced by the motion of the cantilever. Several groups have taken the approach of affixing a droplet to the cantilever to force droplet-droplet interactions for study (**Figure 1.7C**).[54,55] This is an excellent way to study droplet-droplet interactions and substrate interactions at high spatial resolution in the liquid phase. While the induction of such events is useful for study in that one doesn't have to rely on the stochastic nature of the processes, it does also preclude their observation in their native state. That is, the interaction as it occurs in the native sample cannot be studied. The emulsion must also be pre-formed, and low in complexity (*i.e.,* multiple or bicontinuous morphologies are not amenable to this technique).[52]

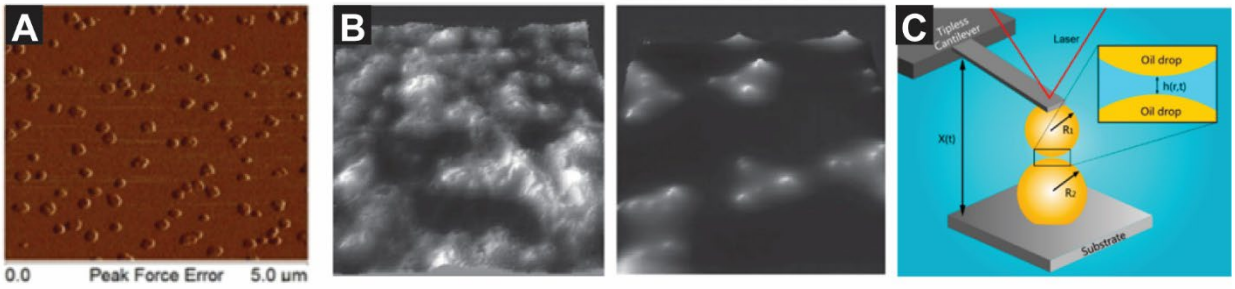

Figure 1.7 Atomic force microscopy of emulsions via several approaches
(A) Conventional AFM of curcumin-loaded nanocapsules [52] (B) AFM of TW-30 (left) and WPI-stabilized (right) nanoemulsions demonstrating aggregation tendency[52] (C) Schematic depiction of droplet-cantilever attachment for probing interdroplet interactions.[54]

1.3.4. Transmission Electron Microscopy

Transmission electron microscopy (TEM) is analogous to optical microscopy, except that electrons are focused for sample illumination, rather than light.[46] This technique is complementary to SEM in that here, electrons transmitted through the sample are collected. This means that specimens are much more limited in thickness (sub-micron is optimal). The same constraints of the vacuum as previously discussed still apply, but the sample need not be conductive. For an emulsion, if the system of interest has a solidified structure (such as a polymerized latex or metallic nanoparticle synthesized *in situ*), conventional TEM grid sample preparation is useful to image the structures which remain after solvent evaporation (**Figure 1.8A, B**).[56–58] However, given that the majority of emulsions have solvation-dependent structures, one of the aforementioned preservation techniques must generally be used to probe emulsion structure.

1.3.4.1. Chemical Fixation

Fixation of a sample is fundamentally trapping a sample in its current state to preserve it for prolonged study. This can help to mitigate damage imposed by the electron beam and increase contrast to permit higher resolution imaging.[59] Such techniques are especially useful for biological materials, which are sufficiently complex to necessitate such approaches. However, limitations of

chemical fixation include alteration of structure and, in soft materials, may even displace components of the system. These methods typically utilize heavy element-containing compounds (such as osmium tetraoxide or uranyl acetate) to both stabilize structures and enhance contrast.[60–62] These approaches are particularly used in structural biology, where the complexation with such fixatives with various cellular components is well known. Paraffin or epoxy embedding is often used in conjunction with microtomy in order to generate stable thin samples (**Figure 1.8C, D**).[62,63]

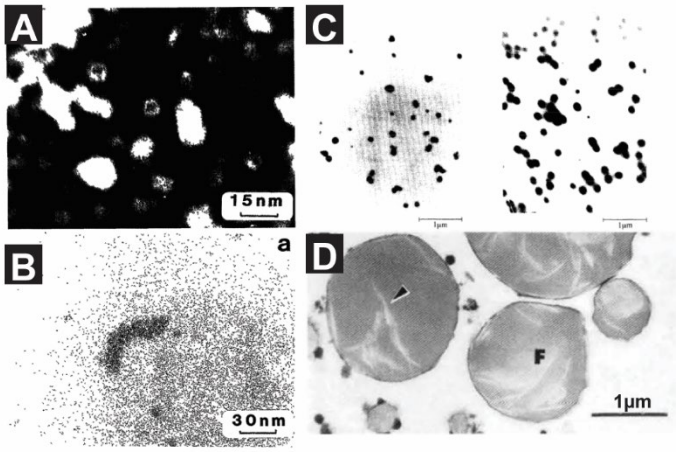

Figure 1.8 Conventional TEM of emulsions.
(A) and (B) showcase reverse micelles by bright and dark field electron spectroscopy imaging, respectively[56] (C) Demonstration of the influence of the core-shell ratio on emulsion morphology in acrylic-polyurethane emulsions, with a 50/50 core-shell ratio on the left and a 70/30 ratio on the right. Samples were embedded in a water-soluble epoxy resin for sectioning [62] (D) Micrograph of fat globules stabilized by Polysorbate80 in an ice cream mixture, which was fixed in an agarose gel before staining with osmium tetroxide, paraffin embedding, and sectioning[63]

1.3.4.2. Cryogenic fixation

While cryogenic transmission electron microscopy (cryo-EM) has single handedly revolutionized structural biology's ability to image preserved structures and materials, such advances are not necessarily transferrable to all areas of materials science.[64] Such techniques are incredibly useful for aqueous, dilute systems such as polymeric assemblies and peptide-based materials and can be sufficient for dilute emulsions with an aqueous continuous phase.[65] Dilute

aqueous emulsions may be imaged by conventional cryo-EM vitrification techniques and while it is not possible to image the transitions between states, careful sample preparation may reveal morphology at elevated temperature (**Figure 1.8A**).[66]

However, such sample preparation techniques fall short for high viscosity materials, samples in non-aqueous solvents, or materials with multiple phases present.[67–69] In these systems, vitrification is much more difficult, and generally is determined by the specific phase diagrams of the solvents in use. For example, cryo-EM has been done of polymers in toluene, but required vitrification in nitrogen, as solid toluene would dissolve in ethane.[70] Even under the most optimal conditions, the tendency of linear hydrocarbon molecules to crystalize upon freezing makes vitrification of such substances practically impossible.[71]

Several advanced sample preparation techniques have been developed for cryo-EM of complex materials—namely, freeze fracture. Freeze fracture is a technique whereby a thicker liquid layer is vitrified and subsequently fractured to generate an interface in the sample which is able to show material topology.[72–75] This is often achieved by high pressure freezing, which vitrifies the sample under extreme pressures so as to circumvent issues of reduced thermal conductivity.[76] In these samples, rates of cooling are often far lower than what is typically used in conventional cryo-EM, either due to sample thickness or use of alternative cryogens (e.g., liquid nitrogen). This slowed cooling can lead to excess nucleation and growth of crystalline ice, thereby obscuring and altering the sample. The application of high pressures slows such processes to rates commensurate with achievable cooling rates. Cryoprotectants may also be used to additionally slow these rates, but again may alter structures.[67,72,76,77] High pressure freezing is typically followed by creating of a fracture surface to permit imaging of the interface.[59,73,76,78] For stability, this interface is often replicated via coating, and then this replicate may be imaged without the

need to maintain the sample in its vitrified environment.[77] The freeze fracture surface may also be directly imaged, rather than creating and imaging a replica, which is referred to as freeze fracture direct imaging (FFDI).[72] While HPF is a useful sample preparation technique, extensive parameter optimization is needed for each alternative solvent due to differences in material properties.[7] However, given the issues associated with low solvent vapor pressure, this has historically been one of the only ways to fix reverse (w/o) emulsions for nanoscale imaging. Marchand *et al.* presented one of the few examples in their 2002 work, where they vitrified micelles of water in n-heptane and subsequently deposited platinum and carbon vapors in order to image their microemulsions (**Figure 1.8B**).[77] While this enabled morphology visualization, they do note that their observed micelle dimensions differ from that recorded by scattering and attribute the discrepancy to alterations incurred during the freeze fracture process.

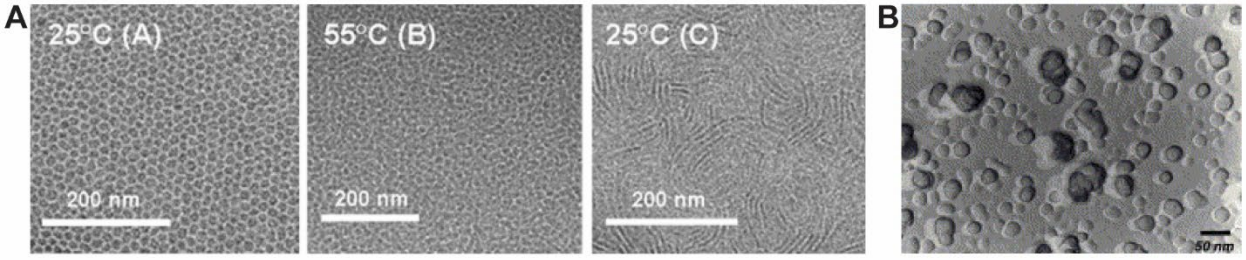

Figure 1.9 Cryogenically-fixed EM micrographs of emulsion structure
(A) Cryo-EM of vitrified samples showing the phase transitions in o/w lauryl acrylate emulsions during phase inversion[66](B) AOT-based microemulsion by freeze fracture TEM[77]

1.4. Liquid Phase Electron Microscopy

In situ microscopy, and liquid phase electron microscopy in particular, has been an increasingly adopted set of techniques over the last 20 years.[79] Such techniques permit observation of samples in their native states and with applied stimuli, thus circumventing the need to prepare time series samples. We note here that the contrast of the images shown in this section is inverted with respect to those shown in the SEM section above, given the reversed relationship between

intensity and contrast between the two techniques. Contrary to environmental SEM/TEM, rather than acclimating the microscope to the sample conditions, *in situ* electron microscopy relies on compartmentalization of the sample, typically by sealing it between impermeable membranes. This permits the use of high-resolution detectors, rather than detecting gaseous scattering (such as in ESEM). Additionally, by sequestering the sample via the holder and sample cell, a dedicated environmental instrument is not required, and all that is needed is physical compatibility of the *in situ* holder with the microscope. In the case of graphene liquid cells, a designated *in situ* holder is not even needed, as such samples are typically fabricated on standard TEM grids, which may be imaged in a conventional TEM holder.[80] These factors make this approach more facile than environmental electron microscopy, as it is far simpler to change the sample cell instead of the microscope condition.

Most of the early LPTEM studies focused on evolution and dynamics of aqueous metallic nanoparticles under the irradiation of the electron beam.[81] Materials in organic solvents have more recently been explored, and in fact may be advantageous over aqueous systems due to reduced rates of radiolysis.[82] LPTEM has only lately been used to examine mixed phase systems, beginning with studies of *in situ* liquid-liquid phase separation processes, and more recently, studies of morphology and formation of both o/w and w/o emulsions.[5,6,83–87] TEM benefits from superior spatiotemporal resolution with respect to many of the previously described techniques, both as a function of illumination source and detector technologies. Thus, it is feasible to acquire nanometer resolution images at sub-second time intervals. The contrast in LPTEM arises from the density differential between the two materials, so phases require no additional dyes or tags for differentiation.

Prior to our work leveraging LPTEM to methodically image emulsion morphology and dynamics (discussed in **Chapter 2**), there were few literature examples of imaging such materials by this technique. In particular, there are two studies of note which warrant discussion. Stawski *et al.* used a w/o microemulsion to sequester their reagents prior to imaging, before subsequently destabilizing the droplets by flowing in ethanol, resulting in the crystallization of $CaCO_3$ (**Figure 1.10A**).[87] Their use of an isooctane/AOT/water microemulsion represents the first known *in situ* imaging of this system. However, the purpose of this study was to image nucleation and growth processes of $CaCO_3$, and thus the microemulsion served to delay reagent mixing prior to imaging. Droplet morphology was imaged prior to the disruption of the emulsion by addition of ethanol, but it was not the focus of study and thus, the effects of formulation, imaging conditions, *etc*., were not considered. Further, emulsion dynamics and demulsification were not considered. In other words, the emulsion was simply used as a tool to sequester reagents.

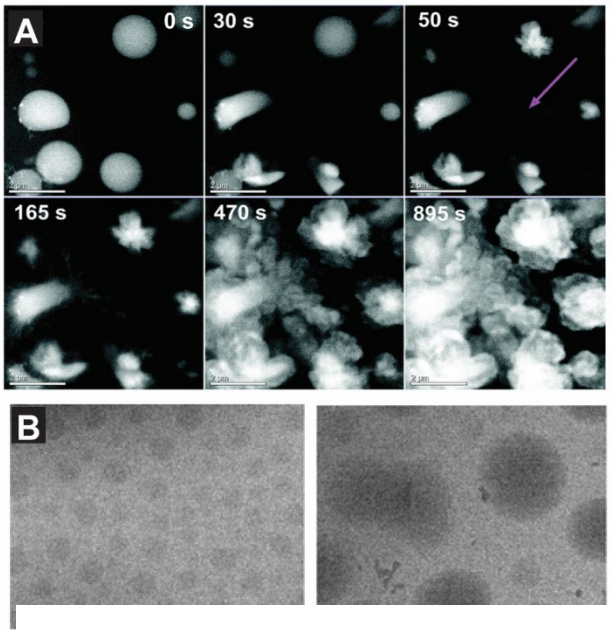

Figure 1.10 Previous *in situ* studies of emulsion morphology

(A) Isooctane/AOT/water emulsion to separate reagents prior to imaging, where ethanol was used to rupture droplets and induce nucleation.[87] (B) Oleic acid in water emulsion stabilized with CTAB without (left) and with (right) gold nanorods.[86]

The other study which we would like to note is that of Wang *et al.*'s visualization of gold nanorods dynamics in an emulsion of oleic acid in water (**Figure 1.10B)**.[86] This oil-in-water emulsion was stabilized by cetyltrimethylammonium bromide (CTAB), a commercial cationic surfactant, and was primarily used to localize gold nanorods in order to observe their self-assembly and dynamics. Emulsion destabilization is noted, with the observation that anti-Ostwald ripening

behavior is present in some cases. While this is an interesting study, we contend that the liquid water is no longer present in these liquid cells – fundamentally, because the oleic acid is less dense than the water, in bright field images, it should appear lighter than the background (as we will demonstrate in this thesis – see **Chapters 2** and **4**). However, the images published here show dark droplets. Where gold nanoparticles have been included, they also appear as a high contrast material, so the images are not dark field or inverted contrast. The only way in which the less dense oil phase can appear dark in this case is if the continuous phase of water has dried (an unfortunately common phenomenon in LPTEM). Thus, while their discussion of the gold nanorod dynamics may have some validity within the remaining oil droplets, we feel that more careful consideration of emulsion dynamics themselves is necessary, both in terms of experimental conditions (low flux) and corroborative controls. Videographic data was captured at 1 or 2 frames per second, a rate which exceeds that achievable in ESEM, but still precludes visualization of the dynamic processes of interest to us (*e.g.,* coalescence). Additionally, gold is a known sensitizer for radiolysis, and thus there may be significant material damage that could also be contributing to anomalous behavior.[88–90]

These studies of emulsion morphology via LPTEM were incidental, and emulsions were used only as a tool by which to study other processes of interest, and thus we maintain that more careful and methodical studies of emulsions themselves are warranted. The addition of solutes and nanoparticles have known effects of the behavior of these materials, and thus they must be studied in isolation to truly establish this technique's utility.

If we consider the *in situ* formation of these materials, there are some examples of studies of liquid-liquid phase separation from which we can draw inspiration.[85,91,92] Liquid-liquid phase separation is a sort of emulsification where amphiphiles are induced to assemble upon some

stimulus (typically, a change in solvent conditions), and is a process of significant synthetic and biological interest.

Ianiro *et al.* examined phase separation phenomena during amphiphilic block copolymer assembly, observing the formation of polymer-rich liquid droplets and the subsequent transformation to micelles and vesicles as a result of solvent switching (**Figure 1.9A)**.[92] These structures were beautifully corroborated by correlative cryo-EM, and they were able to resolve the reorganization of amphiphiles from a disordered cluster to radial bilayers. From this, they were able to comment on proposed pathways of assembly and provide a unifying description of the process, which would be impossible by any other method. Ianiro also highlighted their struggles with reproducibility, noting that "vesicles were successfully formed on four occasions out of more than 50 attempts". We appreciate their transparency, and experienced similar rates of success in our own work on similar processes.[6]

Shortly after the publication of Ianiro's work, a similar study of biological materials was published by Le Ferrand *et al.*[85] Instead of block copolymers, this paper examined the condensation of an intrinsically disordered protein, Histadine-rich Beak Protein 2, soluble proteins into dense microdroplets under acidic conditions in the addition of salt (**Figure 1.9B**). The formation pathways of the protein nanoclusters were observed at rates which matched bulk measurements well. Different polymorphs were observed as function of solvent conditions, which exhibited differing levels of stability – under high salt conditions, the nanoclusters will redissolve.

Rizvi *et al*.'s work focuses on the self-assembly pathways of amphiphilic block copolymers initiated by solvent switch (**Figure 1.9C**). Polymers were dissolved in a good solvent before exchanging to a selective solvent (in which only one block is soluble), which induced coacervation,

and subsequently droplet merging and bilayer formation. The dense liquid droplets formed homogeneously across the viewing region and demonstrated significant dynamic motion prior to coalescence before stabilizing into a continuous film. This work again provided insight into the pathways by which these condensates were formed and their subsequent evolution into a supported bilayer. Further, Rizvi was able to probe alternate assembly pathways by studying the transformation of pre-formed vesicles as well.

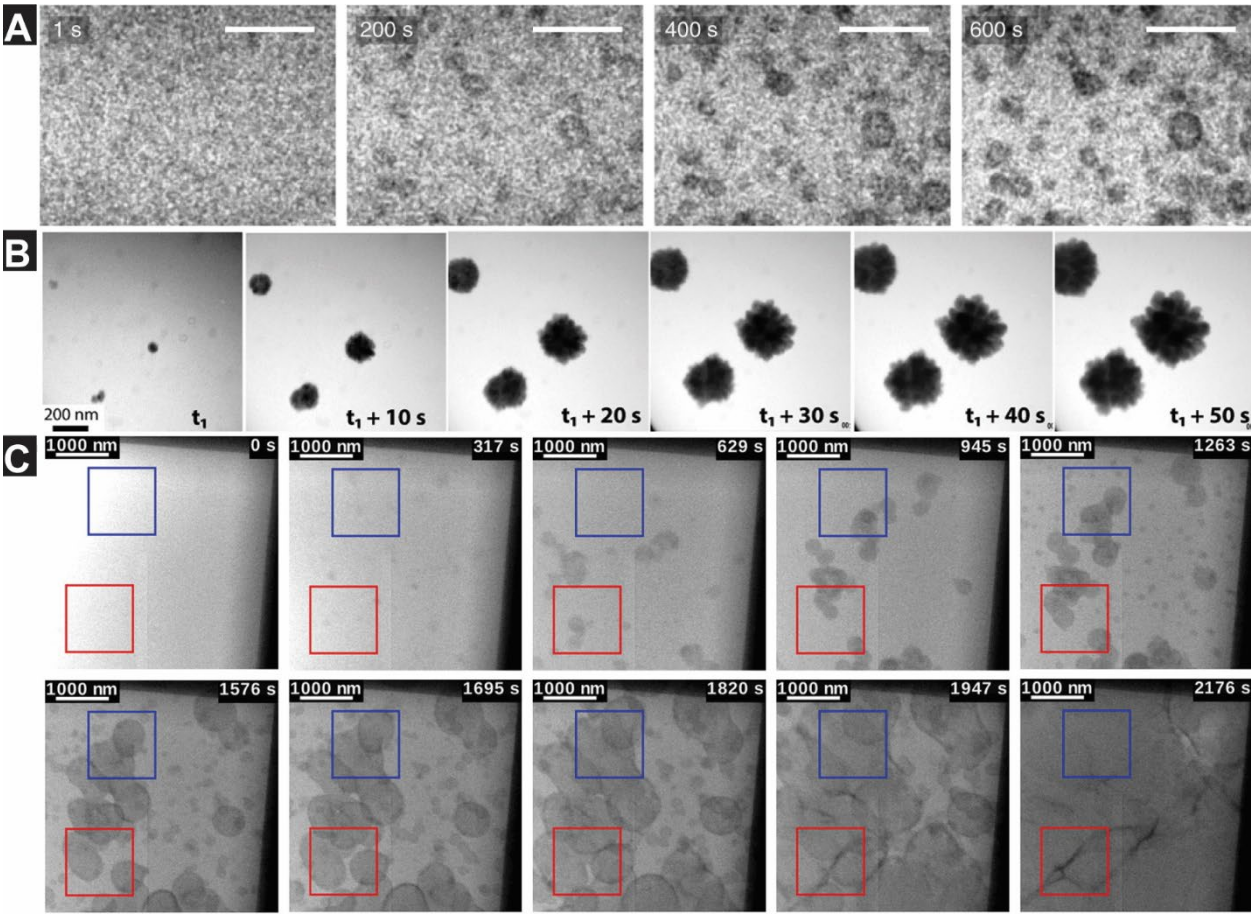

Figure 1.11 *In situ* observation of liquid-liquid phase separation phenomena in natural and synthetic systems.

(A) Polymer-rich liquid droplets condense and grow into micelles, then vesicles upon exchanging solvent from acetone to water[92] Scale bar is 400nm (B) Biomolecular condensates formed under high salt conditions was also achieved *in situ* and corroborated bulk measurements of rate[85] (C) Formation of polymer-rich droplets and subsequent bilayer development upon flow of a selective solvent.[91]

These are significant works in this area and illuminate the area of liquid-liquid phase separation and formation of biomolecular condensates. Collectively, they harness the ability of amphiphilic molecules to transform and assemble into structures in response to environmental changes. In **Chapter 3**, we will expand upon this body of work by studying surfactant-mediated emulsification and surfactant-free spontaneous emulsification, which is a similar process to those discussed above, with the differentiation that ethanol takes the place of the amphiphilic polymers to stabilize the formed droplets.[6] Emulsification of small molecule surfactants has not been previously studied *via* LPTEM and is of significant interest for industrial and commercial applications, which rely upon the formation of such structures.

Another study on similar materials has recently been published regarding the use of *in situ* SEM of gold nanoparticles in an oleic acid emulsion.[93] This approach uses an analogous experimental set up to the LPTEM one previously described (SiN_x membrane encapsulation) and is able to reach comparable magnification (**Figure 1.10**). Correlative LPTEM studies of the emulsion were performed (**Figure 1.10A**). The primary focus in this study was on the application of LPTEM liquid cell techniques to SEM for the study of gold nanoparticle dynamics, but demulsification was also observed (**Figure 1.10B**, **C**).

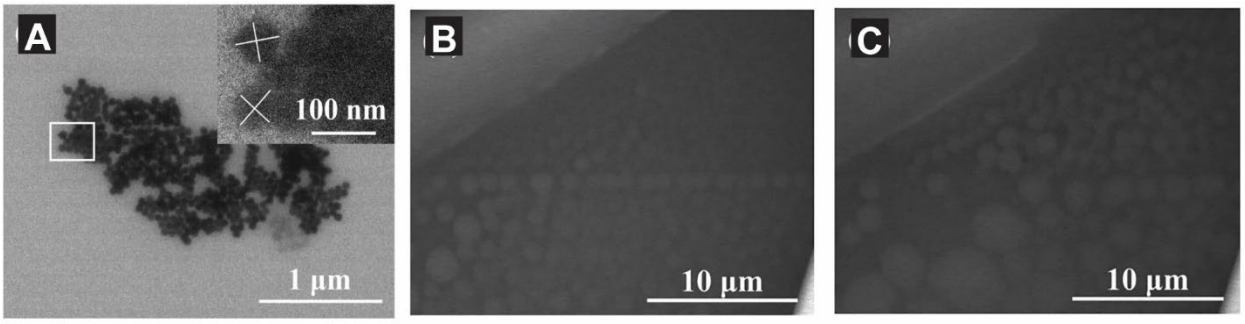

Figure 1.12 Liquid phase TEM and SEM of oleic acid in water emulsion

(A) LPTEM of gold nanoparticles in oleic acid in water emulsion [93] (B, C) LPSEM micrographs of o/w emulsion dynamics. Phase separation over time is visible in the presence of fewer, larger droplets in panel C than in panel B. The time differential is not indicated in the paper in question.

1.4.1. Experimental Considerations of LPEM

We would like to emphasize that all of the above examples utilized SiN_x sample encapsulation, which underscores the robustness of this technique for studying various aspects of various materials with minimal need to optimize between samples. SiN_x LPEM, unlike graphene liquid cells, creates a sample environment with sufficient space for dynamics of the desired scale to occur. Additionally, we contend that this approach is significantly more straightforward than fixation methods. Though LPEM is a challenging technique to learn, once it has been mastered, it is immensely translatable across materials and length scales. Rather than experimenting with high pressure freezing conditions or vitrifying parameters, one can just decide whether or not to make the SiN_x surface hydrophilic via plasma cleaning depending on the properties of the continuous phase.

1.5. Conclusions and Outlook

There are a plethora of characterization methods which are employed to generate information regarding the formation, structure, and stability of emulsions. [2,94] Most often, these techniques are employed in parallel, so as to give more complete information. Sample preparation is a particular challenge for such phase separated systems as a result of the presence of an interface and mixed phases, as well as their dynamic nature. We have outlined above methods in a range of complexity by which such phenomena may be studied, with a particular emphasis on direct observation. For the majority of direct observation techniques, sample preparation is the rate limiting factor for studying emulsions, as they are typically laborious to prepare, and sample prep protocols must be re-optimized for every system. However, LPEM circumvents this by avoiding

the issue of fixation. We will demonstrate in this thesis the versatility of this technique across many mixed phase systems, regardless of formulation (*e.g.,* w/o or o/w) or morphological complexity. Further, this technique is able to assess morphology and dynamics in real time, thereby streamlining the experimental burden to a single experiment. LPEM, we contend, is able to simultaneously replace several of these methods in a single experiment, requiring less than a microliter of sample and minimal sample-to-sample optimization. As such, we believe that LPEM studies of such materials will become commonplace, and an effective high throughput technique for analysis of emulsions, especially when complemented by post-mortem verification strategies and parallel bulk techniques.

In **Chapter 2**, we will demonstrate a methodical study of emulsion morphology and dynamics as a function of formulation and imaging conditions at high spatiotemporal resolution. **Chapter 3** expands on this work by examining the formation of surfactant-based and surfactant-free emulsions. **Chapter 4** outlines a thorough analysis of the observed motion of emulsion droplets *in situ*, and considers broader implications for such motion in the context of LPTEM. **Chapters 5** and **6** consider the applications of our previous work on emulsions and focus on emulsion polymerization and industrial materials, respectively. Finally, in **Chapter 7**, we will provide a brief perspective on the outlook of such work in the field.

Chapter 2 Direct Observation of Emulsion Morphology and Dynamics

This chapter is adapted from the following publication:

Vratsanos, M. A., Gianneschi, N. C. Direct Observation of Emulsion Morphology, Dynamics, and Demulsification. *ACS Nano*, **2022,** 16, 5, 7783–7793

2.1. Introduction

Emulsions are defined as dispersions of two or more immiscible liquids and found with utility everywhere from the human gastrointestinal tract, to condiments, to many common cosmetics.[95] Due to the desire to minimize the contact surface area between two immiscible substances, emulsions are thermodynamically unstable and will eventually completely phase separate.[96] However, surface active agents, or surfactants,[97] may be employed to slow this separation and stabilize the emulsion for longer periods of time. Surfactants are amphiphilic molecules having moieties soluble in both phases, which lowers the interfacial tension so as to allow droplet formation of one phase in the other.[98] There exists an extensive library of classes of surfactant molecules, each with their own respective advantages. However, the commonality among these materials is that for most industrial applications, there is significant interest in minimizing the amount of surfactant included in the formulation.[99] While increasing surfactant content generally extends shelf life, it may also have significant effects on other properties of the substance, such as changing its taste or texture, or causing adverse reactions when used to formulate therapeutics, and may be environmentally detrimental.[99–102] Generally then, there exists a need to optimize formulations with respect to both maximal shelf life and judicious choice of surfactant type and concentration. To achieve this, analytical methods are needed that provide an understanding of how emulsions degrade, and how this is influenced by surfactants and other

additives. To that end, for a given system, fundamental knowledge of the various degradation pathways and emulsion behavior is valuable (**Figure 2.1**).

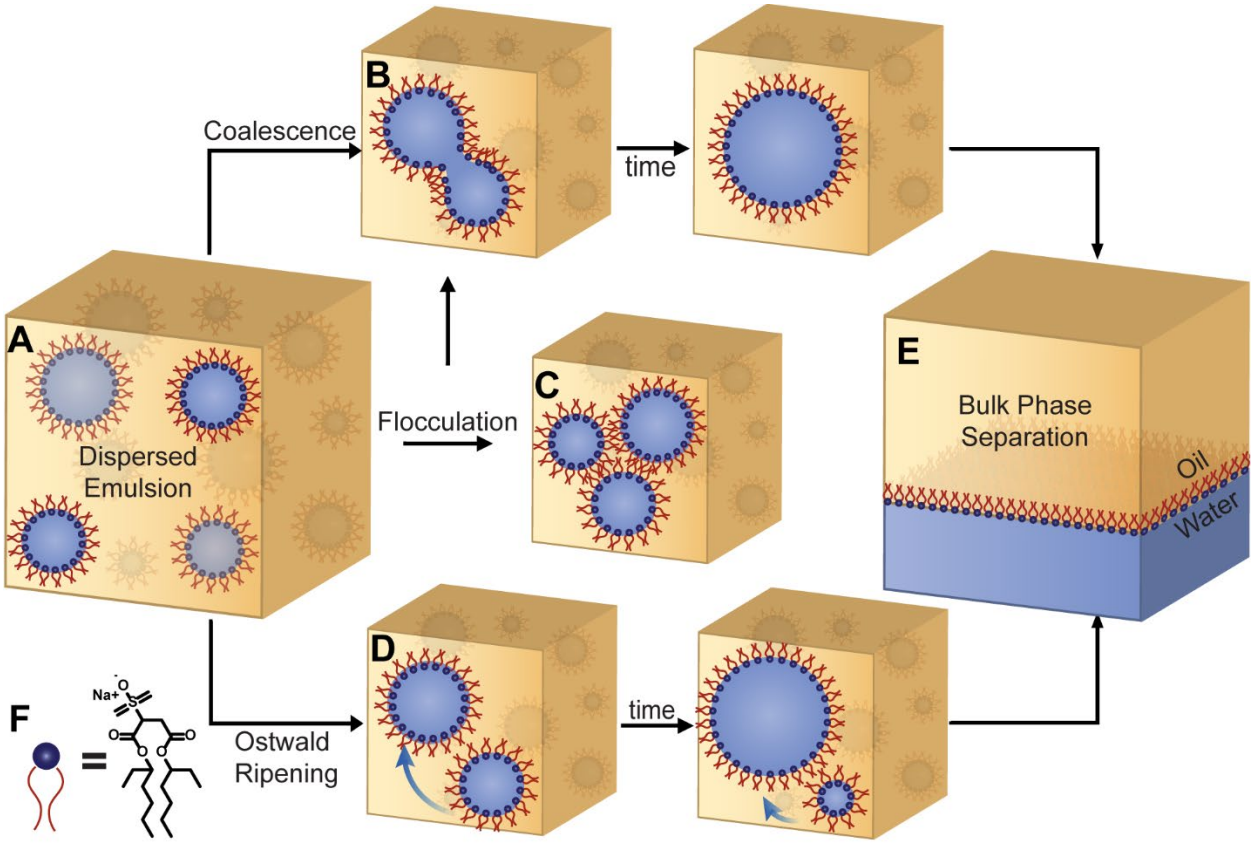

Figure 2.1 Overview of Emulsification Pathways**.**

Emulsions begin as dispersed droplets of one immiscible phase in a continuous one, shown here (A) as a water-in-oil dispersion. Emulsions will experience (B) coalescence, (C) flocculation, and/or (D) Ostwald ripening in time, eventually leading to (E) bulk phase separation. (F) Surfactant molecules are represented by blue and red shape, with the structure of AOT as shown.

Emulsion characterization is currently almost entirely dependent on ensemble methods like light scattering[24,103,104] and rheology.[96,105–107] While these powerful techniques provide information about global populations (such as size distributions and time scales), the inability to directly observe emulsion morphology and behavior at the nanoscale leaves many questions unanswered, especially with regards to demulsification. There are three main pathways for emulsion degradation progressing from an initial dispersed state: coalescence, flocculation, and Ostwald

ripening. Emulsions exhibit these processes, either sequentially or concurrently, to eventually yield a completely phase separated system (**Figure 2.1A-E**).[17,108–114] At various times, the field has focused on either Ostwald ripening or coalescence as the predominant pathway, but it is becoming clear that the relative contributions of each are largely system dependent, both with respect to phases and surfactants (**Figure 2.1F**).[12] However, scattering techniques are insufficient to disentangle the details of multiple processes and are unable to distinguish between the various pathways over time.[115] Further, conclusions drawn from scattering data regarding the kinetics of such processes are based on constitutive models. In Ostwald ripening, many of these predictions are predicated on Lifshitz-Slezov-Wagner (LSW) theory, which was originally derived for particles in a solid matrix, but has been applied with moderate accuracy to oil-in-water (o/w) emulsions.[15,104,108,116] Studies of its application to water-in-oil (w/o) systems have shown deviation from predicted behavior at longer time points (in part attributable to the slower kinetics of the greater molar volume of the solute phase), and have noted its failure to account for the presence of surfactant micelles, as well as its disregard for the effects of droplet concentration.[105,117] Thus, conclusions made regarding emulsions predicated on this theory may not hold true, especially in cases of nanoemulsions. That is, having droplets < 200nm removes sedimentation as a confounding mechanism of degradation, making the understanding of the processes at play even more critical.[108] Further, new models have demonstrated that individual droplets may significantly deviate from predicted Fickian behavior, undergoing anomalous diffusion due to complex mass transfer processes.[110] In this view, ensemble characterization can miss the mark by relying on statistical averaging that destroys the nuances of the process, especially given the reliance of dynamic light scattering on the assumption of Brownian motion.[118] Measurements of optical transmission over time are used to indirectly determine whether Ostwald ripening is occurring, as optical

transparency may qualitatively indicate the degree of dispersity of the droplets.[96] However, this takes a rather coarse view of the process and is easily skewed, as the appearance of even a small population of micron-scale droplets will influence these measurements. Thus, there is a distinct need to develop new methods capable of evaluating these processes. This is further motivated because there is little in the literature focused on the cooperative effects between the various modes. For example, it should be the case that coalescence may be accelerated by Ostwald ripening, and Ostwald ripening may be slowed by coalescence as a result of their respective concentration dependencies.[12] However, many studies only examine either coalescence[119–121] or Ostwald ripening.[17,122,123] Directly observing these processes in concert would complement this work, so as to develop a more complete picture of the system dynamics as a whole. Along these lines, recent study sought to elucidate the relationship between coalescence and temperature of emulsions on the microscale using microfluidic flow and analyzed via optical microscopy, albeit with the necessarily lower spatial resolution afforded by the imaging method.[124] Further, once such fundamental processes are understood, it may also be possible to investigate more complex morphologies and interactions, such as nested or bicontinuous structures and predator-prey inter-droplet behavior.[29,125–127]

Here, we describe a characterization method for direct observation that enables classification and quantification of demulsification mechanisms. Liquid phase transmission electron microscopy (LPTEM)[128–134] enables these observations at the nanoscale with high temporal resolution, leveraging advances in image capture technology.[135,136] For this initial study, we sought to investigate an emulsion that is relatively well understood by more conventional methods (e.g. scattering,[137–140] molecular dynamics and simulations[141–143]), but which was not conducive to traditional methods of imaging. Water-in-oil (w/o) emulsions are an ideal candidate

for this, as they are common in the food and cosmetics industries, but have a continuous organic phase which prevents them from being studied by dry state or cryogenic TEM without extensive optimization of sample preparation.[77,116,144,145] LPTEM, on the other hand, eschews the need to vitrify or dry these materials, and avoids high pressure freezing, while maintaining morphological integrity. The system of choice was the sodium salt of dioctyl sulfosuccinate (Aerosol OT or AOT) with water and isooctane. This system is well characterized and may be made as either the oil-in-water or water-in-oil formulation by varying the relative quantities of each phase. Further, the system is well characterized such that our *in situ* findings can be corroborated with a substantial body of data.[137,139,141,146–150] In addition, this system is ideal in its modularity – the size of the initial micelles may be tuned by adjusting the surfactant loading ratio (i.e., the molar ratio of water to surfactant, referred to as w_o).[141] The emulsion was prepared via established protocols and dispersed via vortex mixing, then kept in a sonication bath to maintain its morphological integrity prior to observation by LPTEM.[87,141,151] Critically, imaging by this method could be reproducibly achieved to capture morphology and, with rapid frame rates of videographic image capture, emulsion dynamics could be observed.[88,152,153]

2.2. Results and Discussion

2.2.1. Emulsion Morphology

Prior to study via LPTEM, formulation of the emulsion was confirmed via dynamic light scattering to ensure that the population was in good agreement with the theoretically-predicted size (~20nm) (**Figure 2.2**). Theoretical size was predicted using the relation $d_{water} = 0.29 * w_o + 1.1$.[154] From this, the size of $w_o = 70$ droplets should be 21.4nm, which is in good agreement with DLS data. When the surfactant loading ratio is decreased to $w_o = 30$, this size expectation decreases to 10.8nm.

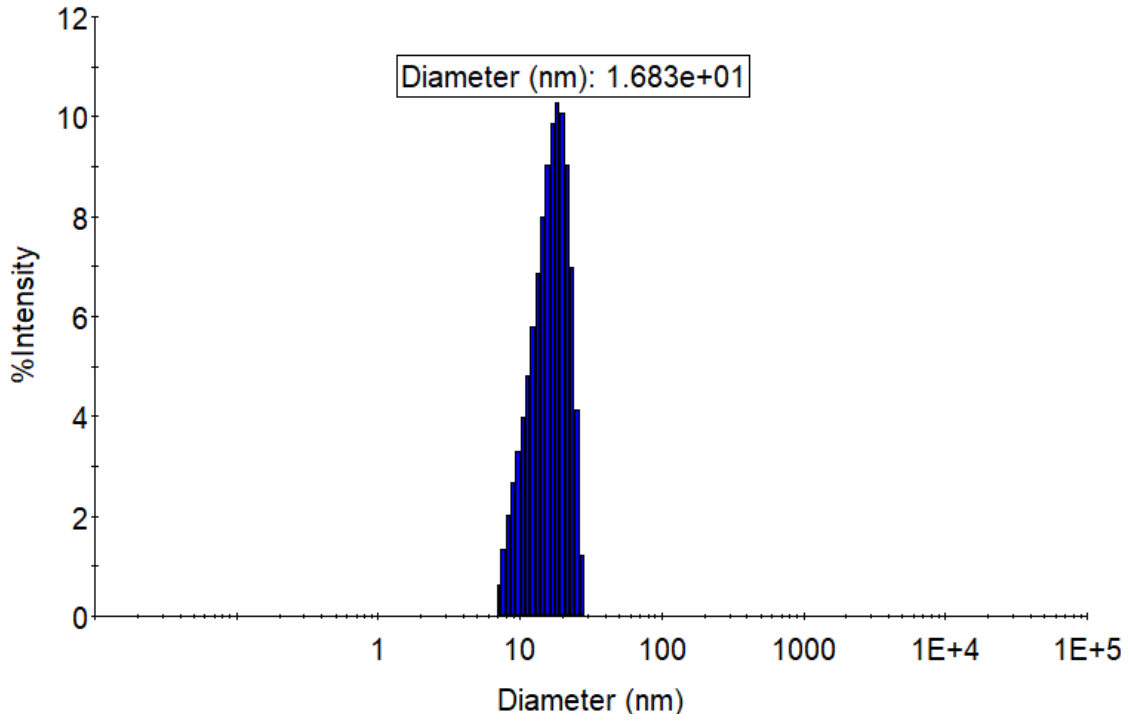

Figure 2.2 DLS trace of water-in-isooctane droplets at wo=70.
Average diameter is approximately 17nm.

Dry state TEM was then attempted on the samples. However, due to the nature of sample preparation (*i.e.,* drying), no structures were detected, as anticipated. Next, the samples were loaded into a solution cell in preparation for LPTEM (**Figure 2.3**).

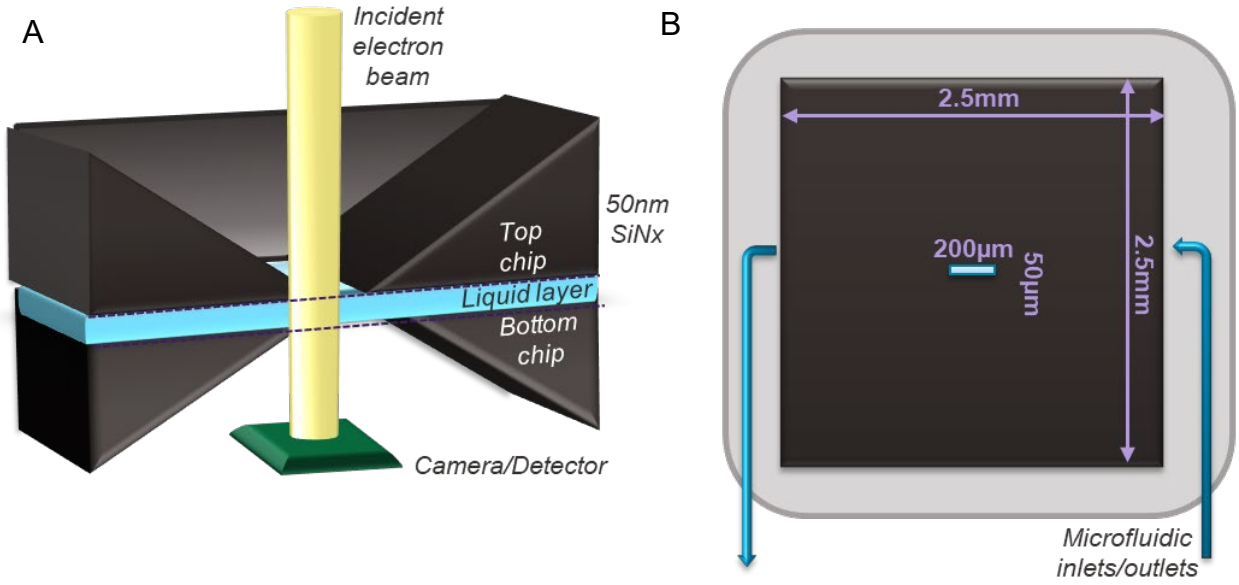

Figure 2.3 Side (A) and top (B) view of LPTEM chip assembly.

Two SiNx chips with beveled 200 by 50 um windows were aligned orthogonally to generate a crossed region of the windows, through which it is possible to observe the encapsulated liquid. The electron beam passes through this region of 50nm SiNx windows and the liquid, before capture via detector. The holder is also functionalized with microfluidic inlets and outlets (blue arrows in B) to allow flow of solvent.

Initial efforts to image these materials relied on a typical LPTEM workflow which includes plasma cleaning the chips to increase hydrophilicity (achieved with a Pelco EasiGlow at negative polarity for 30-60s).[155–159] Depositing the emulsion onto these cleaned chips resulted in a visually inhomogeneous wetting. Observation showed what seemed to be a 'semi-hydrated' cell – particles matching the anticipated size range were seen very briefly at early exposure times, which then degraded and gave way to larger regions of phase separation (**Figure 2.4**). This seems to be the result of non-preferential interactions between the nonpolar continuous phase, potentially leaving a thin film trapped between the windows and showcasing the smaller aqueous micelles (dark phase). After imaging, the minute amount of solution, coupled with the influence of the electron beam, degraded these structures. To better observe the emulsion in its unperturbed state, the liquid cell chips were not plasma cleaned in subsequent experiments to

maintain hydrophobicity and encourage cell hydration. Upon removing the plasma cleaning step, deposited samples wet the chips more uniformly and resulted in liquid cells that were clearly hydrated, based on visual inspection via optical microscopy prior to study by TEM.

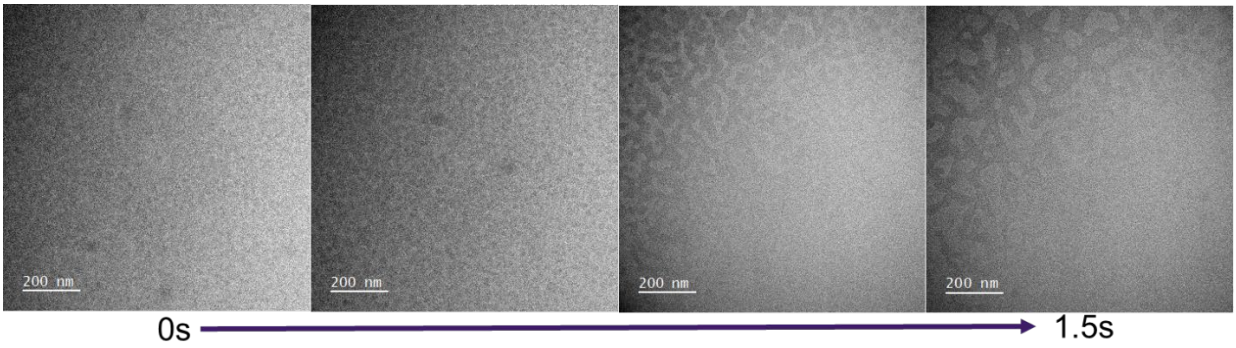

Figure 2.4 Series of single frames of a semi-hydrated liquid cell.

Small structures may be seen in the earliest images (0, 0.5s), which then seem to degrade into larger phase separated domains (1, 1.5s). Images were captured with the Gatan OneViewIS at an exposure of 0.5s

However, without plasma cleaning, the cells produced are clearly hydrated, with uniform and discrete droplets filling the cell (**Figure 2.5**). Hydration is evidenced by the intensity gradient across the cell, which is indicative of the characteristic bulging of the liquid.[160] Upon initial irradiation, dispersed droplets are visible within the liquid cell (**Figure 2.5A** and **B**, **Video 2.1, Video 2.2,** and **Video 2.3**,). Prolonged beam exposure resulted in droplet growth, movement, and interaction (**Video 2.1**). These droplets were higher contrast against a lower contrast matrix and exhibited smooth and continuous motion. Qualitatively, this suggests that the droplets are completely solvated – because they do not adhere to the SiN_x window, there is almost certainly a layer of the continuous phase between the droplet interface and the window. Typically, when *in situ* motion is analyzed, particles will move in jumps and will periodically 'stick' and remain stationary between 'slips' in motion[161–164] – this behavior was absent, suggesting that there are fewer interactions with the SiN_x interface. Subsequently, we were able to modulate the size of the initial droplets via surfactant loading ratio (w_o)– below, we show that by lowering w_o by a factor

of ~2, we reduced the size of the droplets at the time of initial irradiation (**Figure 2.5A** and **Video 2.2** vs **Figure 2.5B** and **Video 2.3**).

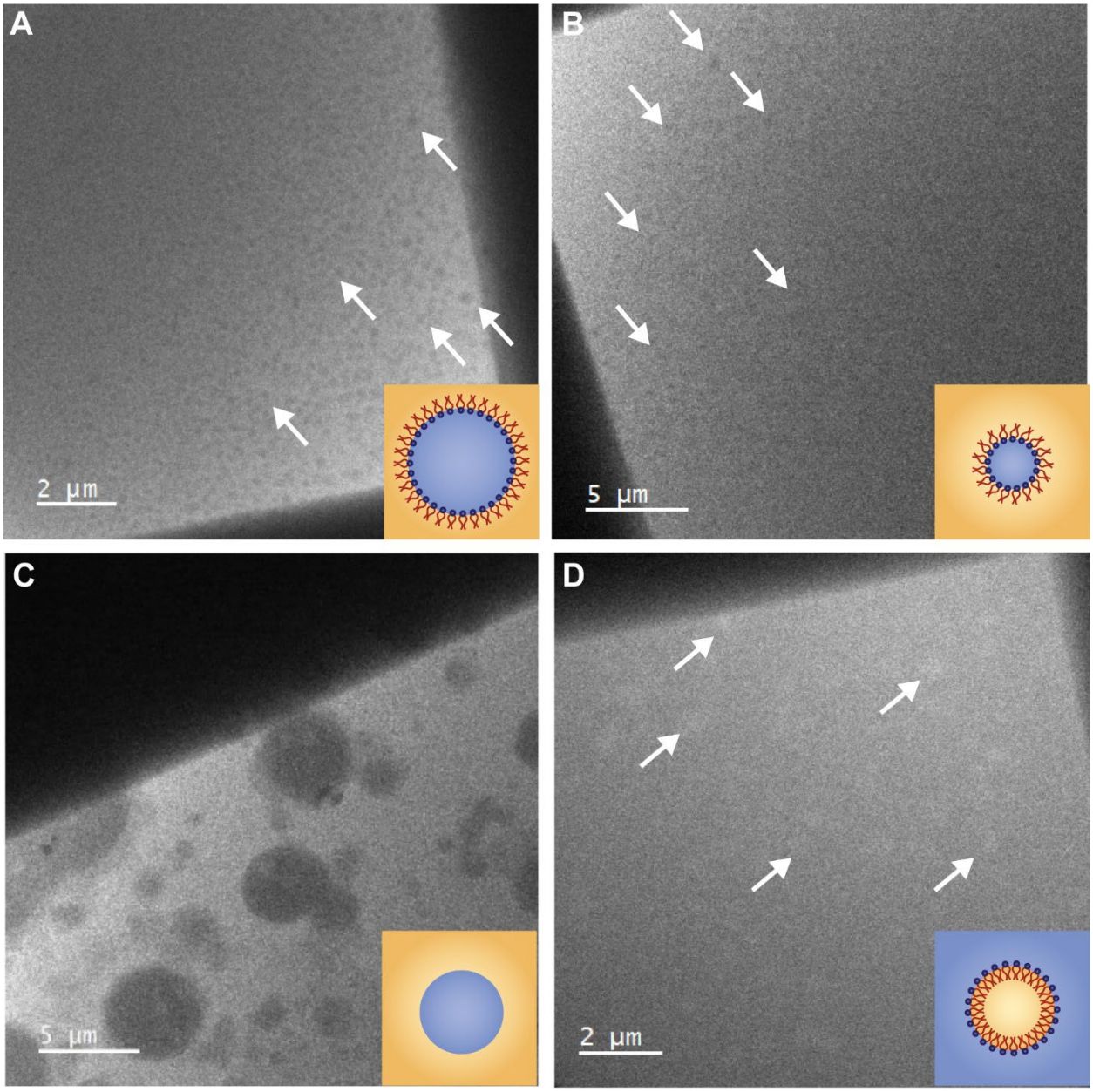

Figure 2.5. Initial emulsion formulations imaged by LPTEM, with schematic depictions in lower right. Images acquired at $0.1e^{-}/Å^{2}s$ with Gatan OneView IS. (A) water-in-isooctane emulsion at $w_o = 70$, see also **Video 2.1**. (B) water-in-isooctane emulsion at $w_o = 30$ see also **Video 2.2**. (C) water-in-isooctane emulsion without AOT stabilization, see also **Video 2.4**. (D) isooctane-in-water emulsion at $w_o = 70$, see also **Video 2.5**.

Next, water was mechanically dispersed in isooctane without addition of surfactant. The results show that, despite following identical sample preparations, the observed droplets are far less uniform and often appear to have layered droplets, containing isooctane within the water droplets (**Figure 2.5C**). The aqueous domains have diffuse borders and are not well-defined droplets, resulting from the lack of a surfactant-stabilized interface. When viewed in motion, the behavior of these droplets is distinctly different from those stabilized by the surfactant, with the water appearing to smear across and adhere to the SiNx windows (**Video 2.4**). The distinction between the two types of behaviors observed is an indication that the observation of well-defined droplets is dependent on surfactant being present. Therefore, the sample may be safely imaged, maintaining surfactant integrity at electron fluxes of $<1 e^-/Å^2 s$ and fluences of 400 $e^-/Å^2$.

Subsequently, we shifted the formulation to generate an oil-in-water emulsion (**Figure 2.5D**). The o/w formulation at the same surfactant loading ratio, yielded isooctane droplets that appeared roughly the same size as the initial water droplets from previous experiments. They are stable for longer under imaging conditions which may be attributed to the hindered transport of oil through water due to its larger molar volume with respect to the reverse formulation. The isooctane droplets appear lower in contrast against the denser aqueous phase, which scatters electrons more strongly than in the reverse case. Thus, the droplets appear light against a dark background, and are more difficult to resolve, but may still be seen to be moving freely (**Video 2.5**). This seemingly unhindered motion persisted for an extended period of imaging (several minutes at low flux), and qualitatively accelerated upon increasing beam strength, consistent with previous reports of beam-induced motion.[161,163,165] Capturing these dynamic events necessitates consideration of frame rates and image acquisition parameters. With a finite amount of signal, high frame rates give better temporal resolution, but also reduces the signal acquired per frame, thus reducing spatial

resolution. Conditions of electron flux, camera capture speed, and image resolution must be chosen judiciously (**Figure 2.6**). While the default tendency when capturing dynamic processes may be to maximize frame rates, low dose imaging conditions begin to impose limitations. With a finite amount of signal, images acquired at low exposures (*i.e.,* high frame rates) suffer from very low signal to noise ratios, which makes extracting meaningful information difficult. The usual strategies to address this are to bin the noisy images either spatially (bilinear interpolation of adjacent pixels) or temporally (summing or averaging pixels from adjacent frames). However, these approaches sacrifice signal to extract meaningful features, as in the illustrative example below (**Figure 2.6**). To circumvent this loss of resolution, signal must either be increased, or new processing techniques must be devised.[166]

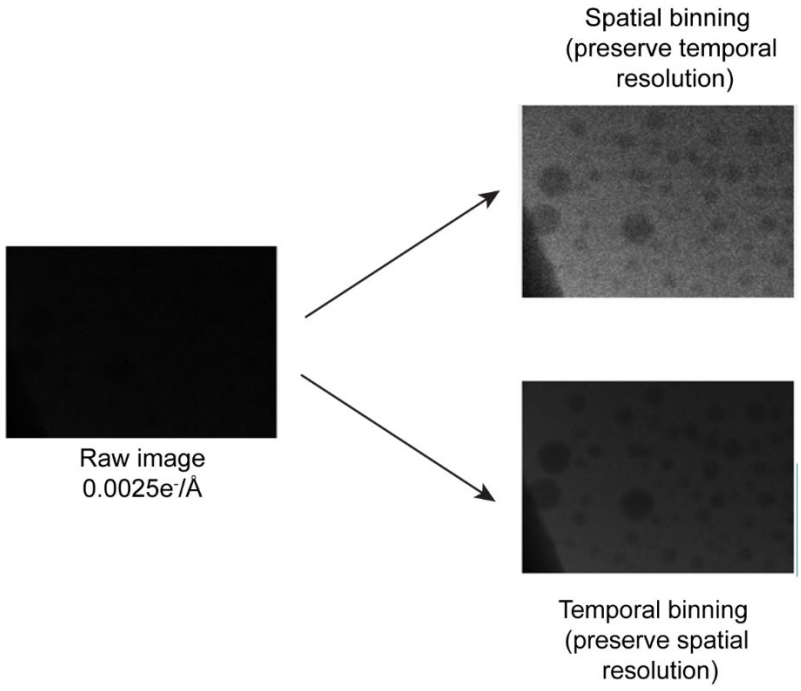

Figure 2.6 Frame captured at 0.013s exposure.
Raw image shown at left, with spatial and temporal binning shown at right.

We verified the identity of the phases based first on solvent density, which should be directly proportional to its contrast, indicating that the dark droplets observed were the aqueous

phase (as described above) for the water in oil emulsion, as intended (**Figure 2.7**).[167] However, to further corroborate this conclusion, citrate-stabilized aqueous gold nanoparticles were included in the aqueous phase (**Figure 2.7A**). These nanoparticles are insoluble in the oil phase and are of sufficient contrast to be easily distinguishable against either solvent. Upon imaging, the 100nm Au particles were solely observed in the dark droplets, further verifying the assignment of phases. These observations were further supported by STEM imaging of the same formulation of the isooctane system (w/o, w_o=70). Annular dark field (ADF) images show the nucleated droplets lighter against a darker background, in contrast to the dark droplets seen in bright field imaging, indicating these droplets were of a higher density than the surrounding fluid (**Figure 2.7B**, **C**).

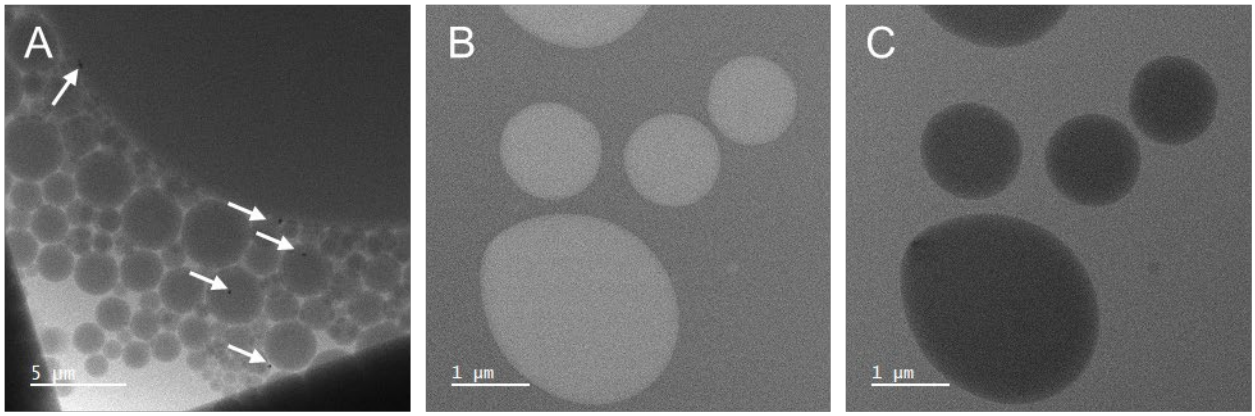

Figure 2.7 Phase determination of emulsified droplets.
(A) Aqueous citrate-stabilized gold nanoparticles (indicated by white arrows) in isooctane stabilized by AOT, (B) ADF and (C) BF STEM of water in isooctane stabilized by AOT.

In addition, emulsions could be generated using decane and n-octane as the solvent and using formamide and dimethyl formamide as dispersed phases following the same sample preparation procedure (**Figure 2.8**). These experiments were successful in observing morphology and dynamics across all four systems while employing identical sample preparation protocols, highlighting the facile nature of such a technique. This speaks to the versatility of LPTEM for imaging emulsions generally, without the need for optimized sample preparation that one would encounter for freeze-fracture and for high pressure freezing.[77,123]

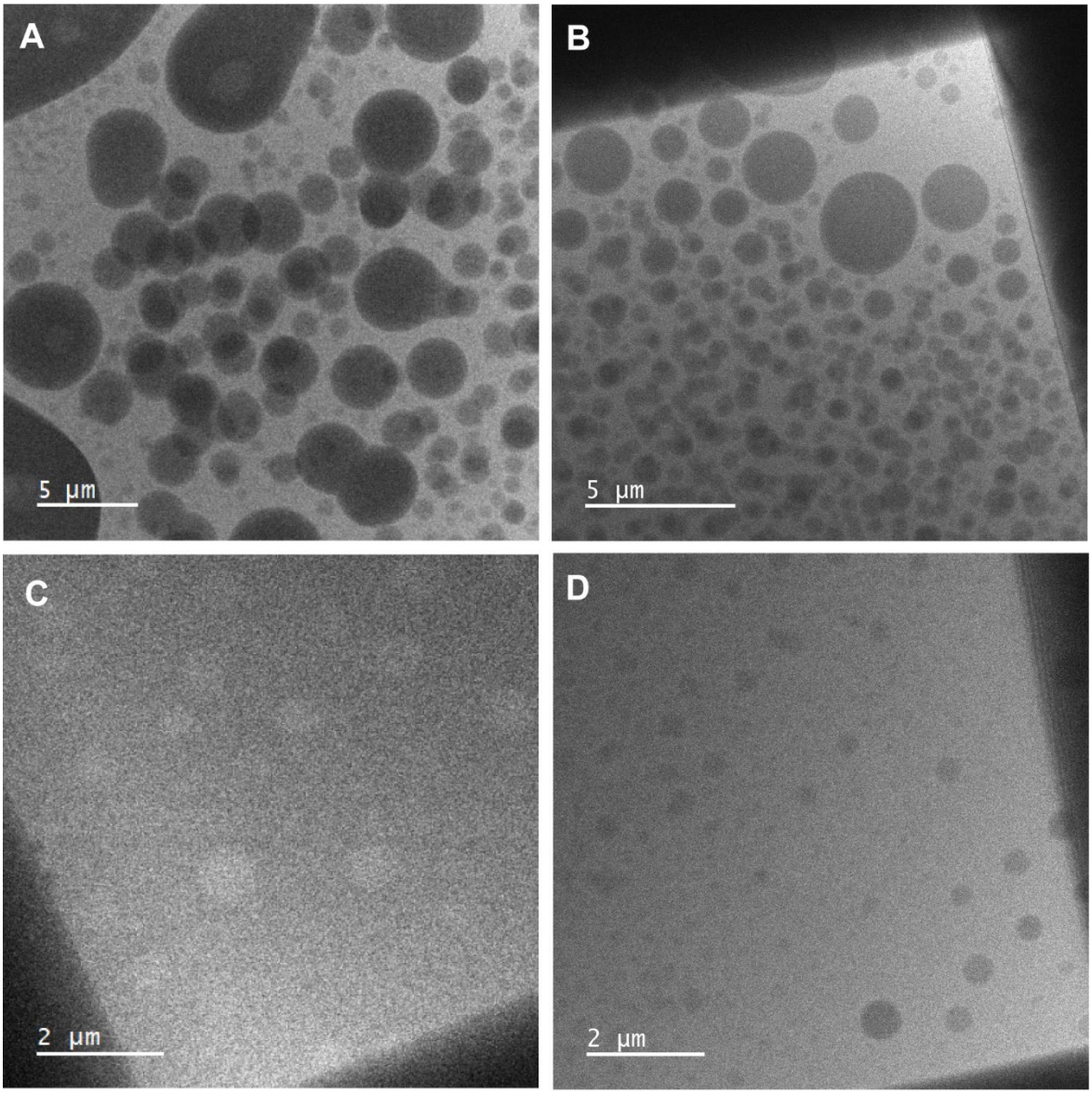

Figure 2.8 Alternate systems explored via LPTEM.
(A) Decane is the lighter, continuous phase, with water dispersed and stabilized by AOT. (B) shows the same, with n-octane as the continuous phase. (C) is formamide dispersed in isooctane, stabilized by AOT. (D) shows dimethyl formamide (DMF) as the dispersed phase in isooctane, with AOT as surfactant. Images acquired with Gatan OneViewIS at a frame rate of 0.5FPS.

2.2.2. Quantification of Demulsification

Qualitatively, we consistently observed all of the aforementioned modes of demulsification in the surfactant-stabilized experiments (**Figure 2.1**). However, it is necessary to

be able to classify these processes and compare them to *ex situ* behavior and to understand differences based on formulation. In the case where droplet growth was observed, this was achieved by applying a simple image binarization algorithm to videos of stationary droplets which were observed to be increasing in size. After binarization, a function was applied to measure the area of each of the observed droplets; assuming a near-circular morphology, the resulting droplet diameter was then calculated. This process was iterated over subsequent frames to establish growth curves over time (**Figure 2.9A-C**, **Video 2.6)**. For w/o formulations undergoing Ostwald ripening, it was anticipated that r^3 would be linear in time, which was the case (**D**).[15,116,119,168,169] Utilizing methods outlined by Jiao et. al[116], the estimated rate of Ostwald ripening for this formulation was 6.034×10^{-22} m^3/s. The process is briefly outlined below:

$$\omega(o) = \frac{\partial r^3}{\partial t} = \frac{8DC_\infty V_m^2 \gamma}{9RT} \qquad \text{Equation 2.1}$$

$$\omega(\varphi) = k(\varphi) * \omega(0) \qquad \text{Equation 2.2}$$

where $k(\varphi) = 1.75$.[116] Literature values of γ were used (23 mN/m)[139], and the following relations were used to estimate D and C_∞:

$$D = 7.4 * 10^{-8} * \frac{(xM)^{\frac{1}{2}}T}{\eta * V_m^{0.6}} \qquad \text{Equation 2.3}$$

Where x is the association parameter of the solvent (1 for hydrocarbons), M is the molar weight of the solvent, η is the viscosity of the solvent (0.51cP), and V_m is the molar weight of the solute (18.069 cm^3/g).

$$\ln(C_\infty) = \frac{-79.6677 - 6.6547 * CN}{9.5470 + CN}$$ Equation 2.4

Where C_∞ is the molar fraction of the solute and CN is the number of carbons in the solvent (here, since we are using a branched hydrocarbon, we used 5 from the backbone).

Initial observations at low electron flux (0.19e/Å^{2}s), resulted in experimental Ostwald ripening rates on the expected order of magnitude (2.87x10^{-22}m^3/s) (**Figure 2.9E**).

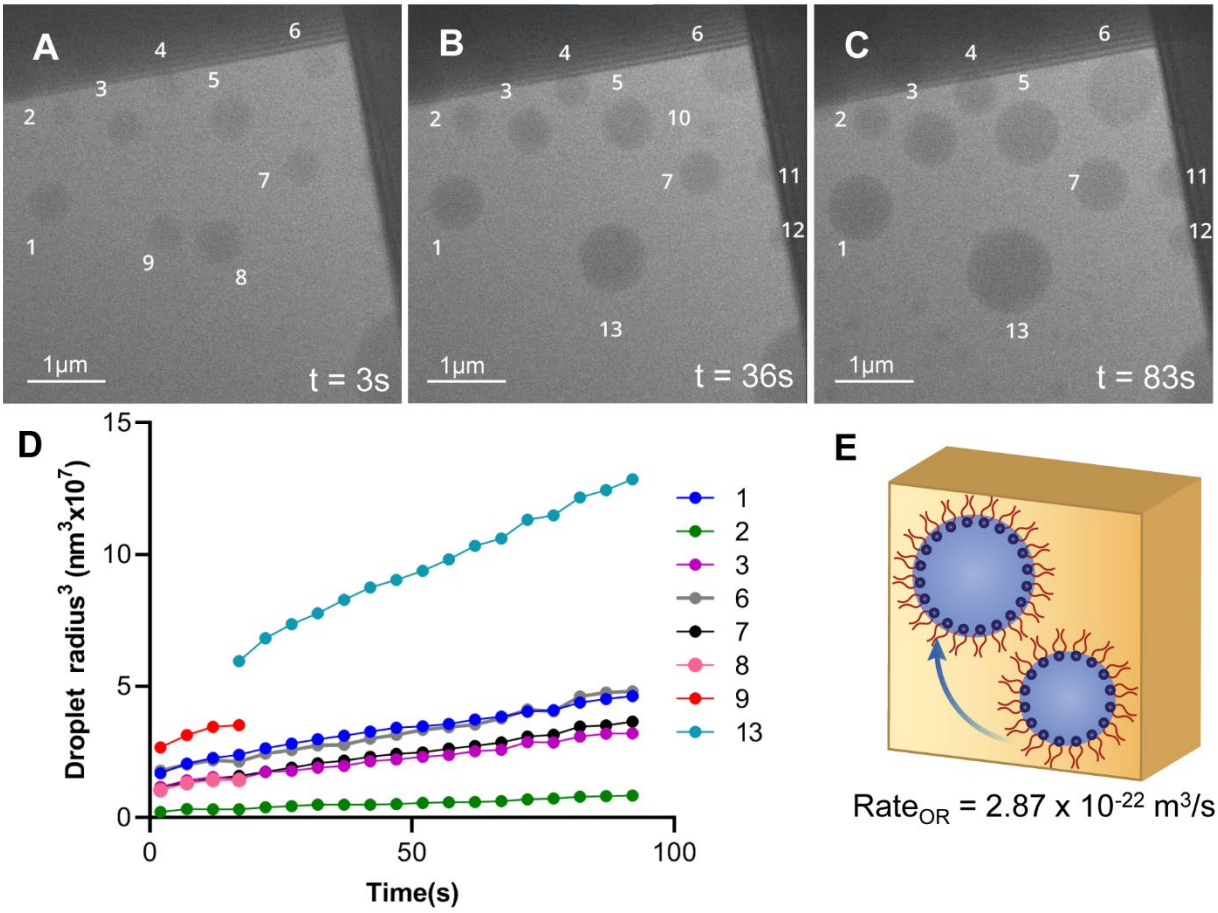

Figure 2.9 Quantification of Ostwald ripening of water droplets at low electron flux.
(A, B, C) Observation of Ostwald ripening in water droplets at a flux of 0.19e/Å^{2}s and 12.5 FPS with Gatan OneView IS. Frames have been temporally binned 12 times for ease of observation. Droplets 8 and 9 merge at t=15s, and the resulting droplet is referred to as Droplet 13. (D) Growth of selected droplets as $r^3(t)$, to evaluate rates of Ostwald ripening (slope of curves). Data sets are pruned to show selected droplets and are averaged every ten points. Full data set in **Figure 2.10**. (E) Schematic depiction of growth process and calculated Ostwald ripening rate.

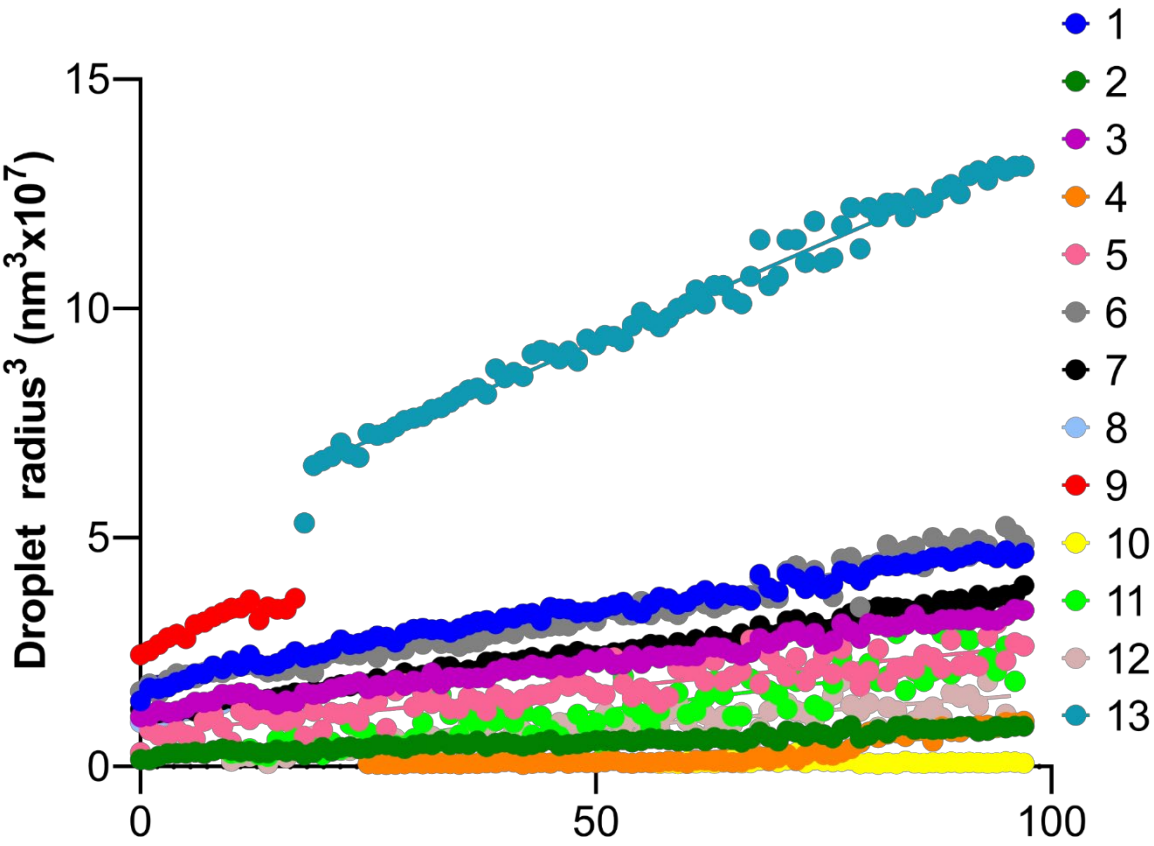

Figure 2.10 Plot of r^3over time for water droplets in isooctane at low electron flux (0.19e/Å^{2}s**)** This plot includes all data points for all droplets seen in **Video 2.6**.

Notably, in these images, we see that the diameters of the droplets are on the order of a few hundred nanometers, with the largest approaching micron scale. This exceeds the dimension of the liquid cell in the z-axis, and thus the droplets are assumed to be spheroidal, rather than true spheres. Accordingly, accumulated volume will disproportionately expand the droplet in the x-y plane, leading to a more rapid increase of radius than a sphere experiencing equivalent mass transport – this phenomenon would be expected to inflate calculated rates of Ostwald ripening. In contrast, these confined droplets are only able to receive mass through a fraction of their total surface area, unlike a true sphere. The magnitude of these two deviations is approximately equal and opposite, such that we may continue to accurately model these ellipsoidal droplets as spheres (**Figure 2.11**). To briefly consider surface tension effects, one may consider that as the droplets are compressed,

the curvature of the available surface area increases. This is an effective decrease in the radii of curvature, which would increase surface tension, and accordingly, the anticipated rate of Ostwald ripening. In that vein, one might expect that the most compressed droplets (*i.e.*, those nearest the corner of the cell) should undergo the fastest growth. However, this is not the case, with the rates of Ostwald ripening not differing significantly as a function of location in the cell. Thus, we consider such effects negligible. To evaluate the influence of the spatial constraints in the liquid cell experiments (i.e., limitations in the z-dimension), we can consider a set of droplets which all have the same initial radius (here, 500nm). We can impose degrees of compression along the z axis such that the compressed spheres may be considered ellipsoids, which we will define as having a circular cross section in the xy-plane, and are thus defined by r and c (**Figure 2.11A)**. Given that the theoretical rate of Ostwald ripening is a function of diffusivity, solubility, and surface tension (and thus, largely independent of geometry),[116] we can consider our set of droplets to experience the same rate of Ostwald ripening (here, arbitrarily chosen as $5x10^{-22}$ m^3/s). The time scale was chosen to reflect the duration of the experimental measurements (up to 90s). In this scenario, we can calculate how r changes in time as a function of confinement (c), varying from no confinement (where r is isotropic and able to expand equally in all directions) to significant confinement (c = 100nm), where the c-axis of our ellipsoid is held constant, and the droplet is only able to expand in the x-y plane to accommodate the added volume. Here, the rate of change of radius does not vary significantly as a function of c; rather, it is the magnitude of the radius which is most significantly impacted – the most confined droplet (c=100nm) has a radius nearly double that of the isotropic sphere (**Figure 2.11B**). In considering this compressed geometry, it is also necessary to consider the effect that this has on the surface tension of the droplets, which may be obtained from the Young Laplace equation:

$$\Delta P = \gamma(\frac{1}{R1} + \frac{1}{R2})$$ Equation 2.5

This particular variation shows the equation for a spheroid with two differing axes of interest.[170] We may consider a constant gamma and vary the radius of compression (R1) from 100nm to 500nm (as above), while holding the R2 constant at 500nm. For a perfect sphere, R1 = R2 = 500nm. When R1 is at its minimum, we see a maximum variation in ΔP, wherein $\Delta P_{spheroid}/\Delta P_{sphere} = 3$, which decreases to unity as the spheroid approaches a sphere (*i.e.,* R1 approaches 500nm). Given that we are not often in our most compressed case, we can consider such variation to be minimal, and thus neglect such effects for the present analysis.

When considering the surface area through which the mass is able to transport, we will now treat the confined droplets as cylinders for the sake of simplicity, and the only interface available for transport is that along the z axis of the droplet (i.e., $2\pi r * c$). We can consider how this area will evolve in time under the same conditions as previously outlined (i.e., $5x10^{-22}$ m^3/s). Here, the trend is reversed—confinement greatly reduces available surface area for transport (**Figure 2.11C**). Again, the magnitude of this differential is the most significant parameter to consider. Here that magnitude ranges from a factor of 2 to a factor of 3, depending on the value of c. Given that this shift is opposite and approximately equal in magnitude to the droplet radius trends, we can consider these to two effects to cancel each other out, and thus conclude that it is fair to approximate our droplets as spheres and thus use the predictions from LSW theory.

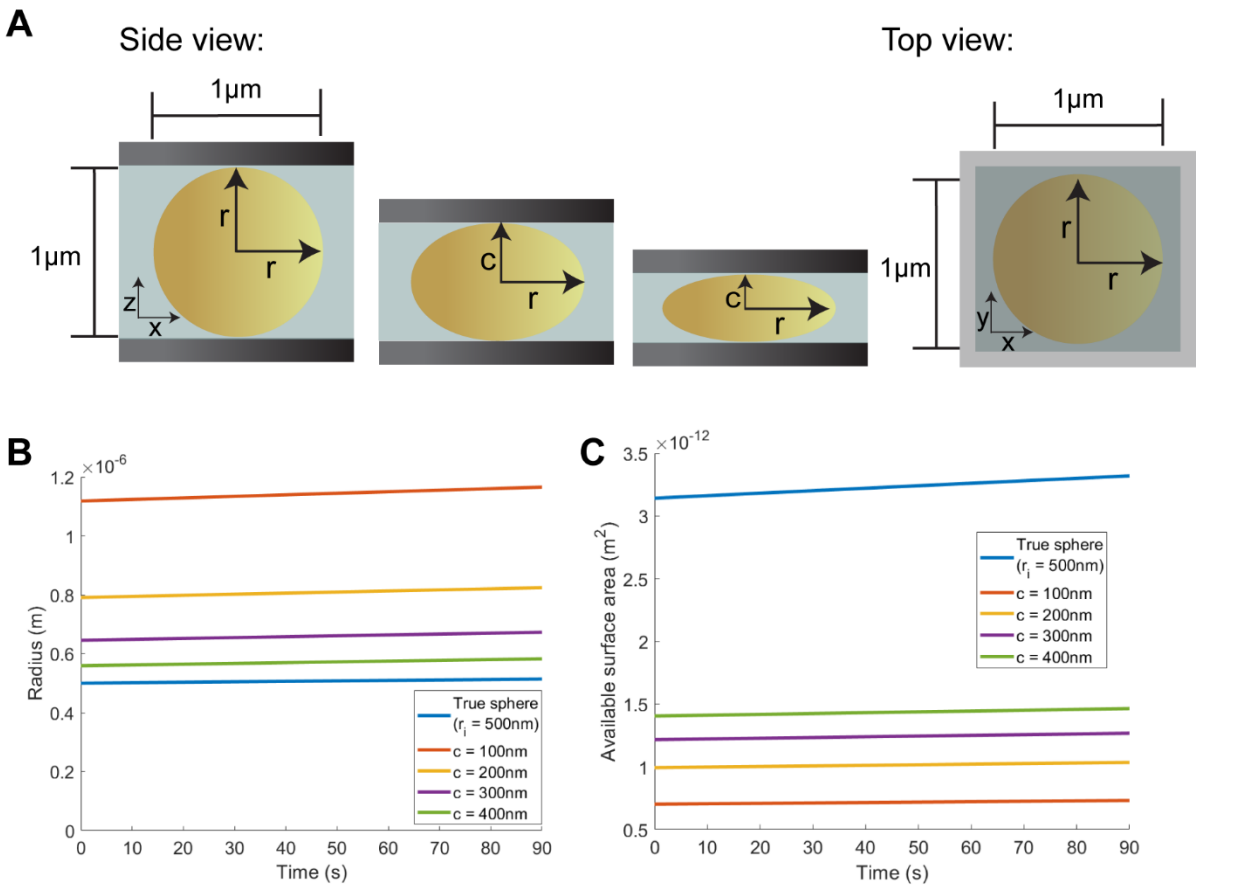

Figure 2.11 Consideration of non-spherical droplets with respect to validity of Ostwald ripening calculations. **(**A) In the liquid cell, thickness constraints of the liquid may impose an ellipsoidal morphology on the droplets, which may vary with the thickness of the liquid. (B)Radial growth as a function of confinement is calculated for a given Ostwald ripening rate while considering droplets starting with the same initial radius. (C) Growth of interfacial surface area available for mass transport as a function of confinement over time.

Upon increasing electron flux, an increase in the rate of droplet growth was observed (**Figure 2.12**, **Video 2.7**). An identical analysis to that previously described for the low flux Ostwald ripening data was followed, and the rates of Ostwald ripening were accordingly measured to be 1.27×10^{-21} m^3/s (**Figure 2.12D** and **E**), an order of magnitude greater than that of the low flux experiment, and thus an order of magnitude greater than expected. Being able to modulate dynamics by adjusting the electron beam is an indication that it may be possible to use this technique for characterizing accelerated aging. That is, understanding how these materials will behave over longer lifetimes at a shorter experimental timescale.

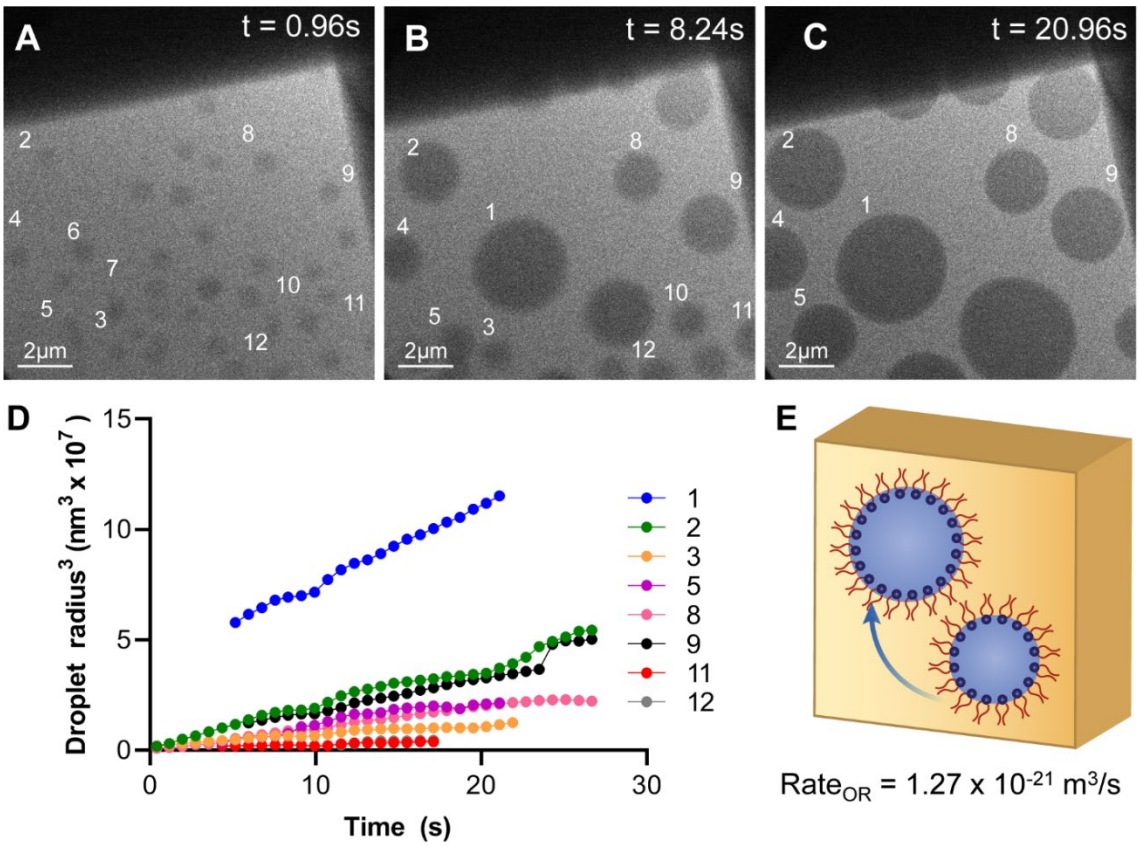

Figure 2.12. Observed Ostwald ripening at moderate electron flux.
(A, B, C) Ostwald ripening of water in isooctane at a flux of 0.5e-/Å^{2}s at selected time steps from 0-30 seconds. (D) Growth of the radius cubed over time to quantify the rate of Ostwald ripening (slope of curves). Data sets are pruned to show selected droplets and are averaged every five points. Full data set available in **Figure 2.13**. (E) Schematic depiction of Ostwald ripening and calculated Ostwald ripening rate.

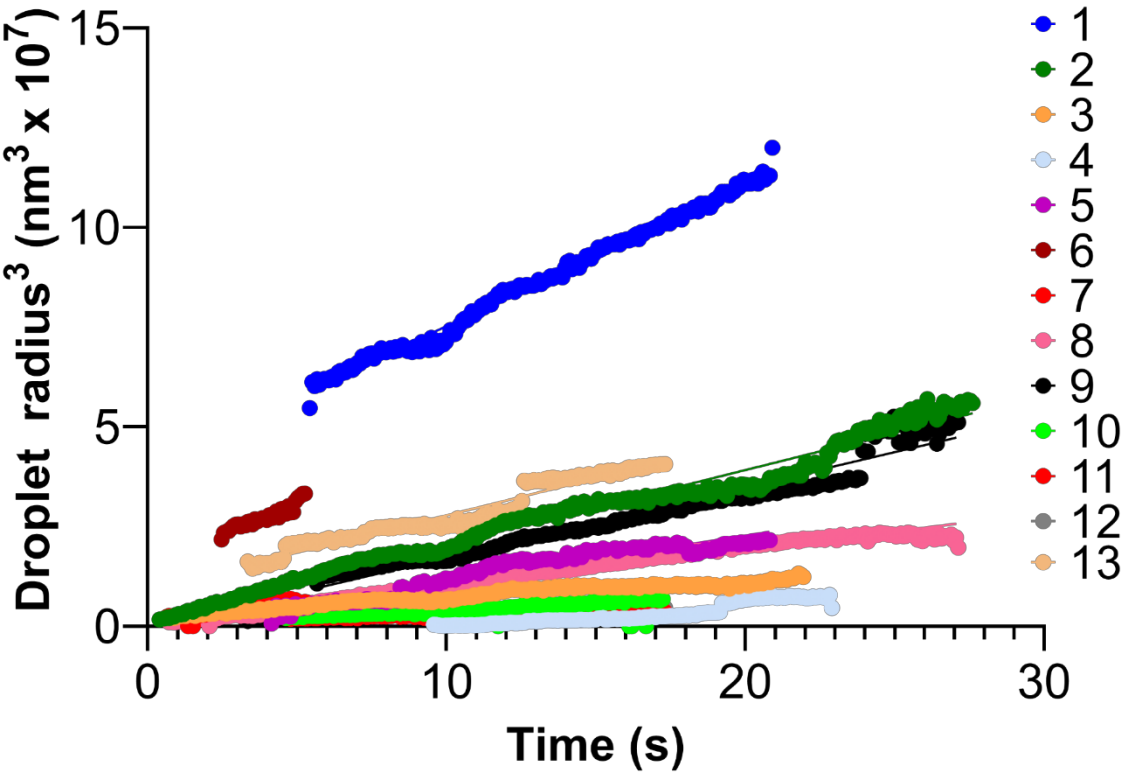

Figure 2.13 Plot of r^3 over time for water droplets in isooctane at an electron flux of 0.5e/Å^{2}s. This plot includes all data points for all droplets seen in **Video 3.7**.

2.2.3. Identification of Coalescence Intermediates:

Coalescence was observed across all emulsions containing surfactants. Notably, by increasing frame rates from those typically used for *in situ* microscopy (e.g., 1-10 frames per second) to up to 100 frames per second, it was possible to observe merging events and to identify intermediates which have not previously been directly observed (**Figure 2.1**). In accordance with the models of coalescence, we were able to observe several intermediate phases, consisting of both

thin film drainage and subsequent rupture, wherein we were able to observe discrete merging events (**Figure 2.14A**, **B**, and **C**, **Video 2.8** and **Figure 2.14D**, **E**, and **G**, **Video 2.9**, respectively).

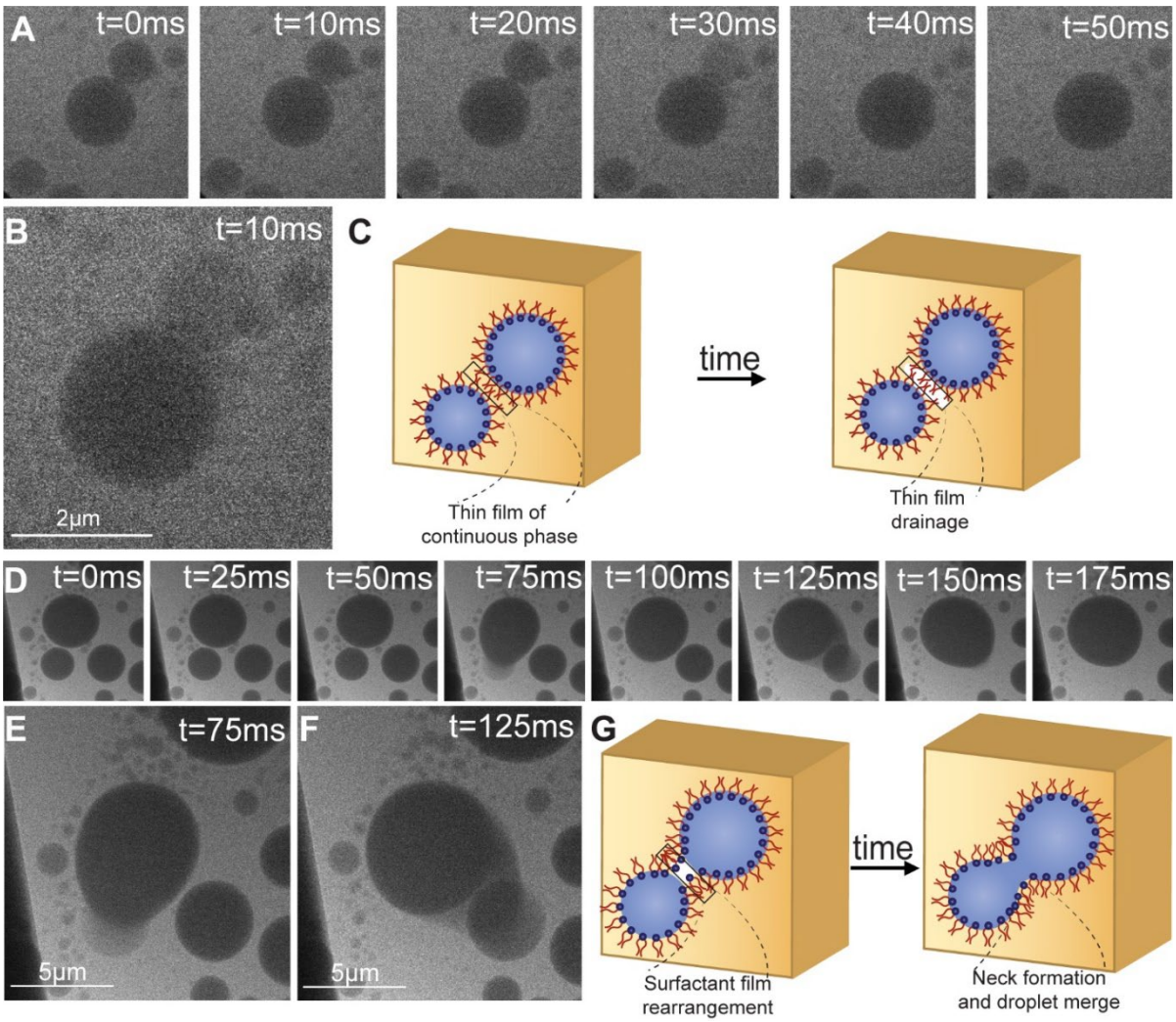

Figure 2.14. Observation of two distinct droplet coalescence intermediates
(A) Sequential frames before, during, and after first stage coalescence event. Each box measures 4.65μm square. (B) Intermediate dumbbell at t = 30 ms, shown approximately 1.5x larger for detail. (C) Schematic representation of continuous phase thin film formation and drainage. (D) Observation of second droplet coalescence intermediate, with sequential frames before, during, and after two coalescence events at t = 75 and 125ms, shown approximately 2x larger in (E) and (F), respectively. Boxes here are 6.83μm square. (G) Schematic depiction of surfactant film rearrangement and droplet drainage. Images were captured at 100 FPS with Gatan OneViewIS at a flux of 0.3 e-/Å^{2}s.

The smaller droplet observed was in contact with the larger one for several seconds prior to merging, indicating that simply colliding with another droplet is not sufficient to initiate this process (**Figure 2.14A**). Rather, the continuous phase needs to dissipate such that the surfactant molecules are able to interact and rearrange (**Figure 2.14B**, **C**).[107] This is referred to as thin film formation and drainage, wherein a small layer of isooctane remains between the two water droplets, attracted to the nonpolar portions of the AOT, and subsequent suction and disjoining pressure induced by electrostatic and van der Waals dispersion forces lead to its drainage (**Figure 2.14B**, **C**).[171,172] Indeed, this thin film is visible in the videographic data, wherein a sliver of continuous phase may be seen between the two droplets in contact for an extended period (**Video 2.8**). This is consistent with the identification of thin film drainage as the rate limiting step in this process. Once the thin film of isooctane has dissipated, the surfactants are able to come into contact and rearrange, permitting the flow of water from one droplet into another (**Figure 2.14D-G**).[171] This occurred twice during the acquisition of videographic data on this sample, observed at 40 frames per second (**Video 2.9**). In these intermediate frames, the flow of water from the smaller to the larger droplet can clearly be seen (**Figure 2.14E**, **F**). Information about such processes on the nanoscale can be utilized to glean information regarding the energetics of such interactions and the surface tension of the droplets involved.

2.2.4. Using Additives to Shift Degradation Modes:

Given our observation of demulsification for a given formulation (water in isooctane, w_o = 70), the next step was to see if that degradation could be altered via known strategies—namely, the inclusion of a co-surfactant or additional solute components (**Figure 2.15**). These additives are known to inhibit coalescence and Ostwald ripening, respectively, due to increased steric hindrance of the droplets and equalized Laplace pressure.[173–176] If these shifts were observed *in situ*, it would

further confirm that the behaviors are reflective of bulk solution behavior. For co-surfactant, BRIJ-52, a non-ionic polyethylene glycol-based surfactant, was selected due to its ability to increase the solubilization capacity of water.[148] This was mixed with AOT in equimolar quantities, such that the overall surfactant to water ratio remained consistent with previous experiments ($w_o = 70$). This formulation showed a propensity for flocculation prior to coalescence, as a result of the steric hindrance introduced by BRIJ-52. Droplets were consistently observed to collide and adhere for a greater time scale (several seconds) prior to coalescence than in comparable formulations without the inclusion of BRIJ-52 (such as those previously discussed with **Figure 2.14**) (**Figure 2.15 A-G**, **Video 2.10**).

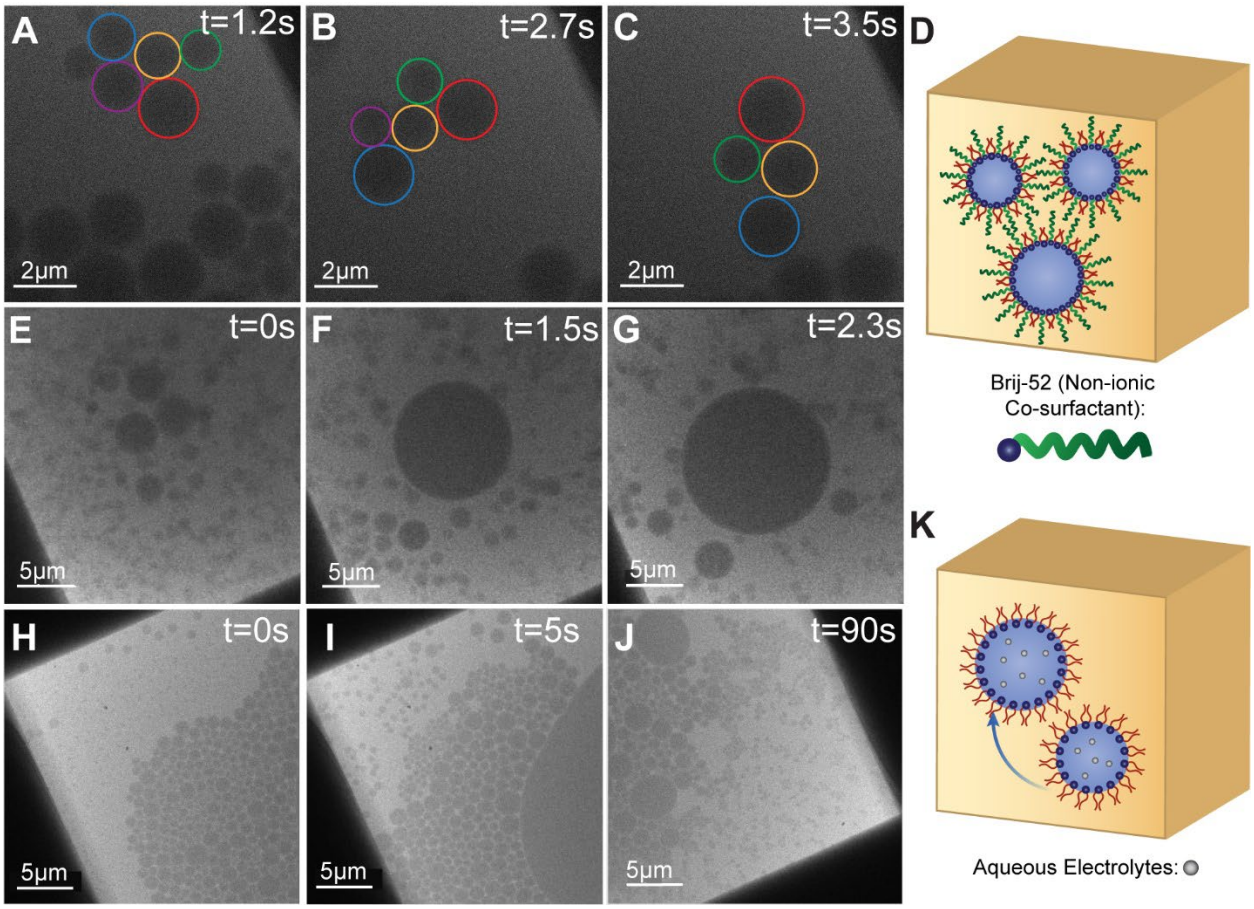

Figure 2.15. Shifting of observed demulsification modes via inclusion of specific additives.
(A, B, and C) Promotion of flocculation via addition of non-ionic co-surfactant; colored circles included as droplet identifiers. (D) shows schematic depiction of droplets containing non-ionic surfactant (green lines) and how this relates to steric interactions. (E-G) show droplets only stabilized with AOT over a comparable time period for reference. (H, I, J) Morphology and growth of DPBS stabilized by AOT in isooctane over time. Notably, the population of very small droplets persists for significantly longer time scales due to electrolyte-inhibited Ostwald ripening. (K) Schematic depiction of slowed Ostwald ripening, with electrolytes denoted by grey spheres.

To modulate Ostwald ripening, electrolytes were chosen as solutes, due to their incompatibility with isooctane and other alkanes.[173,174] Hence, water was replaced with Dulbecco's phosphate buffered saline (DPBS). In this scenario, the observed population of small (sub-300nm) droplets was significantly larger than previously seen, and the lifetime of these droplets was significantly prolonged, as evidenced by their presence over several minutes of imaging (**Figure 2.15H**, **I** and, **J**, **Video 2.11**). Further, a foam-like morphology was observed upon initial

irradiation, showing increased droplet stability to flocculation (**Figure 2.15H** and **I**). While this was unanticipated, it is possible that this may have been the result of Coulombic interactions introduced by the saline, leading to increased hindrance to coalescence. Competing forces of adhesion and compression are also at play, which may contribute to the foam morphology seen. The appearance and duration of such a foam-like structure were not seen with any of the other variations studied. The introduction of increased electrostatic interactions may also contribute to repulsive forces between the droplets, leading to increased stability upon adhesion. Further, when used in conjunction with an ionic surfactant such as AOT, the included electrolytes will contribute to charge screening effects, which can further increase stabilization and affect emulsion morphology.[177,178]

2.2.5. Evaluation of Beam Influence:

As with all *in situ* experiments, the effect of electron beam irradiation must be considered. While we are able to mitigate some of this effect by using minimal fluxes and fluences, interactions between the high energy incident electrons and the sample still remain. Copious qualitative evidence demonstrates the acceleration of demulsification upon increasing flux, and the measured rate of Ostwald ripening confirms this.[17] Thus, despite efforts to lessen the beam's confounding influence, it must still be considered. High flux experiments demonstrated that beyond a certain fluence (400 $e^-/Å^2$), the observed phases of water-in-isooctane emulsions will reverse. That is, the water becomes the continuous phase within the imaging region, and droplets of lighter isooctane are observed (**Figure 2.16**). In that high flux experiment ($1e/Å^2s$), the anticipated morphology (dark droplets in a light continuous phase) was seen at the beginning of the imaging session (**Figure 2.16A**). However, as imaging continued, the dark droplets aggregated to the point where the aqueous phase predominated and the oil phase became dispersed (as evidenced by the light

droplets in a dark matrix) (**Figure 2.16B**). This phase reversal was repeatedly observed above the safe imaging threshold (400 e/Å^2) for the water-in-isooctane system, and at early time points for other formulations (formamide in isooctane, **Figure 2.8C**).

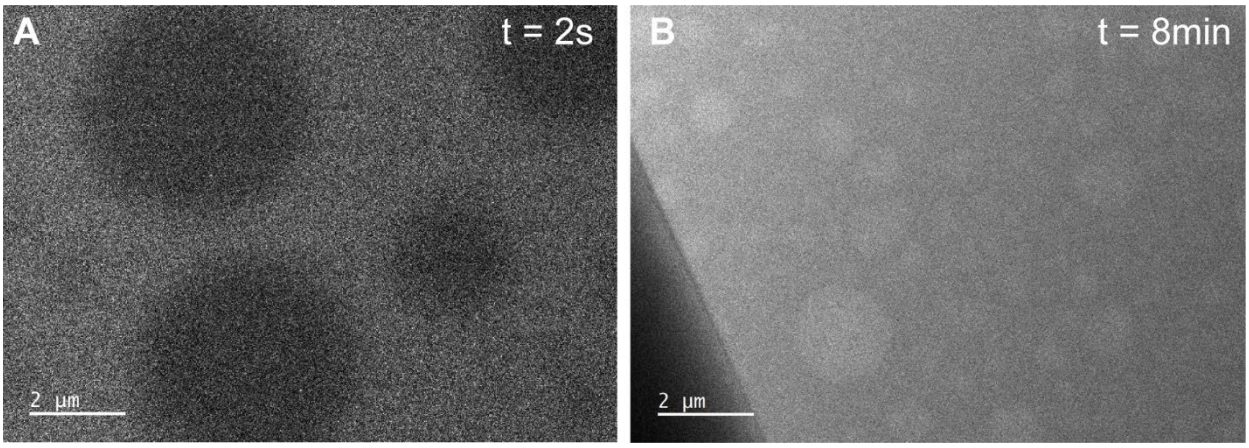

Figure 2.16 Observation of phase reversal at elevated electron fluence.
(A) A w/o emulsion of water in isooctane with a w_o =70 imaged at initial irradiation of 1e/Å^{2}s. The cell has the anticipated morphology of dark droplets in a light matrix. (B) Upon continued irradiation (8min), the same cell from (A) has exhibited a reversal in phase contrast – light droplets are present in a dark matrix, indicating that the sample is now an o/w emulsion. Images were acquired with the Gatan K3 at exposures of 0.1s

This behavior is consistent across multiple high fluence experiments (both high flux and extended imaging conditions). In such cases, beam blanking will permit the return of the oil phase to the cell; however, the oil-in-water emulsion quickly flows in from the corner (**Video 2.12**). We hypothesize that this preferential interaction between the water and the beam is the result of charging imposed upon the SiN_x by the electron beam. Thus, this compositional shift seems to be irreversible and may result from either damage to the surfactant or heightened local concentrations of water such that the original formulation is no longer thermodynamically favorable. We posit that such drastic changes in phase distribution within the cell may be an interesting strategy to induce mixing or changes in phase behavior during *in situ* experiments. Additionally, during STEM experiments, droplets nucleated with a teardrop morphology, with the point forming at the upper left and the bulb forming at the lower right (**Figure 2.7B** and **C**). This orientation is consistent

with the raster pattern of the electron probe, indicating that the impinging electrons are affecting the nucleation and growth. These mechanisms and transformations are not yet understood, and are an intriguing area for further study. However, our collective observations and characterizations indicate to us that at low fluxes and fluences, the beam serves to accelerate the observed processes.

2.3. Study Conclusions

Using low electron flux LCTEM imaging, we have observed the unperturbed morphology of emulsions in the solution phase. This is difficult or impossible by other methods. Further, LCTEM allows for the observation of emulsion evolution over time. We have been able to directly monitor the way these processes change as a result of formulation modifications, and subsequently confirm these changes via image analysis. Further, the observed changes in the emulsion behavior from additives are consistent with bulk trends, making this an effective way of investigating surfactant-solute interactions. In summary, this methodology is a relatively simple and streamlined way of evaluating emulsions. The implementation of such a method may accelerate emulsion and surfactant development, as well as lead to further insight into the mechanisms of formation and demulsification.

2.4. Experimental Details

2.4.1. General Information and Materials

2,2,4-methylpentane (isooctane) was purchased from TCI America. All other chemicals, including dioctyl sulfosuccinate, sodium salt (Aerosol OT/AOT) Brij-52 were purchased from Sigma. All reagents were used as received.

AOT was dissolved in isooctane at the desired molar concentration, after which deionized MilliQ water was added to achieve the proper surfactant loading ratio (w_o). The dispersion was then

vortexed for two minutes to mechanically disperse the droplets, which was subsequently stabilized in a sonication bath until studied. For the reverse phase emulsion (o/w), the AOT was first dissolved in water, with isooctane subsequently added and dispersed as above. For all other included components (buffer, salts, alternate solvents), the same protocol was followed.

2.4.2. Dynamic Light Scattering

DynaPro NanoStar was used to acquire DLS data.

2.4.3. Microscopy

A JEM-ARM300F (JEOL Ltd., Tokyo, Japan) transmission electron microscope was used for *in situ* experiments at an operating voltage of at 300keV and current of 15μA (FEG source). Images were acquired with a Gatan 2k × 2k OneView-IS CCD camera and a Gatan K3-IS direct electron detector (Gatan Inc., Pleasanton, CA, USA) via Gatan Digital Micrograph imaging software (Roper Technologies, Sarasota, FL, USA). Exposure durations ranged from 0.01s to 1s. Electron fluxes were measured by both the K3 and via the detected beam current, which has previously been calibrated via a Faraday Holder in conjunction with the respective apertures used. Video acquisition was done by either the *in situ* camera functionalities or by screen recording with Camtasia Studio 2018 (TechSmithCorporation, USA). Frame rates for each data set are as indicated in figure captions. STEM images were acquired under the same operating conditions, using a probe size of 8C, camera length of 40cm, and a 40μm aperture, with a pixel dwell time of 2.4μs. Images were collected with bright field and annular dark field detectors as indicated.

LPTEM experiments were performed using Hummingbird Scientific Dual Flow Mixing and Protochips Poseidon Select holder. In both cases, the cell preparation was as follows: the lines were left unfilled with solvent. SiN_x chips for the respective holders were not plasma cleaned for

solutions with a nonpolar dispersed phase, or plasma cleaned for 30s for aqueous samples. 0.8μL samples were deposited onto the bottom chip via micropipette. Top chips were placed to ensure orthogonal alignment of the windows (creating a 50 μm by 50μm viewing area) and were manually aligned before sealing with the holders' appropriate hardware (lid for Protochips, top clamp for Hummingbird) (**Figure 2.3B**). Assembled cells were vacuum tested in an external pumping station to ensure liquid cell integrity at relevant pressures (8.6e-6 mbar) prior to insertion in the microscope..

2.4.4. Image Acquisition, Processing, and Analysis

Image processing was carried out in MATLAB and ImageJ. In MATLAB, we employed the DIPlib package[179] to apply average and median filters, which were followed by Otsu thresholding and segmentation. Built-in MATLAB functions were used to subsequently identify and quantify connected regions for further analysis. Specifically, droplet area in pixels was measured for connected regions. This area was then used to calculate an equivalent diameter, under the assumption that the droplets are circular. For adaptive denoising, the LPEM image processing pipeline from Marchello et. al was employed.[180] ImageJ was utilized for sequence identification and splicing.

2.4.5. Supplemental Materials

Video 2.1: LPTEM data of isooctane/AOT/water at $w_o = 70$ acquired with an electron flux of 0.078 $e^-/(Å^2\ s)$

Video 2.2: LPTEM data of isooctane/AOT/water at $w_o = 30$ acquired with an electron flux of 0.078 $e^-/(Å^2\ s)$

Video 2.3: LPTEM data of droplet growth and behavior

Video 2.4: LPTEM data of mechanically dispersed water in isooctane acquired with an electron flux of 0.19 $e^-/(Å^2\ s)$

Video 2.5: LPTEM data of water/AOT/isooctane at $w_o = 70$ acquired with an electron flux of 1.0 $e^-/(Å^2\ s)$

Video 2.6: LPTEM data of water droplets undergoing Ostwald ripening in isooctane, acquired with an electron flux of 0.19 $e^-/(Å^2\ s)$

Video 2.7: LPTEM data of water droplets undergoing Ostwald ripening in isooctane, acquired with an electron flux of 0.5 $e^-/(Å^2\ s)$

Video 2.8: LPTEM data of water droplets coalescing with a visible thin film formation, acquired with an electron flux of 0.3 $e^-/(Å^2\ s)$

Video 2.9: LPTEM data of water droplets coalescing with a visible thin film drainage, acquired with an electron flux of 0.3 $e^-/(Å^2\ s)$

Video 2.10: LPTEM data of water droplets flocculating as a result of the inclusion of a non-ionic cosurfactant (Brij-52), acquired with an electron flux of 0.1 $e^-/(Å^2\ s)$

Video 2.11: LPTEM data of slowed Ostwald ripening of water droplets as a result of the inclusion of electrolytes, acquired with an electron flux of 0.1 $e^-/(Å^2\ s)$

Video 2.12: LPTEM data of reversed-phase emulsion behavior at high cumulative fluence (~500 $e/Å^2$)

Videos are available in provided OneDrive repository, and at

https://doi.org/10.1021/acsnano.2c00199.

Chapter 3 *In situ* Observation of Emulsification *via* LPTEM

3.1. Surfactant-Mediated Emulsification

3.1.1. Introduction

As thermodynamically unfavorable materials, the inevitable tendency of these systems is towards a state of minimum free energy. In emulsions, this state is one of minimal interfacial surface area between the immiscible phases, which presents as bulk phase separation.[181] Thus, the vast majority of dispersed phase materials rely on some interfacial layer in order to prevent rapid phase separation. Typically, such interfaces are stabilized by either chemical surfactants or particles (yielding a Pickering emulsion), which generate electrostatic and/or steric repulsions between droplets, and thus slowing their coalescence and demulsification.[182–185] Having a superior understanding of the formation and rearrangement of these interfaces would inform emulsion formulation and development, and potentially unlock new phases. Given our previously demonstrated our ability to image pre-formed emulsions, and having an LPTEM holder equipped with microfluidic functionalities, studying the formation of such materials seemed like a logical next step. Further, our previous work has demonstrated our ability to monitor the real time demulsification of these materials after formation, so a direct view of their formation would be an excellent complementary piece of the puzzle.

3.1.2. Results and Discussion

To probe emulsion formation, the liquid cell was loaded with a solution of surfactant dissolved in the continuous phase. The minor phase was then flowed into the liquid cell via the microfluidic inlets, such that its dispersal could be observed microscopically. Given the excellent contrast of the w/o emulsions studied previously, initial efforts focused on flowing water into cells containing solutions of AOT in isooctane (**Figure 3.1**). Here, the transition from a homogeneous

solution (**Figure 3.1A**) to a heterogeneous morphology is visible after 11 minutes of diluent flow (**Figure 3.1B, C**) and continued evolution in morphology under flow (**Figure 3.1D, E**).

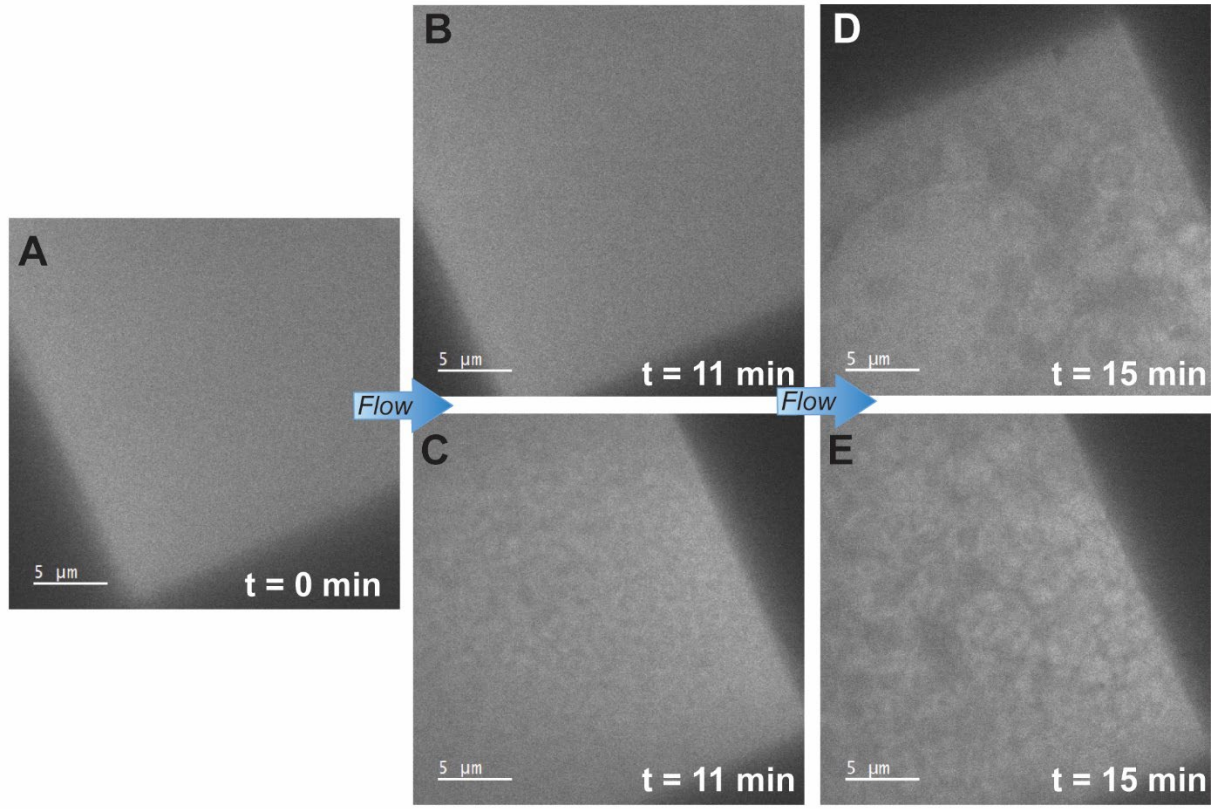

Figure 3.1 Overview of *in situ* dispersal of water in oil.
Liquid cell containing AOT in isooctane solution at various time points of flowing water (5ul/min). (A) liquid cell with only oil and surfactant, (B) lower left corner of liquid cell after 11 minutes of flow, with no structures visible, (C) lower right corner of liquid cell after 11 minutes of flow, with heterogeneous morphology seen, (D) multiple emulsion morphology visible in upper right corner of liquid cell after 15 minutes of flow (E) lower right corner of liquid cell with co-continuous morphology after 15 minutes of flow.

Interestingly, the growth and development of the emulsion structures are anisotropic: structures appear in some areas prior to others (**Figure 3.1B** and **C**). We attribute this to the diffusion-limited nature of *in situ* mixing, whereby the diluent is flowed into an external reservoir surrounding the liquid cell, whereupon diffusion proceeds along the narrow interface at the chips. In such an environment, we posit that this anisotropy is the result of the laterally-arranged microfluidic inlets through which the dispersed phase is introduced. To ensure that the

initial moments of mixing were observed, these lines were left empty until a first image of surfactant solution could be captured. Only then was flow of the dispersed phase initiated, resulting in a slight lag time until reaching the sample cell. Thus, despite the exterior solvent reservoir, it is reasonable to conclude that the directional flow observed results from the choice of microfluidic inlet.

Upon continued flow, this spatial variation persists (**Figure 3.1D** and **E**), and the observed morphology takes on additional complexity, exhibiting both co-continuous phases and nested core-shell morphologies. Typically, such complex morphologies are not straightforward to create, and their appearance is assumed to be the result of kinetic trapping from the spatial constraints of the liquid cell environment, which may prevent reorganization into the most optimal configuration.

When the reverse experiment is done (liquid cell loaded with water and oil flowed in), we see a uniform spherical droplet morphology develop (**Figure 3.2**), counter to the result shown previously. While the formed droplets grow in size under continued flow, they appear in all regions of the cell, as shown in the various panels. It is unclear why this phase of the emulsion develops more homogeneously than the w/o variation, but we hypothesize that it is a matter of differing diffusivity between water and isooctane, and its ability to diffuse through a continuous matrix of the other.

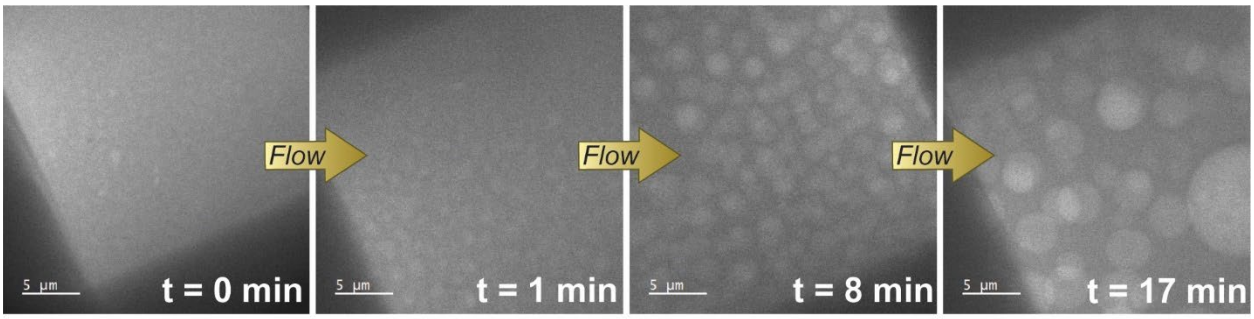

Figure 3.2 Overview of *in situ* emulsification of oil into water
Time series of micrographs showing development of morphology as oil is flowed into liquid cell containing water and surfactant. Time points as indicated on images.

Notably, in addition to the morphological development outlined above, significant droplet dynamics were observed. After a sufficient period of flowing water, pools of oil containing water droplets formed within the continuous matrix of water. Within these oil pools, the water droplets exhibited Marangoni flow, or flow induced by a gradient of surface tension (**Figure 3.3, Video 3.1**).

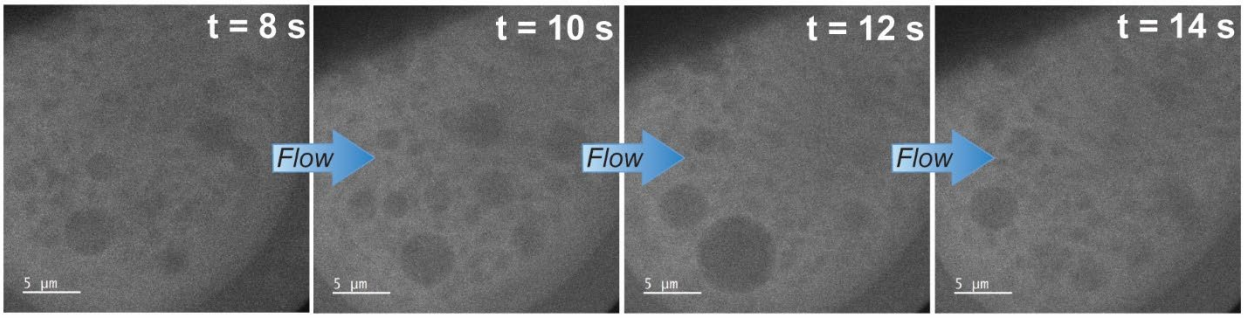

Figure 3.3 Time series of micrographs depicting compartmentalized Marangoni flow induced by 3µl/min external flow

Vortex-like flow was seen as droplets swirled in an anticlockwise direction until the oil pool was flushed out of the viewing window. In another instance, many such oil pools were seen, and the same Marangoni flow was occurring in each pool. The observed compartmentalization is replicated in each droplet across the cell demonstrating that such partitions are repeatable and reproducible (**Figure 3.4**, **Video 3.2**).

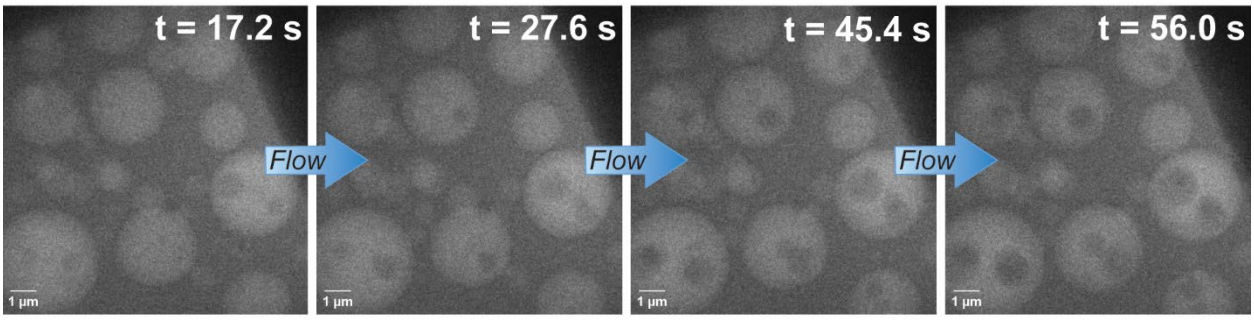

Figure 3.4 Time series of micrographs depicting compartmentalized Marangoni flow induced by 1µl/min external flow.

We want to highlight this finding for two primary reasons: firstly, because such sustained and relatively unhindered motion is highly unusual for *in situ* experiments[163,186–189], and secondly, because this compartmentalized phenomena strongly suggests that emulsions of this class can be used in the future as microreactors to dictate the *in situ* environment. While this motion is almost certainly induced by the force of the external flow of the water, this degree of motion is significant in demonstrating the non-stick behavior of such droplets with respect to the SiN_x windows. Further, we were able to reproducibly induce and observe such phenomena.

3.1.3. Study Conclusions

The formation of heterogeneous materials was successfully observed in these experiments. Ultimately, uniform morphology was not consistently observed, which is attributed to the minimal shear forces in the liquid cell environment and inability to properly control mixing. Shear is needed to disrupt interfaces and create sufficient interfacial area for a dispersed emulsion. Despite this, complex morphologies, such as bicontinuous and nested morphologies, were formed due to the kinetic trapping of the liquid cell. An unanticipated result was the observation of Marangoni flow, which strongly suggests that we can use emulsions as compartments for studied processes. With respect to emulsion formation, we chose to refocus our efforts instead on spontaneous

emulsification processes, which, by definition, do not rely on such dispersal mechanisms, and are thus more suited to replication by *in situ* microscopy.

3.1.4. Supplemental Materials

Video 3.1: Videographic data of water flowed into liquid cell at 3μL/min demonstrating Marangoni flow of water droplets within an oil pool

Video 3.2: Videographic data of water flowed into liquid cell at 1μL/min, where Marangoni flow is observed recurrently across liquid cell

Supplemental videos are available in the provided OneDrive repository.

3.2. Spontaneous Emulsification

This section is adapted from the following publication:

Vratsanos, M. A., Wangyang, X., Rosenmann, N. D., Zarzar, L. D., Gianneschi, N. C. Ouzo Effect Examined at the Nanoscale via Direct Observation of Droplet Nucleation and Morphology, *ACS Central Science* **2023** *9* (3), 457-465 DOI: 10.1021/acscentsci.2c01194

3.2.1. Introduction

The ouzo effect is a well-known phenomenon occurring in alcohols flavored with anise (including ouzo, arak, pastis, and raki) (**Figure 3.5**). The distinctive licorice flavoring of these beverages is the result of the anise extract, *trans*-anethole (melting point = 20 ºC, **Figure 3.5A**).[190] When these drinks (approx. 40% v/v ethanol in water and approx. 1% *trans*-anethole)[191] are sufficiently diluted with water, they become opaque (**Figure 3.5B**). This opacity is the result of the precipitation of *trans*-anethole droplets, as the oil is insoluble in water (**Figure 3.5C**).[190] This effect is generalized for ternary systems, wherein the requirement is that one co-solvent (A) is

soluble in two other solvents (B and C), but wherein B and C are immiscible with each other. Thus, when B is added to a mixture of A and C, it mixes with A and forces C to phase separate.[192]

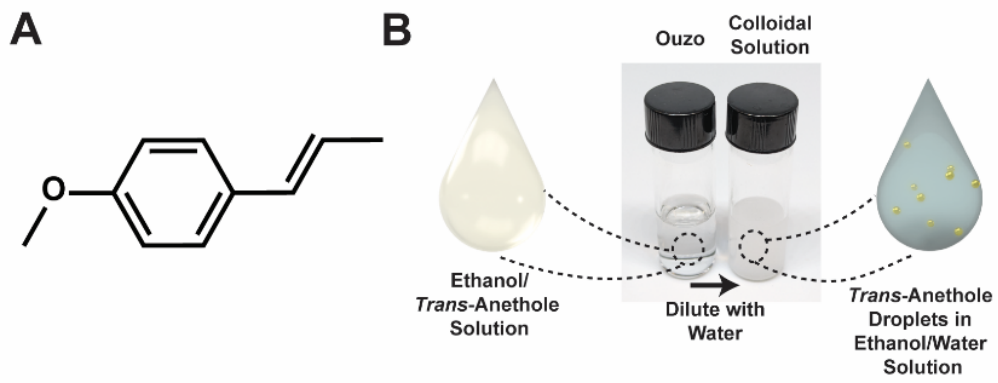

Figure 3.5 Structure of *trans*-anethole and depiction of the ouzo effect.
(A) structure of *trans*-anethole, the small molecule that results in the anise taste. (B) Photographs of the ethanol/*trans*-anethole solution before (left) and after (right) the addition of water, with schematic depictions shown as insets below.

Despite the ubiquity of this phenomenon, it has only recently attracted scientific attention, and was first named in 2003 in Vitale and Katz's seminal work.[190] Since that publication, numerous subsequent efforts to elucidate and understand the mechanism of ouzo droplet formation have emerged[192–197], and such low-energy emulsification strategies have found numerous applications from drug encapsulation to material templating.[197–204] This is a very promising area of study, as the ouzo effect is a definitive example of spontaneous, surfactant-free emulsification, wherein minimal energy is required to disperse the insoluble phase, and yet results in small, low dispersity, homogeneous droplets.[204,205] Further, these droplets show astounding stability despite the system's lack of surfactant stabilizers (the standard mechanism by which emulsion shelf life is extended), for reasons yet eluding researchers.[190] Thus, the ouzo effect has the potential to allow the straightforward scale up of many emulsified products, as it is difficult to achieve sufficient shear on industrial scales, all without requiring the addition of surfactants, which may adversely affect formulations and are often environmentally detrimental.[99,183]

Although there is a substatntial body of work in this area, a satisfactory understanding of the origin of this stability eludes researchers.[192] Many recent efforts regarding the ouzo effect have focused on understanding the so-called 'pre-ouzo' phase region, wherein weakly associated structures on the order a few nanometers are formed, prior to the evolution of the more stable droplets.[206–209] While these structures are of interest, this size regime is limited to the initial time points of the effect, and will give little structure-property understanding of the meta-stable structures formed at later time points. These later structures are within the size regime that may be reliably resolved via electron microscopy techniques. Thus, we have chosen to focus on the behavior and growth of these droplets once in the meta-stable ouzo region.

In this work, we have not only been able to directly observe the nucleated *trans*-anethole droplets in their native state, but we have also been able to induce and observe said nucleation *in situ*. Such direct observation emulsification via the ouzo effect has never been achieved before on the nanoscale and is only possible through liquid phase transmission electron microscopy (LPTEM) techniques. LPTEM is a nascent *in situ* microscopy technique which encapsulates picoliters of liquid sample against the vacuum environment of the microscope, allowing direct observation of solvated samples without fixation at unprecedented spatiotemporal resolutions.[5,82,88,210–212] Notable advances in the understanding of nucleation and growth pathways[131,134,213–218], crystallization[87,219,220], nanoparticle behavior,[163,221–223] self-assembly processes,[155,157,224] thermoresponsive materials,[225,226] and liquid-liquid phase separation[84,85,227,228] have been achieved via LPTEM since its inception. LPTEM presents a unique benefit for the study of liquid systems in that the contrast is directly proportional to the densities of the materials being studied. Other microscopy techniques, such as optical and super-resolution microscopy, are dependent on the refractive index of the materials or the inclusion of tags, respectively.[229] Further,

though super-resolution microscopy may be able to get comparable spatial resolution in some cases, the imaging is dependent on the inclusion of fluorescent dyes, which inherently raises uncertainty with respect to the identification and assignment of phases. By contrast, LPTEM yields contrast as a function of density differential, which allows the unambiguous assignment of phases as a function of intensity and contrast. Additionally, LPTEM is useful in its relative simplicity – image acquisition and processing are straightforward, and minimal post-processing or algorithmic deconvolution is needed to interpret the data, which further permits improved temporal resolution. Here, we use this technique not only to study multiphase solvated systems, but to also introduce other solvents *via* microfluidic lines and ports built into commercial LPTEM holders (). Studies of mixed phase systems via LPTEM, and specifically, the *in situ* mixing of multiple phases, remain an unexplored area of the field. Other works in this area have previously reported *in situ* observation of liquid-liquid phase separations, primarily in systems with amphiphilic block copolymers and intrinsically disordered proteins.[84,85,92,227] Here, we use LPTEM to observe *in situ* emulsification events of small molecules such as *trans*-anethole. Further, this present work is the first *in situ* observation of so-called 'surfactant-free microemulsions' (SFMEs). Observation of this process allows us to directly observe the morphology and evolution of emulsions produced via the ouzo effect.

3.2.2. Results and Discussion

3.2.2.1. Multimodal Microscopy of Pre-Formed Ouzo Emulsions

Based on previous successes imaging the morphology of traditional, surfactant-containing emulsions formed in the bulk[5], we started by imaging the pre-formed ouzo droplets to investigate whether they are of sufficient contrast to resolve *in situ* (**Figure 3.6**). Shown here with

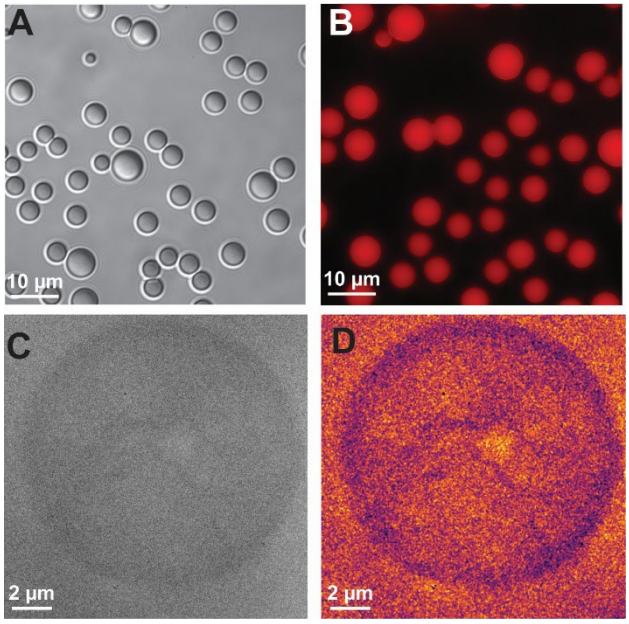

Figure 3.6 Multimodal microscopy of pre-formed ouzo droplets.
(A) Brightfield optical and (B) fluorescence microscopy of bulk ouzo droplets. Droplets in (B) contained added Nile Red dye. (C) TEM micrograph of preformed ouzo droplets formed from 5 v% *trans*-anethole solution. (D) False color image processing applied to TEM micrograph.

complementary optical and fluorescence microscopy (**Figure 3.6A, B**), we see that droplets of the same size regime are visible in the liquid cell experiments (**Figure 3.6C, D**).

The optical and fluorescence microscopy was carried out by adding drops of DI water to induce the ouzo effect in 20 v% trans-anethole solution, analogously to the LPTEM set up (**Figure 3.7**). Brightfield optical micrographs were taken on a Nikon Ti-U inverted microscope using an Imaging Source 23UX249 color camera. Nikon Plan Fluor 100x/1.30 Oil objective was used to image the samples. Differential interference contrast was used. Fluorescence images were taken by a Zeiss Axio Observer inverted microscope with Zen pro software and an Axiocam 503 mono camera. A Zeiss Plan-APOCHROMAT 63x/1.4 oil objective was used to observe the droplets and Nile Red, the fluorescent dye used for dying trans-anethole droplets, was excited by Colibri 7 LED light. A 91 HE CFP/YFP/mCherry filter was used to give off excitation from 494 – 528 nm and receive emission from 546 – 564 nm. The apparatus for containing the solution is as shown below (Figure 3.7). Adding 3 drops (~150 µL) of DI water to the 1 mL *trans*-anethole in ethanol solution would induce formation of *trans*-anethole droplets. To observe the droplets on an inverted microscope, 1 mL of *trans*-anethol / ethanol solution was transferred to a coverslip-bottom dish to which 3 drops of DI water is subsequently added.

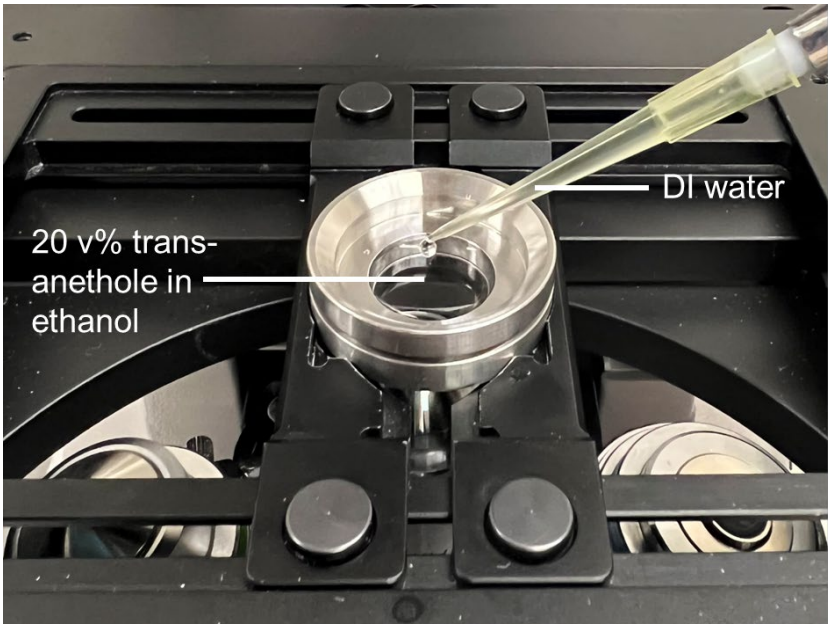

Figure 3.7 Experimental set up for optical and fluorescence microscopy.
Sample chamber contains ethanol and trans-anethole, which is manually diluted via pipette.

We can conclude that the dark droplets in the LPTEM images are the *trans*-anethole rich regions, given the higher density of this phase with respect to ethanol. Closer inspection of the TEM micrographs reveals internal structuring of the droplet, which we have here used false color to emphasize (**Figure 3.6D**). Interestingly, droplets with internal structure have not been previously seen in any other investigated emulsion formulations. To further probe this structuring, we have also applied some basic image processing to aid visualization of the internal structure. This not only emphasizes the ringed structure of the droplets, but also reveals internal structuring as well.

3.2.2.2. *In Situ* Formation of Ouzo Emulsions

Given that the visibility of *trans*-anethole droplets had been established, we could investigate the formation of such droplets by harnessing the microfluidic capabilities of the liquid cell holder, which allow us to flow solutions into the sample chamber during imaging. To ensure that a true time zero image was captured, the flow lines were left empty of diluent to prevent

premature mixing, and the flow of water was not started until representative images of the sample as loaded had been taken. Some simple calculations considering the geometry of the microfluidic system and the relevant flow rates estimate that the water should enter the sample chamber between 15 and 40 minutes after initiation. The flow lines have an internal diameter of approximately 360 μm, and a length of approximately 40 cm. The fluid velocity varies linearly with volumetric flow rate, so under these constraints, so the fluid fronts were moving at approximately 0.49 mm/s and 0.16 mm/s at the higher and lower flow rates, respectively. Thus, diluent should have taken from 13-39 minutes to reach the tip of the holder. There is some variability associated with the actual mixing of the inlet solution and the sample between the chips. Because the solution is flowed into the chamber holding the SiN_x chips (**Figure 3.8**), there is some exterior volume that must be filled before mixing can occur.

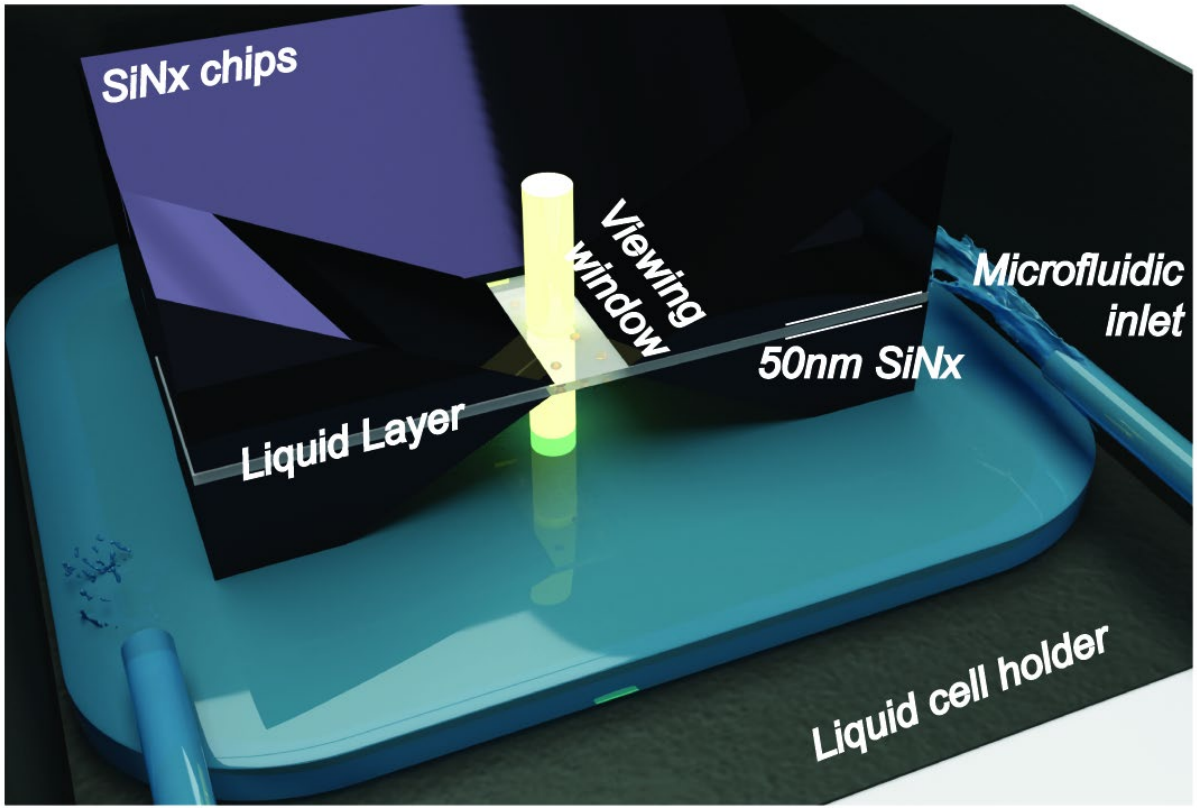

Figure 3.8 Schematic depiction of SiN_x liquid cell assembly.
Notable features here include the 50 nm thick SiN_x windows through which the imaging occurs, the variable thickness liquid layer (ranging from 200-500 nm), and the microfluidic ports on the periphery of the SiN_x enclosure.

Preliminary emulsification experiments were carried out with surfactant-loaded oil phases which were imaged prior to flowing in water. In such experiments, anisotropic appearance of the dispersed phase from the port of origin confirms these calculations and demonstrates the diffusive-driven nature of the *in situ* transport (**Figure 3.9**).

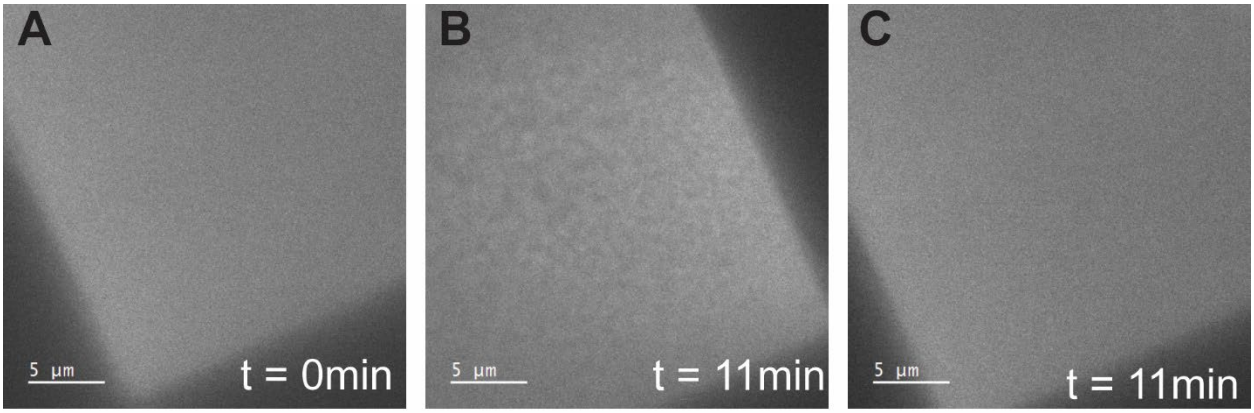

Figure 3.9 Time series of representative micrographs of *in situ* experiment flowing water into sample of AOT dissolved in isooctane**.**
(A) Initial image of cell prior to beginning flow of water (t=0 min), demonstrating homogeneous and structure-less morphology. Water flowed at 5 µl/min resulted in appearance of structures in one corner (B), but not another (C) after 11 minutes of dilution.

When the exterior volume is filled, diffusive mixing between this external reservoir and the narrow region of available sample surface area occurs. Thus, the observed nucleation of trans-anethole droplets at the 30-minute mark is consistent with expectation.

Initially, we studied a 20 v.% *trans*-anethole solution diluted at a rate of 3 µL/min and were able to observe the formation and growth of oil droplets upon dilution of the ethanol solution (**Figure 3.10**). These droplets faintly appeared after approximately 30 minutes of dilution and exhibited growth and morphological evolution under continued stroboscopic imaging (**Figure 3.10A**).

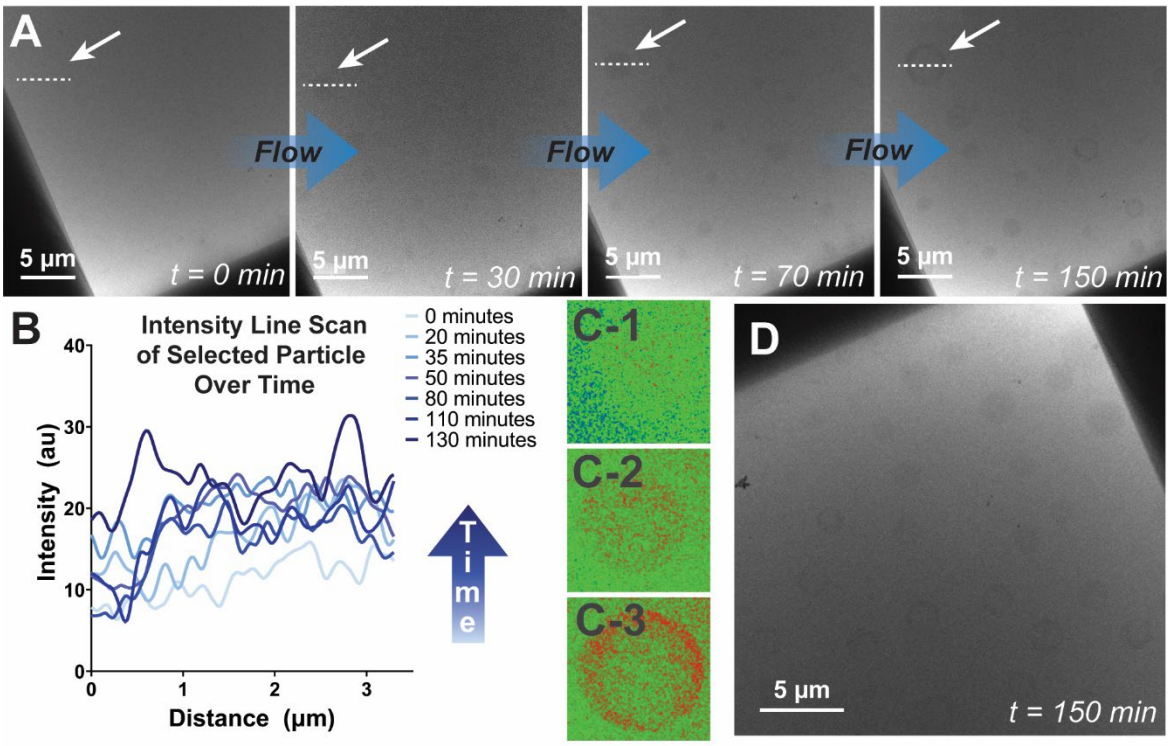

Figure 3.10 Time series of the ouzo effect in a solution of 20 v% *trans*-anethole in ethanol, diluted at a rate of 3 µl/min.
(A) Initial images reveal no structures, and droplets appear, grow, and develop a ringed morphology during continued flow and stroboscopic imaging (to minimize fluence). Arrow indicates selected region for analysis. (B) Line scan across a representative droplet (denoted by white arrows and dashed lines) from the time series in A to demonstrate the change in pixel intensity over time. Greater intensity indicates darker pixels, corresponding to greater contrast in the image. Line scans were taken across the area indicated with the white arrow, and a representative line scan is depicted in the image at t=150 min. (C1-3) Cropped image of analyzed droplet (as indicated with white arrows) with false coloration applied to enhance visibility of evolution in time (30, 70, and 150 minutes, respectively). (D) Micrograph of a less-imaged corner of the liquid cell at the end of the experiment (t=150 min). These droplets demonstrate that their presence and structure does not rely on incident electron beam.

These droplets are first visible at sizes over a micron, and much of the evolution over time was in intensity, rather than size (**Figure 3.10B**), which results in a dark ring around the exterior of the droplet and a lighter interior (**Figure 3.10C**). Recent work has revealed the presence of 1 and 100 nm structures in the monophasic region, which are likely of insufficient contrast for visualization. Thus, we are most likely observing the larger structures resulting from phase separation.[230] Unlike efforts to emulsify substances *in situ* via surfactants (**Figure 3.9**), these droplets appeared homogeneously, developing simultaneously across all visible areas (**Figure 3.10D**), indicating that the solvent had reached some critical concentration of water to render the

trans-anethol insoluble. The presence of structuring in both these and the preformed droplets may suggest that the droplets undergo some internal microphase separation after nucleation. The changes in contrast suggest that an ethanol/water-rich region develops at the center of the droplet, while the shell remains predominantly composed of *trans*-anethole (as indicated by the relative contrasts).

3.2.2.3. Evaluation of E-Beam Influence and Verification of Chemical Integrity

Previously, the same e-beam of our LPTEM has been used to initiate *in situ* polymerization.[155] To ensure that this e-beam induced polymerization is not the cause of our observations (given the unsaturated alkene present in *trans*-anethole), we additionally studied *N*, *N*-dimethylaniline as the oil phase. *N*, *N*-dimethylaniline is also know to undergo the ouzo effect, but lacks the unsaturated carbons, so any observed droplet formation cannot be the result of beam-induced polymerziation.[190] Following identical experimental protocol, (20 v% oil in ethanol by volume, 3 μL/min dilution), the spontaneous nucleation of droplets was observed again, confirming that droplet appearance is not the result of polymerization (**Figure 3.11**). Internal

anisotropy of the droplet structure was also seen here as well, though less pronounced than *trans*-anethole.

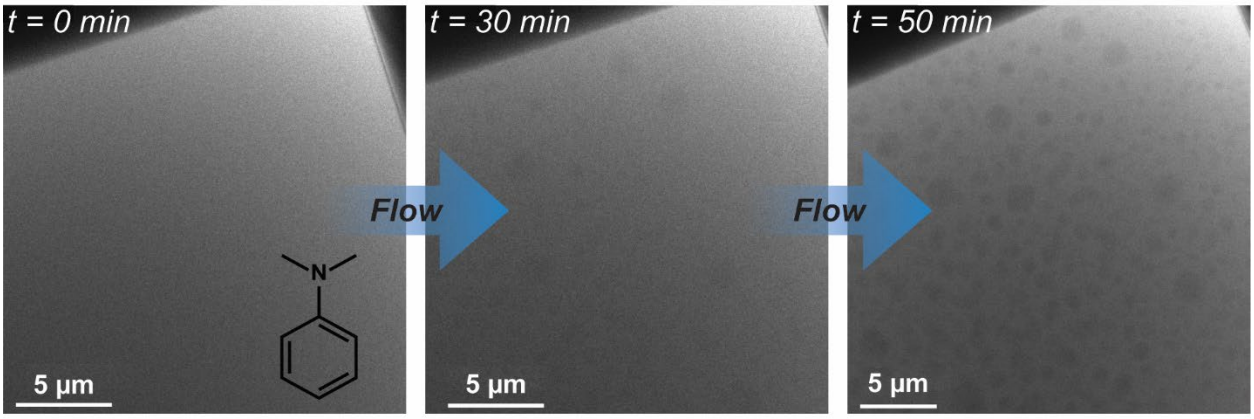

Figure 3.11 *N*ucleation of *N*, *N*-dimethylaniline droplets from 20 v% ethanol solution by dilution with water at 3 µl/min.
Micrographs show progression from initial cell without structures to the appearance of high contrast oil droplets under continual dilution. Structure of *N*, *N*-dimethylaniline is shown as an inset in first panel.

To quantitatively characterize the observed droplet formation processes, droplet growth rates were measured and post-mortem performed micro-Fourier Transform Infrared Spectroscopy (µFTIR) was performed (**Figure 3.12**). Droplet sizes over time (**Figure 3.12A**) were manually measured and plotted as a function of time, with logistic fits applied to establish a growth rate (**Figure 3.12B**). This protocol was followed for all data acquired, and complete data sets are available below (**Table 3.1)**.

Table 3.1 Tabulated droplet population and growth statistics for all experimental sample formulations

Content	Flow rate (µL/min)	Number of droplets	Growth constant (min^{-1})	Average starting diameter (µm)	Average final diameter (µm)
20 v% trans-anethole	3	49	0.2917±0.3325	1.39±0.26	1.97±0.50
20 v% trans-anethole	1	28	0.0240±0.0274	1.65±0.37	2.28±0.41
10 v% trans-anethole	3	15	0. 1293±0.2412	1.69±0.73	2.31±0.82
10 v% trans-anethole	1	6	0.04855 ± 0.02937	1.02±0.42	1.49±0.35
5 v% trans-anethole	3	3	0.05712±0.03628	1.69±0.38	2.96±0.45
20 v% dimethylaniline	3	>200	0.1824 ± 0.1353	1.33 ± 0.35	1.62 ± 0.44

To further investigate whether or not the active small molecule (*trans*-anethole) chemically degraded during observation, we used µFTIR analysis, which allows us to take FTIR spectra of the imaged region on the micron scale and compare spectra of the unimaged region and controls (**Figure 3.12C**). Here, the three spectra were acquired at the points indicated by arrows to generate two spectra of unimaged region (Scans 1 and 3) for comparison with the spectrum of imaged region (Scan 2). Additionally, a control sample was created by drop-casting the same solution on an unused SiN_x chip, which remained unimaged. Given that the signal from the imaged region matches the spectra of both the unimaged regions on the experimental chip and unimaged control, we are confident that the *trans*-anethole remains undamaged by the beam at these conditions (0.1 $e^-/Å^2s$), and thus droplet growth and evolution is not the result of e-beam induced damage. Conversely, high-flux experiments (>1 $e^-/Å^2s$) showed large discrepancies between Scan 2 and Scans 1 and 3, indicating that this post-mortem technique can successfully differentiate between intact and damaged material (**Figure 3.13**). Thus, we are sufficiently confident that the observed

growth is not the result of e-beam mediated damage and can draw conclusions from our evaluations of kinetics.

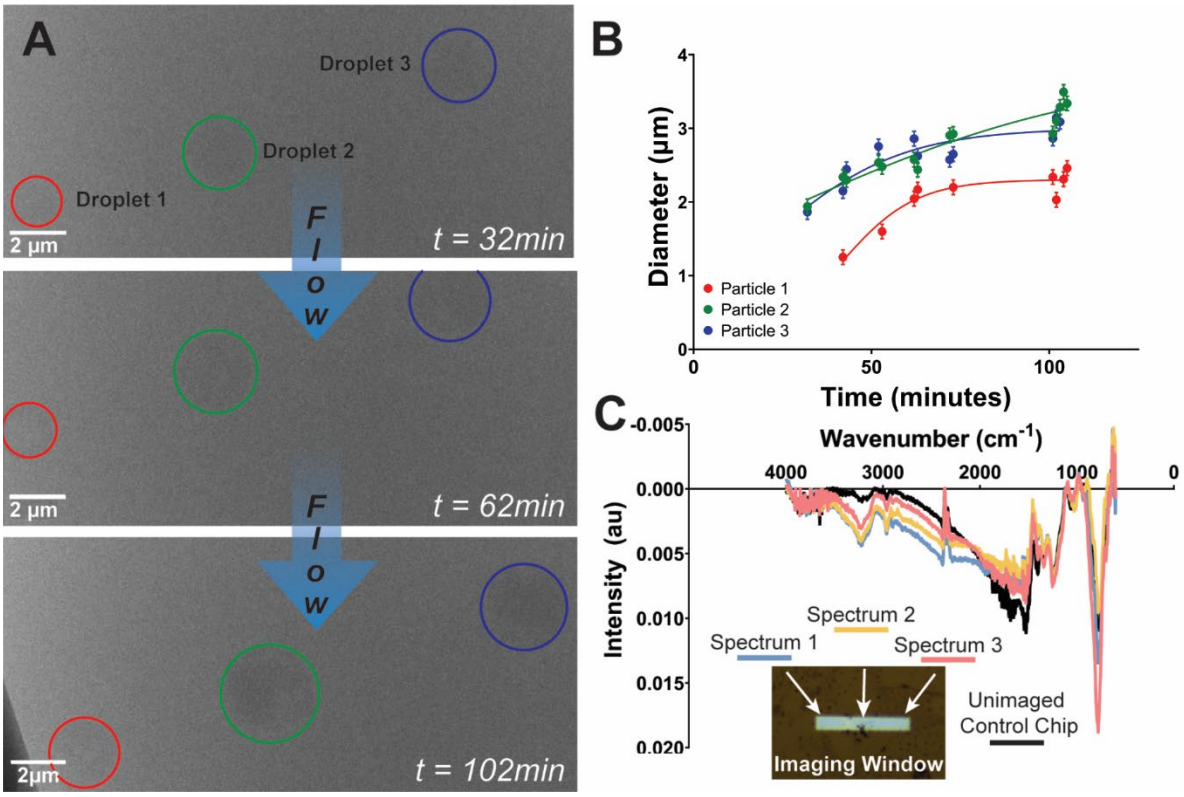

Figure 3.12 *In situ* formation and growth of *trans*-anethole droplets from a 5 v% trans-anethole in ethanol solution, diluted at a rate of 3 µl/min, and subsequent analysis.
(A) Selected micrographs from a time series documenting the evolution of 3 droplets, denoted by arrows. (B) Plot of droplet diameter growth in time and accompanying linear fits of data. Linear fitting here indicates the growth mechanism does not follow typical ripening rates. (C) µFTIR spectra of experimental SiN_x chip (pictured in inset). Spectra were acquired at the three indicated locations, Spectrum 2 being the imaged region, and Spectra 1 and 3 being outside the imaging region. Black spectrum shows unimaged control chip, with dropcast *trans*-anethole solution for reference. Here, we see the spectra match closely between the imaged and unimaged regions, indicating that minimal damage has occurred to the material.

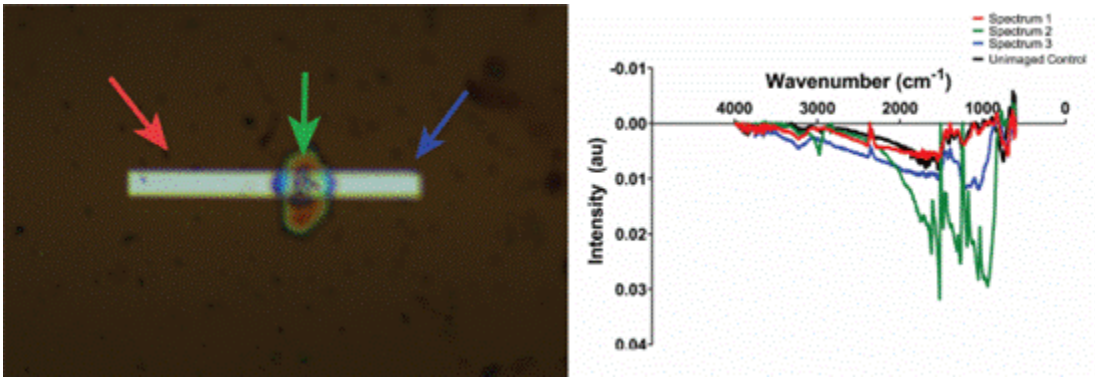

Figure 3.13 Post mortem analysis of high flux experiment
Optical micrograph of used SiN_x chip showing location of FTIR spectra, with visible damage at center and corresponding FTIR spectra showing damage in the imaged area.

3.2.2.4. Quantitative Analysis and Comparison of Droplet Growth Rates

Using the image analysis techniques outlined above, we analyzed droplet growth data from emulsification experiments across a range of concentrations (5, 10, and 20 v.% trans-anethole) and flow rates (1 or 3 μL/min) (**Figure 3.14**) in order to evaluate differences in nucleation and growth rates. Growth rates were determined via logistic fit in Prism software, and k values (or logistic growth rates) are compared below (**Table 3.2**). It was anticipated that slower flow rates would result in slower growth rates and a greater, more homogeneous droplet population than a higher flow rate, resulting from the increased equilibration time. A weak concentration dependence was observed, but the high standard deviations for these measurements rendered them statistically insignificant. However, one way ANOVA indicated significant differences in k values between flow rates (**Figure 3.15** and **Figure 3.16**). The primary variation observed was droplet number as a function of *trans*-anethole concentration (**Figure 3.15**). Both linear and logarithmic growth fits were considered for both droplet diameter and the cube of the droplet radius (**Table 3.2**). Here, we see that the logistic fit has both a higher R^2 and lower standard error, indicating it is a better fit than the linear model. Additionally, we see that the r^3 plot is not well fit by a linear curve, which

suggests that the droplet growth kinetics are not consistent with traditional models of Ostwald ripening.

Table 3.2 Comparison of curve fits for 5% trans-anethole data

	Linear Regression R^2	Linear Regression Error	Logistic Fit R^2	Logistic Fit Error
Droplet 1 - diameter	0.6413	0.2479	0.8858	0.1511
Droplet 2 - diameter	0.8962	0.1522	0.9024	0.1542
Droplet 3 - diameter	0.7602	0.2087	0.8102	0.1857
Droplet diameter - average	0.7659	0.203	0.866	0.1637
Droplet 1 – r^3	0.6673	0.3199	0.8198	0.2543
Droplet 2 – r^3	0.8694	0.5028	0.8687	0.5265
Droplet 3 – r^3	0.7672	0.4763	0.7637	0.5089
Droplet r^3 - average	0.7680	0.433	0.8174	0.4299

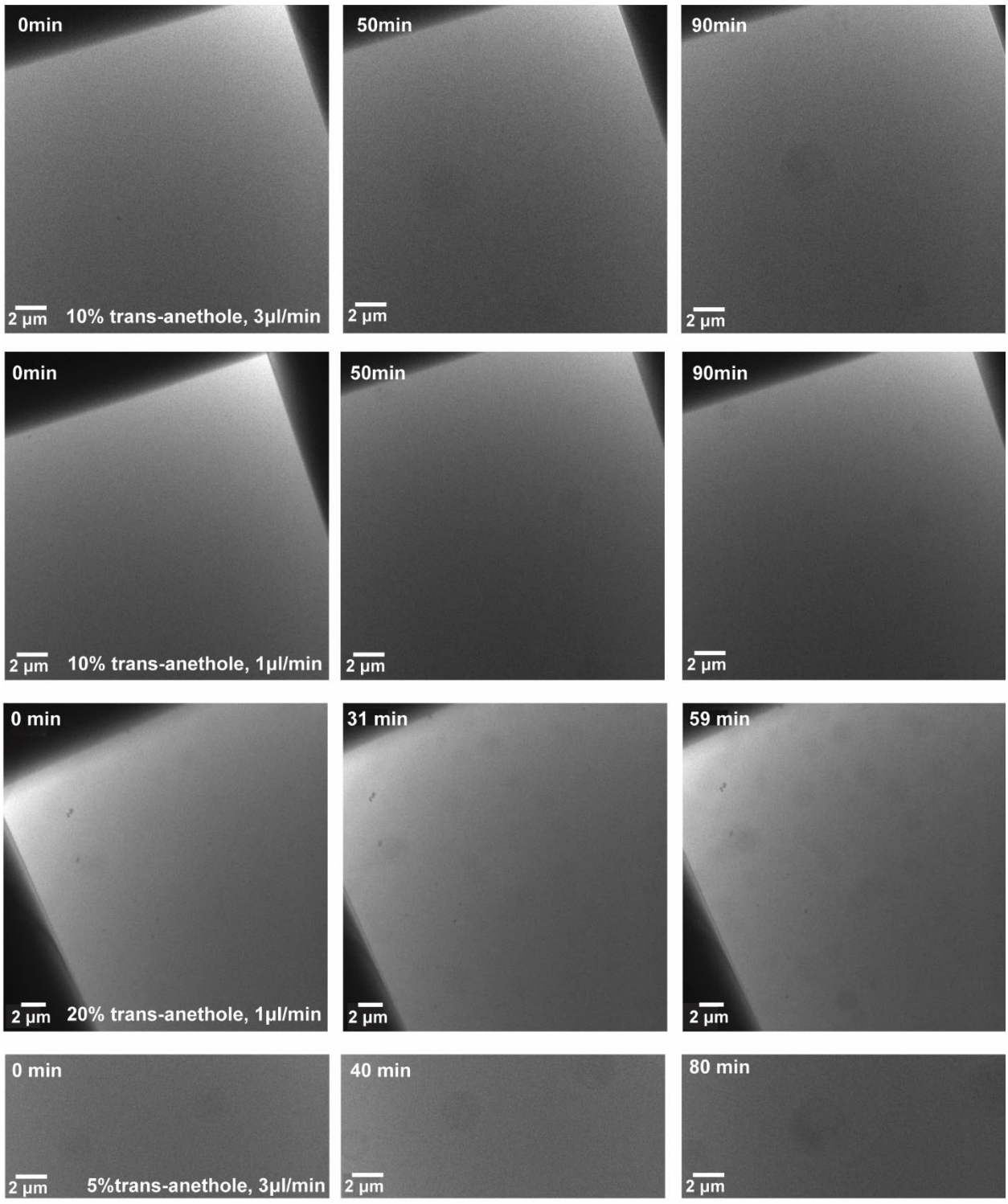

Figure 3.14 Representative time series of Ouzo nucleation across varying concentration and flow conditions. Times and scales as annotated.

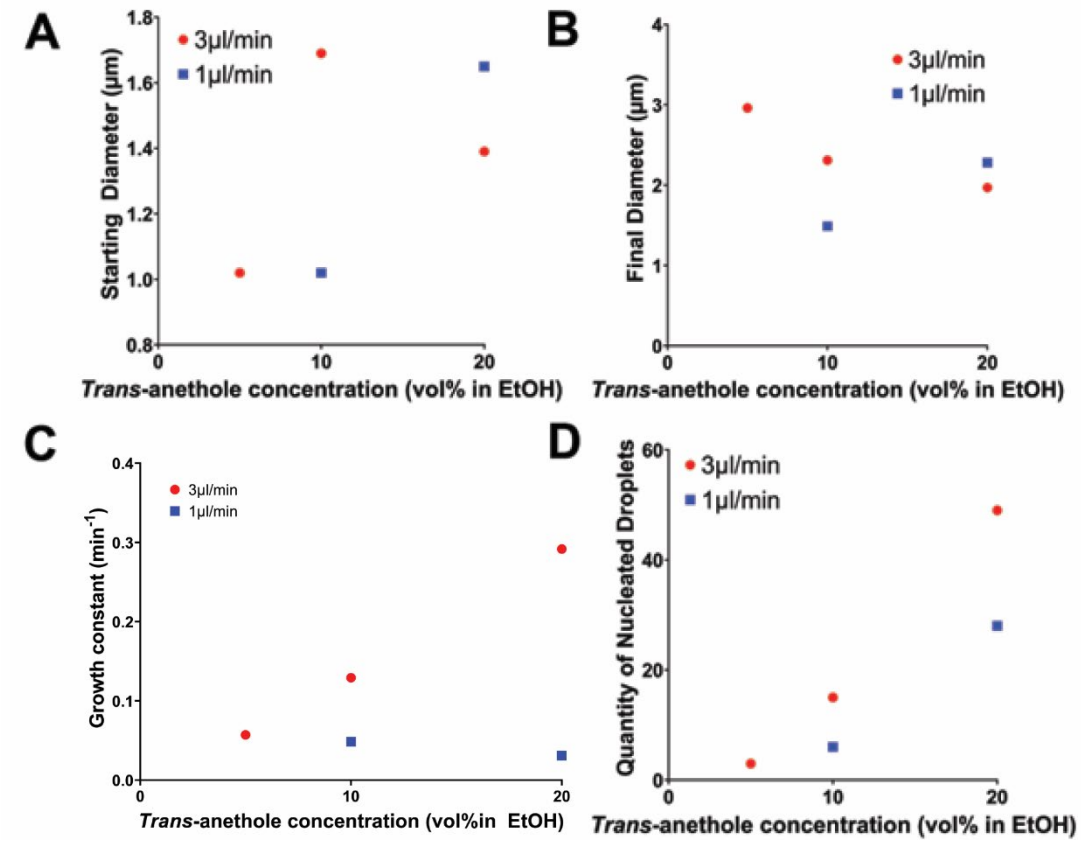

Figure 3.15 Particle growth statistics plotted as a function of trans-anethole concentration and dilution rate. (A) Droplet diameter at nucleation. (B) Droplet diameter at final imaging time point. (C) Growth rate in min^{-1} of droplets. (D) Number of droplets quantified.

One way ANOVA indicated that there is significant difference in growth constants as a function of flow rate ($p<0.001$) (**Figure 3.16**).

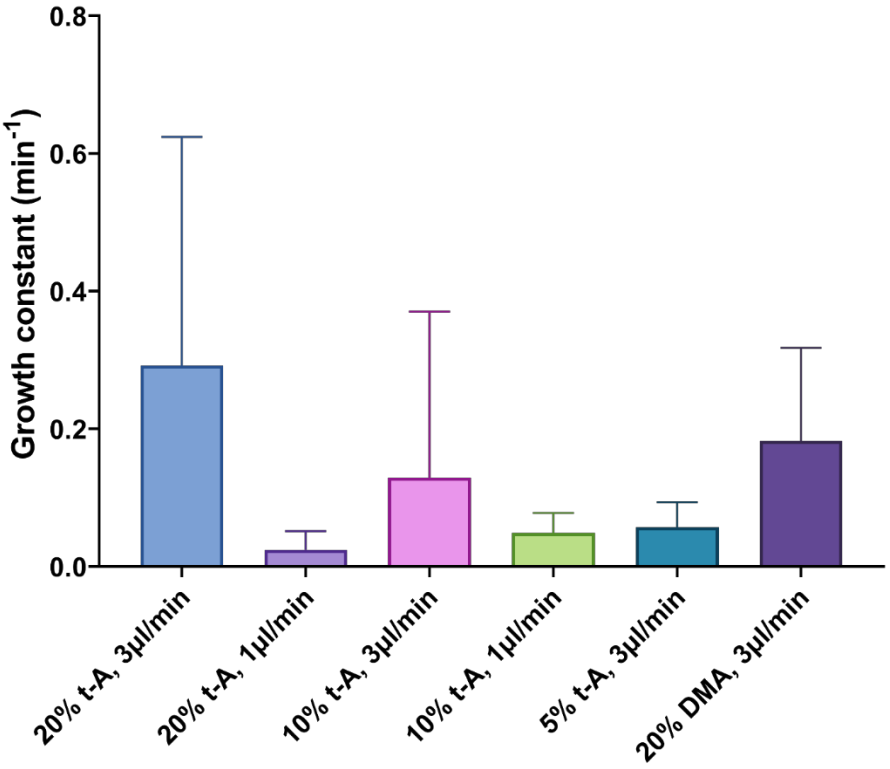

Figure 3.16 Comparison of growth constants as a function of oil concentration and flow rate.

The *trans*-anethole concentration is directly correlated with the number of droplets nucleated in the cell, consistent with findings in the literature (**Figure 3.15**).[193] Several mechanisms of droplet formation and growth for ouzo emulsions have been hypothesized, and these follow the destabilization methods of classical emulsions: diffusion-driven processes (ripening), or combination events (coalescence).[200] Here, no coalescence events were observed under any conditions, despite previously establishing that such events are visible by this technique at comparable time and length scales[5] However, droplet growth was logistic in time, which is contrary to classical ripening mechanisms, wherein r^3 is linear in time.[17] Thus, our findings strongly suggest that the predominant mechanism here is the diffusion-driven growth of initial nuclei, but not Ostwald ripening. We have previously considered the effect of spatial constraints on droplets in this size regime. Indeed, droplets with diameters on the micron scale exist as

spheroids *in situ,* and have different curvature and surface areas than spheres typically considered in the bulk.[5] However, these deviations act in an approximately equal and opposite manner so as to yield an effective Ostwald ripening rate of the same order of magnitude as predicted. Thus, we do not consider it is likely that the anomalous ripening rate results from *in situ* artifacts. It is possible that coalescence events may occur while the sample is in the pre-ouzo region, which would suggest that it occurs on such small length scales that we are unable to resolve them.[207] If this is the case, the coalescence events have concluded prior to the resolution of the droplets via LPTEM. Our findings support the theory that these droplets grow via diffusion-driven mechanisms, or that such growth happens via a two-step process, the second part of which we are observing.

With such models, we can compare growth constants, k, to evaluate differences in conditions. A weak concentration dependence was observed, but not determined to be statistically significant[193] Flow rate was shown to have a significant impact on growth rate at both the 20% and 10% *trans*-anethole conditions. Nucleation at slower flow rates had significantly lower growth rates than those nucleated at higher flow rates, (**Figure 3.16**). This supports the hypothesis that a more rapid addition of water would result in the nucleation of fewer, larger droplets as a result of kinetic trapping. It is possible that these variations were, altered by the confinement of the liquid cell, which significantly limits diffusion and constrains particle behavior to the x-y plane.[161,187,188] Thus, we are hesitant to draw quantitative conclusions from these rate evaluations, and we consider

the significance to be the observed trends between flow rates and compositions, as well as the structural observations made.

3.2.2.5. Ouzo Effect in Commercial Samples

In the interest of authenticity, experiments were also carried out with a commercial ouzo formulation. 12 Ouzo™ was loaded into the liquid cell and diluted at a rate of 3 μl/min (**Figure 3.17**). Though the exact *trans*-anethole content in this formulation is unknown, it is reasonable to assume that it is around 1 v%, and we will assume that the overall solvent composition is 42 v% ethanol, with the remainder being water.[191] Here, we again saw the evolution of droplets after an initial absence of structures at approximately 30 minutes, though these droplets were much smaller than those seen previously using pure *trans*-anethole (**Figure 3.17A**). By following our established image processing protocol, we were able to visualize the droplets' growth and densification in time (**Figure 3.17B**). We can use this data to quantify droplet growth by evaluating area above a given background intensity, which shows a logistic growth (**Figure 3.17C**).

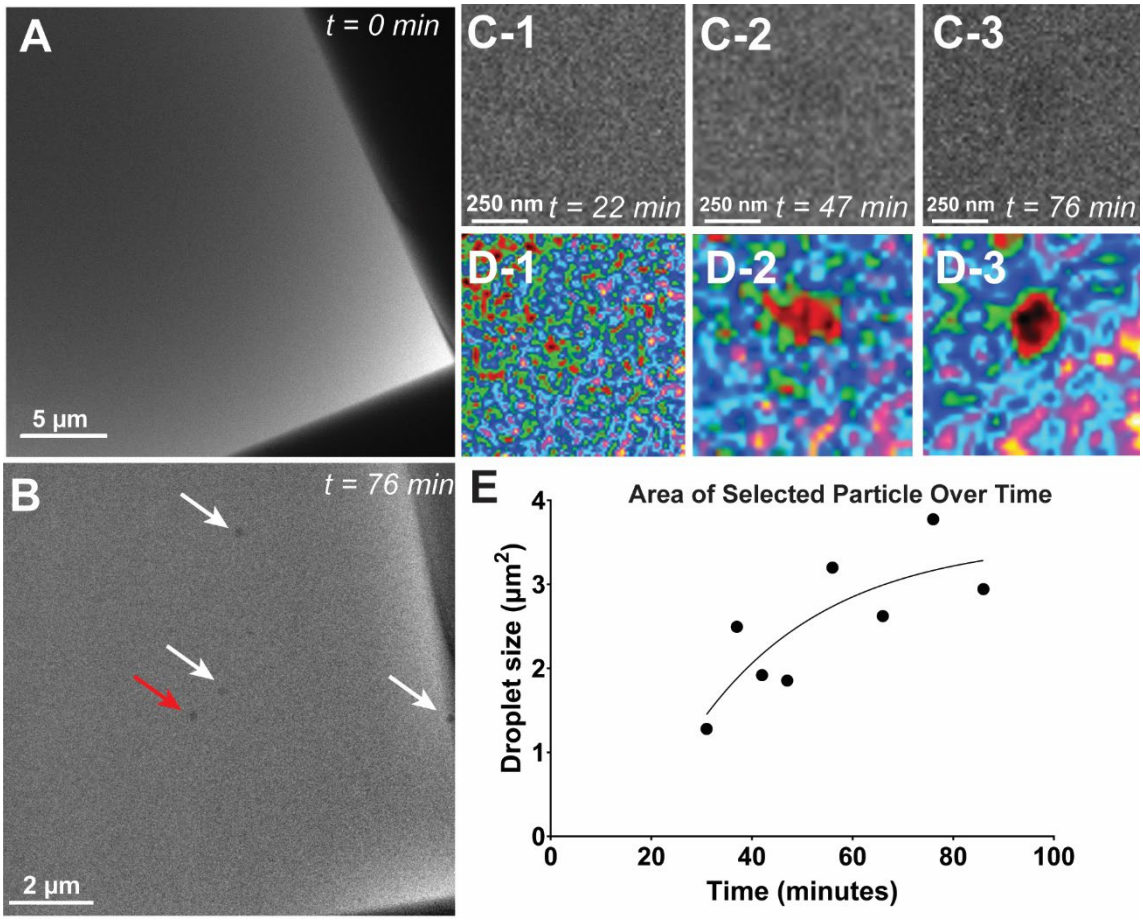

Figure 3.17 Droplet nucleation in a commercial ouzo sample.
(A) Initial image of commercial ouzo, no structures visible. (B) Micrograph of ouzo after dilution with water at 5 µl/min for 76 minutes, with droplets indicated by arrows. Red arrow denotes droplet for subsequent analysis. (C-1 – C-3) Sequential micrographs of droplet indicated by red arrow. Micrographs have been cropped to a region of interest around the droplet and have been background subtracted for visibility. (D1-D3) False coloration applied to above micrographs to enhance visibility of droplet nucleation and growth. (E) Plot of droplet area growth in time for selected region indicated above.

Droplet "ringing" was observed across the majority of experiments indicating microphase separation of an ethanol-rich region within the trans-anethole droplet (particularly evident in **Figure 3.6C and D and Figure 3.9A and C**). We were unable to observe this microphase separation inside droplets with optical or fluorescence microscopy, and it has not been reported under any other conditions or compositions.[5] This separation may be the result of local concentration gradients appearing around the droplet and inducing further structuring as a result of preferential substrate wetting. Thus, while this is most likely an artifact of the *in situ* flow cell

environment, it brings up interesting possibilities and opportunities to intentionally generate such structures *via* designed nano-confinement and surface chemistry. Similar events have been observed on other length scales.[230]

It is notable that coalescence was not observed for this system of emulsions, as it lends credence to hypotheses that ripening-type behaviors dominate the evolution of such emulsions in time[230,231]. Further, as is the nature of microscopy, quantitative evaluation can be made from direct observations as compared to the suite of parallel techniques which must otherwise be employed to glean similar information.[231]

3.2.3. Study Conclusions

The observation of both the formation and morphology of spontaneously emulsified oil in water droplets via the ouzo effect was achieved *via in situ* liquid phase transmission electron microscopy and is the first example of such *in situ* emulsification. Here, mechanistic studies of droplet formation and growth found that both the growth constant and number of nucleated, confined droplets was directly proportional to *trans*-anethole concentrations. Coalescence was not observed, and kinetics of observed ripening did not match established models of Ostwald ripening, perhaps suggesting a more rapid depletion of smaller species. Interestingly, internal droplet structuring was observed *in situ* but not by correlative fluorescence microscopy. Post-mortem characterization and strategic controls demonstrate that these morphologies and growth are not the result of e-beam induced processes and may be the result of surface interactions triggered by confinement. Such insights have not been possible by the indirect characterization methods previously used and lend credence to some of the theorized mechanisms of stability. Given the demonstrated successful imaging of this relatively simple liquid-liquid phase separation, we

anticipate that this *in situ* microscopy technique may be useful in gaining insight into other emulsifications, such as phase inversion temperature, and more complex multi-phase systems.

3.2.4. Experimental Methods and Supplemental Information

3.2.4.1. LPTEM Sample Preparation

Liquid cells were prepared as previously described in literature.[5] Briefly, solutions of ethanol and *trans*-anethole were drop cast onto non-glow discharged SiN_x chips in amounts less than 0.8 μL (**Figure 3.8**). Top chips were deposited such that the windows were aligned orthogonally, and the holder was sealed with the top clamp assembly. Lines were left unfilled with solvent so as to avoid premature dilution of the sample with diluent. The holder was then pumped down using the external pumping station, and the cell windows were visually inspected using the attached optical microscope. Once the cell has reached 8.6×10^{-6} mbar, the fluidic ports were unsealed and the flow line was attached, so as to ensure cell integrity during dilution. This flow line was attached to a syringe and syringe pump, which were used to flow in water to the cell at rates from 1-5 μL/min. A JEM-ARM300F *trans*mission electron microscope operating at a voltage of 300 keV and current of 15 μA (FEG source) was used for liquid cell experiments. Images were acquired via Gatan 2*k* × 2*k* OneView IS CMOS camera *via* Gatan Digital Micrograph imaging software with exposures of 1 s.

3.2.4.2. Image Analysis:

Images were binned to a resolution of *1k* x *1k* and background adjusted by subtracting a heavily Gaussian blurred copy of the same. This helps to compensate for the gradient background present from the bulged liquid layer, and doing so helps to enhance visibility of structures. Structures were then manually measured in ImageJ and resulting data were analyzed in GraphPad Prism.

3.2.4.3. Materials

Trans-anethole (>98.0%) was purchased from TCI Tokyo, ethyl alcohol anhydrous (>99.98%) from (Electron Microscopy Science), and Nile Red from CHEM-IMPEX. All other reagents, including N,N-dimethylaniline, dioctyl sulfosuccinate, sodium salt (Aerosol OT/AOT), and 2,2,4-methylpentane (isooctane), were received from Sigma and used without further purification.

3.2.4.4. Sample Preparation

Solutions of *trans*-anethole in ethanol were prepared and stored for no more than 24 hours before use so as to ensure sample integrity. All formulations are given in volume percentages. To pre-form the droplets, an aliquot of this solution was chilled, and DI water was added dropwise until the solution was homogeneously cloudy. The same protocol was followed for the N, N-dimethylaniline solutions.

3.2.4.5. μFTIR Analysis

In order to verify the molecular integrity of the *trans*-anethole after imaging, post-mortem μFTIR was performed. A Bruker MicroFTIR was used to analyze the windows of the SiN_x chips after the conclusion of the experiment as a post-mortem characterization to confirm the molecular integrity of our small molecules. Given the thickness of the SiN_x chips and windows, it was necessary to run these experiments in reflectance mode, which also required 500 scans in order to generate signal with sufficient intensity. 2 cm wavelength resolution was used. As a control, the same *trans*-anethole solution was dropcast onto a SiNx chip and allowed to dry, so as to serve as a representative spectrum of the material without imaging

Chapter 4 Critical Analysis of the *In Situ* Dynamics of Emulsion Droplets

This chapter is adapted from the following manuscript (currently in preparation as of 18 May 2023)

Maria A. Vratsanos, Evangelos Bakalis, Chiwoo Park, Francesco Zerbetto, and Nathan C. Gianneschi, *Complex Motion Emulsion of Emulsion Droplets Captured via Liquid Phase Transmission Electron Microscopy*

4.1. Introduction

Since the advent of electron microscopy, observation of *in situ* materials and processes has been a fundamental goal. Recent developments in material fabrication techniques and technology have enabled researchers to stabilize a liquid sample between electron transparent membranes (*e.g.,* silicon nitride (SiN_x) or graphene) within the high vacuum environment of the microscope.[79,152,223,232] Corresponding advances in detectors have enabled visualization and image acquisition of such systems at increasing spatiotemporal resolution.[64,233–238] While these innovations have enabled direct observation of reactions,[131,239,240] solvated morphology,[5,241–244] assembly pathways[84,92,132,134,155,156,245,246], fundamental questions regarding the observation of *in situ* dynamics remains. In principle, observing the motion of inert nanoparticles should be the simplest LPTEM experiment – simply load the liquid cell with nanoparticles, turn on the beam, and record. However, a variety of factors result in anomalous observed motion: spatial confinement, solvent ordering at the SiN_x interface, charging of the SiN_x window by the e-beam, local chemopotential gradients resulting from solvent radiolysis, and more.[161,163,186–189,221,247–253] Many of these effects (namely, downstream radiolytic effects) will also be exacerbated by the choice of sample – metallic nanoparticles will act as local dose enhancers, accelerating radiolysis in their vicinity.[88–90,254] Given that such materials also benefit from high Z contrast (making their

tracking and identification feasible), they have been the focus of much of the study in this area.[186,187,189,221,223,247,248,250–252,255,256]

We assert that it is vital to the field to understand to what extent *in situ* diffusivity is altered from the bulk. Diffusion of molecular species is clearly occurring in LPTEM because diffusion-limited nucleation and growth processes have been observed.[131,217] However, if motion of larger species is significantly hindered by spatial confinement and the effects highlighted above, these considerations must be considered when using *in situ* observations to make quantitative conclusions about the rate at which observed processes are occurring. Essentially, we need to identify and quantify the discrepancy from the bulk and apply such findings to the observed processes to reconcile them. If it is possible to routinely observe unhindered motion, then answering more fundamental questions about species transport and growth kinetics becomes possible. If it is not, it becomes clear that experimental results from LPTEM need to be viewed through a more critical lens, and additional caveats must be included when extrapolating from the liquid cell to the bulk.

Mølhave *et al*. recently claim to have imaged unhindered Brownian motion of gold nanoparticles in a thick (3.5μm), aqueous cell at low electron fluences in STEM, resulting in measured diffusivities exceeding those of a bulk system and exhibiting apparent superdiffusional motion.[247] Whilst this study and analysis is carefully done, and we commend them on this work, the moving particles are in the vast minority of the population in the field of view – close to 90% of the particles seen are completely stationary for the entire video. The paper discounts these, and only analyzes the observed motion. It seems there are still factors preventing the observation of true Brownian motion for all species. Though gold nanoparticles are the ‘gold standard’ for LPTEM experiments due to their high contrast and facile preparation, even at low fluxes, these

particles will interact very strongly with the beam. Additionally, though STEM gives better spatial resolution through a thicker liquid medium, this mode of imaging creates additional uncertainties when it comes to the consideration of electron dose, and the rastering of the beam creates spatial and temporal inhomogeneities. We propose that to more effectively probe diffusion in the liquid cell, it is necessary to consider the motion of less reactive materials that have minimal interaction with both the electron beam and the SiNx interface. Initially, we had attempted to observe such motion in commercial polymeric nanoparticles (such as polystyrene); however, the low density differential between the particles and water rendered them impossible to resolve at the necessary spatiotemporal resolutions. Thus, we turned to systems of colloidal emulsion droplets, which have shown exceptional contrast and size control as a result of their modular formulation.[5]

4.2. Results and Discussion

4.2.1. Modeling of Droplet Motion to Establish Experimental Parameters

Prior to attempting such experiments, we can make some *a priori* estimation of experimental and imaging conditions necessary to capture such motion by considering some simple models and calculations. If we consider only the spatial confinement of samples within a typical SiN_x liquid cell, we can estimate how hindered the diffusion should be based on the relative size of the particle with respect to cell thickness.[257] Independent of e-beam effects, the proximity of the particle to the walls should indicate the degree of drag forces exerted on the particle, thus slowing it down from a bulk environment. With this relationship in hand, we can then approximate the frame rates necessary to capture images representative of motion. While direct electron detectors have increased image acquisition rates to thousands of frames per second, these rates are inherently constrained by signal limitations – essentially, if one images too fast at a low dose, insufficient signal will be acquired per frame. It is possible to extract information from such data

sets by spatially or temporally binning them (summing adjacent pixels or frames, respectively), but this defeats the purpose of capturing at such frame rates in the first place. Essentially, one is left with an optimization situation: with a finite amount of signal, how often do you have to acquire an image in order to capture particle motion in such a way that allows accurate particle tracking? This is further compounded by the accompanying issue of data storage and processing – with current cameras and devices, one can easily acquire terabytes of data in a single sitting, therefore judicious choice of image acquisition parameters is required to avoid unnecessarily cumbersome data processing.

In the bulk state, a spherical particle in a fluid having a low Reynolds number will exhibit a diffusivity given by the Stokes-Einstein formula (Equation 1), which is dependent on particle size (R), solvent viscosity (η), temperature (T), and the Boltzmann constant (k_B).[258]

$$D = \frac{k_B T}{4\pi\eta R} \qquad \text{Equation 4.1}$$

This relation is for two dimensions so long as the particle is sufficiently far from boundaries and other particles, making it possible to ignore the drag imposed by any walls or interparticle forces. However, when a particle exists in a more confined environment, such as between two parallel plates, it is not sufficiently free to explore that space, leading to deviations from the above expression.[259–261] Rather, the influence of drag near the walls, while negligible on the bulk scale, significantly hinders the particle's progress and slows its motion.[262] The extent of this confinement with respect to the size of the particle will determine the degree of reduction in diffusivity. Aforementioned efforts to image this motion *in situ* have repeatedly resulted in anomalous behavior and calculated diffusivities that are two to nine orders of magnitude below expected values given by Equation 4.1.[247]

Given that the SiN_x liquid cell geometry can be approximated as two parallel plates, we can draw from literature exploring particle motion when confined in one dimension, such as the work of Faucheux *et al*., wherein the motion of micron-scale polystyrene particles between two glass slides was recorded and quantified.[257] These experiments showed that the reduction in diffusivity was directly related to a parameter γ, defined as a dimensionless variable relating the particle's average z position to its size (Equation 4.2). We have reproduced their calculations here such that they may be adapted for our approximation of the *in situ* environment.[257]

$$\gamma = \frac{h - r}{r} \qquad \text{Equation 4.2}$$

Here, r is defined as the particle radius and h is calculated from the Boltzmann density profile for particles of a given size and density in a fluid (Equation 4.3).

$$P_B(z) = \left(\frac{1}{L}\right)\left(\frac{e^{-\frac{z}{L}}}{e^{-\frac{r}{L}} - e^{\frac{(r-t)}{L}}}\right) \qquad \text{Equation 4.3}$$

t is the thickness of the liquid layer, and L is the characteristic Boltzmann length scale, which we will define as *L* below:

$$L = \frac{k_B T}{\frac{4}{3}\pi r^3 g(\rho - \rho_o)} \qquad \text{Equation 4.4}$$

We can then define h as the following, which represents the average z position of the particle:

$$h = \int_r^{t-r} z P_B(z) dz = \frac{e^{-\frac{r}{L}}[rL + L^2] - e^{\frac{r-t}{L}}[(t-r)L + L^2]}{L(e^{-\frac{r}{L}} - e^{\frac{r-t}{L}})} \qquad \text{Equation 4.5}$$

Empirically, the reduction in diffusivity as a function of γ is shown in Faucheux et. al's work, which can be approximated as Equation 4.6.[257]

$$\frac{D}{D_o} = 0.0002\gamma^3 - 0.008\gamma^2 + 0.1069\gamma + 0.3361$$ Equation 4.6

Thus, if we input the geometrical constraints of the liquid cell and the solvent and particle properties, we can obtain a predicted γ, which in turn tells us how reduced the effective diffusivity should be, and extrapolate experimental and imaging parameters *a priori* (**Figure 4.1**). From here, we can approximate a particle's mean square displacement, which can tell us what the minimum camera capture rate should be to successfully image a given displacement. For a typical liquid cell, we will assume a uniform liquid thickness of 500nm. Considering a range of nanoparticles with typical sizes (diameters ranging from 50 to 450nm), we can see below how their diffusivity in the liquid cell will vary from the bulk, and, intuitively, that this effect becomes more pronounced as the particle size approaches the length scale of the constrained environment (**Figure 4.1A**). Using the same size range of particles, it is also possible to calculate the frame rate at which images would need to be captured to record displacements of a given magnitude (**Figure 4.1B**). Here, capturable displacements range linearly from 10nm to 1μm, and the reduced diffusivity coefficient is used to calculate the time step required for the particle to travel that distance. The inverse of this time step is taken to give the required frame rate. Different particle tracking algorithms rely on different mechanisms of interpolation, or guessing the pathway from point A to point B for a given particle. Most visual tracking methods rely on linking algorithms, which search a predefined radius around an identified particle.[263] If no particles are found within that radius for a set number of subsequent frames, the particle trajectory is ended. This parameter of linking radius can significantly impact findings and conclusions in a data set with mean adjacent particles, as it can be nearly impossible to distinguish them from one another in experimental data. Thus, linking accuracy is inversely proportional to linking radius, as expanding the search area inherently

increases the odds of misidentifying particles. However, shrinking the detected mean square displacement quickly outpaces the capabilities of the camera (**Figure 4.1B**), indicating the need to find an optimum between tracking accuracy and image acquisition constraints (signal and data storage). The superimposed box indicates the ranges of droplet sizes and imaging parameters considered in the experimental portion of this paper. Another critical consideration here is the relationship between frame rate and image resolution. Camera frame rate is inversely proportional to signal acquisition, resulting in a conundrum of image processing – the microscopist is forced to try to extract the same information about particles with less and less information. While there are many useful tools for this purpose, such as image segmentation and binarization algorithms, denoising functions, and machine learning, these are only able to help to a degree – it is not possible to enhance contrast that is not there.[163,264] The resolution of the microscope is inversely proportional to electron fluence, and is additionally a function of sample and microscope conditions (**Figure 4.1C**).[265] Here, we have adapted the calculations of deJonge to our typical sample parameters and electron fluences in order to consider the limitations of signal as it relates to resolution. [265] The code provided in deJonge's work was modified to match the typical sample parameters of the materials used in our experimental conditions (window and liquid thickness, solvent density, *etc*.). For the organic materials used here, we typically consider low dose to be an electron flux of 0.2 $e^-/Å^2s$ in order to avoid damage to the sample. However, at the frame rates established in **Figure 4.1B**, this translates to a fluence per image of $<0.02e^-/Å^2$, and thus we cannot hope to discern objects less than 50nm under such conditions. As such, we have shifted out of necessity to larger, but more mobile emulsion droplets, and have utilized advanced low contrast feature detection algorithms.[266] The algorithm adopts a robust statistics approach to identify and subtract the image background due to uneven illumination and background material, and each of

the remaining foreground images are fitted by an ellipse model to identify elliptical boundaries of particles.

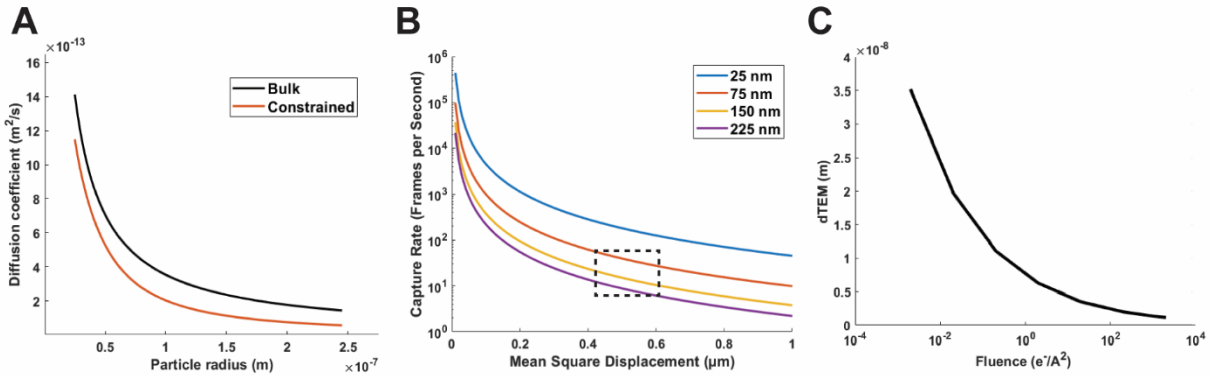

Figure 4.1 Diffusivity constants in bulk and constrained environments as a function of particle radius. (A) Stokes-Einstein and reduced diffusivity as a function of droplet size in a 500nm thick environment. (B) Camera capture rate required to capture displacements of a given magnitude, as a function of droplet size. The boxed region indicates the range of droplet sizes and steps that we are analyzing in this work, and the capture rate we have used corresponds. (C) The inverse relationship between object resolution in the TEM and electron fluence, which dictates the amount of signal available to the detector. As camera frame rates increase, fluence per frame decreases, and thus smaller objects become unresolvable.

The above calculations may also be used to identify optimal candidate systems for studying nanoscale dynamics *in situ* – particles of various sizes and densities may be put into solvents of varying viscosities and thicknesses, and the same frame rate measurement may be done to estimate whether it is feasible to capture the unencumbered dynamics of that particular system with the available hardware (*i.e.*, camera). For instance, a common strategy for observing dynamics is to suspend nanoparticles in a solvent mixed with glycerol, as its high viscosity rapidly slows motions (**Figure 4.2**)[186,187,248] Here, we have considered imaging conditions for particles in solvents of viscosity ranging from that of pure water to that of pure glycerol either in circumstances of displacement proportional to droplet size (**Figure 4.2A**) or a constant displacement (**Figure 4.2B**).

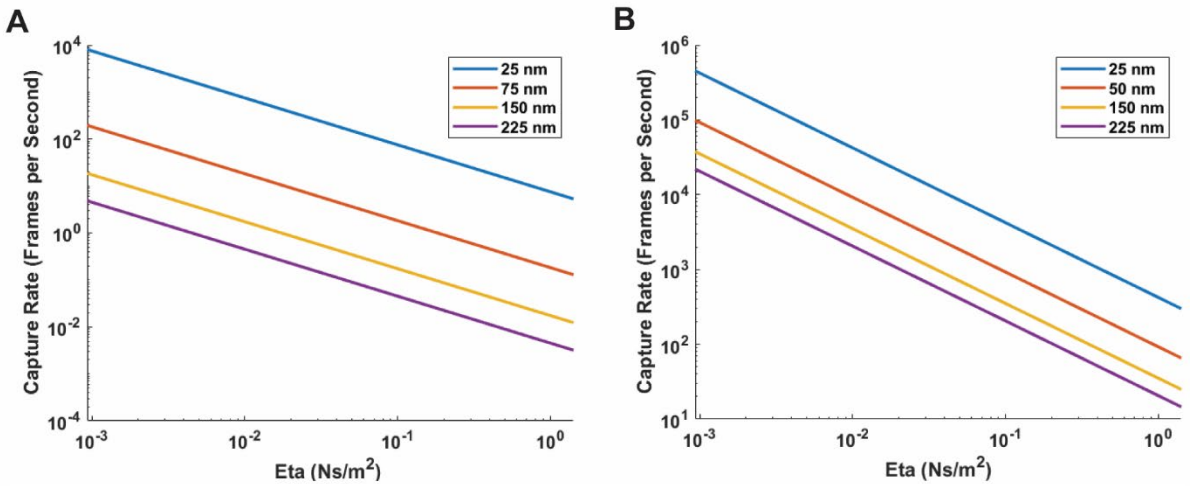

Figure 4.2 Capture rate as solvent viscosity varies from water to glycerol.
(A) considers a displacement proportional to droplet size (3*r), and (B) considers a constant displacement of 10nm

These plots demonstrate the influence of viscosity on capturable particle motion, and demonstrate that such strategies bring the necessary frame rates down by several orders of magnitude, thus rendering such studies feasible for more of the cameras available.

4.2.2. Experimental Observation of Droplet Motion

Having established that the necessary imaging conditions to capture the motion of interest are achievable, we began attempting to record experimental observations of such. Significant effort to observe motion of a plethora of polymeric nanoparticles under various solvents and conditions (**Table 4.1**) did not yield results of sufficient contrast for significant particle tracking and analysis.

Table 4.1 Overview of nanoparticles studied by LPTEM

Particle Material	Particle Diameter (nm)	Solvent(s)
Commercial Polystyrene	25, 100	Water, isopropanol
Core-dyed fluorescent polystyrene	35	Water,
Uranyl acetate incubated polystyrene	25, 100	Water
$NiCl_2$ stained Polystyrene	25, 100	Water
PISA micelles	50, 100	Water

Initial observations of motion occurred serendipitously during experiments for previous work (**Video 4.1**).[5] Here, isooctane was emulsified in water using the sodium salt of dioctyl sulfosuccinate (Aerosol OT or AOT), an anionic surfactant. Given the relative densities of these materials, the isooctane droplets appear lighter than the aqueous continuous phase for these datasets. Videographic data shows the low contrast droplets moving in a random, sustained manner for >30 seconds. The lower contrast of these droplets necessitated advanced image processing techniques, as they are of insufficient contrast for typical segmentation algorithms.

To yield droplets of increased contrast, perfluorohexane (PFH) was emulsified using Capstone FS-30, a commercial fluorosurfactant. Given the excellent contrast of the PFH, droplets were clearly visible without additional processing; thus, videos were recorded using a screen capture software at lower spatial resolution (1k instead of 4k) to reduce the computational load of storing and processing these data. Once acquired, the videographic data had sufficient contrast to be segmented using the TrackMate plugin, which yields droplet location and size for each frame.[267,268] Once individual droplet trajectories were determined over the entire video, the mean square displacement was calculated and plotted with respect to τ such that an equation of the form $MSD = 4D * \tau^n$, which yields both the diffusivity constant (D) and the exponent (n) which indicates the character of the droplet motion (n=1 indicating Brownian, n>1 or n<1 being sub/superdiffusional, respectively).[161,269] Given the ease with which PFH trajectories were extracted, and their significant duration, we chose to first analyze those datasets (**Figure 4.3**).

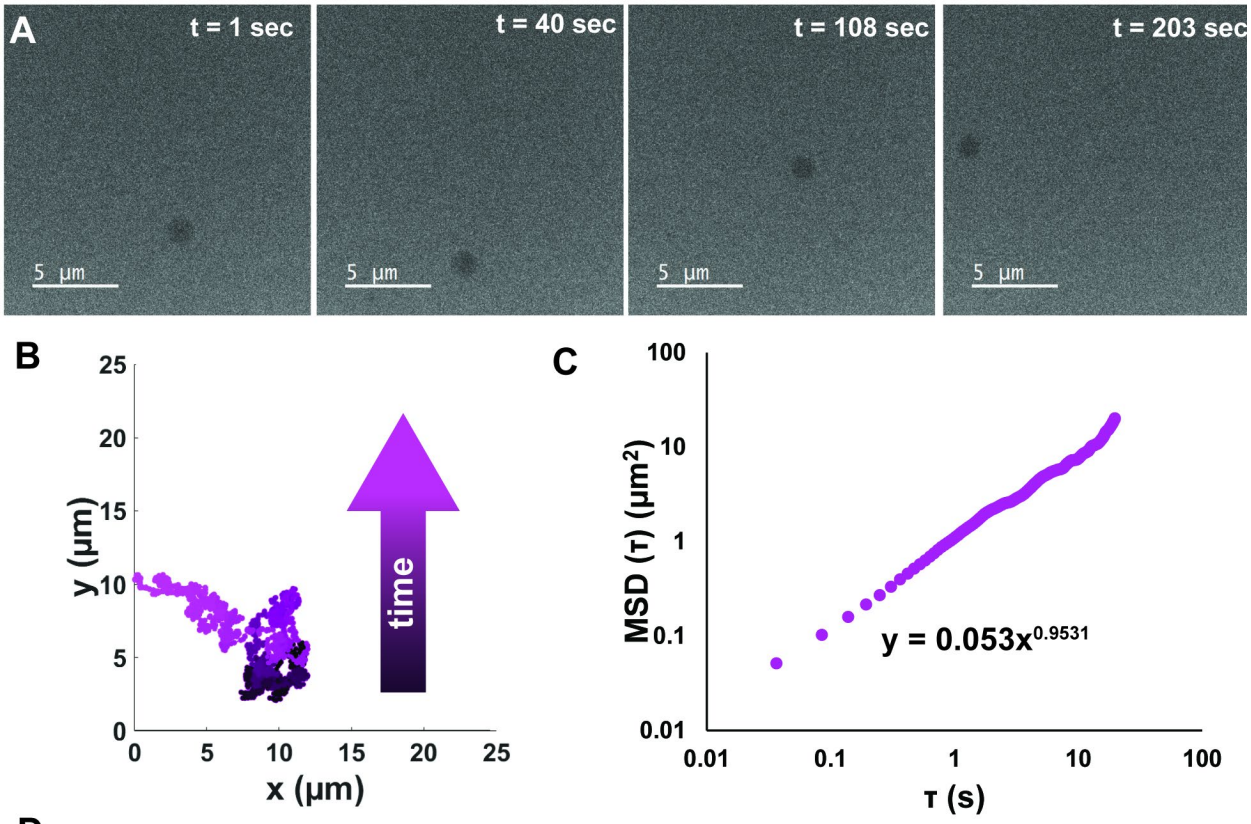

D

Trajectory	Number of timepoints	Average particle radius (µm)	Stokes-Einstein Diffusivity	Reduced Diffusivity	MSD Coefficient	MSD Diffusivity	MSD Exponent	Source
PFH_1	2052	0.75	9.42E-13	4.93E-13	0.053	1.33E-14	0.95	Video S2
PFH_2	232	2	3.53E-13	8.40E-14	0.0246	6.15E-15	1.37	Video S3
Average		1.38	6.48E-13	2.89E-14	0.0388	9.73 E-15	1.16	

Figure 4.3 Motion overview and analysis for perfluorohexane droplet PFH_1.
(**A**) Selected micrographs from videographic data at indicated time points, showing displacement of droplet in time. (**B**) Plot of overall droplet trajectory, with coloration indicating time. Colors range from black to pink as time progresses. (C) Graph of mean square displacement over time, plotted logarithmically. Power law fit of data is displayed on plot, where A = 4D. (**D**) table of relevant values, including average droplet radius (r), Stokes-Einstein diffusivity (D_{SE}), reduced diffusivity (D_{red}), experimentally measured diffusivity (D_{exp}), and power law exponent (n) for all analyzed PFH droplets

Here, we see dark droplets moving for several minutes a time (**Figure 4.3A, Video 4.2**), yielding a robust trajectory to analyze (**Figure 4.3B**). Upon analysis of the MSD, the power law fit indicates motion of a Brownian nature (exponent ~ 1) (**Figure 4.3C**), and diffusivity that closely matches what is predicted by Equation 1 (**Figure 4.3D**)[270,271]. Average diffusivity for PFH droplets was $9.7*10^{-15}$, which is within an order of magnitude of the value predicted by **Equation 1**

($3.24*10^{-14}$). We see that *D* was consistently within an order of magnitude of the values predicted by Stokes-Einstein, even when considering the spatial hindrance. Experimentally measured diffusivities for droplets of differing radii were inversely proportional to droplet size, as is consistent with theory (**Figure 4.3D**).

While the PFH droplets have superior contrast, the previously observed isooctane droplets were observed in greater populations (**Video 4.1).** However, the number of droplets, coupled with their low contrast, makes the extraction of trajectories more difficult. We employed the multi-object tracking algorithm.[272] The algorithm is capable of handling tracking complexities due to image artifacts and temporary particle disappearances for some image frames, to identify the trajectories accurately. Once extracted, we analyzed these trajectories in the same manner as the previous PFH data (**Figure 4.4**). Sustained motion was again observed (**Figure 4.4A**, **B**). However, these motions were found to be significantly sub-diffusive in nature ($n<1$) (**Figure 4.4C, D**, **Table 4.2**).

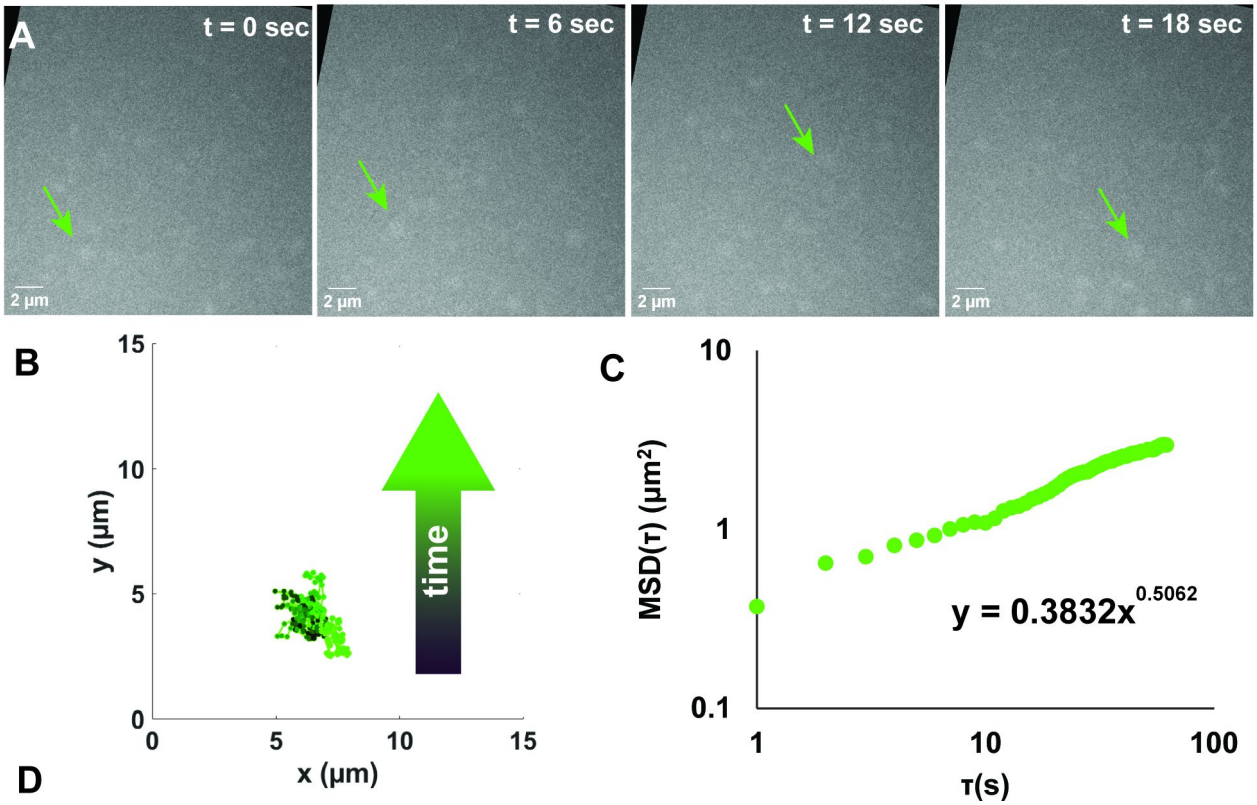

Trajectory	Number of timepoints	Average particle radius (µm)	Stokes-Einstein Diffusivity	Reduced Diffusivity	MSD Coefficient	MSD Diffusivity	MSD Exponent	Source
Iso_1	248	0.15±0.09	2.36E-13	2.25E-13	0.3832	9.58E-14	0.506	Video S1
Iso_2	104	0.15±0.07	2.36E-13	2.25E-13	0.2116	5.29E-14	0.569	Video S1
Iso_3	260	0.50±0.09	7.22E-14	2.45E-14	2.6684	6.67E-13	0.812	Video S1
Iso_4	140	0.20±0.05	1.77E-13	4.04E-14	0.904	2.26E-13	0.545	Video S4
Iso_5	605	0.20±0.06	1.77E-13	6.10E-14	1.07	2.71E-13	0.487	Video S4
Average		0.24	1.8E-13	1.15E-13	1.047	2.63E-13	0.584	

Figure 4.4 Motion overview and analysis for a representative isooctane droplet (Iso_1)
(**A**) Selected micrographs from videographic data at indicated time points, showing motion of droplet denoted by green arrow over time. (**B**) Plot of overall droplet trajectory, with coloration indicating time. Colors range from black to green as time progresses. (**C**) Graph of mean square displacement over time, plotted logarithmically. Power law fit of data is displayed on plot. (**D**) table of relevant values, including average droplet radius (r), Stokes-Einstein diffusivity (D_{SE}), reduced diffusivity (D_{red}), experimentally measured diffusivity (D_{exp}), and power law exponent (n) for isooctane droplets used in ADOMA.

When we consider the trajectories of isooctane droplets as observed *in situ*, experimental diffusivities are found to be an order of magnitude greater than the prediction of Stokes-Einstein, which is counter to expectation and to observations of fluorinated oils, which showed reduced diffusivities.

Some of the extracted isooctane trajectories were not of sufficient length for ADOMA analysis, and thus were not included in **Figure 4.4**. We have compiled the tabulated data for those shorter trajectories below (**Table 4.2**, **Video 4.1**, **Video 4.4**, **Video 4.5**). Here, the number of time points indicates the number of video frames over which the droplet in question was tracked. Droplet size was measured by the aforementioned tracking algorithm. Stokes-Einstein and reduced diffusivities were calculated via Equations 4.1 and 4.6, respectively. MSD coefficient reflects the coefficient of the power law fitting, and MSD diffusivity is this coefficient divided by 4. MSD Exponent is the exponent value from the power law fitting. Average values for each are listed at the bottom of the table.

Table 4.2 Tabulated experimental details and calculated values for remaining isooctane data

Trajectory	Number of timepoints	Average measured particle radius (μm)	Stokes-Einstein Diffusivity	Reduced Diffusivity	MSD Coefficient	MSD Diffusivity	MSD Exponent	Source
Iso_6	108	0.55±0.08	6.51E-14	2.13E-14	6.8363	1.71E-12	0.589	Video 4.1
Iso_7	86	0.45±0.07	7.73E-14	2.68E-14	3.3993	8.50E-13	0.685	Video 4.1
Iso_8	73	0.15±0.06	2.36E-13	2.25E-13	2.8394	7.10E-13	0.241	Video 4.1
Iso_9	51	0.15±0.05	2.36E-13	2.25E-13	0.358	8.95E-14	0.401	Video 4.1
Iso_10	80	0.20±0.06	1.77E-13	4.81E-14	1.18	2.96E-13	0.406	Video 4.4
Iso_11	83	0.20±0.07	1.77E-13	4.02E-14	0.952	2.38E-13	0.621	Video 4.4
Iso_12	32	0.3±0.06	1.19E-13	4.81E-14	0.762	1.91E-13	0.683	Video 4.5
Iso_13	21	0.35±0.07	1.05E-13	4.04E-14	1.29	3.23E-13	0.489	Video 4.5
Iso_14	21	0.35±0.05	1.05E-13	4.02E-14	2.59	6.481E-13	1.355	Video 4.5
Iso_15	57	0.25±0.06	1.41E-13	6.10E-14	0.53	1.321E-13	1.355	Video 4.5

Iso_16	30	0.3±0.05	1.28E-13	5.32E-14	1.40	3.501E-13	0.973	Video 4.5
Average		0.30	1.42E-13	7.54E-14	2.01	5.03E-13	0.71	

4.2.3. Anomalous Diffusion Object-Motion Analysis of Droplet Trajectories

Our initial analyses of motion are relatively high level, and we can probe these motions in more detail using anomalous diffusion object-motion analysis (ADOMA). A detailed account of the method analysis have been given elsewhere, but the primary tenet is that a detailed description of object motion is extracted by considering motion in the x and y axes independently.[161] Below, we have shown representative ADOMA results for one PFH droplet (**Figure 4.5**) and one isooctane droplet (**Figure 4.6**).

Given the statistical constraints of ADOMA, only the longest trajectories (number of time points >100) were analyzed. Plots and results for all other ADOMA analyses are given below (**Figure 4.7-Figure 4.11**). A key element of the ADOMA is the scaling of the metric $<||\Delta X_i||^q>$, where $||\Delta X_i||$ is the Euclidean distance of the increments ΔX_i, with X_i being the elements of the recorded time series along x-y axes. The parameter, q, expresses the order of the moment, which here is varied in the range [0.25, 4] with steps of 0.25. For the lateral motion, we create the sequence $l_i = \sqrt{x_i^2 + y_i^2}$. We assume that the recording time series, for time lags much smaller than the total length, pose a kind of self-similarity, where zooming in or out on the time series reveals the same patterns scaled by a certain amount, and accordingly we expect Equation 4.7 to be satisfied.[273]

$$<||\Delta X_i||^q> \approx \tau^{z(q)} \qquad \text{Equation 4.7}$$

Here, τ is the time lag and z(q) is the structure function – its form provides insights on the stochastic mechanisms affecting the motion. The value of z(q) for q=1 corresponds to the Hurst exponent, and for q=2, gives the scaling of the MSD. If, and only if, a single origin of noise is present, z(q)=mq, (**Table 4.3**). Instead, if more noise sources contribute and drive the motion, then z(q) departs from linearity, and its convex shape is an indication of multiplicative effects. Two special forms of z(q) are:

$$z(q) = hq - c(q^2 - q)$$

for log-normal distribution, and

$$z(q) = hq - cq\log(q)$$

for log-Cauchy distribution.

Both are special cases of

$$z(q) = hq - \frac{c}{a-1}(q^a - q)$$

for a = 2 and 1, respectively. The exponent a takes values in the range (0,2], a-stable distribution.

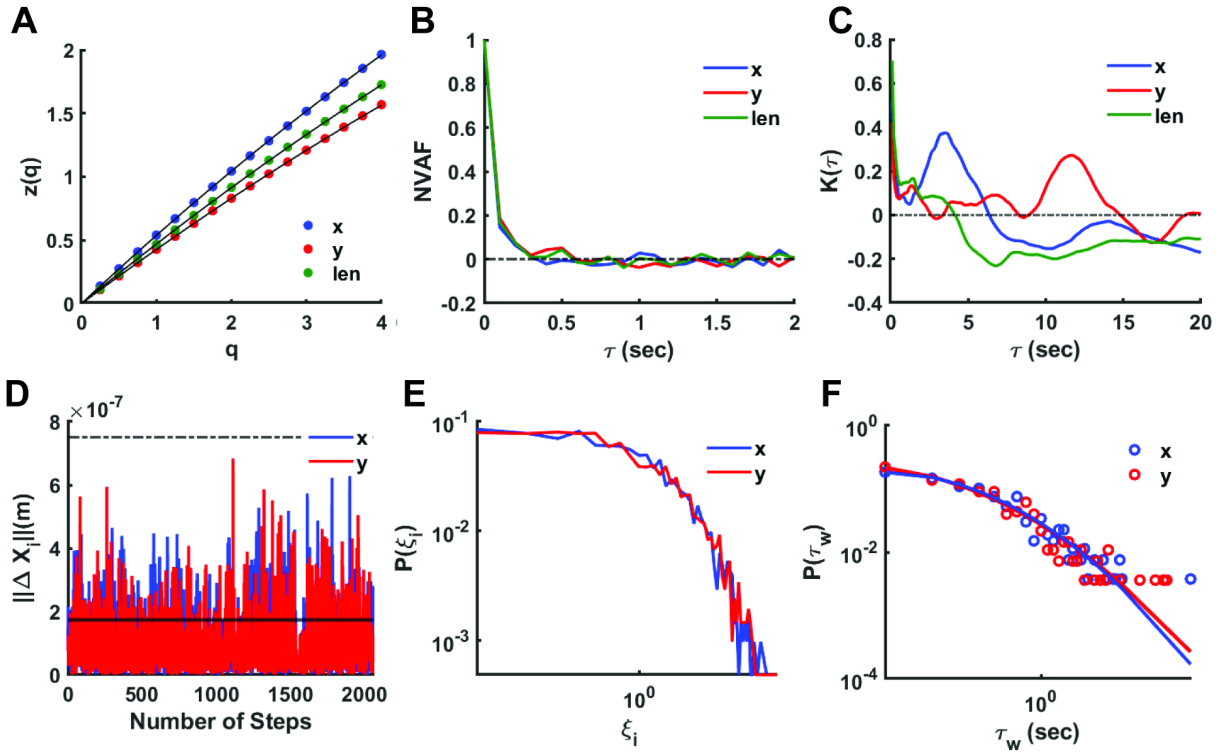

Figure 4.5 ADOMA results for PFH_1.
A) structure functions, b) normalized velocity autocorrelation functions, c) excess kurtosis, d) increments along x- and y-axes, e) probability distribution of $\xi_i=\|\Delta X_i\|/\langle\|\Delta X_i\|\rangle$, f) probability distribution of waiting times, whereas the value $\xi_i=2s$ (s is the standard deviation) has been set as cut-off distance

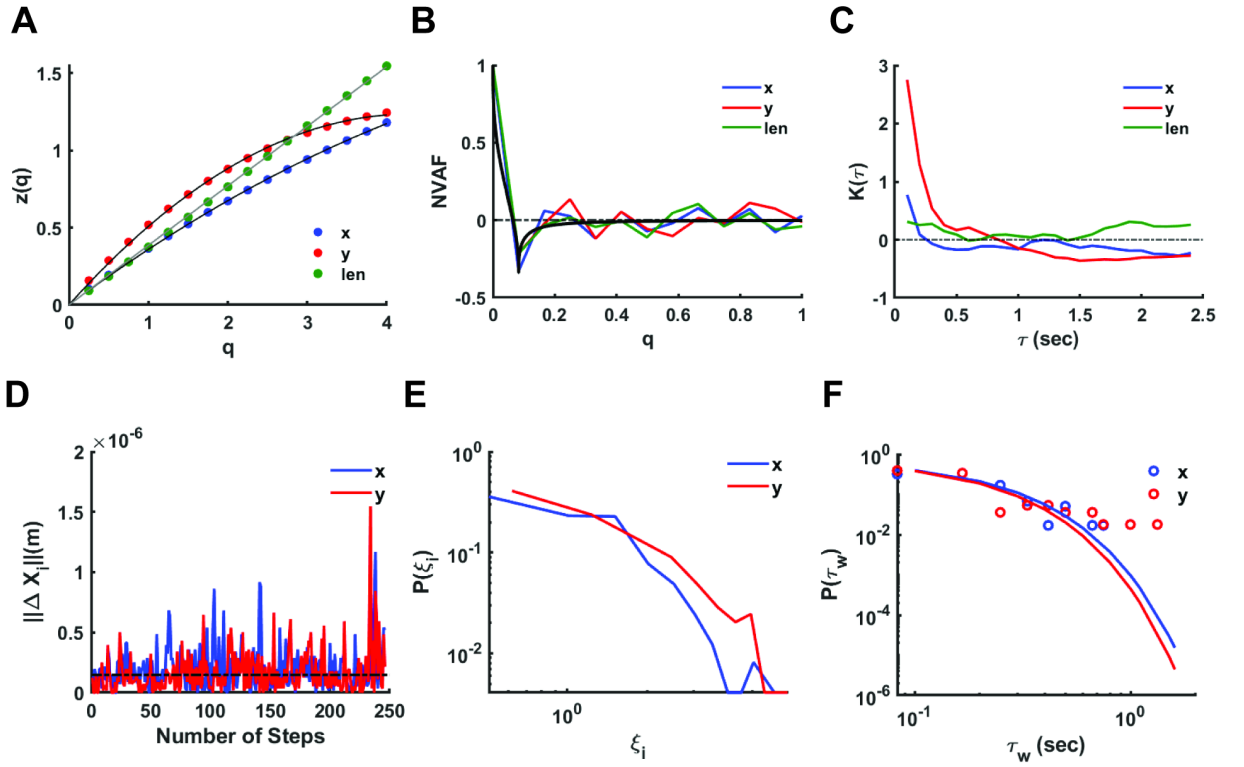

Figure 4.6 ADOMA analysis for isooctane droplet Iso_1
(**A**) structure functions z(q), (**B**) normalized velocity autocorrelation function (NVAF) C) excess kurtosis K(τ) D) increments along x- and y-axes, E) probability distribution of $\xi_i=||\Delta X_i||/<||\Delta X_i||>$, F) probability distribution of waiting times, whereas the value ξ_i=s

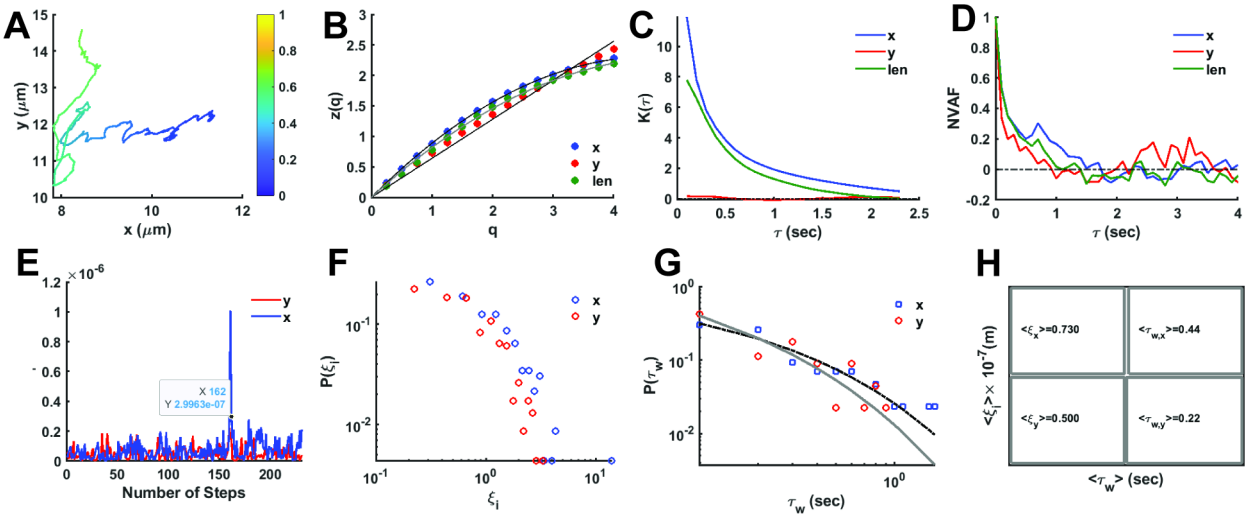

Figure 4.7 ADOMA results for PFH_2
(A) Plot of droplet trajectory, with t_0 being blue and moving to yellow over time (B) Plot of structure functions as a function of q (C) excess kurtosis over time (D) normalized velocity autocorrelation functions over time (E) movement increments along x- and y-axes, (F) probability distribution of $\xi_i=||\Delta X_i||/<||\Delta X_i||>$, (G) probability distribution of waiting times, whereas the value ξ_i=2s (s is the standard deviation) has been set as cut-off distance, g)

probability distribution of waiting times, and (H) mean of the length take along x- and y- axes and the mean of the waiting time, for the particle PFH_2 are displayed.

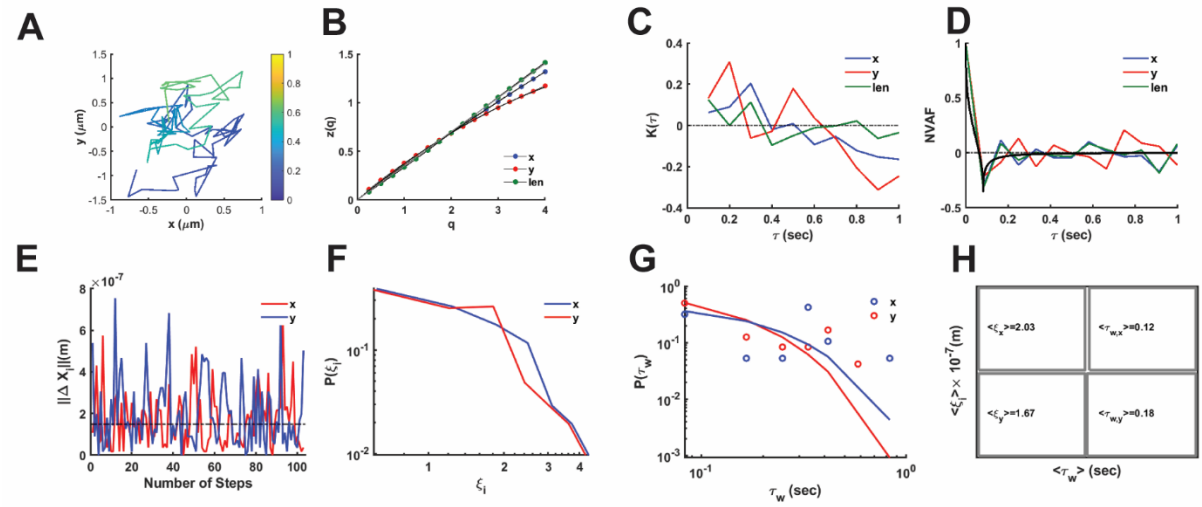

Figure 4.8 ADOMA results for Iso_2
(A) Plot of droplet trajectory, with t_0 being blue and moving to yellow over time (B) Plot of structure functions as a function of q (C) excess kurtosis over time (D) normalized velocity autocorrelation functions as a function of time (E) movement increments along x- and y-axes over time (F) probability distribution of $\xi_i=||\Delta X_i||/<||\Delta X_i||>$, (G) probability distribution of waiting times, whereas the value $\xi_i=2s$ (s is the standard deviation) has been set as cut-off distance, g) probability distribution of waiting times, and (H) mean of the length take along x- and y- axes and the mean of the waiting time

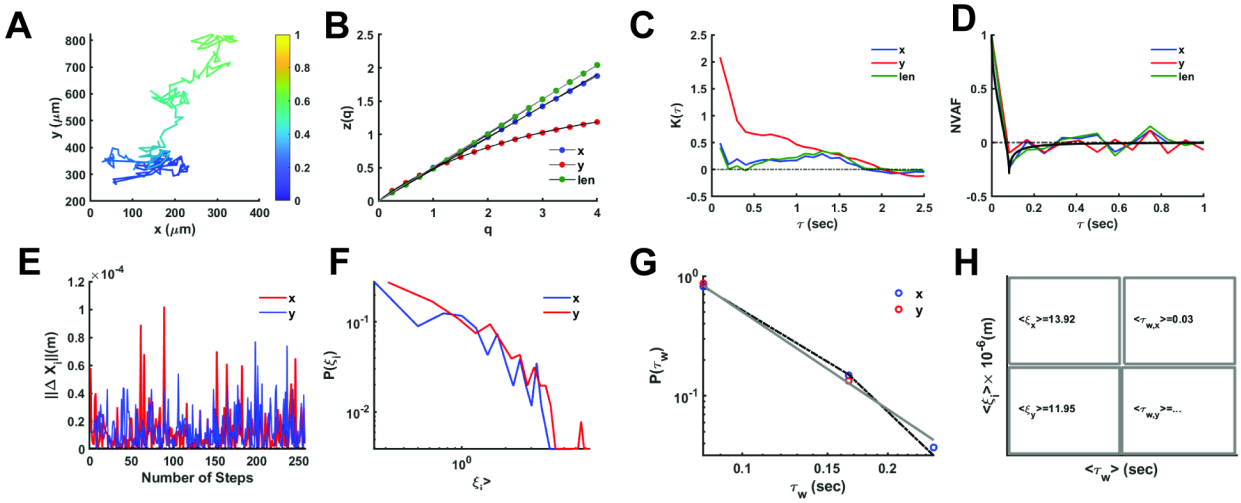

Figure 4.9 ADOMA results for Iso_3
A) Motion trajectory, (B) structure functions, (C) excess kurtosis, (D) normalized velocity autocorrelation functions, (E) movement increments along x- and y-axes, (F) probability distribution of $\xi_i=||\Delta X_i||/<||\Delta X_i||>$, (G) probability distribution of waiting times, whereas the value $\xi_i=2s$ (s is the standard deviation) has been set as cut-off distance, g) probability distribution of waiting times, and (H) mean of the length take along x- and y- axes and the mean of the waiting time

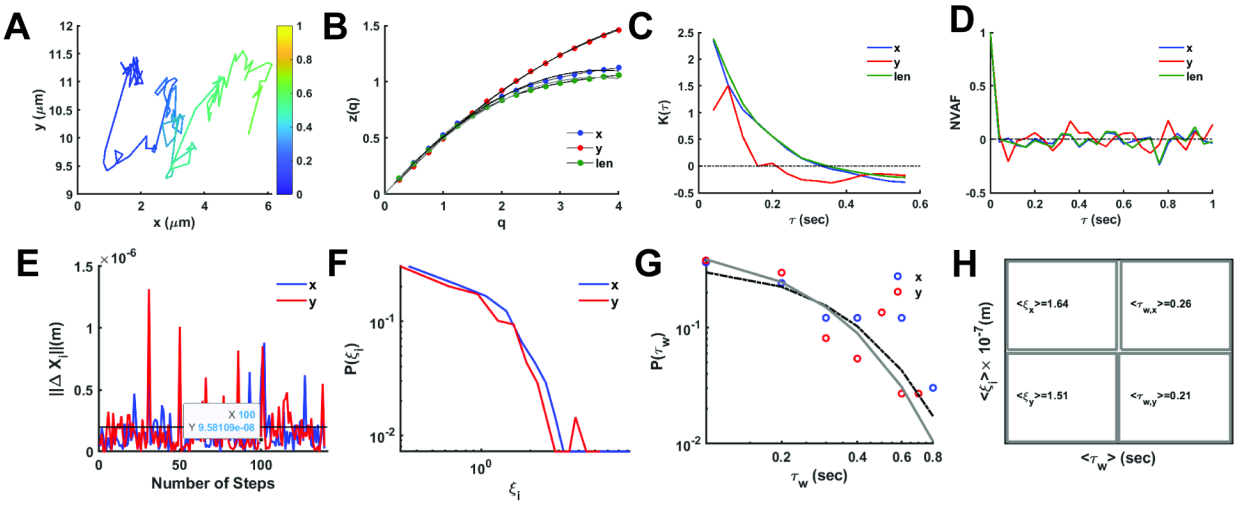

Figure 4.10 ADOMA results for Iso_4
(A) Motion trajectory, (B) structure functions, (C) excess kurtosis, (D) normalized velocity autocorrelation functions, (E) movement increments along x- and y-axes, (F) probability distribution of $\xi_i=\|\Delta X_i\|/\langle\|\Delta X_i\|\rangle$, (G) probability distribution of waiting times, whereas the value $\xi_i=2s$ (s is the standard deviation) has been set as cut-off distance, g) probability distribution of waiting times, and (H) mean of the length take along x- and y- axes and the mean of the waiting time

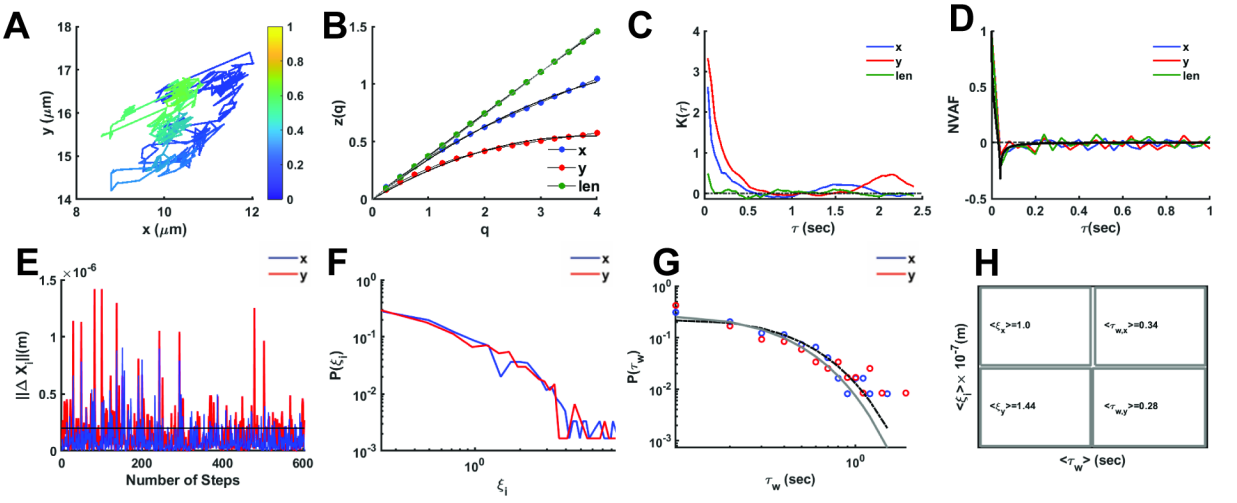

Figure 4.11 ADOMA results for Iso_5
(A) Motion trajectory, (B) structure functions, (C) excess kurtosis, (D) normalized velocity autocorrelation functions, (E) movement increments along x- and y-axes, (F) probability distribution of $\xi_i=\|\Delta X_i\|/\langle\|\Delta X_i\|\rangle$, (G) probability distribution of waiting times, whereas the value $\xi_i=2s$ (s is the standard deviation) has been set as cut-off distance, g) probability distribution of waiting times, and (H) mean of the length take along x- and y- axes and the mean of the waiting time

Table 4.3 Details of Structure Functions

Trajectory	Number of timepoints	Structure Function z(q)	x-axis	y-axis	Lateral
Perfluorohexane					
PFH_1	2052	$z(q)=hq-c(q^2-q)$	h = 0.538 +/- 0.001 c= 0.016 +/- 0.001	h = 0.427 +/- 0.001 c = 0.012 +/- 0.001	h = 0.470 +/- 0.001 c= 0.013 +/- 0.001
PFH_2	232	$z(q)=hq-c(q^2-q)$ $z(q)=mq$	h =0.887 +/-0.003 c= 0.107 +/- 0.001	m= 0.640 +/- 0.008	h= 0.817 +/- 0.008 c= 0.089 +/- 0.004
Isooctane					
Iso_1	248	$z(q)=hq-c(q^2-q)$ $z(q)=mq$	h= 0.359+/- 0.001 c= 0.022 +/- 0.001	h = 0.508 +/- 0.003 c = 0.067 +/- 0.001	m = 0.385 +/- 0.001
Iso_2	104	$z(q)=hq-c(q^2-q)$ $z(q)=mq$	m= 0.336+/-0.002	h= 0.371+/- 0.002 c= 0.027 +/- 0.001	m= 0.350 +/- 0.001
Iso_3	260	$z(q)=mq$ $z(q)=kq-(d/(a-1))(x^a-x)$	m= 0.475+/-0.002	k = 0.488 +/- 0.001 d = 0.109 +/- 0.002 a= 1.327 +/- 0.020	m= 0.51 +/- 0.001
Iso_4	140	$z(q)=hq-c(q^2-q)$	h= 0.511+/- 0.004 c= 0.079+/- 0.002	h= 0.502 +/- 0.002 c= 0.045 +/- 0.001	h= 0.494 +/- 0.004 c= 0.079 +/- 0.002
Iso_5	605	$z(q)=hq-c(q^2-q)$ $z(q)=mq$	h= 0.345+/- 0.004 c= 0.030+/- 0.002	h= 0.248 +/- 0.004 c= 0.037 +/- 0.002	m= 0.368 +/- 0.001

The walk dimension, d_w, of a trajectory and the exponent α, characterizing the anomalous diffusion, are connected to each other by the relation $\alpha = 2/d_w$, where $< r^2(t) > \sim t^\alpha$ and $\alpha = z(q = 2)$, The walk dimension takes values in the range: $1 < d_w < 2$ for super-diffusion, $d_w > 2$, for sub-diffusion, $d_w = 2$ for Brownian motion, and $d_w = 1$ for ballistic motion. In addition, the fractal dimension, d_f, is a measure of how complex a self-similar structure is (*e.g.,* line, plane, volume). It actually counts the available sites (number of points) occupied by a random walker

within a given boundary; e.g., for motion evolving in two-dimensions, the boundary can be defined by a circle of radius *r*. We define the number of available sites as *AS*, and assume that it scales as $AS \sim r^{d_f}$. One can use the square root of the mean square displacement (MSD) or the first moment of the displacement as the radius of the boundary circle. It has been reported that $AS \sim t^{d_f/d_w}$ [274] where the square of MSD has been used, albeit its applicability is questionable even for fractals having spectral dimensions, $d_s = \frac{2d_f}{d_w} < 2$.[274,275] Alternatively, the fractal dimension is defined through the Hurst exponent or the value of the structure function for q=1, as $d_f = 2 - H$ where $H = z(q = 1)$. We weigh the measure of *AS* with the MSD, and we use the new measure as a criterion for distinguishing between fractional Brownian motion (fBm) and random walk on fractals (RWF).

$$g(t) = \frac{AS}{MSD} = \frac{r^{d_f}}{<r^2(t)>} \sim t^{\delta} \qquad \text{Equation 4.8}$$

If the walk explores a given region homogeneously, then *AS* and MSD scale in the same way, and accordingly, the exponent of Equation 4.8 goes to zero. This condition is met for fBm but not for RWF, for which $\delta < 0$.

By using Equation 4.7, we obtain the structure functions z(q) for the lateral motion, or motion on the surface, of the droplets, as well for along the x- and y-axes. The x and y movements are intrinsically coupled. The analytical expressions of z(q) are listed in **Table 4.3**, and the shape of z(q) versus q has linear dependence in some cases. Linearity underlines a quasi-Gaussian behavior and suggests either a fractional Brownian motion (fBm) - sub/super diffusive - driven by fractional Gaussian noise or truly Brownian motion when the Hurst exponent is 0.5. If the linear form of z(q) and the scaling exponent of the MSD were the only criteria to classify the type of motion, then some of the droplets would be considered Brownian. However, linear dependence of

z(q) for the lateral motion, when not supported by linear forms for the corresponding structure functions, instead reflects movement coupling which results from environmental constraints. The presence of these constraints leads to sophisticate random walks with a strong sub-diffusive character, which retain their Gaussian nature (as in the case of isooctane droplets).

The details for ADOMA of PFH droplet PFH_1 (**Video 4.2**) are shown in **Figure 4.5**. Recording time is about of 3.42 min (minimum time lag of 0.1 sec) and the droplet does not explore the entire available surface (about 70 μm^2). Based only on the exponent of the second moment, one classifies the motion as Brownian along x-axis (n_x ~1.04), sub-diffusive along y-axis (n_y ~0.83), and slightly sub-Brownian for the lateral motion (n=0.92). Such a classification is in line with the values of z(q=1) and z(q=2) along x- and y-axes as well for lateral motion because of the relation z(q=2)=2z(q=1) (**Figure 4.5A**, **Table 4.4**).

Table 4.4 Hurst Exponents
Note: $H = z(q = 1)$, for a truly Brownian motion H=1/2, and the scaling of the MSD and/or variance, $< \Delta x^2 > \sim t^n$, is n=2H. It should be noted that the scaling of the second moment, n is equal to $z(q = 2)$.

Trajectory	Number of timepoints	x-axis	y-axis	Lateral
Perfluorohexane				
PFH_1	2052	z(q=1)=0.54 z(q=2) = 1.04 var ~ 0.98	z(q=1)=0.43 z(q=2) = 0.83 var ~ 0.79	z(q=1)=0.47 z(q=2) = 0.92 var ~ 0.89
PFH_2	232	z(q=1)=0.88 z(q=2) = 1.57 var ~ 1.31	z(q=1)=0.73 z(q=2) = 1.36 var ~ 1.15	z(q=1)=0.78 z(q=2) = 1.48 var ~ 1.41
Isooctane				
Iso_1	248	z(q=1)=0.36 z(q=2) = 0.67 var ~ 0.57	z(q=1)=0.52 z(q=2) = 0.88 var ~ 0.61	z(q=1)=0.37 z(q=2) = 0.76 var ~ 0.79
Iso_2	104	z(q=1)=0.36 z(q=2) = 0.69 var ~ 0.63	z(q=1)=0.38 z(q=2) = 1.04 var ~ 0.56	z(q=1)=0.33 z(q=2) = 0.69 var ~ 0.72
Iso_3	260	z(q=1)=0.50 z(q=2) = 0.96	z(q=1)=0.49 z(q=2) = 0.81	z(q=1)=0.49 z(q=2) = 1.00

		var ~ 0.90	var ~ 0.60	var ~ 1.04
Iso_4	140	z(q=1)=0.52 z(q=2) = 0.96 var ~ 0.65	z(q=1)=0.49 z(q=2) = 0.92 var ~ 0.84	z(q=1)=0.51 z(q=2) = 0.83 var ~ 0.62
Iso_5	605	z(q=1)=0.36 z(q=2) = 0.63 var ~ 0.51	z(q=1)=0.27 z(q=2) = 0.42 var ~ 0.30	z(q=1)=0.37 z(q=2) = 0.74 var ~ 0.74

However, this characterization is challenged twice: first, by the presence of a convex shape of structure functions, and second, by the form of the normalized velocity autocorrelation function (NVAF) (**Figure 4.5B**). If motion were Brownian, the NVAF (blue line) would be delta correlated, while, if motion were sub-diffusive fBm (red and green lines), then a distinguishable minimum at negative values would exist.[273] By contrast, NVAF retains a memory of about three to four steps (0.3 to 0.4 sec), then starts to fluctuate around zero. In addition, excess kurtosis (**Figure 4.5C**) underlines that the distribution of the events are not of Gaussian type – its values are significantly different from zero. Therefore, both Brownian and fractional Brownian motion as the types of motion are definitively rejected.

At the time scale of observation, the departure from Gaussian behavior signals the existence of droplet-wall and droplet-fluid interactions. The lengths of steps $||\Delta X_i||$ along x- and y-axes are constantly much smaller than the droplet radius of ($\sim 7.5 \times 10^{-7}$ m) (**Figure 4.5D**), and their mean values are 0.996×10^{-7} and 1.031×10^{-7} m in x/y-axes respectively, and their standard deviation is 0.880×10^{-7} m for both axes. Note that a handful of events exist where step-length is about half of the radius. The dimensionless variable $\xi_i = ||\Delta X_i|| / \langle ||\Delta X_i|| \rangle$ (**Figure 4.5E**) is defined and its shape can shed light on the type of stochastic mechanism: if $P(\xi)$ vs ξ is centered around a value of one, then fBm is a potential stochastic mechanism, which is not seen. If the maximum is at zero then, the process is probably continuous time random walk (CTRW). We can also discard

the possibility of CTRW, as the maximum appears at the one fifth of the mean, which is, by definition, always equal to 1. Thus, the droplet undertakes very small steps or slips, and must overcome a significant barrier in order to take a large step or move a certain distance. If a cut-off distance of twice the standard deviation is defined, we obtain the probability distribution of waiting times, or how frequently the droplet undertakes these larger steps either in x- or in y-axes whose length is larger than the cut-off value (**Figure 4.5F**). The log normal distribution works well for both axes.

PFH_1 is well described by $P(\tau) = \frac{a}{\tau b\sqrt{2\pi}} e^{-\frac{(\log(\tau)-c)^2}{2b^2}}$, and PFH_2 is fit to a power law truncated by a special str*etc*hed exponential $P(\tau) = \tau^{-d-1} e^{-f\sqrt{\tau}}$.

The parameters of the fit are listed in **Table 4.5** and return mean waiting times $<\tau_w>$ = 0.89 sec and 0.98 sec for x- and y-axes, respectively. Assuming that the simplest form of transition state theory (TST) applies and the mean waiting time is the reciprocal of the rate constant, k, then the energy barrier is provided by the formula:

$$\Delta E = -k_B T \log\left(\frac{h}{k_B T <\tau_w>}\right) \qquad \text{Equation 4.9}$$

where $k_B T$ is the Boltzmann's constant times the temperature of the sample and h is the Planck's constant. Considering T=293.25 K and $<\tau_w> = 0.89/0.98$ returns a barrier of 17.1 kcal/mol in x-axis and 17.15 kcal/mol in y-axis.

Table 4.5 Parameters of best fittings for distribution of waiting times for PFH droplets, PFH_1 and PFH_2.

	axis	*a*	*b*	*c*
PFH_1	*x*	0.112±0.007	1.222±0.081	-0.866±0.079
	y	0.120±0.010	1.374±0.132	-0.964±0.105

PFH_2	*axis*	*d*	*f*	
	x	-0.996±0.058	3.671±0.255	
	y	-0.799±0.100	4.345±0.540	

The second PFH droplet (**Figure 4.7**, **Video 4.3**) presents features of directional motion, which lead to super-diffusion despite very small increments with respect to its radius. After reducing the cut-off distance to one standard deviation, we found an equivalent barrier of about 16.5 kcal/mole, which is comparable to the findings for droplet PFH_1. The latter likely indicates the time needed for the re-organization of droplet-surfactants interactions. Following the same path of analysis applied for droplet PFH_1, we observe that NVAF retains a memory of the order of 10/15 steps for x-/y-axes, (**Figure 4.7D**). Excess kurtosis shows a Gaussian-type distribution for motion in y-axis and of a non-Gaussian type for x-axis and lateral motion (**Figure 4.7C**). The probability distribution for waiting times is not conclusive for cut-off distance of twice the standard deviation, so it was reset it at one standard deviation. The motion is also super-diffusive (**Table 4.4**). Note that the lengths of the increments are very small with respect to the droplet radius, except for a very small number of steps approximately equal to half the radius (**Figure 4.7E**). The super-diffusive character, in conjunction with the small increments, indicates directionality, which is probably imposed by the cell walls. Waiting times to overcome a distance of one standard deviation corresponds to an equivalent barrier of about 16.5 kcal/mole, which is approximately equivalent to the barrier of 17 kcal/mole found for PFH_1. If the aforementioned directionality were the result of a random walk on fractal or of constraints set by the cell wall reducing the dimension of the actual walk, then we would expect a linear structure function if steps draw values from a Gaussian distribution or structure function of convex shape for steps drawing values from a power law

distribution. Neither the first nor the second hold true (**Figure 4.7B**). What remains is the strong confinement set by the cell and probably the barrier reflects the reorganization of surfactants droplet interactions.

We can perform an analogous analysis of the isooctane droplet trajectories (**Figure 4.6-Figure 4.11**). The droplets' radii average around 0.15μm, and the recorded motion was approximately 20 seconds, and presents consistent characteristics of motion. Droplets explore a small portion of the available surface and tend to continuously scan a small subspace before moving with a longer step to an adjacent subspace (**Figure 4.12**). The structure functions have convex shapes for motion in y-axis, and linear or convex shape for motion in x-axis. The lateral motion is linear for the majority of isooctane droplets analyzed (**Table 4.3**). Structure functions suggest an intrinsic coupling of x- and y-axes, which returns a linear structure function for lateral motion and thus the existence of a unique scaling at all time scales (**Figure 4.6A**). Bearing in mind the values of the scaling exponents for the first and second moment as well for the variance (**Table 4.4**), the process shows a sub-diffusive behavior for most of them, with the exception of droplet Iso_3, which points to anti-persistent random walks, which, under certain conditions, can be classified as sub-diffusion fractional Brownian motion driven by fGN. The form of the NVAF supports this type of motion (**Figure 4.6B**). If fBm were the source of noise and given that fBm is of Gaussian type, the excess kurtosis, $K(\tau)$, would be zero. Excess kurtosis can be considered zero, thereby confirming fGn as driving mechanism of the droplet (**Figure 4.6C**). However, the different structure functions along x- and y-axes demand closer scrutiny since this can also be due to a random walk on a fractal (RWF), given that RWF may also be described by a Gaussian distribution.[276] RWF and fBm have similar NVAF but differ with respect to the mean number of

visited sites up to time t. This property scales with exponent equal to the exponent of the MSD for fBm, while for RWF, the scaling exponent is smaller than the scaling exponent of the MSD.[277]

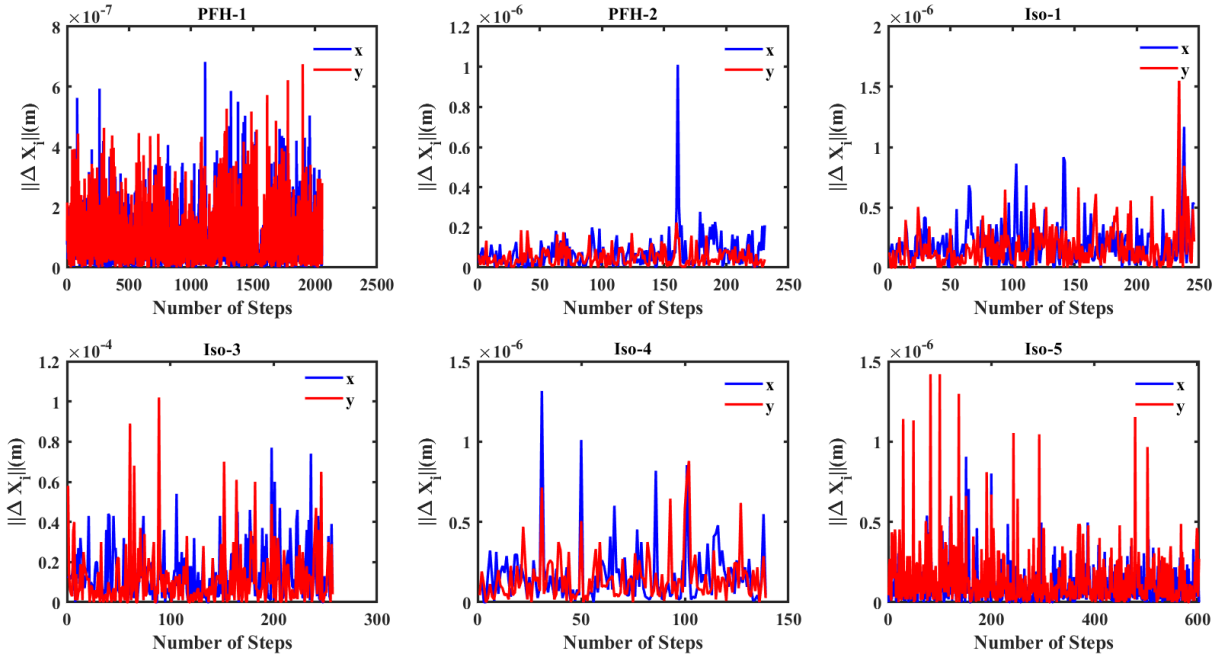

Figure 4.12 Increments $||\Delta X_i||$ for all droplets
Movements along x- and y-axes are shown in blue and red, respectively. It is noteworthy that the increments are significantly larger for isooctane droplets.

For all droplets, g(τ) decreases as a function of time, discarding the hypothesis of fBm as underlying mechanism, with the exception of droplet Iso_3 where g(τ) retains a constant value (**Table 4.6, Figure 4.13)**. More specifically, the lateral motion of droplets Iso_1 and Iso_5can be classified as RWF with fractal dimension, d_f, equal to ~ 1.68, respectively. The lateral motion of Iso_3 is classified as fBm, while the rest cannot be classified. The observed fractal dimension corresponds to a Sierpinski carpet , which we posit arises from the dense population of droplets in a local environment, which are functionally constrained to the same plane.[278]

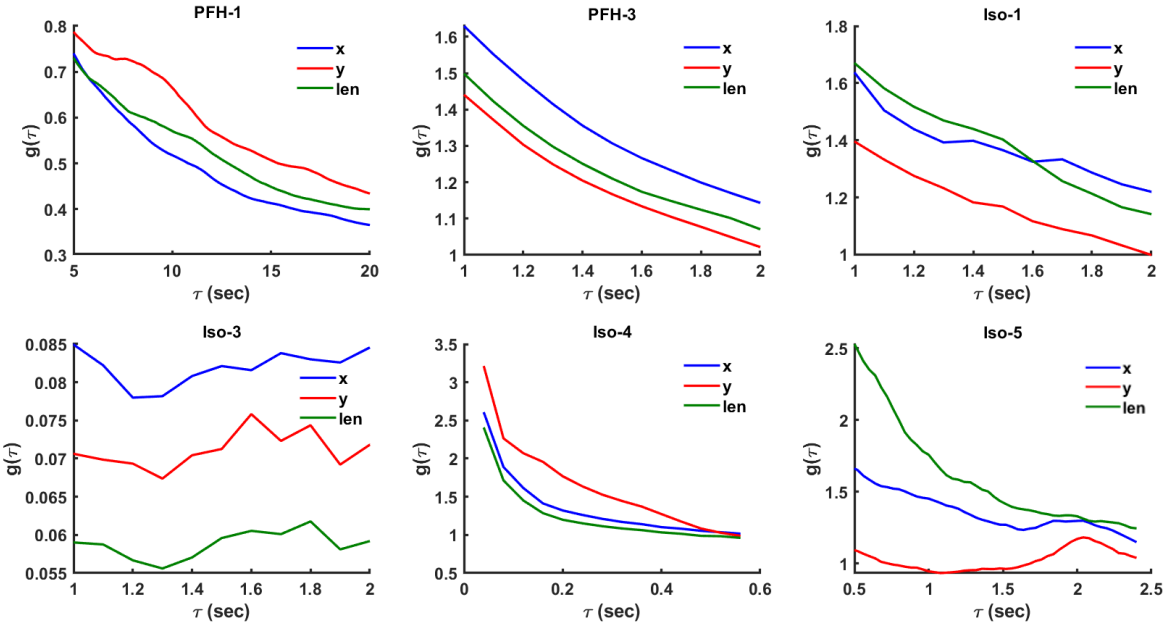

Figure 4.13 The quotient of the mean number of visited sites per the central second moment, g(τ), for 6 analyzed droplets.
g(τ) starts decreasing and converges to a plateau value for fBm, while for RWF, it continues with decreasing values.[277] The initial decreasing part of g(τ) is not displayed.

Table 4.6 Excess kurtosis and quotient values, as well as Gaussian nature of motion

Trajectory	axis	Shape of Structure Function	Normalized Velocity Autocorrelation Function	K(τ)	g(τ)	Mechanism
Perfluorohexane						
PFH_1	x-axis	Convex	Short positive	<0	Decreasing	Confined Diffusion
	y-axis	Convex	Short positive	≠ 0	Decreasing	Confined Diffusion
	lateral	Convex	Short positive	<0	Decreasing	Confined Diffusion
PFH_2	x-axis	Convex	Short positive	>0	Decreasing	Confined Diffusion
	y-axis	Linear	Short positive	=0	Decreasing	Confined Diffusion
	lateral	Convex	Short positive	>0	Decreasing	Confined Diffusion
Isooctane						
Iso_1	x-axis	Convex	Short negative	<0	Decreasing	Coupled x and y
	y-axis	Convex	Short negative	<0	Decreasing	Coupled x and y
	lateral	Linear	Short negative	>0	Decreasing	RWF (d_f=1.68)
Iso_2	x-axis	Linear	Short negative	<0	Inconclusive	------
	y-axis	Convex	Short negative	<0	Inconclusive	------
	lateral	Linear	Short negative	≈0	Inconclusive	------
Iso_3	x-axis	Linear	Short negative	≈0	Constant	fBm
	y-axis	Convex	Short negative	<0	Constant	Unknown
	lateral	Linear	Short negative	≈0	Constant	fBm
Iso_4	x-axis	Convex	Delta type	<0	Decreasing	Unknown
	y-axis	Convex	Short negative	<0	Decreasing	Unknown
	lateral	Convex	Delta type	<0	Decreasing	Unknown
Iso_5	x-axis	Convex	Short negative	≈0	Decreasing	Coupled x and y
	y-axis	Convex	Short negative	≈0	Decreasing	Coupled x and y
	lateral	Linear	Short negative	=0	Decreasing	RWF (d_f=1.68)

$K(\tau) = \frac{<X^4>}{3<X^2>^2} - 1$ provides the Gaussian character of the distribution when it is zero, and the non-Gaussian otherwise, $g(\tau) = \frac{Mean\ Number\ of\ Visited\ Sites}{<X^2>}$ and distinguishes between fBm

(fractional Brownian motion) and RWF (random walk on fractal), it decreases as time increases for RWF, and it remains constant for fBm, and d_f provides the fractal dimension of the walk.

4.2.4. ADOMA Discussion and Conclusions

In summary, the motion of PFH and isooctane droplets are significantly different from one another, probably because of the constraints imposed by the liquid cell, whose thickness is ~500 nm. Indeed, the PFH droplets analyzed here have radii 700-2000 nm, much larger than the thickness of the liquid cell and, as such, are compressed to a spheroidal form by the liquid cell membranes, which has been discussed previously. On the other hand, the radii of isooctane droplets are in the range 100 - 489 nm, comparable or smaller than the thickness of the liquid cell, and there is room for a non-significantly obstructed motion. All droplets exhibit anisotropic motion with respect to the x- and y-axes. PFH droplets, being significantly larger, showed slip motion with an energy barrier of approximately 17kcal/mole, which equates to breaking of approximately 4 H bonds. This energy is presumed to be the required activation in order to detach the surfactant-covered droplet surface from the SiN_x and could easily be imparted by the high voltage electrons of the beam.[279]

Isooctane droplets underwent fractional Brownian motion if their diameter was near the dimension of the liquid cell. If they were significantly smaller, the motion had characteristics of random walks on fractal surfaces. Motion in x- and y-axes still differs; they are intrinsically coupled. Main characteristics of this motion are the strong sub-diffusive behavior in conjunction with huge steps taken during the walk, orders of magnitude larger than the radius of the droplet. Analysis identified two of them as random walks on fractal surface (RWF) with fractal dimension of $d_f \sim 1.68$, and such a value corresponds to Sierpinski carpet.

Such discrepancies highlight the importance of the material in question. While the fluorinated oil emulsion utilizes a nonionic surfactant and the isooctane emulsion uses an anionic one, such changes have not previously yielded significant differences in observed motion.[5] Thus, we are inclined to believe that such differences arise from differences in the material properties of the emulsified oil—namely, density and viscosity, as well by possible activated hydrophobic interactions between droplets and water molecules. We hypothesize that the observed coupling and anisotropy in the x- and y-axes is the result of SiN_x membrane bulging, which is a known phenomenon in liquid cell.[160] While we have previously assumed this to be uniform, it is possible that the orthogonal orientation of the liquid cell windows leads to discrepancies in membrane deformation, which propagates as anisotropic motion along the gradient of liquid thickness.

Isooctane droplets exhibit behavior consistent with a fractal Sierpinski carpet, which is comprised of several occupiable sites adjacent to forbidden sites. To understand the physical origins of such a phenomenon, we consider several potential sources. Residual membrane features from fabrication, periodic membrane charging, local environmental fluctuations are all potential candidates for the imposition of such fractal behavior.

Regarding the possibility of SiN_x patterning, such membranes are typically manufactured via chemical vapor deposition. which may reflect a fractal nature of the SiN_x surface. Under certain synthetic conditions (microwave electron cyclotron resonance CVD), fractal aggregation behavior of SiN_x particles is occasionally observed during microwave electron cyclotron resonance chemical vapor deposition.[280] However, it seems unlikely that such features would not result in observable variations in membrane contrast if present.

In consideration of the possibility of patterned membrane charging, we can look to e-beam lithography literature. Under certain conditions, we can consider the two processes sufficiently analogous to extrapolate the charging effects from one to the other (e.g., at accelerating voltages of 100kVs and fluxes of hundreds of $\mu C/cm^2$).[281–284] In the work by Lee *et al.*, a mask of 100nm SiN_x on a silicon construct is considered and is shown to have an inhomogeneous membrane potential. The potential falls off towards areas where the membrane is in contact with the silicon grounding struts, but is not periodic in nature. Additionally, Lee shows that the membrane reaches a steady-state potential 17.3V after a sufficient fluence. We are operating beyond that threshold in the aforementioned experiments, so it seems reasonable to conclude that our SiN_x windows are in a similar condition.

Finally, it seems unlikely that thermal or chemical variations in the immediate environment of the droplet to be the source of such fractal driving forces, as these trajectories occur over time scales far exceeding that of the aforementioned fluctuations.[88]

Thus, in the absence of surface effects that seem likely to give rise to such fractal behaviors, we are left to conclude that this behavior is most likely the effect of the population density of the droplets. ADOMA considers droplets in isolation, and thus does not account for neighboring entities. Given the spheroidal nature of our droplets, it seems reasonable that such packing occurs within the densely populated liquid cell (**Video 4.1**) and is the source of such motion. The lack of this motion is observed under more dilute conditions (PFH droplets).

To probe this, future work could examine these materials with STEM, as a condensed electron probe is known to affect the surface of the SiN_x membrane differently than the parallel

beam. Alternately, the SiN_x surface could be coated with a layer such as graphene to mask any residual characteristics from fabrication.

4.3. Study Conclusions

Here, we have presented results demonstrating the less hindered motion of emulsion droplets *in situ* via liquid phase TEM. While the nature of the observed motion is still not truly Brownian, the effective diffusivity is within two orders of magnitude of the bulk. We posit that the interfacial surfactants present in these systems permit this motion to occur in a less hindered fashion by creating a surface which is able to slip and slide across the SiN_x windows with minimal pinning events. Such motion is modular based on droplet size. Further, we posit that the use of soft materials with a 'slippery' interface is instrumental in observing motion so consistent with expectations. Additionally, we observe anisotropy in this motion which is attributed to the bulging of the SiN_x membranes. Motion in the larger perfluorohexane droplets reflects the spatial constraint of the *in situ* environment, while that of the smaller isooctane droplets is that of a random walk on a fractal surface, which we hypothesize is the result of planar droplet packing.

4.4. Experimental Details

4.4.1. Materials

2, 2, 4-methylpentane (isooctane) was purchased from TCI America. Tetradecafluorohexane (perfluorohexane) was acquired from Alfa Aesar. Capstone FS-30 was purchased from ChemCruz. All other chemicals were purchased from Sigma Aldrich.

4.4.2. Sample Preparation

To prepare emulsions, surfactant was dissolved in the continuous phase before addition of the dispersed phase. The minor phase was dispersed via probe sonication or vortexing. Samples were prepared within an hour prior to imaging.

4.4.3. Liquid Cell Assembly

Liquid cells were assembled as previously reported.[5] Briefly, emulsions were drop cast onto a prepared SiN_x chip before sealing with another SiN_x top chip and holder clamping mechanism. A Hummingbird Scientific Dual Flow Mixing holder was used, and the integrity of the sample cell was verified via an external pumping station prior to microscope insertion.

4.4.4. Microscope and Imaging Conditions

A JEM-ARM300F (JEOL Ltd., Tokyo, Japan) transmission electron microscope was used for *in situ* experiments at an operating voltage of at 300keV and current of 15μA (FEG source). Images were acquired with a Gatan 2k × 2k OneView-IS CMOS camera and a Gatan K3-IS direct electron detector (Gatan Inc., Pleasanton, CA, USA) via Gatan Digital Micrograph imaging software (Roper Technologies, Sarasota, FL, USA). Exposure durations ranged from 0.01s to 1s. Electron fluxes were measured by both the K3 and via the detected beam current, which has previously been calibrated via a Faraday Holder in conjunction with the respective apertures used. Video acquisition was done by either the *in situ* camera functionalities or by screen recording with Camtasia Studio 2018 (TechSmithCorporation, USA). Frame rates for each data set are indicated in figure captions.

4.4.5. Image Processing

High bandpass filters were used to reduce the noise inherent to low dose, high framerate imaging and to mitigate the gradient of contrast inherent to variable liquid thickness.

4.4.6. List of Supplemental Videos

Video 4.1: Videographic data of isooctane droplets stabilized by AOT in water, from which trajectories of droplets Iso_1 to Iso_4 and Iso_6 to Iso_9 were extracted

Video 4.2: Videographic data of trajectory of droplet PFH_1 in aqueous liquid cell

Video 4.3: Videographic data showing trajectory of droplet PFH_2

Video 4.4: Videographic data of isooctane droplets from which Iso_10 and Iso_11 trajectories were extracted

Video 4.5: Videographic data of isooctane droplets from which trajectories of droplets Iso_12 through Iso_16 were extracted

Videos are available in the provided OneDrive repository.

Chapter 5 Direct Observation of Emulsion Polymerizations

This work outlined in the following chapter is an ongoing effort in collaboration with Prof. Brent Sumerlin and his student Megan Lott at the University of Florida. A manuscript detailing these efforts is in preparation.

Emulsion polymerizations are a tremendously useful class of industrial reactions in that they are tremendously scalable – often, in reactions at scale, polymerizations become extremely viscous, and thus processing the formed polymers becomes much more difficult. However, forming the polymers in an emulsion circumvents this issue, as the continuous phase is maintained.[285] Further, these reactions are highly modular – continuous and dispersed phases may be chosen to suit the given application, and surfactant type and quantity will dictate the properties of the dispersion formed. Such approaches also generate well defined polymer latexes of low dispersity and controlled sizes, reducing the subsequent processing necessary.[286] Emulsion polymerizations have also been leveraged to prepare complex nanomaterials inaccessible through other synthetic methods.

There are multiple regimes into which these reactions can be classified: conventional emulsions, miniemulsions, and microemulsions. This parameter is chosen by adjusting the solvent and surfactant conditions to dictate droplet formation. A comparative schematic is shown below in order to qualitatively demonstrate the differences in morphology and species present before and after polymerization (**Figure 5.1**). In the case of miniemulsions, reactants and initiator are confined to the same droplet, which does not undergo exchange with other droplets. This is in contrast to a classical emulsion, which draws from reserves of large monomer droplets (also called reservoirs) and some monomer swollen micelles, which are able to capture the increasingly hydrophobic

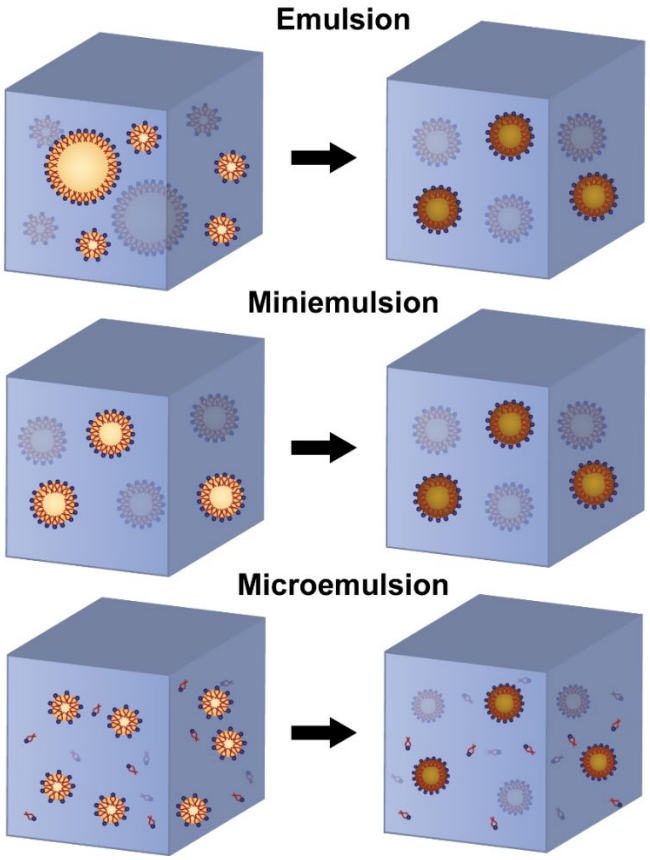

Figure 5.1 Schematic comparison of conventional, mini, and microemulsion polymerizations, as inspired by Rao *et al.* [289]

polymer formed by water-soluble initiators as a result of their higher surface area in comparison to monomer reservoirs.[287] Monomer then diffuses from the reservoirs to the loci of nucleation. If sufficient surfactant is included and shear applied, a more uniform population of submicron droplets is formed, termed a miniemulsion. Unlike the conventional emulsion polymerization, there is no longer a significant discrepancy in available surface area for transport between the two droplet populations, and thus they exchange significantly less and the locus of particle nucleation shifts to the monomer droplets themselves.[287,288] Microemulsions exhibit the least interdroplet exchange of the three varieties. Microemulsions, on the other hand, are stabilized by an excess of surfactant. Additional relevant parameters and characteristics may be found in **Table 5.1** (adapted from Rao *et al.*[289] and Capek *et al.*[286]). These reactions typically occur in water because of its high thermal conductivity, which allows it to maintain consistent reaction conditions (*i.e.,* temperature), but may also be carried out in inverse formulations (*i.e.,* water in oil) in the case of water soluble reagents.[285]

Table 5.1 Comparison of relevant characteristics of conventional, mini-, and microemulsions. Adapted from Rao *et al.*[289] and Capek *et al.* [286]

Property	Conventional Emulsion	Miniemulsion	Microemulsion
Duration of Stability	Seconds to months	Hours to months	Indefinite (thermodynamically stable)
Size Range	1-10μm	100-500nm	10-50nm
Droplet Polydispersity	Low	Very Low	Very Low
Emulsifier Content	1-3wt%	5wt%	15-30wt%
Transparency	Milky	Opaque/milky	Transparent or translucent

Generally, these materials are difficult to study by conventional scattering techniques due to the disparity in length scales of the relevant species – diffusing monomers (Angstrom-scale), polymer nanostructures (nanometer), and monomer droplets (micron) are all features of interest. While LPTEM is not able to observe the monomeric species, it is able to simultaneously resolve features on both the nanoscale and the microscale (up to a few microns). Thus, we posit that LPTEM, coupled with a judicious choice of correlative scattering studies, can reveal previously unknown mechanisms or refine proposed models which have been extrapolated from previous indirect studies. In this chapter, we will detail our work attempting to observe polymerizations via both mechanisms in mini, micro, and macroemulsions so as to glean mechanistic information which has not been previously directly observed.

5.1. Miniemulsion Polymerizations

Miniemulsion polymerizations are an ideal candidate for LPTEM given their size (submicron) and stability (hours to days).[290] Unlike conventional emulsion polymerizations, all reagents and initiators are contained within the same droplet microreactor, and thus there is no mass transfer from monomer reservoirs to polymer latex. Such compartmentalization enables the

use of water-insoluble components, as they no longer have to diffuse through the continuous phase. These are typically oil-in-water dispersions, but we have chosen to investigate inverse miniemulsions to take advantage of the lower density material as the continuous phase for superior contrast. The Sumerlin group was already investigating a system fitting this description for its ability to yield ultra-high molecular weight polymers with extremely low dispersities (**Figure 5.2**). Specifically, this system is able to maintain the high viscosity required for the suppression of diffusion-driven chain termination which allows for continued polymer growth to ultra-high molecular weights, without adversely affecting the bulk properties of the reaction solution, as the high viscosity component is contained in the miniemulsion droplets. Thus, this reaction is immensely scalable. As designed, this scheme uses a photoiniferter to facilitate a controlled radical polymerization (**Figure 5.2A**), which we hoped to mimic with the e-beam, and uses the commercial nonionic surfactant Span60 (**Figure 5.2B**). A parallel effort was also made to investigate the thermally initiated analogue using VA-044 (**Figure 5.2C**), given that the primary interest was in observing the mechanism of the miniemulsion polymerization, rather than achieving an ultra-high molecular weight.

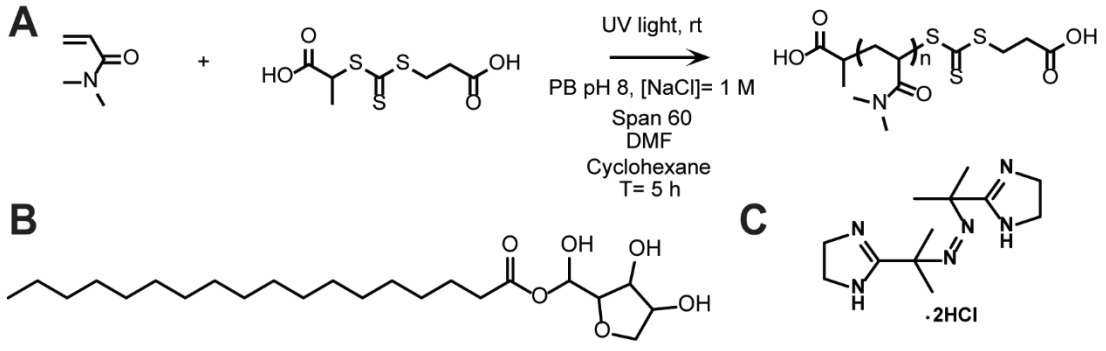

Figure 5.2 Synthetic scheme and structures for RAFT miniemulsion polymerization of DMA

(A) Synthetic scheme for RAFT polymerization of DMA in an inverse miniemulsion in cyclohexane, courtesy of Megan Lott (B) Structure of Span60 surfactant (C) Structure of thermal initiator VA-044

When considering polymerization schemes, there are two main initiation mechanisms available to us: light and temperature. UV-mediated controlled polymerization is the Sumerlin group's specialty and provides excellent control over molecular weight.[291,292] It has also been previously *in situ*, harnessing the e-beam as a UV mimic.[155] Thermal initiation is another possibility which has been previously demonstrated by leveraging the heating capabilities of our LPTEM holder.[226] The relative advantage of the thermal approach is that it grants a greater degree of control over the rate of polymerization (as compared with the relatively uncontrolled e-beam initiation), and allows the reaction to proceed even in the absence of the damaging e-beam

5.1.1. UV Initiation

Our preparation of the inverse miniemulsion yielded a well defined population of droplets approximately 230nm in diameter (**Figure 5.3A**), which formed a cloudy suspension (**Figure 5.3B**). Initial efforts to observe the UV-mediated polymerization *in situ* were consistently plagued by issues of cell bursting. We attributed this to the uncontrolled nature of the e-beam initiation, which is not directly translatable to UV. Thus, in order to observe the process of the UV-mediated polymerization without damaging the microscope, we proceeded to study this reaction by imaging static liquid cells of aliquots taken from the bulk polymerization. By performing this reaction *ex situ* and preparing our liquid cells under ambient conditions, the reaction was sufficiently quenched to prevent cell bursting and allow acquisition of images (**Figure 5.3C**). Over time, we observed unanticipated phase separation (which is particularly evident in the t= 60 minute micrograph).

Notably, there persists a population of droplets in the 250nm size regime even at the 120 minute mark, which is consistent with expectations.

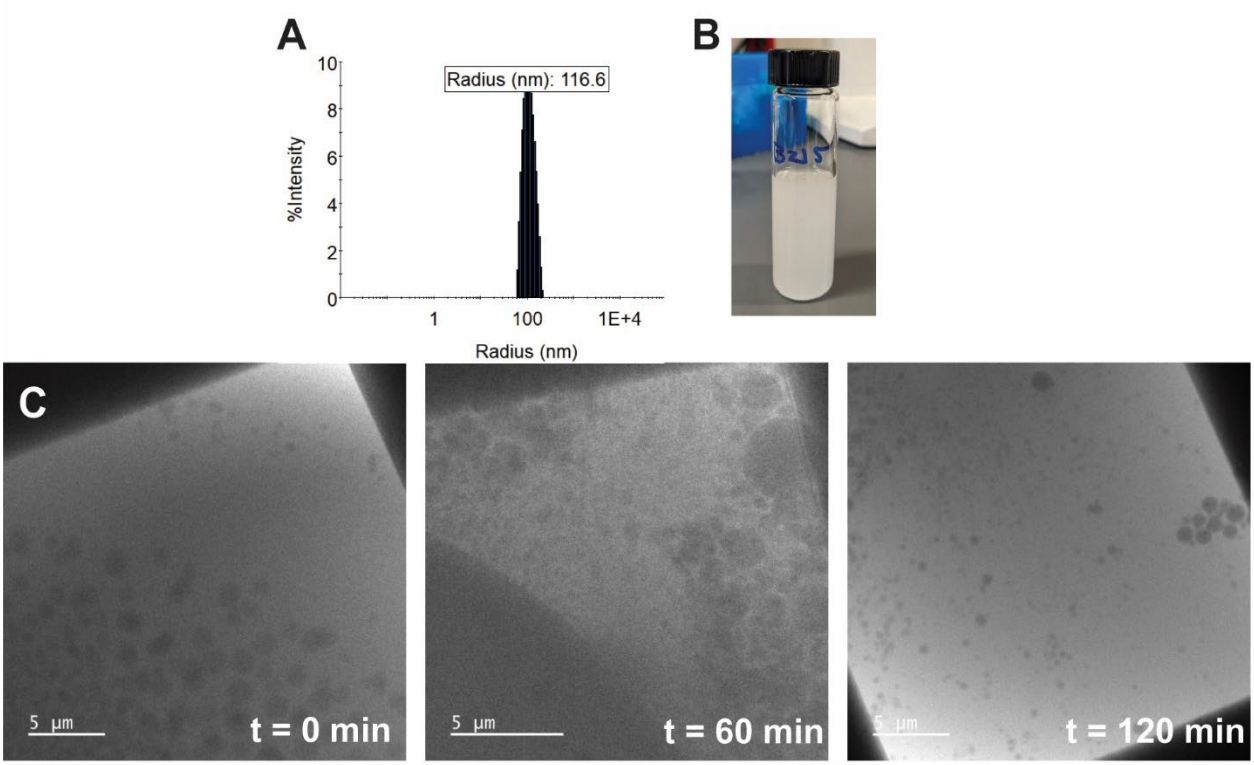

Figure 5.3 UV-initiated RAFT miniemulsion polymerization of DMA and associated characterization

(A) DLS trace of miniemulsion of reactants, with a narrowly distributed peak around 115 nm (B) Image of dispersed reactants (C) Sequential micrographs of bulk polymerization, with aliquots taken from reactants, 60 minutes, and 120 minutes of UV exposure. Aliquots were imaged as static liquid cells, with time points as indicated.

We attempted to combat the issue of cell bursting by lowering both monomer and photoiniferter concentration in order to slow the generation of unstable species, but this proved unsuccessful. Given our inability to perform the *in situ* polymerization UV-mediated synthesis without potentially damaging the microscope, our focus shifted to the thermal initiation.

5.1.2. Thermal Initiation

The aforementioned issues of cell bursting did not seem to affect thermally-initiated polymerizations of the same material, so we moved forward with this aspect of the experiments.

This route seemed especially promising because it did not rely on constant e-beam illumination in order to drive the reaction – rather, we could heat the holder and blank the beam so as to minimize the electron fluence to the sample, while knowing that conditions for the reaction were maintained. This also helps to minimize damage to the formed polymer. In order to observe this polymerization *in situ* under the same conditions as the bulk, it was necessary to maintain an air free sample, so that atmospheric oxygen did not quench the generated radicals. Typically, the best way to keep something air free is to handle it in a glove box maintained under an atmosphere of an inert gas (usually nitrogen); however, assembly of a liquid cell while using the gloves of a glove box is functionally impossible. Thus, we employed two strategies: first, flowing the sample in through a gas-tight syringe, and additionally drop-casting the sample under a flow of nitrogen, as previously demonstrated by Scheutz *et al.*[226] While the method of flowing in is a more methodical approach, it is also significantly more time intensive, and requires at least 40 minutes of flow in order to fill the cell, and thus this method is not ideal for performing sequential experiments during a session. Thus, it's desirable to verify whether the drop casting method maintains sufficiently air-free conditions for this non-aqueous polymerization. The solution prepared was identical to that described in **Section 5.1.1**, with the sole substitution being VA-044 for the photoiniferter in the aqueous components. The cell was then prepared either by flowing in (**Figure 5.4**) or drop casting (**Figure 5.5**), and subsequently heated to 60°C for stroboscopic imaging.

The flowed in cell initially showed an absence of structures in the expected size range, but they did appear in time with imaging (**Figure 5.4A**). As previously mentioned, the e-beam can accelerate demulsification, which seems to be the case here – the outline of the beam is clearly visible in the t = 10, 50, and 70 minute micrographs. This does confirm the presence of monomer droplets at t = 0 minutes, as there must be something to demulsify. The appearance of non-droplet

structures was also observed at 70 minutes and beyond, and post-mortem TEM of the liquid cell chips revealed the presence of stable circular structures (**Figure 5.4B**). The conversion of the polymer was then confirmed using MALDI-IMS as previously described[157] (**Figure 5.4C**). Here, the mass spectra of the top and bottom chip in the imaging region show peaks with a spacing corresponding to 99 g/mol, which is equivalent to the the molecular weight of the DMA monomer, and thus indicates successful polymerization. This indicates that the species seen at t = 70 minutes and in the post-mortem imaging are indeed polymer latexes.

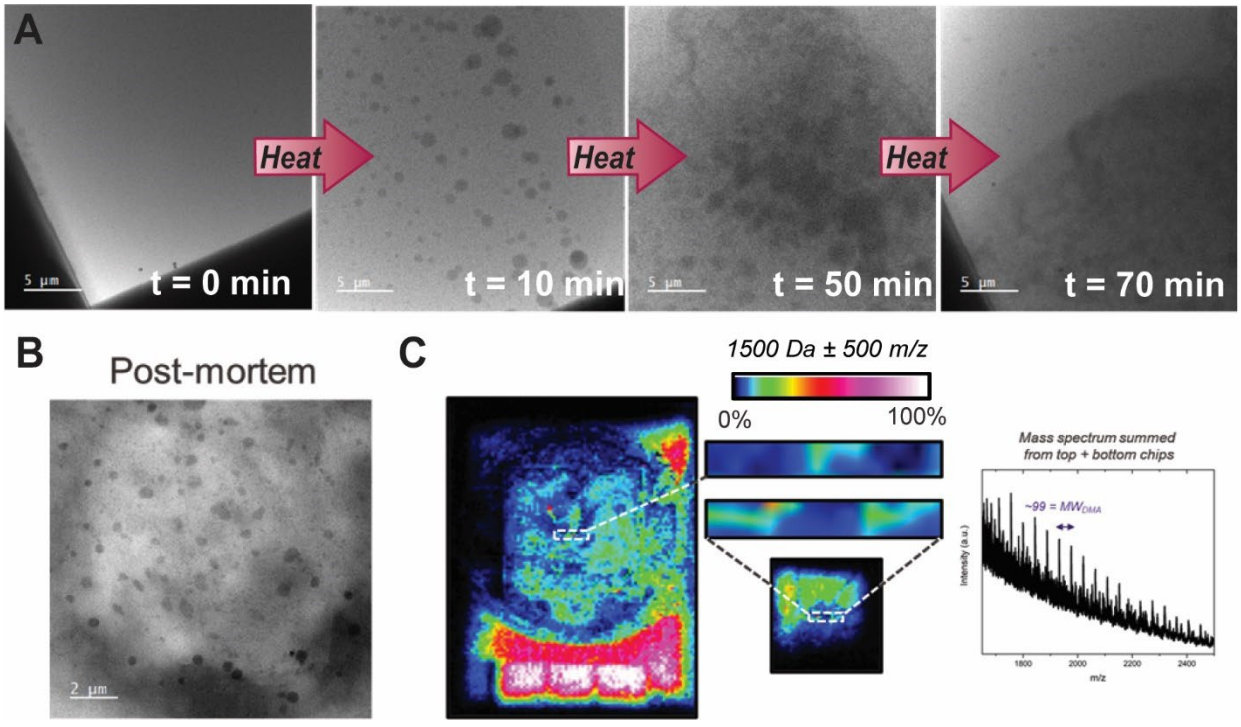

Figure 5.4 Thermally-initiated free radical polymerization of DMA in flowed in liquid cell.

(A) Series of micrographs from *in situ* heating experiment at 60°C (B) Post-mortem micrograph of dried bottom chip (C) MALDI-IMS

When employing the drop-casting method, we observed a significant increase in phase separation at early time points (**Figure 5.5A**). This is surprising, considering that the time from reaction preparation to imaging was reduced by approximately 30 minutes (the time required to flow in). Given the shorter cell preparation time, there was also less time in which demulsification could've

occurred, so it was anticipated that this preparation would yield a better dispersed sample. As the cell was heated, the phase separation remained visible, with the presence of some smaller species appearing (t = 10 minutes). Interestingly, at the 30 minute mark, a triphasic material is observed (as indicated by the three regions of different contrast). The darkest phase observed has a spherical morphology, which suggests that we may be differentiating polymer latex from monomer solution. However, this would be further evidence of significant demulsification, given that for a miniemulsion, this should be one and the same. Post-mortem MALDI-IMS confirmed the formation of polymer (**Figure 5.5B**).

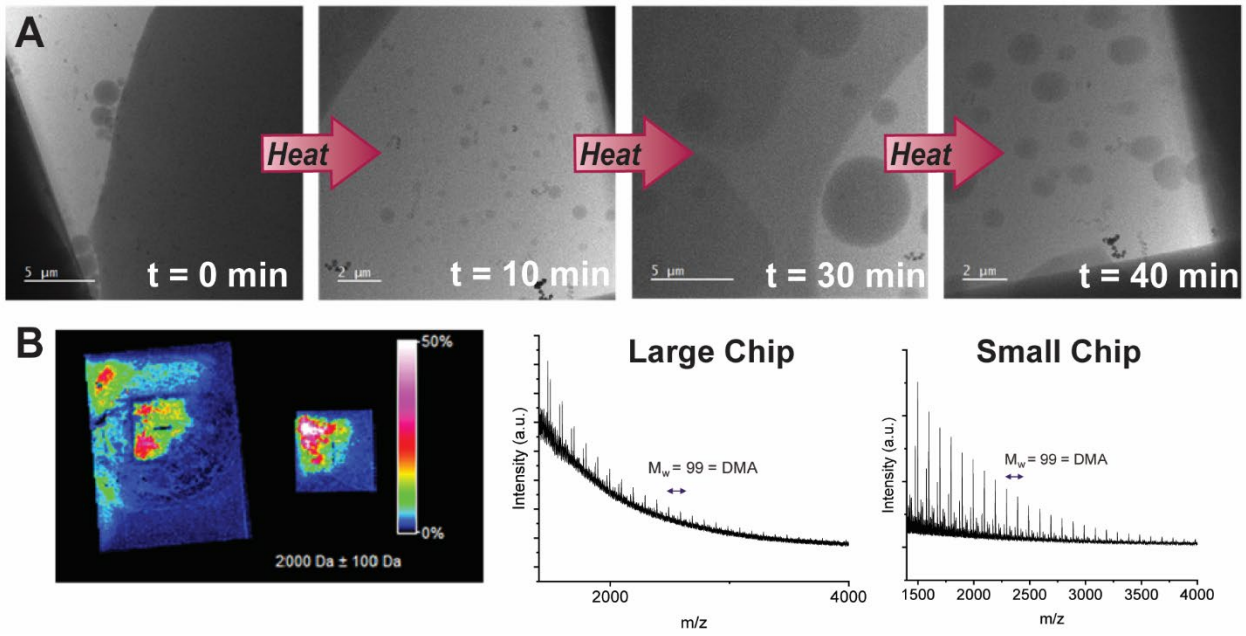

Figure 5.5 Thermally-initiated free radical polymerization of DMA in drop-cast liquid cell.

(A) time series of micrographs from polymerization heated to 60°C (B) MALDI-IMS map and mass spectra indicating the presence of polymerized DMA

5.1.3. Study Conclusions

We encountered a fundamental challenge in imaging miniemulsions in that the only appreciable difference in the emulsion before and after polymerization is droplet density. While

the contrast of these emulsions is quite high, we are not able to discern such differences at the low flux of our imaging conditions, and thus cannot observe an appreciable difference upon polymerization.

5.2. Conventional Emulsions

Most conventional emulsion polymerizations yield polymer latexes of 1μm or greater, and only remain stable for a few minutes without stirring or stabilization.[289] Thus, many of these polymerizations are not amenable to liquid cell with respect to both length and time scale. Instead, we found ourselves interested in imaging what literature refers to as a "true" emulsion polymerization, where styrene is dissolved in a blend of 55% methanol, 45% water solution and spontaneously forms uniform latexes as a result of changing solubility.[293] The solution was prepared in accordance with the literature to yield 1% w/v of styrene in 55%/45% methanol/water blend. Ammonium persulfate as used as initiator at an overall concentration of 2mM.

The above solution was prepared and sparged, and a liquid cell was prepared *via* flowing in to a nitrogen flushed holder (**Figure 5.6**). The sample was then heated to 60°C at a rate of 0.5°C/s to prevent dewetting, and micrographs were acquired every 10 minutes to monitor the formation of particles (**Figure 5.6A**). Faint particulates are visible at the 10 and 20 minute time point, which were taken to be polymer latexes. After 20 minutes of heating, the software encountered an error where the recorded resistance was outside of the tolerable range, and was thus unable to continue heating. This is likely the result of forming material on the heating electrodes, which would inherently increase resistance and interfere with heating. Post-mortem TEM shows the formation of dispersed, discrete high contrast species (**Figure 5.6B**). Post-mortem MALDI-IMS on the SiN_x chips generated spectra with a monomer spacing of 70 m/z, which does not correspond to the molecular weight of the styrene monomer (104 g/mol), so it is does not

appear that the intended polymer was actually formed (**Figure 5.6C**). The presence of peaks with such a spacing typically indicates the presence of polymeric species, but in this case, it is not the desired polystyrene latexes.

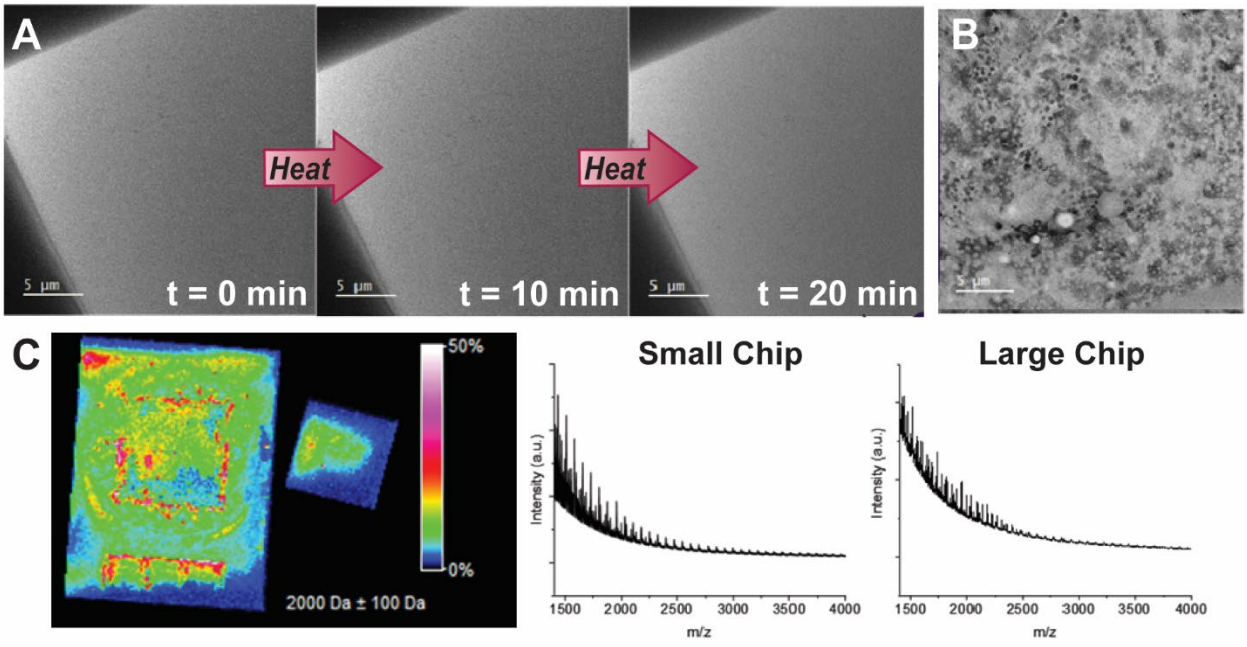

Figure 5.6 True emulsion polymerization of styrene in methanol and water.

(A) Time series of micrographs during *in situ* heating experiment, showing the development of structures after 20 minutes. (B) Post-mortem micrograph of bottom chip from *in situ* polymerization, showing the formation of aggregate structures (C) MALDI-IMS of SiN_x chips. Spacing in spectra does not correspond to styrene or PEG (a common contaminant).

The issue of heating disruption was a consistent problem, and made further studies of this system impossible. Further, the mechanism by which such latexes precipitate is a fairly well understood process of changing solvophilicity. Thus, we chose to shift focus to areas where we might shed more light *via* LPTEM.

5.3. Microemulsions

A consistent problem encountered with the previous types of emulsion polymerization was the need to stir in order to maintain the dispersion. As discussed in **Section 3.1**, the current SiN_x experimental set up is fundamentally unable to stir or mix the materials being studied, beyond

what may be induced by external flow. Microemulsions were proposed to circumvent this issue, as they are a subset of emulsions which are thermodynamically stable, and thus do not rely on mixing to remain dispersed.[294,295] As such, they should remain stable for sufficient periods of time so as to allow for *in situ* study. Microemulsion conditions were optimized for LPTEM considerations (*e.g.,* low density continuous phase, appropriate time scale, suitable size regime) (**Figure 5.7**). While optimizing microemulsion conditions, the combination of BrijO10 and Span80 was found to optimal for stabilizing droplets of N,N-dimethylacrylamide and N,N-dimethyl propionamide (included as a co-stabilizer) (**Figure 5.7A** and **B**).

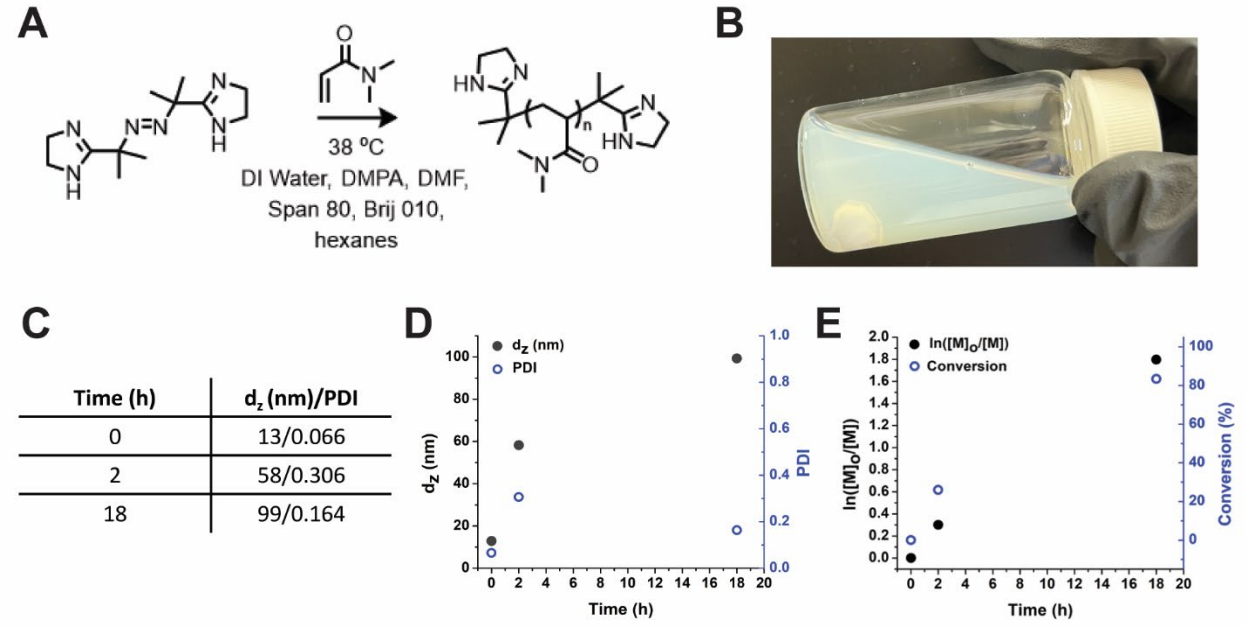

Figure 5.7 Overview of Microemulsion Polymerization

(A) Synthetic scheme for the free radical polymerization of DMA in hexanes with VA-044. (B) Photo of as prepared microemulsion. (C) Tabulated data of droplet size over time (D) DLS traces of size and PDI as polymerization progresses (E) Conversion of polymerization in time, as recorded by NMR. Data attribution: Megan Lott

5.3.1. Thermoresponsive Behavior of Microemulsions

Upon optimization of these conditions, these droplets were found to be significantly thermoresponsive (**Figure 5.8**). Above a critical temperature of 54°C, droplet diameter increases

sharply from 20 nanometers to upwards of 3 microns (**Figure 5.8A**, **B**), a change which is fully reversible upon re-cooling of the sample (**Figure 5.8C**). This change in size is the result of the temperature dependence of HLB, which dictates a surfactant's solubility in polar and nonpolar solvents.[296]

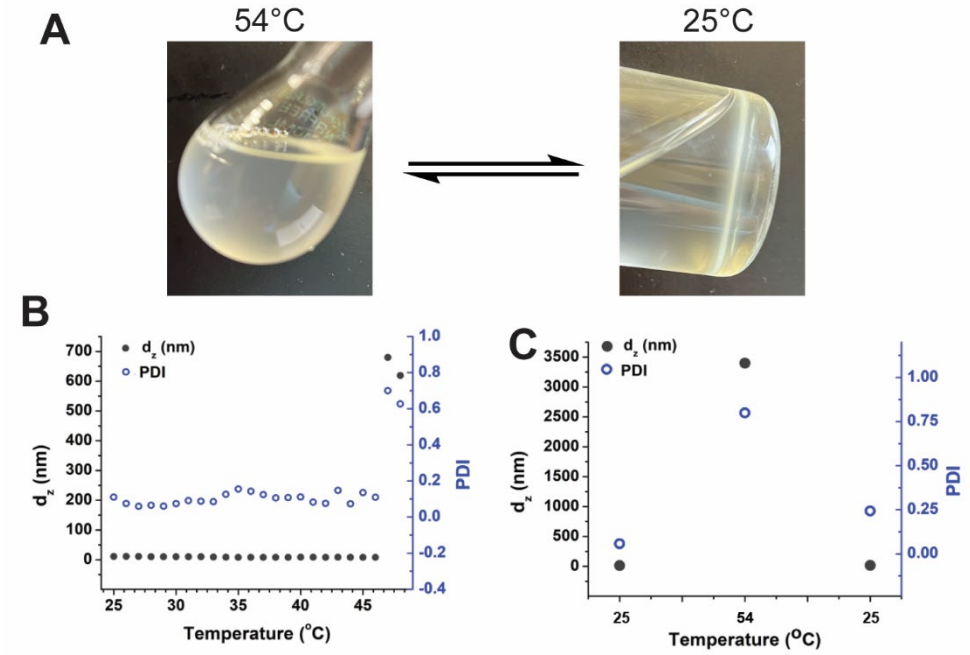

Figure 5.8 Characterization of thermoresponsive behavior of microemulsion

(A) Images of bulk microemulsion at elevated and room temperature, indicating the dispersion is reversible and stable under both conditions. (B) Identification of the critical temperature upon which size increase is observed. Droplet size and dispersity remains consistent below 48°C, and sharply increases above this point. (C) DLS indicating reversibility of droplet growth. Upon re-cooling, the droplet diameter returns to the original size, and the dispersity lowers. Data attribution: Megan Lott

To probe the thermoresponsive behavior of these materials *in situ*, we chose to formulate the microemulsion first with water, rather than DMA and DMPA, and without free radical initiator for the sake of simplicity (**Figure 5.9**). Upon imaging, few small droplets were observed – 13 nm is typically smaller than we are able to resolve in the liquid cell. The beam was blanked and the cell was heated to 54°C for 30 minutes to allow adequate time for equilibration. Upon imaging, many micron-sized water droplets were visible in the imaging area. The beam was again blanked

and the cell was allowed to cool for another 30 minutes, at which time the observed droplets were no longer visible, indicating redispersal.

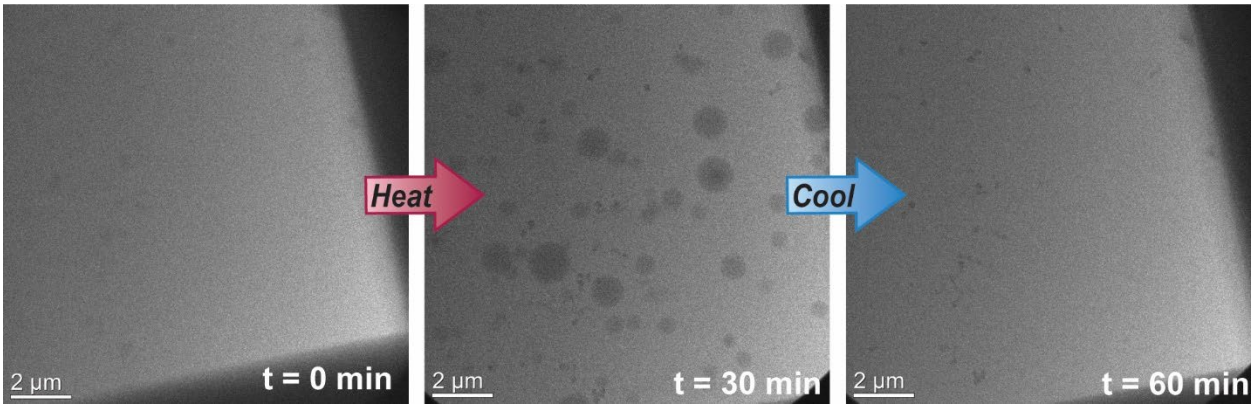

Figure 5.9 Thermoresponsive behavior of microemulsion visualized by LPTEM

Small droplets and minor debris are initially visible. The beam is then turned off, and the cell is allowed to equilibrate for 30 minutes at 54°C prior to taking the second image, in which micron sized droplets of water are visible. The cell was then cooled and allowed to equilibrate at 25°C before taking the third image, in which the water droplets have entirely redispersed.

In order to study this transition more closely, we utilized stroboscopic imaging conditions, rather than constant imaging, in order to minimize electron flux and thus reduce sample damage as much as possible. To do so, we moved to another corner of the same sample cell and imaged every 60 seconds as we heated the cell at a rate of 15°C/s (**Figure 5.10**). Once again, minimal droplets were initially observed, and droplet growth had not yet occurred as of T=43°C, corroborating the critical temperature of 48°C. Upon reaching 55°C, the cell was allowed to sit for 3 minutes at temperature to ensure full equilibration, prior to cooling at 15°C/s. The actual rate of cooling was slower, given that there is no actual cooling mechanism built into the holder – a resistive heating element is used to raise the temperature, and thermodynamics are relied upon for cooling. However, consistent droplet shrinkage was observed after the cell dropped below 44°C. Full reversal was not seen here (unlike **Figure 5.9**), and we attribute this to the cumulative fluence that this sample had received over the course of the experiment. As previously stated, **Figure 5.9**

and **Figure 5.10** were sequentially collected from the same liquid cell experiment, and so by the time of the stroboscopic imaging, the cell had been irradiated for some time, which is known to contribute to demulsification. Thus, we suspect that the low temperature droplet size had increased from the e-beam. However, the retention of their thermoresponsive behavior despite this is quite exciting, as indicates that the surfactants are likely undamaged.

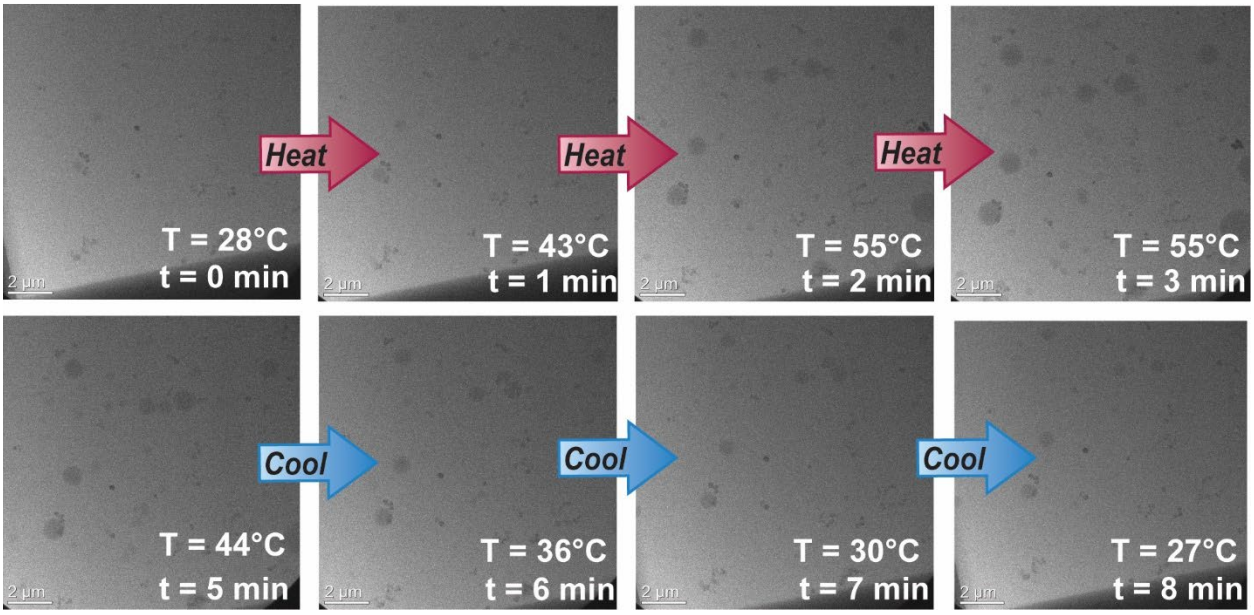

Figure 5.10 Stroboscopic imaging of thermoresponsive microemulsion during heating and cooling.

Images were taken every minute while heating the sample at a rate of 15°C/min. The sample was held at 55°C from t = 2 – 4 minutes, and then cooled at the same rate. The actual rate of cooling was slower than specified due to the resistive heating mechanism employed in the holder.

We want to emphasize that such a degree of reversibility has not been previously observed *in situ*. In studies of other thermoresponsive polymer assemblies, the structures never fully disassembled upon cooling, likely as a result of adherence to the SiN_x membrane, which prevents structural reorganization.[225] We attribute the reversibility observed here to the presence of the surfactant, which has been previously shown to diminish the strength of the interactions with the liquid cell (**Chapter 4**), thereby permitting the structures to transform freely.

5.3.2. Thermally-Initiated Free Radical Microemulsion Polymerization

Inspired by the previous successes, we then attempted to study the polymerization for which the microemulsion was optimized (**Figure 5.11**). VA-044, a water-soluble azo initiator, was chosen as the thermal initiator owing to its low activation temperature ($t_{1/2}$ = 10 hours at 44°C).[297] Due to the proximity to the aforementioned critical temperature, it was decided to run the reaction at a lower temperature (38°C) for a longer time so as to avoid the confounding influence of thermally induced changes. The reaction was prepared by dispersing the surfactants in hexanes and the monomer and co-stabilizer in water. The aqueous phases was then added dropwise to the hexanes while stirring and allowed to disperse for 15 minutes before sparging. In order to keep the reaction air free, a gas-tight syringe was flushed with nitrogen and used to purge the lines of the liquid cell before flowing in the reaction solution, imaging, and heating (**Figure 5.11A**). It was immediately noted that the monomer droplets were extraordinarily beam sensitive, and demulsified rapidly, even at extremely low electron flux (<0.01$e^-/Å^2s$). The reaction was imaged stroboscopically, with micrographs acquired every hour. At the one hour time point, extreme demulsification is noticeable, and at the two hour time point, the cell is completely phase separated – the imaged area is completely monomer, as evidenced by the increased contrast. In order to understand what the products of our reaction should look, the polymerization was run in the bulk and then imaged (**Figure 5.11B**, **C**). In a static liquid cell (**Figure 5.11B**), exceptionally low contrast droplets are barely visible at a size of approximately 1 μm. By dry state (**Figure 5.11C**), the remnants of droplets are seen at a size regime in agreement with DLS.

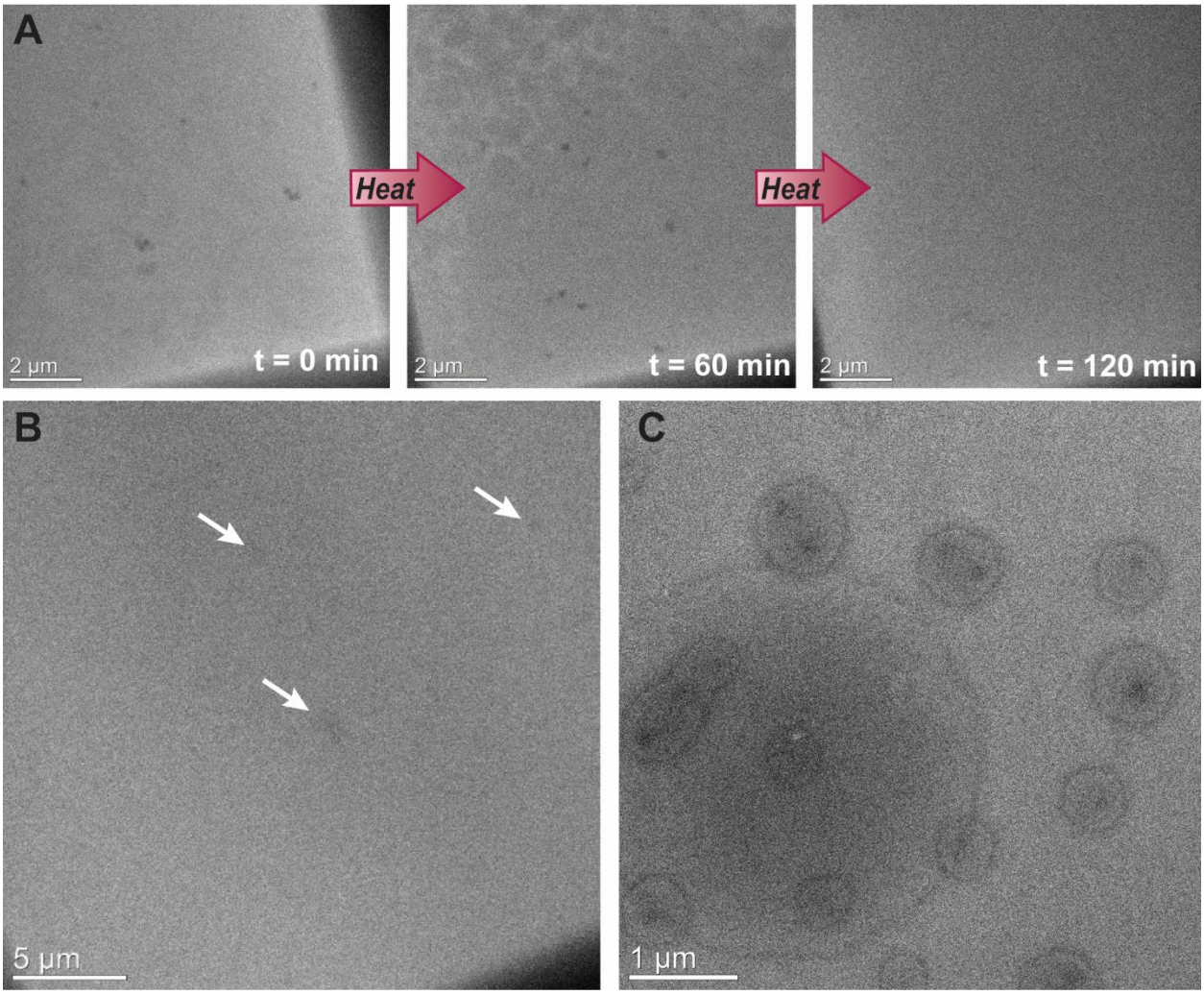

Figure 5.11 Microscopy of thermal microemulsion polymerization

(A) Time series of micrographs from *in situ* heating experiment. ~1µm droplets are visible at t = 0 minutes, and significant demulsification is observed at 60 minutes. By 120 minutes, the viewing area is completely demulsified (as evidenced by the higher contrast). (B) Static liquid cell of bulk polymerized microemulsion. Latexes are visible where indicated with arrows (C) dry state TEM of bulk polymerized microemulsions.

Unfortunately, the droplets of this monomer were prohibitively beam sensitive. The flux cannot be lowered without compromising signal, and the fluence is already minimal. Given that our interest lies in observing the process of this reaction, rather than the end product, it seems that this particular monomer is incompatible with our goal, and that a less beam-sensitive alternative must be found.

5.3.3. Study Conclusions

We were consistently able to induce and observe the stimuli-responsive behavior of temperature-sensitive microemulsions *in situ*. No droplet growth was observed below the critical temperature established by DLS, further supporting our hypothesis that this phenomenon is triggered by a change in solubility of the nonionic surfactant. This phenomenon is of interest due to significant utility of stimuli responsive microemulsions for applications in drug delivery and lubrication.[295,298] *In situ* polymer formation was consistently plagued by beam-driven emulsion instability, but the formed polymer latexes were observed. In short, the above issues seem to be attributable to the choice of monomer, and we anticipate that continued monomer screening will yield success.

5.4. Conclusions and Future Directions

We were able to repeatably form polymers *in situ via* thermal free-radical initiation, but UV polymerization proved problematic. However, the emulsion stability was not sufficient in order to permit the elucidation of mechanistic information. Studies of emulsion formulation seem to indicate that the addition of the DMA monomer significantly alters the stability of these materials with respect to the e-beam, as compared with analogous emulsions of dispersed water. It is unclear why this substitution results in such a significant change to the system's behavior – perhaps it is the result of the inherent reactivity of the monomer. Future investigations may find better results with alternate monomers or the addition of stabilizing species (dissolved salts, co-surfactants, *etc.*). Additionally, a more stable monomer may prove less troublesome for *in situ* UV polymerizations.

5.5. Supplemental Information

5.5.1. Emulsion Polymerization Details

Data regarding polymerization kinetics and conversion of DMA-based systems were collected by Megan Lott, University of Florida. Other synthetic protocols were the result of conversations with the same.

5.5.2. MALDI-IMS

MALDI-IMS data was acquired with assistance from Joanna Korpanty, Northwestern University. For DMA, the matrix employed was trans-2-[3-(4-tert-Butylphenyl)-2-methyl-2-propenylidene]malononitrile at a concentration of 10mg/mL in acetonitrile.

Chapter 6 LPTEM Characterization of Morphology and Dynamics of Industrial Materials

One of the primary goals of this thesis has been to establish the limits of LPTEM's utility – that is, to what extent may this technique be used for non-traditional materials (*e.g.*, high viscosity, non-aqueous, *etc.*). Many of these materials have great relevance as consumer products in the food, cosmetic, and household industries and beyond. To that end, partnerships with industrial research and development collaborators have been developed so as to establish the relevance of such techniques are to consumer product development. For the purposes of intellectual property protection, company names and identifying material names have not been included in this thesis.

6.1. Morphological Transitions of Liposomal Surfactant Formulations

Most commercial detergents, such as laundry soaps and dishwashing solutions, are formulated as aqueous liposomal solutions. Given that these materials are used under additional and variable dilution at the consumers' discretion, it is of significant interest to probe the relationship between concentration and structure. Such relationships may significantly impact the end performance of such products, and are thus instrumental to consider during product development and formulation.

While Company 1 has been able to evaluate structures at different concentrations via cryo-EM (**Figure 6.1**), the transition states between these remain elusive but would reveal significant mechanistic information about the nature of these morphological changes. Further, it was noted that the waiting time parameter of the sample vitrification process significantly impacted the observed morphology, indicating that some portion of the transition is shear dependent, and thus confounding the "true" nature of the liposomal morphology in solution. Thus, there is ample opportunity for LPTEM to fill in a significant knowledge gap.

This detergent has been previously characterized by cryo-EM within Company 1, which observed a change in structure size and morphology as concentration decreased from 33wt% to 0.1wt%.

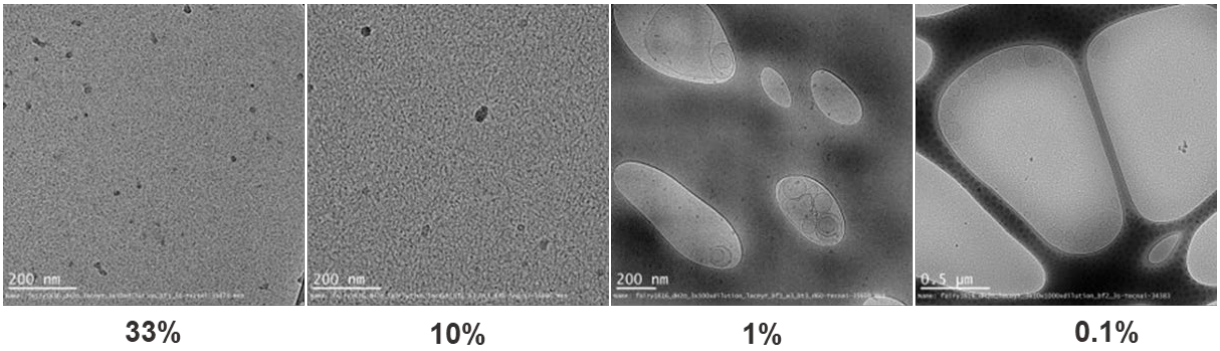

Figure 6.1 Cryo-EM of Detergent 1 at denoted concentrations in DI water**.**
Panels show morphological evolution from micelles to vesicles as a function of dilution. Image provided by Company 1 for reference, and reproduced with permission.

Namely, micelles observed at the highest concentrations grew and transformed into vesicles at lower concentrations. In addition to these findings, it was noted that the blotting parameters during vitrification had a significant impact on sample morphology within a given condition. Specifically, the parameter of waiting time (or the duration between blotting and plunging) was observed to alter the observed structure, which was hypothesized to be the result of shearing artifacts and the resulting relaxation and rearrangement of surfactant (**Figure 6.2**).

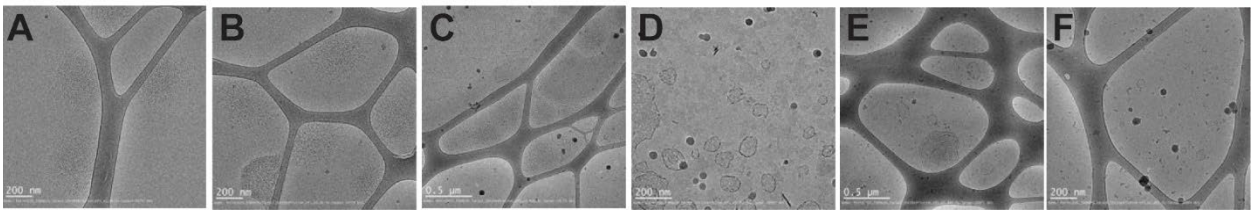

Figure 6.2 Cryo-EM of Detergent 1 as a function of waiting time during vitrification.
1wt% Detergent 1 exhibits different morphology depending on the parameter of waiting time during vitrification (A) 1 second, clustered micelles (B) 5 seconds, clustered micelles (C) 10 seconds, large vesicles(D) 30 seconds, diffuse vesicles with broken membranes (E) 45 seconds, multilamellar vesicles (F) 60 seconds, mixed phase of small vesicles and micelles. Image provided by Company 1 for reference, and reproduced with permission.

LPTEM was proposed as a way to remove these shearing sample preparation artifacts. Though the initial micelles are too small to be resolved well *in situ* (~5nm), the larger multilamellar

vesicles that were seen by cryo-EM in diluted samples are on a much more feasible length scale for observation.

In static liquid cells, the various phases can be discerned (with some difficulty) at very low contrast, despite contrast and brightness adjustments to increase ease of visibility (**Figure 6.3**).

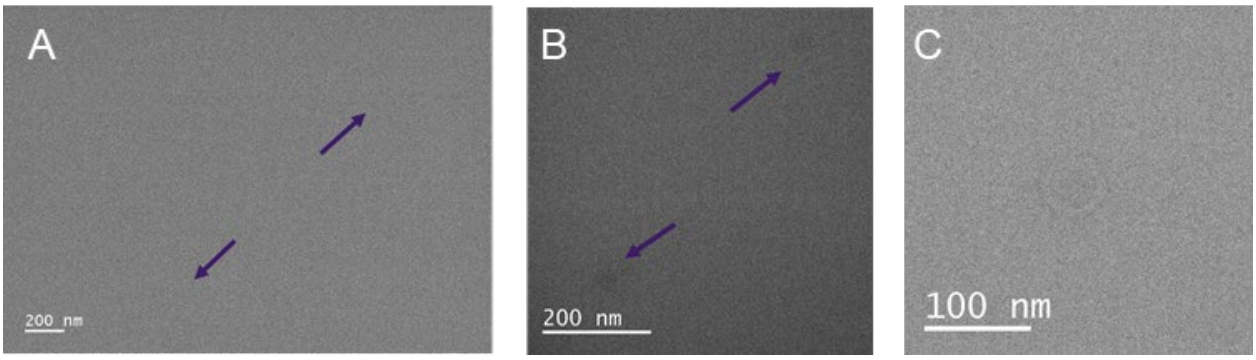

Figure 6.3 LPTEM micrographs of Detergent 1 morphology as a function of concentration.
(A) Small micelles at 33% Detergent 1, (B) larger micelles in 10% Detergent 1, and (C) vesicles in 1% Detergent 1. Arrows added to indicate structures of interest.

These structures were discerned after a significant number of attempts and non-negligible image processing, which is not promising for the hope of observing the transition between these states. Thus, in an attempt to improve visibility, a nascent staining technique using aqueous nickel(II) chloride was used.[239] The inclusion of $NiCl_2$ immediately improved contrast and allowed resolution of structures not previously visible (**Figure 6.4)**. As discussed in Gnanasekaran *et al's* publication on the technique, the structures do seem larger than previously, and this may be the result of membrane disruption from the nickel (**Figure 6.4A**, **B**). Further, it's possible to see what

appear to be substructures within larger vesicles (**Figure 6.4C**), which may give clues as to the mechanism of multilamellar vesicle formation as the solution progresses.

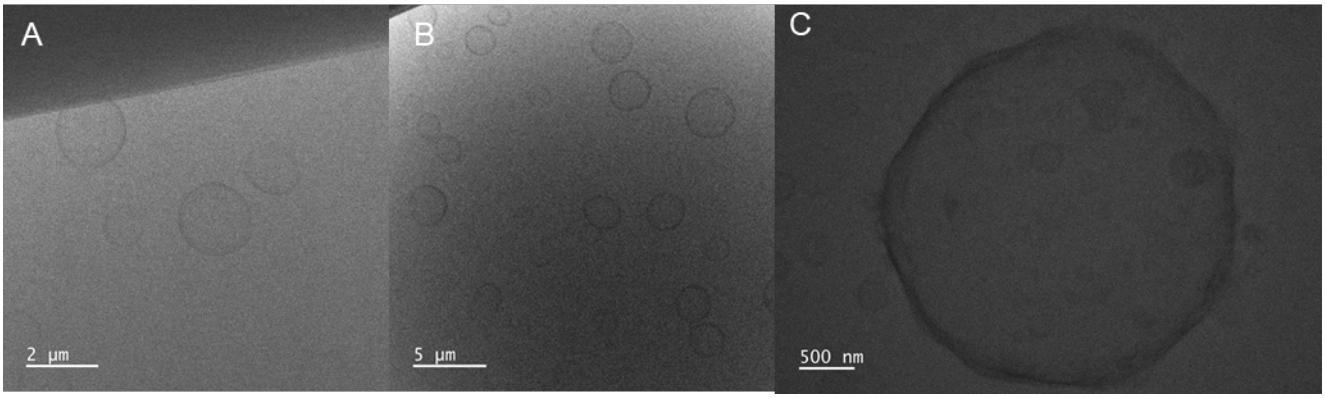

Figure 6.4 10% Detergent 1 diluted with 15mM $NiCl_2$
Images at initial irradiation (A), following extended irradiation (B+C)

In order to work towards watching these transformations *in situ*, the microfluidic capability of the liquid cell holders was used, and diluent was pushed through a cell loaded with a higher concentration of Detergent 1 (33%). However, since damage had previously been observed in static samples after extended imaging periods, 'pulsed' imaging was used (*i.e.*, the beam was only turned on to image at specific intervals). In the purely aqueous system, almost no vesicle growth is observed (**Figure 6.5**). Notably, the structures visible at 33% are much larger than anticipated for the aforementioned micelles (expected to be ~5nm) and may thus be the result of contamination.

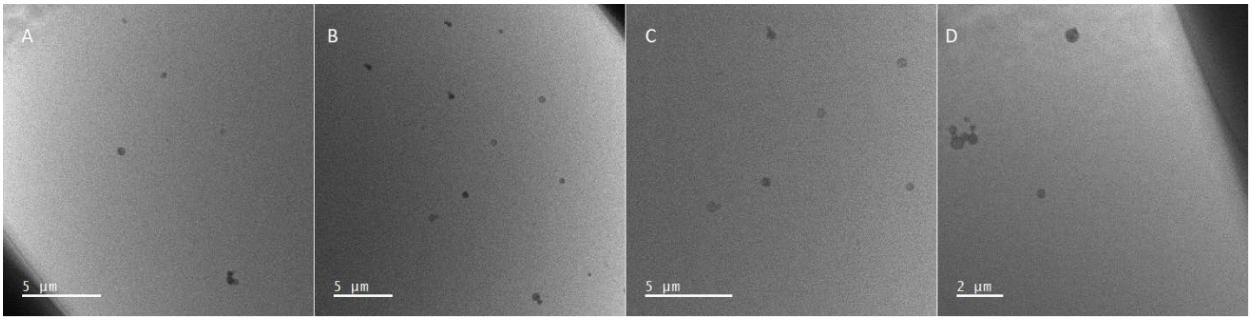

Figure 6.5 33% Detergent 1 diluted with deionized water at a rate of 5µl/minute

(A) t = 0 minutes, (B) t = 10 minutes, (C) t = 20 minutes, (D) t = 30 minutes.

If $NiCl_2$ is added (**Figure 6.6**), while the same anomalous initial structures are visible, the deposition of the Ni^{2+} on the membranes of the structures quickly renders them visible, enabling the visualization of growth between 2 and 15 minutes. After this time, the structures have dissociated, and this is potentially attributable to two things: destabilization by the nickel, or beam damage.

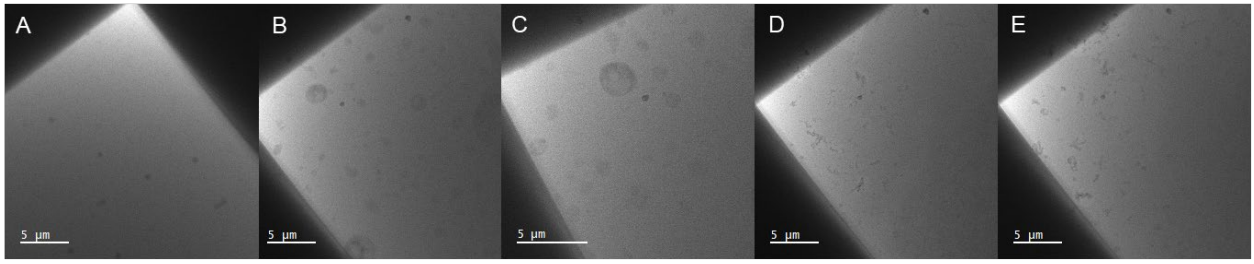

Figure 6.6 33% Detergent 1 diluted with 15mM NiCl2 at a rate of 5 µl/min

(A) t = 0 minutes, (B) t = 2 minutes, (C) t = 15 minutes, (D) t = 20 minutes, (E) t = 30 minutes

6.1.1. Study Conclusions

Here, we were able to evaluate morphology and evolution of such a high viscosity commercial detergent as a function of concentration. This series of experiments was concluded due to shifting corporate interests, but this material is a good proof of concept for being able to observe the high viscosity materials, *in situ* morphological evolution, and the expanding utility of staining techniques. Further, we were able to perform this study without the confounding variables introduced during vitrification

6.2. Fragrance Encapsulation *via* Interfacial Polymerization in Pickering Emulsions

The other system of significant interest to Company 1 was an encapsulation process used to entrap a fragrant oil within a silica shell for the purposes of delayed release with applications to home laundering. This is accomplished by first forming a Pickering emulsion of fragrance in water stabilized by silica microparticles, which then polymerize and harden into a solid shell over time in the presence of silicic acid and heat (**Figure 6.7**). Here, silicic acid (or PEOS) (**Figure 6.7A**) is dispersed in the oil phase, which is emulsified in water *via* silica before heating to 90°C to generate a silica shell (**Figure 6.7B**). As written by Company 1, the protocol yields capsules on the order of 50μm in diameter, which is too large for study by LPTEM as it exceeds the z dimension of the SiN_x cell. Thus, in order to monitor the formation of these capsules, it was necessary to decrease the oil:water ratio (that is, reduce the amount of dispersed phase) while maintaining the silica concentration in order to generate sufficiently small droplets for study *in situ.* Additionally, these materials are not able to be studied *via* conventional TEM – as formulated, they exceed the appropriate size regime. However, even after scaling the droplets to an appropriate size, the effects of drying and subjection to vacuum were too damaging, and no structures were ever observed. CryoSEM was suggested to Company 1 for higher resolution structural study of the formed capsules, but even such methods would not permit the study of the formation of these materials.

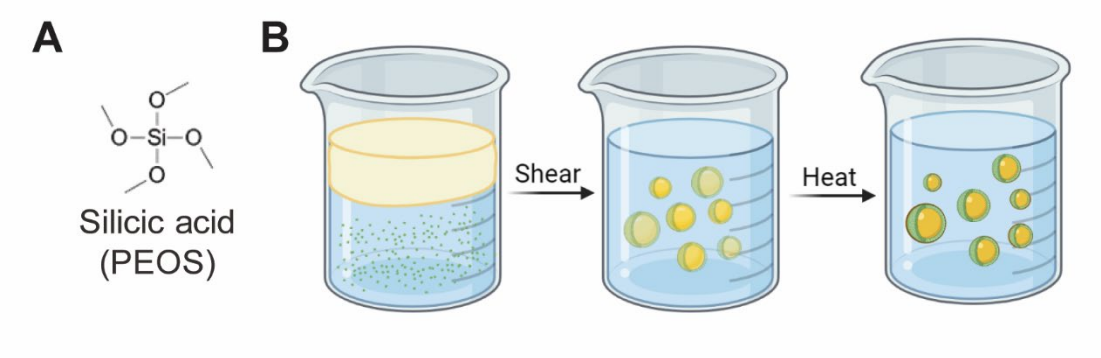

Figure 6.7 Schematic representation of synthetic scheme for System 2.

(A) Structure of silicic acid (also known as PEOS), which facilitates the capsule solidification (B) Process for preparing System 2, where PEOS is dispersed in oil and silica is dispersed in water, before emulsifying via shear and heating to initiate reaction. Figure created with BioRender.

This solution was loaded into the liquid cell and heated to 90°C to observe capsule formation (**Figure 6.8**). Prior to heating, heterogeneity of the sample is observed (t = 0 minutes), indicating successful dispersal and formation of the initial Pickering emulsion. Upon subsequent heating, the development of high contrast spherical particles is observed (30 and 60 minute micrographs). Sustained heating eventually caused the liquid cell to dewet (t = 75 minutes), which revealed the hollow nature of the capsules, as predicted.

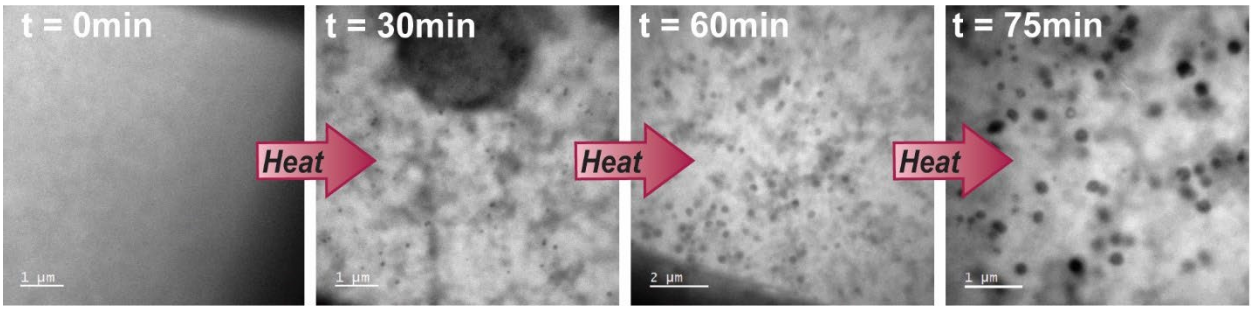

Figure 6.8 Sequential micrographs of *in situ* heating experiment of System 2

From left to right, we start with the dispersion previously described before heating to 90°C for the duration of the experiment. The images at 30, 60, and 75 minutes show the development of spherical capsules whose hollow nature is visible in the later timepoints. It is noteworthy that the t=75min micrograph shows a dewetted cell, increasing contrast.

We were able to repeatably form these materials *in situ* at a variety of experimental concentrations (**Figure 6.9**), though evidently, the results are not the most reproducible. We found time to be quite an important factor, as the system would demulsify if left for a period of time (**Figure 6.9D**)

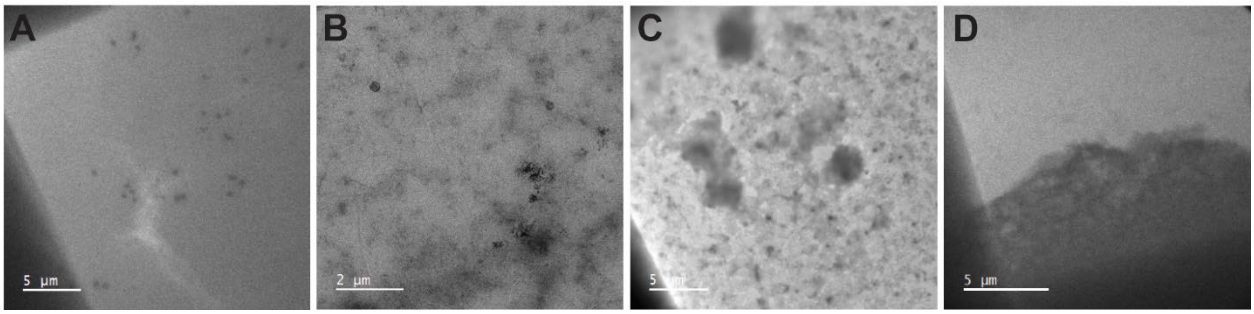

Figure 6.9 LPTEM experiments to form silica capsules

(A) Dilute LC of silica capsules (B) Concentrated LC of silica capsules (C) dried LC of silica capsules (D) phase separated LC, which still formed capsules

6.2.1. Study Conclusions

Silica capsules were successfully formed at the interface of a dispersion of fragrance in water upon *in situ* heating, and we were able to demonstrate the application of this technique successfully to commercial materials. This marks a successful observation of not only a Pickering emulsion, but also of interfacial polymerization in real time. The formed structures were hollow, confirming that this reaction was confined to the surfactant silica particles at the oil-water interface. Despite our success, changing commercial interests shifted focus away from this system and to other materials of interest to Company 1, and thus this study was concluded.

6.3. Demulsification of Residual Water in Natural Gas Condensates

Company 2 reached out to the Gianneschi lab following the publication of our article on demulsification (the subject of **Chapter 2**) with the goal of observing such processes during crude oil refinement. When extracted, natural gas condensate has a significant quantity of debris and

contamination which must be removed and purified for reasons not only of performance, but also of transportation efficiency. Much of the particulate matter can be separated via filtration, but aqueous impurities are significantly more complicated to remove due to the presence of naturally occurring asphaltenes, which act as surfactants to stabilize the oil-water interface.[31,299] There are several methods to remove water from the crude, including centrifugation and electrostatic separation, but chemical demulsification is the most cost effective and thus the most commonly used. To remove the water, the emulsion is broken by adding a demulsifier, or an oil-soluble non-ionic surfactant which is dispersible in water.[299] However, demulsifier chemistry is not well understood has not advanced significantly in several decades, likely due to the difficulty in studying such high viscosity, impure materials under relatively extreme processing conditions. There is significant interest in developing greener, more efficient demulsifiers, as those currently in use have significant ecological impacts when used to mitigate oil spills and other environmental contaminations.

LPTEM was successfully used to evaluate not only material morphology, but to also probe the effects of adding Company 2's proprietary demulsifier. (**Figure 6.10**). It was first confirmed that the emulsion morphology of the dispersed crude oil was visible in a static liquid cell after redispersal (**Figure 6.10A**). Here, the natural gas condensate is evident as the lower contrast continuous phase, while water and other impurities are visible as higher contrast droplets and aggregates. After the emulsifier is added, droplet motion is visible, and the droplets clearly migrate towards the center of the cell (**Figure 6.10B**, **Video 6.1**). This is confirmed when the continuous phase is displaced from the cell, leaving only the separated aqueous phase. This is seen droplet at the center of the cell, with smaller water droplets radially arrayed on their way to merge with the large droplet (**Figure 6.10C**).

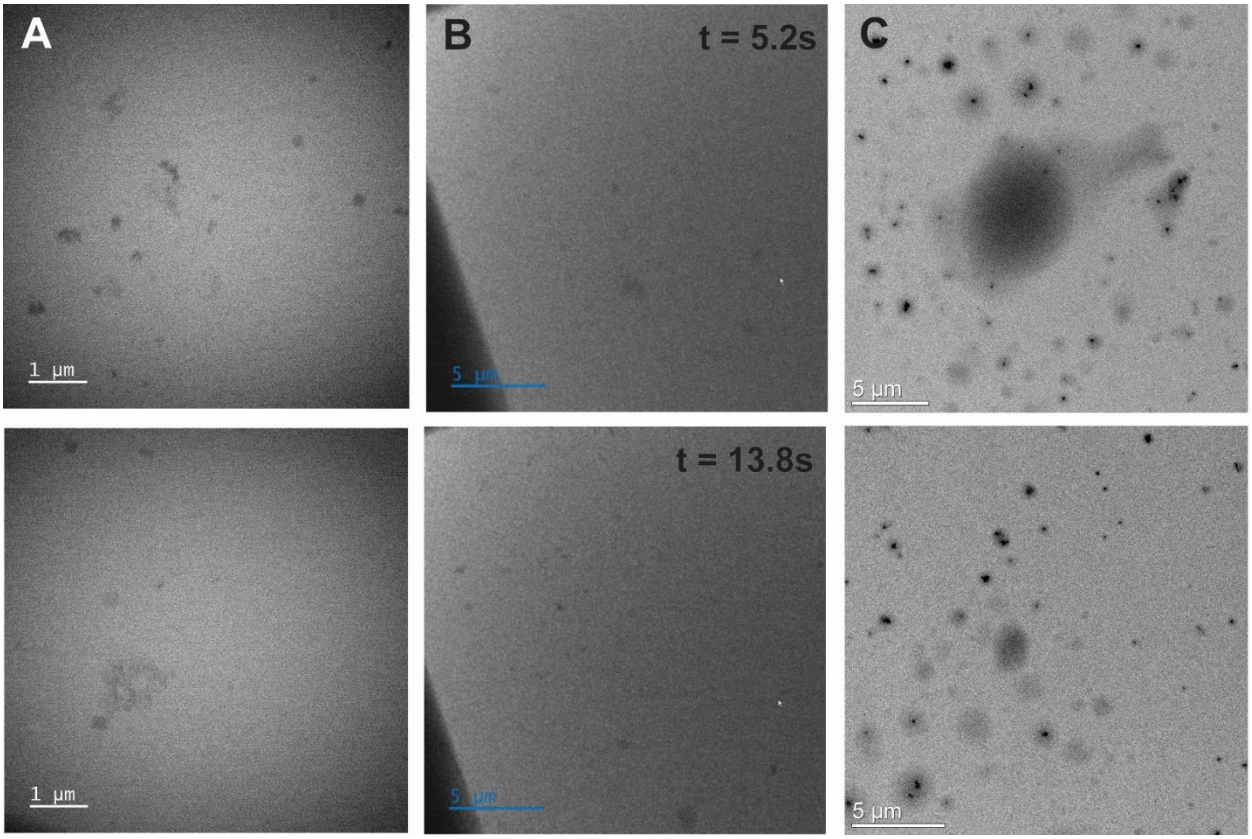

Figure 6.10 Company 2 Material Overview
(A) Morphology of redispersed emulsion. Droplets here are static and do not move. (B) Emulsion after addition of proprietary demulsifier, which exhibit significant motion. Panels show displacement of several features of interest. (C) De-wetted cell after addition of demulsifier, showing separation of aqueous phase to the center of the cell.

This presents the first *in situ* observation of such processes, which are of tremendous commercial and ecological interest.[299–301] We anticipate that such techniques will be used in the future to screen the efficacies of demulsifiers, and that further analysis of the observed droplet motion may correlate to speed of demulsification. Such studies will permit the establishment of increased understand structure-function relationships of chemical demulsifiers under realistic conditions of use.

6.4. Supplemental Materials

6.4.1. Videographic Data

Video 6.1: Videographic data of emulsion mobility upon addition of demulsifier, played at 5x speed.

Chapter 7 Future Perspectives and Directions

Here, we have described the *in situ* characterization of morphology, formation, and dynamics of heterogeneous soft matter systems as elucidated *via* liquid phase transmission electron microscopy. In this thesis, we have been able to routinely and consistently observe and quantify emulsion morphology and demulsification, and have shown such results to be consistent with those obtained by correlative methods (**Chapter 2**). Further, we have also been able to induce the formation of these materials via various mechanisms, and monitor their evolution in time **(Chapter 3**). and monitor their response to stimuli. We have shown emulsions to have unprecedented degrees of mobility *in situ*, and have performed a rigorous analysis of motion within the liquid cell (**Chapter 4**). We have also made significant steps towards imaging processes of emulsion polymerization (**Chapter 5**), and anticipate that future work in this area will be very fruitful. Finally, we have shown the utility of LPTEM in imaging materials of this class for commercial applications, such as the formation of interfacial silica capsules and the demulsification of crude oil (**Chapter 6**). In summary, this work represents a thorough analysis of phase-separated soft materials with a consistent view towards commercial application of such materials. Direct observation of these systems on this length scale has not previously been possible without complex fixation processes, and never in their native states. Here, we have presented quantitative studies of emulsion dynamics and demulsification *via* LPTEM.

We have methodically demonstrated the broad and continued utility of emulsions as a material for study in the field of LPTEM. The modularity inherent to these systems – namely, the degree of contrast between phases and the size of the dispersed droplets – is instrumental to their successful study in LPTEM, as these parameters can be tuned to suit each experiment through material selection. As a result, emulsions consistently have phenomenal, and tunable, contrast. We

additionally attribute the exceptional *in situ* mobility of these materials to the presence of the surfactant interface, which reduces adhesion to the SiN_x windows.

In the future, we anticipate that these materials will be the subject of continued study, particularly as microreactors. Many works in the field of LPTEM cite the confinement of the liquid cell as a limitation and hindrance to observing dynamic processes and reactions. However, emulsions are commonly used on the benchtop to create highly defined and monodisperse nanomaterials by confining reagents to a droplet of determined size. We suggest that this is exactly what makes such processes ideal for observation by LPTEM – by defining the degree of confinement *a priori* through the emulsion droplet, the variable constraint imposed by the SiN_x membrane is effectively mitigated. Thus, we anticipate that such confinement will hold similar benefit for *in situ* materials formation. We hypothesize that emulsion polymerization processes will be a particularly rich area of study going forward. We have detailed here initial efforts to observe such processes with varying degrees of success, but such work would benefit from further study and material optimization. We posit that mechanisms of emulsion polymerization can be gleaned from direct observation in ways that can confirm findings from previous indirect studies. Organogels are another promising class of materials that are fabricated from emulsions and have the potential to shed light on gel assembly and formation. Further, our multifaceted capabilities to confirm the chemical integrity of our reagents and the resulting polymer have been demonstrated, and we contend that such practices are critical to the studies outlined above and those undertaken in the future to confirm that results are not the result of e-beam induced damage and that the desired species are indeed formed.

Ultimately, the majority of this work presented in this thesis stemmed from efforts to watch polymeric nanoparticles move *in situ*, which never yielded fruitful results. Out of

frustration, we turned our attention to studying other materials which are essentially unimageable by other methods (here, reverse emulsions). By serendipity, these studies eventually yielded the results we were hoping for in the initial systems, which is really a testament to persistence and the idea that experiments work when you least expect them to.

Chapter 8 References

(1) Acevedo-Fani, A.; Singh, H. Biophysical Insights into Modulating Lipid Digestion in Food Emulsions. *Prog Lipid Res* **2022**, *85*, 101129. https://doi.org/10.1016/J.PLIPRES.2021.101129.

(2) McClements, D. J. Critical Review of Techniques and Methodologies for Characterization of Emulsion Stability. *Crit Rev Food Sci Nutr* **2007**, *47* (7), 611–649. https://doi.org/10.1080/10408390701289292.

(3) Egger, H.; McGrath, K. M. Aging of Oil-in-Water Emulsions: The Role of the Oil. *J Colloid Interface Sci* **2006**, *299* (2), 890–899. https://doi.org/10.1016/j.jcis.2006.03.022.

(4) Dalgleish, D. G.; West, S. J.; Hallett, F. R. The Characterization of Small Emulsion Droplets Made from Milk Proteins and Triglyceride Oil. *Colloids Surf A Physicochem Eng Asp* **1997**, *123–124*, 145–153. https://doi.org/10.1016/S0927-7757(97)03783-7.

(5) Vratsanos, M. A.; Gianneschi, N. C. Direct Observation of Emulsion Morphology, Dynamics, and Demulsification. *ACS Nano* **2022**, acsnano.2c00199. https://doi.org/10.1021/ACSNANO.2C00199.

(6) Vratsanos, M. A.; Xue, W.; Rosenmann, N. D.; Zarzar, L. D.; Gianneschi, N. C. Ouzo Effect Examined at the Nanoscale via Direct Observation of Droplet Nucleation and Morphology. *ACS Cent Sci* **2023**, *9* (3), 457–465. https://doi.org/10.1021/acscentsci.2c01194.

(7) Mikula, R. J. Emulsion Characterization. **1992**, 79–129. https://doi.org/10.1021/BA-1992-0231.CH003.

(8) Hu, Y. T.; Ting, Y.; Hu, J. Y.; Hsieh, S. C. Techniques and Methods to Study Functional Characteristics of Emulsion Systems. *J Food Drug Anal* **2017**, *25* (1), 16–26. https://doi.org/10.1016/J.JFDA.2016.10.021.

(9) Stetefeld, J.; McKenna, S. A.; Patel, T. R. Dynamic Light Scattering: A Practical Guide and Applications in Biomedical Sciences. *Biophys Rev* **2016**, *8* (4), 409–427. https://doi.org/10.1007/S12551-016-0218-6/FIGURES/1.

(10) Goldburg, W. I. Dynamic Light Scattering. *Am J Phys* **1999**, *67* (12), 1152. https://doi.org/10.1119/1.19101.

(11) Lombardo, D.; Calandra, P.; Kiselev, M. A. Structural Characterization of Biomaterials by Means of Small Angle X-Rays and Neutron Scattering (SAXS and SANS), and Light Scattering Experiments. *Molecules 2020, Vol. 25, Page 5624* **2020**, *25* (23), 5624. https://doi.org/10.3390/MOLECULES25235624.

(12) Schmitt, V.; Leal-Calderon, F. Measurement of the Coalescence Frequency in Surfactant-Stabilized Concentrated Emulsions. *Europhys Lett* **2004**, *67* (4), 662–668. https://doi.org/10.1209/epl/i2004-10100-3.

(13) Filipe, V.; Hawe, A.; Jiskoot, W. Critical Evaluation of Nanoparticle Tracking Analysis (NTA) by NanoSight for the Measurement of Nanoparticles and Protein Aggregates. *Pharm Res* **2010**, *27* (5), 796–810. https://doi.org/10.1007/S11095-010-0073-2/TABLES/4.

(14) Porras, M.; Solans, C.; González, C.; Martínez, A.; Guinart, A.; Gutiérrez, J. M. Studies of Formation of W/O Nano-Emulsions. *Colloids Surf A Physicochem Eng Asp* **2004**, *249* (1–3), 115–118. https://doi.org/10.1016/j.colsurfa.2004.08.060.

(15) Koroleva, M. Yu.; Yurtov, E. V. Ostwald Ripening in Macro- and Nanoemulsions. *Russian Chemical Reviews* **2021**, *90* (3), 293–323. https://doi.org/10.1070/rcr4962.

(16) Rodriguez-Lopez, G.; O'Neil Williams, Y.; Toro-Mendoza, J.; Williams, Y. O.; Toro-Mendoza, J. Individual and Collective Behavior of Emulsion Droplets Undergoing Ostwald Ripening. *Langmuir* **2019**, *35* (15), 5316–5323. https://doi.org/10.1021/ACS.LANGMUIR.8B03959.

(17) Taylor, P. Ostwald Ripening in Emulsions. *Adv Colloid Interface Sci* **1998**, *75* (2), 107–163. https://doi.org/10.1016/S0001-8686(98)00035-9.

(18) Gabriele, D.; Migliori, M.; Di Sanzo, R.; Rossi, C. O.; Ruffolo, S. A.; de Cindio, B. Characterisation of Dairy Emulsions by NMR and Rheological Techniques. *Food Hydrocoll* **2009**, *23* (3), 619–628. https://doi.org/10.1016/J.FOODHYD.2008.05.002.

(19) Santos, J.; Calero, N.; Trujillo-Cayado, L. A.; Garcia, M. C.; Muñoz, J. Assessing Differences between Ostwald Ripening and Coalescence by Rheology, Laser Diffraction and Multiple Light Scattering. *Colloids Surf B Biointerfaces* **2017**, *159*, 405–411. https://doi.org/10.1016/j.colsurfb.2017.08.015.

(20) Chu, B.; Hsiao, B. S. Small-Angle X-Ray Scattering of Polymers. *Chem Rev* **2001**, *101* (6), 1727–1761. https://doi.org/10.1021/CR9900376/ASSET/IMAGES/LARGE/CR9900376F00024.JPEG.

(21) Sunaina; Mehta, S. K.; Ganguli, A. K.; Vaidya, S. Small-Angle X-Ray Scattering as an Effective Tool to Understand the Structure and Rigidity of the Reverse Micelles with the Variation of Surfactant. *J Mol Liq* **2021**, *326*, 115302. https://doi.org/10.1016/J.MOLLIQ.2021.115302.

(22) Sommer, C.; Deen, G. R.; Pedersen, J. S.; Strunz, P.; Garamus, V. M. Microemulsion Droplets Decorated by Brij700 Block Copolymer: Phase Behavior and Structural Investigation by SAXS and SANS. *Langmuir* **2007**, *23* (12), 6544–6553. https://doi.org/10.1021/LA070181J/ASSET/IMAGES/LARGE/LA070181JF00007.JPEG.

(23) Li, T.; Senesi, A. J.; Lee, B. Small Angle X-Ray Scattering for Nanoparticle Research. *Chem Rev* **2016**, *116* (18), 11128–11180. https://doi.org/10.1021/ACS.CHEMREV.5B00690/ASSET/IMAGES/CR-2015-00690Z_M060.GIF.

(24) Czajka, A.; Armes, S. P. Time-Resolved Small-Angle X-Ray Scattering Studies during Aqueous Emulsion Polymerization. *J Am Chem Soc* **2021**, *143* (3), 1474–1484. https://doi.org/10.1021/JACS.0C11183.

(25) Czajka, A.; Liao, G.; Mykhaylyk, O. O.; Armes, S. P. In Situ Small-Angle X-Ray Scattering Studies during the Formation of Polymer/Silica Nanocomposite Particles in Aqueous Solution †. **2021**. https://doi.org/10.1039/d1sc03353k.

(26) Ballauff, M. SAXS and SANS Studies of Polymer Colloids. *Current Opinion in Colloid and Interface Science*. 2001. https://doi.org/10.1016/S1359-0294(01)00072-3.

(27) Wei, Y.; Hore, M. J. A. Characterizing Polymer Structure with Small-Angle Neutron Scattering: A Tutorial. *J Appl Phys* **2021**, *129* (17), 171101. https://doi.org/10.1063/5.0045841.

(28) Zemb, T.; Diat, O. What Can We Learn from Combined SAXS and SANS Measurements of the Same Sample Containing Surfactants? *J Phys Conf Ser* **2010**, *247* (1), 012002. https://doi.org/10.1088/1742-6596/247/1/012002.

(29) Chen, S. H.; Chang, S. L.; Strey, R.; Samseth, J.; Mortensen, K. Structural Evolution of Bicontinuous Microemulsions. *J Phys Chem* **1991**, *95* (19), 7427–7432. https://doi.org/10.1021/j100172a058.

(30) Zemb, T. N.; Klossek, M.; Lopian, T.; Marcus, J.; Schöettl, S.; Horinek, D.; Prevost, S. F.; Touraud, D.; Diat, O.; Marčelja, S.; Kunz, W. How to Explain Microemulsions Formed by Solvent Mixtures without Conventional Surfactants. *Proc Natl Acad Sci U S A* **2016**, *113* (16), 4260–4265. https://doi.org/10.1073/PNAS.1515708113/SUPPL_FILE/PNAS.201515708SI.PDF.

(31) Alvarez, G.; Jestin, J.; Argillier, J. F.; Langevin, D. Small-Angle Neutron Scattering Study of Crude Oil Emulsions: Structure of the Oil - Water Interfaces. *Langmuir* **2009**, *25* (7), 3985–3990. https://doi.org/10.1021/LA802736C/ASSET/IMAGES/LARGE/LA-2008-02736C_0006.JPEG.

(32) Schmiele, M.; Busch, S.; Morhenn, H.; Schindler, T.; Schmutzler, T.; Schweins, R.; Lindner, P.; Boesecke, P.; Westermann, M.; Steiniger, F.; Funari, S. S.; Unruh, T. Structural Characterization of Lecithin-Stabilized Tetracosane Lipid Nanoparticles. Part I: Emulsions. *Journal of Physical Chemistry B* **2016**, *120* (24), 5505–5512. https://doi.org/10.1021/ACS.JPCB.6B02519/ASSET/IMAGES/LARGE/JP-2016-02519G_0005.JPEG.

(33) Rekvig, L.; Frenkel, D. Molecular Simulations of Droplet Coalescence in Oil/Water/Surfactant Systems. *Journal of Chemical Physics* **2007**, *127* (13), 4423. https://doi.org/10.1063/1.2780865.

(34) Venugopal, A.; Ruiz-Perez, L.; Swamynathan, K.; Kulkarni, C.; Calo, A.; Kumar, M.; Calò, A. Caught in Action: Visualizing Dynamic Nanostructures Within Supramolecular Systems Chemistry. *Angewandte Chemie International Edition* **2022**. https://doi.org/10.1002/ANIE.202208681.

(35) Zhao, L.; Choi, P. Molecular Dynamics Simulation of the Coalescence of Nanometer-Sized Water Droplets in n-Heptane. *J Chem Phys* **2004**, *120* (4), 1935. https://doi.org/10.1063/1.1635804.

(36) Niu, Y.; Liu, Y.; Liu, H.; Hu, Y. Time-dependent Density Functional Study for Nanodroplet Coalescence. *AIChE Journal* **2020**, *66* (2), e16810. https://doi.org/10.1002/aic.16810.

(37) Schöttl, S.; Marcus, J.; Diat, O.; Touraud, D.; Kunz, W.; Zemb, T.; Horinek, D. Emergence of Surfactant-Free Micelles from Ternary Solutions. *Chem Sci* **2014**, *5* (8), 2949–2954. https://doi.org/10.1039/C4SC00153B.

(38) Schöttl, S.; Horinek, D. Aggregation in Detergent-Free Ternary Mixtures with Microemulsion-like Properties. *Curr Opin Colloid Interface Sci* **2016**, *22*, 8–13. https://doi.org/10.1016/J.COCIS.2016.02.003.

(39) Schöttl, S.; Lopian, T.; Prévost, S.; Touraud, D.; Grillo, I.; Diat, O.; Zemb, T.; Horinek, D. Combined Molecular Dynamics (MD) and Small Angle Scattering (SAS) Analysis of Organization on a Nanometer-Scale in Ternary Solvent Solutions Containing a Hydrotrope. *J Colloid Interface Sci* **2019**, *540*, 623–633. https://doi.org/10.1016/J.JCIS.2019.01.037.

(40) Skartlien, R.; Sollum, E.; Akselsen, A.; Meakin, P. Direct Numerical Simulation of Surfactant-Stabilized Emulsions: Morphology and Shear Viscosity in Starting Shear Flow. *Rheol Acta* **2012**, *51* (7), 649–673. https://doi.org/10.1007/S00397-012-0628-8/FIGURES/18.

(41) Low, L. E.; Siva, S. P.; Ho, Y. K.; Chan, E. S.; Tey, B. T. Recent Advances of Characterization Techniques for the Formation, Physical Properties and Stability of Pickering Emulsion. *Adv Colloid Interface Sci* **2020**, *277*, 102117. https://doi.org/10.1016/j.cis.2020.102117.

(42) deMan, J. M. Microscopy in the Study of Fats and Emulsions. *Food Microstructure* **1982**, *1* (2).

(43) Zarzar, L. D.; Sresht, V.; Sletten, E. M.; Kalow, J. A.; Blankschtein, D.; Swager, T. M. Dynamically Reconfigurable Complex Emulsions via Tunable Interfacial Tensions. *Nature* **2015**, *518* (7540), 520–524. https://doi.org/10.1038/nature14168.

(44) Hu, Q. Z.; Jang, C. H. A New Strategy for Imaging Biomolecular Events through Interactions between Liquid Crystals and Oil-in-Water Emulsions. *Analyst* **2012**, *137* (22), 5204–5207. https://doi.org/10.1039/C2AN35607D.

(45) Jabermoradi, A.; Yang, S.; Gobes, M. I.; Van Duynhoven, J. P. M.; Hohlbein, J. Enabling Single-Molecule Localization Microscopy in Turbid Food Emulsions. *Philosophical Transactions of the Royal Society A* **2022**, *380* (2220). https://doi.org/10.1098/RSTA.2020.0164.

(46) Williams, D. B.; Carter, C. B. The Transmission Electron Microscope. In *Transmission Electron Microscopy*; Springer US: Boston, MA, 2009; pp 3–22. https://doi.org/10.1007/978-0-387-76501-3_1.

(47) Vernon-Parry, K. D. Scanning Electron Microscopy: An Introduction. *III-Vs Review* **2000**, *13* (4), 40–44. https://doi.org/10.1016/S0961-1290(00)80006-X.

(48) Inkson, B. J. Scanning Electron Microscopy (SEM) and Transmission Electron Microscopy (TEM) for Materials Characterization. *Materials Characterization Using Nondestructive Evaluation (NDE) Methods* **2016**, 17–43. https://doi.org/10.1016/B978-0-08-100040-3.00002-X.

(49) Mathews, R. G.; Donald, A. M. Conditions for Imaging Emulsions in the Environmental Scanning Electron Microscope. *Scanning* **2002**, *24* (2), 75–85. https://doi.org/10.1002/SCA.4950240205.

(50) Stokes, D. J.; Thiel, B. L.; Donald, A. M. Direct Observation of Water-Oil Emulsion Systems in the Liquid State by Environmental Scanning Electron Microscopy. *Langmuir* **1998**, *14* (16), 4402–4408. https://doi.org/10.1021/LA980281C/ASSET/IMAGES/LARGE/LA980281CF00011.JPEG.

(51) Senden, T. J.; Drummond, C. J.; Kékicheff, P. Atomic Force Microscopy: Imaging with Electrical Double Layer Interactions. *Langmuir* **1994**, *10* (2), 358–362. https://doi.org/10.1021/LA00014A004/ASSET/LA00014A004.FP.PNG_V03.

(52) Ho, T. M.; Abik, F.; Mikkonen, K. S. An Overview of Nanoemulsion Characterization *via* Atomic Force Microscopy. *Crit Rev Food Sci Nutr* **2022**, *62* (18), 4908–4928. https://doi.org/10.1080/10408398.2021.1879727.

(53) Yang, H.; Wang, Y.; Lai, S.; An, H.; Li, Y.; Chen, F. Application of Atomic Force Microscopy as a Nanotechnology Tool in Food Science. *J Food Sci* **2007**, *72* (4), R65–R75. https://doi.org/10.1111/j.1750-3841.2007.00346.x.

(54) Shi, C.; Zhang, L.; Xie, L.; Lu, X.; Liu, Q.; Mantilla, C. A.; Van Den Berg, F. G. A.; Zeng, H. Interaction Mechanism of Oil-in-Water Emulsions with Asphaltenes Determined Using Droplet Probe AFM. *Langmuir* **2016**, *32* (10), 2302–2310. https://doi.org/10.1021/ACS.LANGMUIR.5B04392/ASSET/IMAGES/LARGE/LA-2015-043923_0008.JPEG.

(55) Gunning, A. P.; Mackie, A. R.; Wilde, P. J.; Morris, V. J. Atomic Force Microscopy of Emulsion Droplets: Probing Droplet-Droplet Interactions. **2004**. https://doi.org/10.1021/la034835+.

(56) Martin, J. M.; Mansot, J.-L.; Hallouis, M.; Tenailleau, H. High Resolution Electron Spectroscopic Imaging (ESI) of Reverse Micelles. *Microscopy Microanalysis Microstructures* **1990**, *1* (2), 93–102. https://doi.org/10.1051/MMM:019900010209300.

(57) Kumar, V. V.; Kumar, C.; Raghunathan, P. Studies on Lecithin Reverse Micelles: Optical Birefringence, Viscosity, Light Scattering, Electrical Conductivity, and Electron Microscopy. *J Colloid Interface Sci* **1984**, *99* (2), 315–323. https://doi.org/10.1016/0021-9797(84)90118-8.

(58) Martin, J. M.; Mansot, J. L.; Hallouis, M. Energy Filtered Electron Microscopy (EFEM) of Overbased Reverse Micelles. *Ultramicroscopy* **1989**, *30* (3), 321–328. https://doi.org/10.1016/0304-3991(89)90061-2.

(59) Guimaraes, F. D. S. F.; De Oliveira, S. M.; De Oliveira, C. C.; Donatti, L.; Buchi, D. D. F. A Shorter Fixation Protocol for Transmission Electron Microscopy: An Alternative to Spend Less Time. *http://dx.doi.org/10.3109/01913120902889153* **2009**, *33* (4), 169–174. https://doi.org/10.3109/01913120902889153.

(60) Xie, Y.; Chen, J.; Zhang, S.; Fan, K.; Chen, G.; Zhuang, Z.; Zeng, M.; Chen, D.; Lu, L.; Yang, L.; Yang, F. The Research about Microscopic Structure of Emulsion Membrane in O/W Emulsion by NMR and Its Influence to Emulsion Stability. *Int J Pharm* **2016**, *500* (1–2), 110–119. https://doi.org/10.1016/J.IJPHARM.2016.01.032.

(61) Zaragoza-Contreras, E. A.; Hernández-Escobar, C. A.; Navarrete-Fontes, A.; Flores-Gallardo, S. G. Synthesis of Carbon Black/Polystyrene Conductive Nanocomposite. Pickering Emulsion Effect Characterized by TEM. *Micron* **2011**, *42* (3), 263–270. https://doi.org/10.1016/J.MICRON.2010.10.005.

(62) Hirose, M.; Kadowaki, F.; Zhou, J. The Structure and Properties of Core-Shell Type Acrylic-Polyurethane Hybrid Aqueous Emulsions. *Prog Org Coat* **1997**, *31* (1–2), 157–169. https://doi.org/10.1016/S0300-9440(97)00032-5.

(63) Goff, H.; Liboff, M.; Jordan, W.; Kinsella, J. The Effects of Polysorbate 80 on the Fat Emulsion in Ice Cream Mix: Evidence from Transmission Electron Microscopy Studies. *Food Structure* **1987**, *6* (2).

(64) Kühlbrandt, W. The Resolution Revolution. *Science*. American Association for the Advancement of Science March 28, 2014, pp 1443–1444. https://doi.org/10.1126/science.1251652.

(65) Danino, D. Cryo-TEM of Soft Molecular Assemblies. *Current Opinion in Colloid and Interface Science*. December 2012, pp 316–329. https://doi.org/10.1016/j.cocis.2012.10.003.

(66) Spernath, L.; Regev, O.; Levi-Kalisman, Y.; Magdassi, S. Phase Transitions in O/W Lauryl Acrylate Emulsions during Phase Inversion, Studied by Light Microscopy and Cryo-TEM. *Colloids Surf A Physicochem Eng Asp* **2009**, *332* (1), 19–25. https://doi.org/10.1016/J.COLSURFA.2008.08.026.

(67) *Cryotechniques in Biological Electron Microscopy*; Steinbrecht, R. A., Zierold, K., Eds.; Springer Berlin Heidelberg: Berlin, Heidelberg, 1987. https://doi.org/10.1007/978-3-642-72815-0.

(68) Stewart, P. L. Cryo-Electron Microscopy and Cryo-Electron Tomography of Nanoparticles. *Wiley Interdiscip Rev Nanomed Nanobiotechnol* **2017**, *9* (2), e1417. https://doi.org/10.1002/WNAN.1417.

(69) Frederik, P. M.; Stuart, M. C. A.; Bomans, P. H. H.; Busing, W. M.; Burger, K. N. J.; Verkleij, A. J. Perspective and Limitations of Cryo-Electron Microscopy. *J Microsc* **1991**, *161* (2), 253–262. https://doi.org/10.1111/J.1365-2818.1991.TB03088.X.

(70) Oostergetel, G. T.; Esselink, F. J.; Hadziioannou, G. Cryo-Electron Microscopy of Block Copolymers in an Organic Solvent. *Langmuir* **1995**, *11* (10), 3721–3724. https://doi.org/10.1021/LA00010A022/ASSET/LA00010A022.FP.PNG_V03.

(71) Matatyaho Ya'Akobi, A.; Talmon, Y. Extending Cryo-EM to Nonaqueous Liquid Systems. *Acc Chem Res* **2021**, *54* (9), 2100–2109. https://doi.org/10.1021/ACS.ACCOUNTS.1C00077/ASSET/IMAGES/LARGE/AR1C00077_0007.JPEG.

(72) Agarwal, V.; Singh, M.; McPherson, G.; John, V.; Bose, A. Freeze Fracture Direct Imaging of a Viscous Surfactant Mesophase. *Langmuir* **2004**, *20* (1), 11–15. https://doi.org/10.1021/LA035375N/ASSET/IMAGES/LARGE/LA035375NF00009.JPEG.

(73) González-Pérez, A.; Olsson, U. Cryo-Fracture TEM: Direct Imaging of Viscous Samples. *Soft Matter* **2008**, *4* (8), 1625–1629. https://doi.org/10.1039/B803115K.

(74) Kleinerman, O.; Parra-Vasquez, A. N. G.; Green, M. J.; Behabtu, N.; Schmidt, J.; Kesselman, E.; Young, C. C.; Cohen, Y.; Pasquali, M.; Talmon, Y. Cryogenic-Temperature Electron Microscopy Direct Imaging of Carbon Nanotubes and Graphene Solutions in Superacids. *J Microsc* **2015**, *259* (1), 16–25. https://doi.org/10.1111/JMI.12243.

(75) Glaeser, R. M.; Han, B. G.; Csencsits, R.; Killilea, A.; Pulk, A.; Cate, J. H. D. Factors That Influence the Formation and Stability of Thin, Cryo-EM Specimens. *Biophys J* **2016**, *110* (4), 749–755. https://doi.org/10.1016/J.BPJ.2015.07.050.

(76) Dahl, R.; Staehelin, L. A. Highpressure Freezing for the Preservation of Biological Structure: Theory and Practice. *J Electron Microsc Tech* **1989**, *13* (3), 165–174. https://doi.org/10.1002/JEMT.1060130305.

(77) Marchand, K. E.; Tarret, M.; Lechaire, J. P.; Normand, L.; Kasztelan, S.; Cseri, T. Investigation of AOT-Based Microemulsions for the Controlled Synthesis of MoSx Nanoparticles: An Electron Microscopy Study. *Colloids Surf A Physicochem Eng Asp* **2003**, *214* (1–3), 239–248. https://doi.org/10.1016/S0927-7757(02)00412-0.

(78) Massover, W. H. New and Unconventional Approaches for Advancing Resolution in Biological Transmission Electron Microscopy by Improving Macromolecular Specimen Preparation and Preservation. *Micron* **2011**, *42* (2), 141–151. https://doi.org/10.1016/J.MICRON.2010.05.006.

(79) De Jonge, N.; Ross, F. M. Electron Microscopy of Specimens in Liquid. *Nature Nanotechnology*. Nature Publishing Group October 23, 2011, pp 695–704. https://doi.org/10.1038/nnano.2011.161.

(80) Textor, M.; De Jonge, N. Strategies for Preparing Graphene Liquid Cells for Transmission Electron Microscopy. *Nano Letters*. American Chemical Society June 13, 2018, pp 3313–3321. https://doi.org/10.1021/acs.nanolett.8b01366.

(81) Robertson, A. W.; Pu, S.; Gong, C. Liquid Cell Transmission Electron Microscopy and Its Applications. **2020**. https://doi.org/10.1098/rsos.191204.

(82) Korpanty, J.; Gnanasekaran, K.; Venkatramani, C.; Zang, N.; Gianneschi, N. C. Organic Solution-Phase Transmission Electron Microscopy of Copolymer Nanoassembly Morphology and Dynamics. *Cell Rep Phys Sci* **2022**, *0* (0), 100772. https://doi.org/10.1016/J.XCRP.2022.100772.

(83) Ianiro, A.; Wu, H.; van Rijt, M. M. J.; Vena, M. P.; Keizer, A. D. A.; Esteves, A. C. C.; Tuinier, R.; Friedrich, H.; Sommerdijk, N. A. J. M.; Patterson, J. P. Liquid–Liquid Phase

Separation during Amphiphilic Self-Assembly. *Nat Chem* **2019**, *11* (4), 320–328. https://doi.org/10.1038/s41557-019-0210-4.

(84) Rizvi, A.; Mulvey, J. T.; Patterson, J. P. Observation of Liquid–Liquid-Phase Separation and Vesicle Spreading during Supported Bilayer Formation via Liquid-Phase Transmission Electron Microscopy. *Nano Lett* **2021**, *21* (24), 10325–10332. https://doi.org/10.1021/ACS.NANOLETT.1C03556/ASSET/IMAGES/LARGE/NL1C03556_0004.JPEG.

(85) Le Ferrand, H.; Duchamp, M.; Gabryelczyk, B.; Cai, H.; Miserez, A. Time-Resolved Observations of Liquid-Liquid Phase Separation at the Nanoscale Using in Situ Liquid Transmission Electron Microscopy. *J Am Chem Soc* **2019**, *141* (17), 7202–7210. https://doi.org/10.1021/JACS.9B03083/SUPPL_FILE/JA9B03083_SI_004.MPG.

(86) Wang, C.; Chen, X.; Wu, Y.; Li, Y.; Cheng, S. In Situ Liquid Cell Transmission Electron Microscopy Observation of Dynamic Process of Oleic Acid Emulsion with Gold Nanorods. *Journal of Physical Chemistry C* **2020**, *124* (47), 26018–26025. https://doi.org/10.1021/ACS.JPCC.0C07689/ASSET/IMAGES/LARGE/JP0C07689_0006.JPEG.

(87) M. Stawski, T.; Teresa Roncal-Herrero; Alejandro Fernandez-Martinez; Adriana Matamoros-Veloza; Roland Kröger; G. Benning, L. “On Demand” Triggered Crystallization of CaCO 3 from Solute Precursor Species Stabilized by the Water-in-Oil Microemulsion. *Physical Chemistry Chemical Physics* **2018**, *20* (20), 13825–13835. https://doi.org/10.1039/C8CP00540K.

(88) Korpanty, J.; Parent, L. R.; Gianneschi, N. C. Enhancing and Mitigating Radiolytic Damage to Soft Matter in Aqueous Phase Liquid-Cell Transmission Electron Microscopy in the Presence of Gold Nanoparticle Sensitizers or Isopropanol Scavengers. *Nano Lett* **2021**, *21*, 1141–1149. https://doi.org/10.1021/acs.nanolett.0c04636.

(89) Dissanayake, T. U.; Wang, M.; Woehl, T. J. Revealing Reactions between the Electron Beam and Nanoparticle Capping Ligands with Correlative Fluorescence and Liquid-Phase Electron Microscopy. *Cite This: ACS Appl. Mater. Interfaces* **2021**, *13*, 37562. https://doi.org/10.1021/acsami.1c10957.

(90) Woehl, T. J.; Abellan Baeza, P. Defining the Radiation Chemistry during Liquid Cell Electron Microscopy to Enable Visualization of Nanomaterial Growth and Degradation Dynamics. *J Microsc* **2017**, *265*, 135–147. https://doi.org/10.1111/jmi.12508.

(91) Rizvi, A.; Mulvey, J. T.; Patterson, J. P. Observation of Liquid–Liquid-Phase Separation and Vesicle Spreading during Supported Bilayer Formation via Liquid-Phase Transmission Electron Microscopy. *Nano Lett* **2021**, *21* (24), 10325–10332. https://doi.org/10.1021/ACS.NANOLETT.1C03556/ASSET/IMAGES/LARGE/NL1C03556_0004.JPEG.

(92) Ianiro, A.; Wu, H.; van Rijt, M. M. J.; Vena, M. P.; Keizer, A. D. A.; Esteves, A. C. C.; Tuinier, R.; Friedrich, H.; Sommerdijk, N. A. J. M.; Patterson, J. P. Liquid–Liquid Phase Separation during Amphiphilic Self-Assembly. *Nature Chemistry 2019 11:4* **2019**, *11* (4), 320–328. https://doi.org/10.1038/s41557-019-0210-4.

(93) Chen, X.; Tan, L.; Cheng, S.; Liu, Y.; Zhu, M. In Situ Liquid Cell <scp>SEM</Scp> Observation of Dynamic Processes of Au Nanoparticles. *Microsc Res Tech* **2023**. https://doi.org/10.1002/jemt.24325.

(94) Roland, I. Systematic Characterization of Oil-in-Water Emulsions for Formulation Design. *Int J Pharm* **2003**, *263* (1–2), 85–94. https://doi.org/10.1016/S0378-5173(03)00364-8.

(95) Gupta, A.; Eral, H. B.; Hatton, T. A.; Doyle, P. S. Nanoemulsions: Formation, Properties and Applications. *Soft Matter*. Royal Society of Chemistry March 8, 2016, pp 2826–2841. https://doi.org/10.1039/c5sm02958a.

(96) Mason, T. G.; Wilking, J. N.; Meleson, K.; Chang, C. B.; Graves, S. M. Nanoemulsions: Formation, Structure, and Physical Properties. *Journal of Physics Condensed Matter* **2006**, *18* (41), 635–666. https://doi.org/10.1088/0953-8984/18/41/R01.

(97) Griffin, W. C. Calculation of HLB Values of Non-Ionic Surfactants. *J Soc Cosmet Chem* **1954**, *5* (4), 249–256.

(98) Griffin, W. C. CLASSIFICATION OF SURFACE-ACTIVE AGENTS BY "HLB." *Journal of the Society of Cosmetic Chemist*. 1949, pp 311–326.

(99) *Surfactants in Consumer Products: Theory, Technology, and Application*; Falbe, J., Ed.; Springer Berlin Heidelberg: Berlin, Heidelberg, 1987. https://doi.org/10.1007/978-3-642-71545-7.

(100) McClements, D. J. Critical Review of Techniques and Methodologies for Characterization of Emulsion Stability. *Critical Reviews in Food Science and Nutrition*. Taylor & Francis Group September 2007, pp 611–649. https://doi.org/10.1080/10408390701289292.

(101) Zhu, Q.; Pan, Y.; Jia, X.; Li, J.; Zhang, M.; Yin, L. Review on the Stability Mechanism and Application of Water-in-Oil Emulsions Encapsulating Various Additives. *Compr Rev Food Sci Food Saf* **2019**, *18* (6), 1660–1675. https://doi.org/10.1111/1541-4337.12482.

(102) McClements, D. J.; Jafari, S. M. Improving Emulsion Formation, Stability and Performance Using Mixed Emulsifiers: A Review. *Adv Colloid Interface Sci* **2018**, *251*, 55–79. https://doi.org/10.1016/J.CIS.2017.12.001.

(103) Weiss, J.; Herrmann, N.; McClements, D. J. Ostwald Ripening of Hydrocarbon Emulsion Droplets in Surfactant Solutions. *Langmuir* **1999**, *15* (20), 6652–6657. https://doi.org/10.1021/la981739d.

(104) Tadros, T.; Izquierdo, P.; Esquena, J.; Solans, C. Formation and Stability of Nano-Emulsions. *Adv Colloid Interface Sci* **2004**, *108–109*, 303–318. https://doi.org/10.1016/j.cis.2003.10.023.

(105) McClements, D. J. Critical Review of Techniques and Methodologies for Characterization of Emulsion Stability. *Crit Rev Food Sci Nutr* **2007**, *47* (7), 611–649. https://doi.org/10.1080/10408390701289292.

(106) Santos, J.; Calero, N.; Trujillo-Cayado, L. A.; Garcia, M. C.; Muñoz, J. Assessing Differences between Ostwald Ripening and Coalescence by Rheology, Laser Diffraction and Multiple Light Scattering. *Colloids Surf B Biointerfaces* **2017**, *159*, 405–411. https://doi.org/10.1016/J.COLSURFB.2017.08.015.

(107) Narayan, S.; Metaxas, A. E.; Bachnak, R.; Neumiller, T.; Dutcher, C. S. Zooming in on the Role of Surfactants in Droplet Coalescence at the Macroscale and Microscale. *Curr Opin Colloid Interface Sci* **2020**, *50*, 101385. https://doi.org/10.1016/J.COCIS.2020.08.010.

(108) Sommerling, J. H.; De Matos, M. B. C.; Hildebrandt, E.; Dessy, A.; Kok, R. J.; Nirschl, H.; Leneweit, G. Instability Mechanisms of Water-in-Oil Nanoemulsions with Phospholipids: Temporal and Morphological Structures. *Langmuir* **2018**, *34* (2), 572–584. https://doi.org/10.1021/acs.langmuir.7b02852.

(109) Nazarzadeh, E.; Anthonypillai, T.; Sajjadi, S. On the Growth Mechanisms of Nanoemulsions. *J Colloid Interface Sci* **2013**, *397*, 154–162. https://doi.org/10.1016/j.jcis.2012.12.018.

(110) Rodriguez-Lopez, G.; O'Neil Williams, Y.; Toro-Mendoza, J. Individual and Collective Behavior of Emulsion Droplets Undergoing Ostwald Ripening. *Langmuir* **2019**, *35* (15), 5316–5323. https://doi.org/10.1021/acs.langmuir.8b03959.

(111) Wooster, T. J.; Golding, M.; Sanguansri, P. Impact of Oil Type on Nanoemulsion Formation and Ostwald Ripening Stability. *Langmuir* **2008**, *24* (22), 12758–12765. https://doi.org/10.1021/la801685v.

(112) Kabal'nov, A. S.; Pertzov, A. V.; Shchukin, E. D. Ostwald Ripening in Two-Component Disperse Phase Systems: Application to Emulsion Stability. *Colloids and Surfaces* **1987**, *24* (1), 19–32. https://doi.org/10.1016/0166-6622(87)80258-5.

(113) Hunter, S. J.; Cornel, E. J.; Mykhaylyk, O. O.; Armes, S. P. Effect of Salt on the Formation and Stability of Water-in-Oil Pickering Nanoemulsions Stabilized by Diblock

Copolymer Nanoparticles. *Langmuir* **2020**, *36* (51), 15523–15535. https://doi.org/10.1021/acs.langmuir.0c02742.

(114) Santos, J.; Calero, N.; Trujillo-Cayado, L. A.; Garcia, M. C.; Muñoz, J. Assessing Differences between Ostwald Ripening and Coalescence by Rheology, Laser Diffraction and Multiple Light Scattering. *Colloids Surf B Biointerfaces* **2017**, *159*, 405–411. https://doi.org/10.1016/j.colsurfb.2017.08.015.

(115) Nazarzadeh, E.; Anthonypillai, T.; Sajjadi, S. On the Growth Mechanisms of Nanoemulsions. *J Colloid Interface Sci* **2013**, *397*, 154–162. https://doi.org/10.1016/j.jcis.2012.12.018.

(116) Jiao, J.; Burgess, D. J. Ostwald Ripening of Water-in-Hydrocarbon Emulsions. *J Colloid Interface Sci* **2003**, *264* (2), 509–516. https://doi.org/10.1016/S0021-9797(03)00276-5.

(117) Rodriguez-Lopez, G.; Williams, Y. O.; Toro-Mendoza, J. Individual and Collective Behavior of Emulsion Droplets Undergoing Ostwald Ripening. *Langmuir* **2019**, *35* (15), 5316–5323. https://doi.org/10.1021/ACS.LANGMUIR.8B03959.

(118) Hassan, P. A.; Rana, S.; Verma, G. Making Sense of Brownian Motion: Colloid Characterization by Dynamic Light Scattering. *Langmuir* **2014**, *31* (1), 3–12. https://doi.org/10.1021/LA501789Z.

(119) German Urbina-Villalba; Ana Forgiarini; Kareem Rahn; Aileen Lozsán. Influence of Flocculation and Coalescence on the Evolution of the Average Radius of an O/W Emulsion. Is a Linear Slope of R[Combining Macron] 3 vs. t an Unmistakable Signature of Ostwald Ripening ? *Physical Chemistry Chemical Physics* **2009**, *11* (47), 11184–11195. https://doi.org/10.1039/B915470A.

(120) Wang, H.; Davis, R. H. Droplet Growth Due to Brownian, Gravitational, or Thermocapillary Motion and Coalescence in Dilute Dispersions. *J Colloid Interface Sci* **1993**, *159* (1), 108–118. https://doi.org/10.1006/jcis.1993.1302.

(121) Rekvig, L.; Frenkel, D. Molecular Simulations of Droplet Coalescence in Oil/Water/Surfactant Systems. *Journal of Chemical Physics* **2007**, *127* (13), 4423. https://doi.org/10.1063/1.2780865.

(122) Taylor, P. Ostwald Ripening in Emulsions: Estimation of Solution Thermodynamics of the Disperse Phase. *Adv Colloid Interface Sci* **2003**, *106* (1–3), 261–285. https://doi.org/10.1016/S0001-8686(03)00113-1.

(123) Koroleva, M. Y.; Yurtov, E. V. Water Transport by Nanodispersion Droplets in a Water-in-Oil Emulsion. *Colloid Journal of the Russian Academy of Sciences: Kolloidnyi Zhurnal* **2003**, *65* (1), 35–39. https://doi.org/10.1023/A:1022310823060.

(124) Bera, B.; Khazal, R.; Schroën, K. Coalescence Dynamics in Oil-in-Water Emulsions at Elevated Temperatures. *Sci Rep* **2021**, *11* (1), 1–10. https://doi.org/10.1038/s41598-021-89919-5.

(125) Meredith, C. H.; Moerman, P. G.; Groenewold, J.; Chiu, Y.-J.; Kegel, W. K.; van Blaaderen, A.; Zarzar, L. D. Predator–Prey Interactions between Droplets Driven by Non-Reciprocal Oil Exchange. *Nature Chemistry 2020 12:12* **2020**, *12* (12), 1136–1142. https://doi.org/10.1038/s41557-020-00575-0.

(126) Meredith, C. H.; Castonguay, A.; Chiu, Y.-J.; Brooks, A. M.; Moerman, P.; Torab, P.; Kin Wong, P.; Sen, A.; Velegol, D.; Zarzar, L. D. Chemical Design of Self-Propelled Janus Droplets.

(127) Sheth, T.; Seshadri, S.; Prileszky, T.; Helgeson, M. E. Multiple Nanoemulsions. *Nat Rev Mater* **2020**, *5* (3), 214–228. https://doi.org/10.1038/s41578-019-0161-9.

(128) De Jonge, N.; Ross, F. M. Electron Microscopy of Specimens in Liquid. *Nature Nanotechnology*. Nature Publishing Group 2011, pp 695–704. https://doi.org/10.1038/nnano.2011.161.

(129) Evans, J. E.; Jungjohann, K. L.; Browning, N. D.; Arslan, I. Controlled Growth of Nanoparticles from Solution with in Situ Liquid Transmission Electron Microscopy. *Nano Lett* **2011**, *11* (7), 2809–2813. https://doi.org/10.1021/nl201166k.

(130) Abellan, P.; Woehl, T. J. Liquid Cell Electron Microscopy for the Study of Growth Dynamics of Nanomaterials and Structure of Soft Matter. In *In-situ Characterization Techniques for Nanomaterials*; Springer-Verlag Berlin Heidelberg, 2018; pp 1–31. https://doi.org/10.1007/978-3-662-56322-9_1.

(131) Patterson, J. P.; Abellan, P.; Denny, M. S.; Park, C.; Browning, N. D.; Cohen, S. M.; Evans, J. E.; Gianneschi, N. C. Observing the Growth of Metal-Organic Frameworks by in Situ Liquid Cell Transmission Electron Microscopy. *J Am Chem Soc* **2015**, *137* (23), 7322–7328. https://doi.org/10.1021/jacs.5b00817.

(132) L. Gilmore, B.; P. Showalter, S.; J. Dukes, M.; R. Tanner, J.; C. Demmert, A.; M. McDonald, S.; F. Kelly, D. Visualizing Viral Assemblies in a Nanoscale Biosphere. *Lab Chip* **2012**, *13* (2), 216–219. https://doi.org/10.1039/C2LC41008G.

(133) Mirsaidov, U. M.; Zheng, H.; Casana, Y.; Matsudaira, P. Imaging Protein Structure in Water at 2.7 Nm Resolution by Transmission Electron Microscopy. *Biophys J* **2012**, *102* (4). https://doi.org/10.1016/j.bpj.2012.01.009.

(134) Woehl, T. J.; Evans, J. E.; Arslan, I.; Ristenpart, W. D.; Browning, N. D. Direct in Situ Determination of the Mechanisms Controlling Nanoparticle Nucleation and Growth. *ACS Nano* **2012**, *6* (10), 8599–8610. https://doi.org/10.1021/NN303371Y.

(135) McMullan, G.; Faruqi, A. R.; Henderson, R. *Direct Electron Detectors*, 1st ed.; Elsevier Inc., 2016; Vol. 579. https://doi.org/10.1016/bs.mie.2016.05.056.

(136) Gatan. K3 Direct Detection Cameras, Models 1025 and 1024. 1024–1025.

(137) Fletcher, P. D. I.; Parrott, D. Water Droplet Coalescence Rates in Water-in-Oil Microemulsions. In *Reactions in Compartmentalized Liquids*; Springer Berlin Heidelberg: Berlin, Heidelberg, 1989; pp 53–60. https://doi.org/10.1007/978-3-642-74787-8_6.

(138) Bergenholtz, J.; Romagnoli, A. A.; Wagner, N. J. Viscosity, Microstructure, and Interparticle Potential of AOT/H2O/n-Decane Inverse Microemulsions. *Langmuir* **1995**, *11* (5), 1559–1570. https://doi.org/10.1021/la00005a025.

(139) Nave, S.; Eastoe, J.; Penfold, J. What Is so Special about Aerosol-OT? 1. Aqueous Systems. *Langmuir* **2000**, *16* (23), 8733–8740. https://doi.org/10.1021/la000341q.

(140) Aferni, A. El; Guettari, M.; Tajouri, T. Determination of the Water/AOT/Isooctane Reverse Micelles Size Parameters from Their Refractive Index Data. *J Solution Chem* **2017**, *46* (1), 89–102. https://doi.org/10.1007/s10953-016-0563-x.

(141) Eskici, G.; Axelsen, P. H. The Size of AOT Reverse Micelles. *Journal of Physical Chemistry B* **2016**, *120* (44), 11337–11347. https://doi.org/10.1021/acs.jpcb.6b06420.

(142) Hensel, J. K.; Carpenter, A. P.; Ciszewski, R. K.; Schabes, B. K.; Kittredge, C. T.; Moore, F. G.; Richmond, G. L. Molecular Characterization of Water and Surfactant AOT at

Nanoemulsion Surfaces. *Proceedings of the National Academy of Sciences* **2017**, *114* (51), 13351–13356. https://doi.org/10.1073/PNAS.1700099114.

(143) Abel, S.; Sterpone, F.; Bandyopadhyay, S.; Marchi, M. Molecular Modeling and Simulations of AOT−Water Reverse Micelles in Isooctane: Structural and Dynamic Properties. *J Phys Chem B* **2004**, *108* (50), 19458–19466. https://doi.org/10.1021/jp047138e.

(144) Leung, R.; Shah, D. O. *Solubilization and Phase Equilibria of Water-in-Oil Microemulsions I. Effects of Spontaneous Curvature and Elasticity of Interfacial Films*; 1987.

(145) Leung, R.; Shah, D. O. Solubilization and Phase Equilibria of Water-in-Oil Microemulsions. *J Colloid Interface Sci* **1987**, *120* (2), 320–329. https://doi.org/10.1016/0021-9797(87)90360-2.

(146) Frank, S. G.; Zografi, G. Solubilization of Water by Dialkyl Sodium Sulfosuccinates in Hydrocarbon Solutions. *J Colloid Interface Sci* **1969**, *29* (1), 27–35. https://doi.org/10.1016/0021-9797(69)90342-7.

(147) Zulauf, Martin.; Eicke, H. Friedrich. Inverted Micelles and Microemulsions in the Ternary System Water/Aerosol-OT/Isooctane as Studied by Photon Correlation Spectroscopy. *J Phys Chem* **1979**, *83* (4), 480–486. https://doi.org/10.1021/j100467a011.

(148) Chatterjee, S.; Mitra, R. K.; Paul, B. K.; Bhattacharya, S. C. Interface of AOT/Brij Mixed Reverse Micellar Systems: Conductometric and Spectrophotometric Investigations. *J Colloid Interface Sci* **2006**, *298* (2), 935–941. https://doi.org/10.1016/j.jcis.2005.12.061.

(149) Yesibolati, M. N.; Mortensen, K. I.; Sun, H.; Brostrøm, A.; Tidemand-Lichtenberg, S.; Mølhave, K. Unhindered Brownian Motion of Individual Nanoparticles in Liquid-Phase Scanning Transmission Electron Microscopy. *Nano Lett* **2020**, *20* (10), 7108–7115. https://doi.org/10.1021/acs.nanolett.0c02352.

(150) Parent, L. R.; Bakalis, E.; Proetto, M.; Li, Y.; Park, C.; Zerbetto, F.; Gianneschi, N. C. Tackling the Challenges of Dynamic Experiments Using Liquid-Cell Transmission Electron Microscopy. *Acc Chem Res* **2018**, *51* (1), 3–11. https://doi.org/10.1021/acs.accounts.7b00331.

(151) Wang, C.; Chen, X.; Wu, Y.; Li, Y.; Cheng, S. In Situ Liquid Cell Transmission Electron Microscopy Observation of Dynamic Process of Oleic Acid Emulsion with Gold Nanorods. *Journal of Physical Chemistry C* **2020**, *124* (47), 26018–26025. https://doi.org/10.1021/acs.jpcc.0c07689.

(152) Park, J.; Park, H.; Ercius, P.; Pegoraro, A. F.; Xu, C.; Kim, J. W.; Han, S. H.; Weitz, D. A. Direct Observation of Wet Biological Samples by Graphene Liquid Cell Transmission Electron Microscopy. *Nano Lett* **2015**, *15* (7), 4737–4744. https://doi.org/10.1021/acs.nanolett.5b01636.

(153) Wang, H.; Hima Nagamanasa, K.; Kim, Y. J.; Kwon, O. H.; Granick, S. Longer-Lasting Electron-Based Microscopy of Single Molecules in Aqueous Medium. *ACS Nano* **2018**, *12* (8), 8572–8578. https://doi.org/10.1021/acsnano.8b04190.

(154) *Fayer Lab - Nanoscopic Water in Reverse Micelles*. https://web.stanford.edu/group/fayer/research_micelle.html (accessed 2021-05-11).

(155) Touve, M. A.; Figg, C. A.; Wright, D. B.; Park, C.; Cantlon, J.; Sumerlin, B. S.; Gianneschi, N. C. Polymerization-Induced Self-Assembly of Micelles Observed by Liquid Cell Transmission Electron Microscopy. *ACS Cent Sci* **2018**, *4* (5), 543–547. https://doi.org/10.1021/acscentsci.8b00148.

(156) Scheutz, G. M.; Touve, M. A.; Carlini, A. S.; Garrison, J. B.; Gnanasekaran, K.; Sumerlin, B. S.; Gianneschi, N. C. Probing Thermoresponsive Polymerization-Induced Self-Assembly with Variable-Temperature Liquid-Cell Transmission Electron Microscopy. *Matter* **2021**, *4* (2), 722–736. https://doi.org/10.1016/j.matt.2020.11.017.

(157) Touve, M. A.; Carlini, A. S.; Gianneschi, N. C. Self-Assembling Peptides Imaged by Correlated Liquid Cell Transmission Electron Microscopy and MALDI-Imaging Mass Spectrometry. *Nat Commun* **2019**, *10* (1), 1–12. https://doi.org/10.1038/s41467-019-12660-1.

(158) Parent, L. R.; Bakalis, E.; Proetto, M.; Li, Y.; Park, C.; Zerbetto, F.; Gianneschi, N. C. Tackling the Challenges of Dynamic Experiments Using Liquid-Cell Transmission Electron Microscopy. *Acc Chem Res* **2018**, *51* (1), 3–11. https://doi.org/10.1021/acs.accounts.7b00331.

(159) Parent, L. R.; Bakalis, E.; Ramírez-Hernández, A.; Kammeyer, J. K.; Park, C.; De Pablo, J.; Zerbetto, F.; Patterson, J. P.; Gianneschi, N. C. Directly Observing Micelle Fusion and Growth in Solution by Liquid-Cell Transmission Electron Microscopy. *J Am Chem Soc* **2017**, *139* (47), 17140–17151. https://doi.org/10.1021/jacs.7b09060.

(160) Wu, H.; Su, H.; M Joosten, R. R.; A Keizer, A. D.; van Hazendonk, L. S.; M Wirix, M. J.; Patterson, J. P.; Laven, J.; de With, G.; Friedrich, H.; Wu, H.; Su, H.; A Keizer, A. D.; van

Hazendonk, L. S.; Laven, J.; de With, G.; Friedrich, H.; M Joosten, R. R.; M Wirix, M. J.; Patterson, J. P. Mapping and Controlling Liquid Layer Thickness in Liquid-Phase (Scanning) Transmission Electron Microscopy. *Small Methods* **2021**, *5* (6), 2001287. https://doi.org/10.1002/SMTD.202001287.

(161) Bakalis, E.; Parent, L. R.; Vratsanos, M.; Park, C.; Gianneschi, N. C.; Zerbetto, F. Complex Nanoparticle Diffusional Motion in Liquid-Cell Transmission Electron Microscopy. *The Journal of Physical Chemistry C* **2020**, *124* (27), 14881–14890. https://doi.org/10.1021/acs.jpcc.0c03203.

(162) Parent, L. R.; Bakalis, E.; Ramírez-Hernández, A.; Kammeyer, J. K.; Park, C.; De Pablo, J.; Zerbetto, F.; Patterson, J. P.; Gianneschi, N. C. Directly Observing Micelle Fusion and Growth in Solution by Liquid-Cell Transmission Electron Microscopy. *J Am Chem Soc* **2017**, *139* (47), 17140–17151. https://doi.org/10.1021/jacs.7b09060.

(163) Jamali, V.; Hargus, C.; Ben-Moshe, A.; Aghazadeh, A.; Ha, H. D.; Mandadapu, K. K.; Alivisatos, A. P. Anomalous Nanoparticle Surface Diffusion in LCTEM Is Revealed by Deep Learning-Assisted Analysis. *Proc Natl Acad Sci U S A* **2021**, *118* (10), 2017616118. https://doi.org/10.1073/pnas.2017616118.

(164) Verch, A.; Pfaff, M.; de Jonge, N. Exceptionally Slow Movement of Gold Nanoparticles at a Solid/Liquid Interface Investigated by Scanning Transmission Electron Microscopy. *Langmuir* **2015**, *31* (25), 6956–6964. https://doi.org/10.1021/acs.langmuir.5b00150.

(165) Parent, L. R.; Bakalis, E.; Ramírez-Hernández, A.; Kammeyer, J. K.; Park, C.; De Pablo, J.; Zerbetto, F.; Patterson, J. P.; Gianneschi, N. C. Directly Observing Micelle Fusion and

Growth in Solution by Liquid-Cell Transmission Electron Microscopy. *J Am Chem Soc* **2017**, *139* (47), 17140–17151. https://doi.org/10.1021/jacs.7b09060.

(166) Liu, X.; Chee, S. W.; Raj, S.; Sawczyk, M.; Král, P.; Mirsaidov, U. Three-Step Nucleation of Metal-Organic Framework Nanocrystals. **2021**, *118*, 2008880118. https://doi.org/10.1073/pnas.2008880118/-/DCSupplemental.

(167) Gnanasekaran, K.; Korpanty, J.; Berger, O.; Hampu, N.; Halperin-Sternfeld, M.; Cohen-Gerassi, D.; Adler-Abramovich, L.; Gianneschi, N. C. Dipeptide Nanostructure Assembly and Dynamics via in Situ Liquid-Phase Electron Microscopy. *ACS Nano* **2021**. https://doi.org/10.1021/ACSNANO.1C06130.

(168) Koroleva, M. Y.; Yurtov, E. V. Water Mass Transfer in W/O Emulsions. *J Colloid Interface Sci* **2006**, *297* (2), 778–784. https://doi.org/10.1016/j.jcis.2005.10.046.

(169) Voorhees, P. W. The Theory of Ostwald Ripening. *J Stat Phys* **1985**, *38* (1–2), 231–252. https://doi.org/10.1007/BF01017860.

(170) Moran, K.; Yeung, A.; Masliyah, J. Measuring Interfacial Tensions of Micrometer-Sized Droplets: A Novel Micromechanical Technique. *Langmuir* **1999**, *15* (24), 8497–8504. https://doi.org/10.1021/LA990363G.

(171) Malhotra, A. K.; Wasan, D. T. Effect of Film Size on Drainage of Foam and Emulsion Films. *AIChE Journal* **1987**, *33* (9), 1533–1541. https://doi.org/10.1002/AIC.690330913.

(172) Danov, K. D. Effect of Surfactants on Drop Stability and Thin Film Drainage.

(173) García-Río, L.; Leis, R.; Mejuto, J. C.; Peña, M. E.; Iglesias, E. Effects of Additives on the Internal Dynamics and Properties of Water/AOT/Isooctane Microemulsions. *Langmuir* **1994**, *10* (6), 1676–1683. https://doi.org/10.1021/la00018a013.

(174) Leung, R.; Shah, D. O. Solubilization and Phase Equilibria of Water-in-Oil Microemulsions. II. Effects of Alcohols, Oils, and Salinity on Single-Chain Surfactant Systems. *J Colloid Interface Sci* **1987**, *120* (2), 330–344. https://doi.org/10.1016/0021-9797(87)90361-4.

(175) Jaiswal, M.; Dudhe, R.; Sharma, P. K. Nanoemulsion: An Advanced Mode of Drug Delivery System. *3 Biotech*. Springer Verlag April 1, 2015, pp 123–127. https://doi.org/10.1007/s13205-014-0214-0.

(176) M. Koroleva; T. Nagovitsina; E. Yurtov. Nanoemulsions Stabilized by Non-Ionic Surfactants: Stability and Degradation Mechanisms. *Physical Chemistry Chemical Physics* **2018**, *20* (15), 10369–10377. https://doi.org/10.1039/C7CP07626F.

(177) Yekeen, N.; Manan, M. A.; Idris, A. K.; Samin, A. M. Influence of Surfactant and Electrolyte Concentrations on Surfactant Adsorption and Foaming Characteristics. *J Pet Sci Eng* **2017**, *149*, 612–622. https://doi.org/10.1016/J.PETROL.2016.11.018.

(178) Xu, Q.; Nakajima, M.; Ichikawa, S.; Nakamura, N.; Roy, P.; Okadome, H.; Shiina, T. Effects of Surfactant and Electrolyte Concentrations on Bubble Formation and Stabilization. *J Colloid Interface Sci* **2009**, *332* (1), 208–214. https://doi.org/10.1016/J.JCIS.2008.12.044.

(179) *About DIPlib 3 | DIPlib | a library for quantitative image analysis*. https://diplib.org/diplib-docs/ (accessed 2021-10-15).

(180) MARCHELLO, G.; DE PACE, C.; DURO-CASTANO, A.; BATTAGLIA, G.; RUIZ-PÉREZ, L. End-to-end Image Analysis Pipeline for Liquid-phase Electron Microscopy. *J Microsc* **2020**, *279* (3), 242–248. https://doi.org/10.1111/jmi.12889.

(181) Bancroft, W. D.; WILDER D. BANCROFT; Bancroft, W. D. The Theory of Emulsification, I. *J Phys Chem* **1912**, *16* (3), 177–233. https://doi.org/10.1021/j150129a001.

(182) Albert, C.; Beladjine, M.; Tsapis, N.; Fattal, E.; Agnely, F.; Huang, N. Pickering Emulsions: Preparation Processes, Key Parameters Governing Their Properties and Potential for Pharmaceutical Applications. *Journal of Controlled Release* **2019**, *309*, 302–332. https://doi.org/10.1016/J.JCONREL.2019.07.003.

(183) McClements, D. J.; Jafari, S. M. Improving Emulsion Formation, Stability and Performance Using Mixed Emulsifiers: A Review. *Adv Colloid Interface Sci* **2018**, *251*, 55–79. https://doi.org/10.1016/j.cis.2017.12.001.

(184) Pawar, A. B.; Caggioni, M.; Ergun, R.; Hartel, R. W.; Spicer, P. T. Arrested Coalescence in Pickering Emulsions. *Soft Matter* **2011**, *7* (17), 7710–7716. https://doi.org/10.1039/c1sm05457k.

(185) Komatsu, H.; Okada, S.; Handa, T. Suppressive Effects of Salts on Droplet Coalescence in a Commercially Available Fat Emulsion during Freezing for Storage. *J Pharm Sci* **1997**, *86* (4), 497–502. https://doi.org/10.1021/js960166r.

(186) Verch, A.; Pfaff, M.; de Jonge, N. Exceptionally Slow Movement of Gold Nanoparticles at a Solid/Liquid Interface Investigated by Scanning Transmission Electron Microscopy. *Langmuir* **2015**, *31* (25), 6956–6964. https://doi.org/10.1021/acs.langmuir.5b00150.

(187) Yesibolati, M. N.; Mortensen, K. I.; Sun, H.; Brostrøm, A.; Tidemand-Lichtenberg, S.; Mølhave, K. Unhindered Brownian Motion of Individual Nanoparticles in Liquid-Phase Scanning Transmission Electron Microscopy. *Nano Lett* **2020**, *20* (10), 7108–7115. https://doi.org/10.1021/acs.nanolett.0c02352.

(188) Parent, L. R.; Bakalis, E.; Proetto, M.; Li, Y.; Park, C.; Zerbetto, F.; Gianneschi, N. C. Tackling the Challenges of Dynamic Experiments Using Liquid-Cell Transmission Electron Microscopy. *Acc Chem Res* **2018**, *51* (1), 3–11. https://doi.org/10.1021/acs.accounts.7b00331.

(189) Welling, T. A. J.; Sadighikia, S.; Watanabe, K.; Grau-Carbonell, A.; Bransen, M.; Nagao, D.; van Blaaderen, A.; van Huis, M. A. Observation of Undamped 3D Brownian Motion of Nanoparticles Using Liquid-Cell Scanning Transmission Electron Microscopy. *Particle & Particle Systems Characterization* **2020**, *37* (6), 2000003. https://doi.org/10.1002/ppsc.202000003.

(190) Vitale, S. A.; Katz, J. L. Liquid Droplet Dispersions Formed by Homogeneous Liquid−Liquid Nucleation: "The Ouzo Effect." *Langmuir* **2003**, *19* (10), 4105–4110. https://doi.org/10.1021/LA026842O.

(191) Vendramin, V.; Pesce, A.; Vincenzi, S. Anethole Stability in Aniseed Spirits: Storage Condition Repercussions on Commercial Products. *Beverages* **2021**, *7* (4), 73. https://doi.org/10.3390/beverages7040073.

(192) Goubault, C.; Iglicki, D.; Swain, R. A.; McVey, B. F. P.; Lefeuvre, B.; Rault, L.; Nayral, C.; Delpech, F.; Kahn, M. L.; Chevance, S.; Gauffre, F. Effect of Nanoparticles on

Spontaneous Ouzo Emulsification. *J Colloid Interface Sci* **2021**, *603*, 572–581. https://doi.org/10.1016/J.JCIS.2021.06.104.

(193) Sitnikova, N. L.; Sprik, R.; Wegdam, G.; Eiser, E. Spontaneously Formed Trans-Anethol/Water/Alcohol Emulsions: Mechanism of Formation and Stability. *Langmuir* **2005**, *21* (16), 7083–7089. https://doi.org/10.1021/la046816l.

(194) Prévost, S.; Krickl, S.; Marčelja, S.; Kunz, W.; Zemb, T.; Grillo, I. Spontaneous Ouzo Emulsions Coexist with Pre-Ouzo Ultraflexible Microemulsions. *Langmuir* **2021**, *37* (13), 3817–3827. https://doi.org/10.1021/ACS.LANGMUIR.0C02935/SUPPL_FILE/LA0C02935_SI_001.PDF.

(195) Lu, Z.; Klein Schaarsberg, M. H.; Zhu, X.; Yeo, L. Y.; Lohse, D.; Zhang, X. Universal Nanodroplet Branches from Confining the Ouzo Effect. *Proc Natl Acad Sci U S A* **2017**, *114* (39), 10332–10337. https://doi.org/10.1073/PNAS.1704727114/-/DCSUPPLEMENTAL/PNAS.1704727114.SM06.MP4.

(196) Chelli, Z.; Achour, H.; Saidi, M.; Botet, R. The “Ouzo Effect”, Recent Developments and Application to Therapeutic Drug Carrying. *J Phys Conf Ser* **2012**, *352* (1), 012047. https://doi.org/10.1088/1742-6596/352/1/012047.

(197) Goubault, C.; Sciortino, F.; Mongin, O.; Jarry, U.; Bostoën, M.; Jakobczyk, H.; Burel, A.; Dutertre, S.; Troadec, M. B.; Kahn, M. L.; Chevance, S.; Gauffre, F. The Ouzo Effect: A Tool to Elaborate High-Payload Nanocapsules. *Journal of Controlled Release* **2020**, *324*, 430–439. https://doi.org/10.1016/J.JCONREL.2020.05.023.

(198) Kempe, H.; Kempe, M. Ouzo Polymerization: A Bottom-up Green Synthesis of Polymer Nanoparticles by Free-Radical Polymerization of Monomers Spontaneously Nucleated by the Ouzo Effect; Application to Molecular Imprinting. *J Colloid Interface Sci* **2022**, *616*, 560–570. https://doi.org/10.1016/J.JCIS.2022.02.035.

(199) Lamb, A.; He, F.; Zhai, S.; Zhao, H. Silk Fibroin Supraparticles Created by the Evaporation of Colloidal Ouzo Droplets. *AIP Adv* **2021**, *11* (8), 085125. https://doi.org/10.1063/5.0057228.

(200) Aschenbrenner, E.; Bley, K.; Koynov, K.; Makowski, M.; Kappl, M.; Landfester, K.; Weiss, C. K. Using the Polymeric Ouzo Effect for the Preparation of Polysaccharide-Based Nanoparticles. *Langmuir* **2013**, *29* (28), 8845–8855. https://doi.org/10.1021/LA4017867/SUPPL_FILE/LA4017867_SI_001.PDF.

(201) Wang, Y.; Zeng, B.; Zhao, Y.; Li, S.; Zhang, X. Formation of Polystyrene Microlenses via Transient Droplets from the Ouzo Effect for Enhanced Optical Imaging. *Journal of Physical Chemistry C* **2019**, *123* (23), 14327–14337. https://doi.org/10.1021/ACS.JPCC.9B00587/SUPPL_FILE/JP9B00587_SI_001.AVI.

(202) Peng, S.; Xu, C.; Hughes, T. C.; Zhang, X. From Nanodroplets by the Ouzo Effect to Interfacial Nanolenses. *Langmuir* **2014**, *30* (41), 12270–12277. https://doi.org/10.1021/la502821m.

(203) Lepeltier, E.; Bourgaux, C.; Couvreur, P. Nanoprecipitation and the “Ouzo Effect”: Application to Drug Delivery Devices. *Adv Drug Deliv Rev* **2014**, *71*, 86–97. https://doi.org/10.1016/j.addr.2013.12.009.

(204) Ganachaud, F.; Katz, J. L. Nanoparticles and Nanocapsules Created Using the Ouzo Effect: Spontaneous Emulsification as an Alternative to Ultrasonic and High-Shear Devices. *ChemPhysChem* **2005**, *6* (2), 209–216. https://doi.org/10.1002/cphc.200400527.

(205) Klossek, M. L.; Touraud, D.; Zemb, T.; Kunz, W. Structure and Solubility in Surfactant-Free Microemulsions. *ChemPhysChem* **2012**, *13* (18), 4116–4119. https://doi.org/10.1002/CPHC.201200667.

(206) Prévost, S.; Krickl, S.; Marčelja, S.; Kunz, W.; Zemb, T.; Grillo, I. Spontaneous Ouzo Emulsions Coexist with Pre-Ouzo Ultraflexible Microemulsions. *Langmuir* **2021**, *37* (13), 3817–3827. https://doi.org/10.1021/ACS.LANGMUIR.0C02935/ASSET/IMAGES/LARGE/LA0C02935_0008.JPEG.

(207) Marcus, J.; Touraud, D.; Prévost, S.; Diat, O.; Zemb, T.; Kunz, W. Influence of Additives on the Structure of Surfactant-Free Microemulsions. *Physical Chemistry Chemical Physics* **2015**, *17* (48). https://doi.org/10.1039/c5cp06364g.

(208) Carteau, D.; Pianet, I.; Brunerie, P.; Guillemat, B.; Bassani, D. M. Probing the Initial Events in the Spontaneous Emulsification of Trans-Anethole Using Dynamic NMR Spectroscopy. *Langmuir* **2007**, *23* (7), 3561–3565. https://doi.org/10.1021/LA062339Q/SUPPL_FILE/LA062339QSI20060808_034621.PDF .

(209) Carteau, D.; Bassani, D.; Pianet, I. The “Ouzo Effect”: Following the Spontaneous Emulsification of Trans-Anethole in Water by NMR. *Comptes Rendus Chimie* **2008**, *11* (4–5), 493–498. https://doi.org/10.1016/J.CRCI.2007.11.003.

(210) Patterson, J. P.; Proetto, M. T.; Gianneschi, N. C. Soft Nanomaterials Analysed by in Situ Liquid TEM: Towards High Resolution Characterisation of Nanoparticles in Motion. *Perspect Sci (Neth)* **2015**. https://doi.org/10.1016/j.pisc.2015.10.003.

(211) Parent, L. R.; Gnanasekaran, K.; Korpanty, J.; Gianneschi, N. C. 100th Anniversary of Macromolecular Science Viewpoint: Polymeric Materials by in Situ Liquid-Phase Transmission Electron Microscopy. *ACS Macro Lett* **2021**, *10* (1), 14–38. https://doi.org/10.1021/acsmacrolett.0c00595.

(212) Parent, L. R.; Vratsanos, M.; Jin, B.; De Yoreo, J. J.; Gianneschi, N. C. Chemical and Physical Transformations of Carbon-Based Nanomaterials Observed by Liquid Phase Transmission Electron Microscopy. *MRS Bulletin*. Cambridge University Press September 1, 2020, pp 727–737. https://doi.org/10.1557/mrs.2020.224.

(213) Van Vleet, M. J.; Weng, T.; Li, X.; Schmidt, J. R. In Situ, Time-Resolved, and Mechanistic Studies of Metal-Organic Framework Nucleation and Growth. *Chem Rev* **2018**, *118*, 3681–3721. https://doi.org/10.1021/acs.chemrev.7b00582.

(214) Wang, M.; Park, C.; Woehl, T. J. Quantifying the Nucleation and Growth Kinetics of Electron Beam Nanochemistry with Liquid Cell Scanning Transmission Electron Microscopy. *Chemistry of Materials* **2018**, *30* (21), 7727–7736. https://doi.org/10.1021/acs.chemmater.8b03050.

(215) Evans, J. E.; Jungjohann, K. L.; Browning, N. D.; Arslan, I. Controlled Growth of Nanoparticles from Solution with in Situ Liquid Transmission Electron Microscopy. *Nano Lett* **2011**, *11* (7), 2809–2813. https://doi.org/10.1021/nl201166k.

(216) Radisic, A.; Ross, F. M.; Searson, P. C. In Situ Study of the Growth Kinetics of Individual Island Electrodeposition of Copper. *Journal of Physical Chemistry B* **2006**, *110* (15), 7862–7868. https://doi.org/10.1021/jp057549a.

(217) Vailonis, K. M.; Gnanasekaran, K.; Powers, X. B.; Gianneschi, N. C.; Jenkins, D. M. Elucidating the Growth of Metal–Organic Nanotubes Combining Isoreticular Synthesis with Liquid-Cell Transmisson Electron Microscopy. *J Am Chem Soc* **2019**, *141*, 10177–10182. https://doi.org/10.1021/jacs.9b04586.

(218) Hutzler, A.; Fritsch, B.; Jank, M. P. M.; Branscheid, R.; Martens, R. C.; Spiecker, E.; März, M. In Situ Liquid Cell TEM Studies on Etching and Growth Mechanisms of Gold Nanoparticles at a Solid–Liquid–Gas Interface. *Adv Mater Interfaces* **2019**, *6* (20), 1901027. https://doi.org/10.1002/ADMI.201901027.

(219) Yamazaki, T.; Kimura, Y.; Vekilov, P. G.; Furukawa, E.; Shirai, M.; Matsumoto, H.; Van Driessche, A. E. S.; Tsukamoto, K. Two Types of Amorphous Protein Particles Facilitate Crystal Nucleation. *Proc Natl Acad Sci U S A* **2017**, *114* (9), 2154–2159. https://doi.org/10.1073/pnas.1606948114.

(220) Cookman, J.; Hamilton, V.; Price, L. S.; Hall, S. R.; Bangert, U. Visualising Early-Stage Liquid Phase Organic Crystal Growth: Via Liquid Cell Electron Microscopy. *Nanoscale* **2020**, *12* (7), 4636–4644. https://doi.org/10.1039/c9nr08126g.

(221) White, E. R.; Mecklenburg, M.; Shevitski, B.; Singer, S. B.; Regan, B. C. Charged Nanoparticle Dynamics in Water Induced by Scanning Transmission Electron Microscopy. *Langmuir* **2012**, *28* (8), 3695–3698. https://doi.org/10.1021/la2048486.

(222) Powers, A. S.; Liao, H.-G.; Raja, S. N.; Bronstein, N. D.; Alivisatos, A. P.; Zheng, H. Tracking Nanoparticle Diffusion and Interaction during Self-Assembly in a Liquid Cell. *Nano Lett* **2017**, *17* (1), 15–20. https://doi.org/10.1021/acs.nanolett.6b02972.

(223) Chen, X.; Wen, J. In Situ Wet-Cell TEM Observation of Gold Nanoparticle Motion in an Aqueous Solution. *Nanoscale Res Lett* **2012**, *7*, 1–6. https://doi.org/10.1186/1556-276X-7-598.

(224) Li, C.; Tho, C. C.; Galaktionova, D.; Chen, X.; Kral, P.; Mirsaidov, U. Dynamics of Amphiphilic Block Copolymers in an Aqueous Solution: Direct Imaging of Micelle Formation and Nanoparticle Encapsulation. *Nanoscale* **2019**. https://doi.org/10.1039/C8NR08922A.

(225) Korpanty, J.; Parent, L. R.; Hampu, N.; Weigand, S.; Gianneschi, N. C. Thermoresponsive Polymer Assemblies via Variable Temperature Liquid-Phase Transmission Electron Microscopy and Small Angle X-Ray Scattering. *Nature Communications 2021 12:1* **2021**, *12* (1), 1–8. https://doi.org/10.1038/s41467-021-26773-z.

(226) Scheutz, G. M.; Touve, M. A.; Carlini, A. S.; Garrison, J. B.; Gnanasekaran, K.; Sumerlin, B. S.; Gianneschi, N. C. Probing Thermoresponsive Polymerization-Induced Self-Assembly with Variable-Temperature Liquid-Cell Transmission Electron Microscopy. *Matter* **2020**, *0* (0). https://doi.org/10.1016/j.matt.2020.11.017.

(227) Rizvi, A.; Patel, U.; Ianiro, A.; Hurst, P. J.; Merham, J. G.; Patterson, J. P. Nonionic Block Copolymer Coacervates. *Macromolecules* **2020**, *53* (14), 6078–6086. https://doi.org/10.1021/ACS.MACROMOL.0C00979/SUPPL_FILE/MA0C00979_SI_004.MP4.

(228) Gibson, W.; Patterson, J. Observing Nano-Scale Dynamics of Active Soft Materials by In Situ Electrochemistry and Liquid Cell Transmission Electron Microscopy. *Microscopy and Microanalysis* **2022**, *28* (S1), 96–99. https://doi.org/10.1017/S1431927622001295.

(229) Schermelleh, L.; Ferrand, A.; Huser, T.; Eggeling, C.; Sauer, M.; Biehlmaier, O.; C Drummen, G. P. Super-Resolution Microscopy Demystified. https://doi.org/10.1038/s41556-018-0251-8.

(230) Li, M.; Yi, L.; Sun, C. Spontaneously Formed Multiscale Nano-Domains in Monophasic Region of Ternary Solution. *J Colloid Interface Sci* **2022**, *628*, 223–235. https://doi.org/10.1016/J.JCIS.2022.07.152.

(231) Iglicki, D.; Goubault, C.; Nour Mahamoud, M.; Chevance, S.; Gauffre, F. Shedding Light on the Formation and Stability of Mesostructures in Ternary "Ouzo" Mixtures. *J Colloid Interface Sci* **2023**, *633*, 72–81. https://doi.org/10.1016/J.JCIS.2022.11.060.

(232) Wang, C. M.; Liao, H. G.; Ross, F. M. Observation of Materials Processes in Liquids by Electron Microscopy. *MRS Bull* **2015**, *40* (1), 46–52. https://doi.org/10.1557/mrs.2014.283.

(233) Ruskin, R. S.; Yu, Z.; Grigorieff, N. Quantitative Characterization of Electron Detectors for Transmission Electron Microscopy. *J Struct Biol* **2013**, *184* (3), 385–393. https://doi.org/10.1016/j.jsb.2013.10.016.

(234) Faruqi, A. R.; Henderson, R.; Pryddetch, M.; Allport, P.; Evans, A. Direct Single Electron Detection with a CMOS Detector for Electron Microscopy. In *Nuclear Instruments and Methods in Physics Research, Section A: Accelerators, Spectrometers, Detectors and*

Associated Equipment; Elsevier, 2005; Vol. 546, pp 170–175. https://doi.org/10.1016/j.nima.2005.03.023.

(235) Xuong, N. H.; Jin, L.; Kleinfelder, S.; Li, S.; Leblanc, P.; Duttweiler, F.; Bouwer, J. C.; Peltier, S. T.; Milazzo, A. C.; Ellisman, M. Future Directions for Camera Systems in Electron Microscopy. *Methods in Cell Biology*. Academic Press January 1, 2007, pp 721–739. https://doi.org/10.1016/S0091-679X(06)79028-8.

(236) Moldovan, G.; Li, X.; Wilshaw, P.; Kirkland, A. I. Direct Electron Detectors for TEM. *EMC 2008 14th European Microscopy Congress 1–5 September 2008, Aachen, Germany* **2009**, *1*, 85–86. https://doi.org/10.1007/978-3-540-85156-1_43.

(237) Moldovan, G.; Li, X.; Kirkland, A. Can Direct Electron Detectors Outperform Phosphor-CCD Systems for TEM? *J Phys Conf Ser* **2008**, *126*. https://doi.org/10.1088/1742-6596/126/1/012089.

(238) Stach, E. A.; Zakharov, D.; Rivas, R. D.; Longo, P.; Lent, M.; Gubbens, A.; Czarnik, C. Exploiting a Direct Detection Camera for In-Situ Microscopy. *Microscopy and Microanalysis* **2013**, *19* (S2), 392–393. https://doi.org/10.1017/s1431927613003954.

(239) Gnanasekaran, K.; Chang, H.; Smeets, P. J. M.; Korpanty, J.; Geiger, F. M.; Gianneschi, N. C. In Situ Ni2+Stain for Liposome Imaging by Liquid-Cell Transmission Electron Microscopy. *Nano Lett* **2020**, *20* (6), 4292–4297. https://doi.org/10.1021/acs.nanolett.0c00898.

(240) Yuk, J. M.; Seo, H. K.; Choi, J. W.; Lee, J. Y. Anisotropic Lithiation Onset in Silicon Nanoparticle Anode Revealed by in Situ Graphene Liquid Cell Electron Microscopy. *ACS Nano* **2014**, *8* (7), 7478–7485. https://doi.org/10.1021/nn502779n.

(241) Parent, L. R.; Gnanasekaran, K.; Korpanty, J.; Gianneschi, N. C. 100th Anniversary of Macromolecular Science Viewpoint: Polymeric Materials by in Situ Liquid-Phase Transmission Electron Microscopy. *ACS Macro Lett* **2021**, *10* (1), 14–38. https://doi.org/10.1021/acsmacrolett.0c00595.

(242) Mirsaidov, U. M.; Zheng, H.; Casana, Y.; Matsudaira, P. Imaging Protein Structure in Water at 2.7 Nm Resolution by Transmission Electron Microscopy. *Biophys J* **2012**, *102* (4), L15–L17. https://doi.org/10.1016/j.bpj.2012.01.009.

(243) Parent, L. R.; Bakalis, E.; Ramírez-Hernández, A.; Kammeyer, J. K.; Park, C.; De Pablo, J.; Zerbetto, F.; Patterson, J. P.; Gianneschi, N. C. Directly Observing Micelle Fusion and Growth in Solution by Liquid-Cell Transmission Electron Microscopy. *J Am Chem Soc* **2017**, *139* (47), 17140–17151. https://doi.org/10.1021/jacs.7b09060.

(244) Rizvi, A.; Patel, U.; Ianiro, A.; Hurst, P. J.; Merham, J. G.; Patterson, J. P. Nonionic Block Copolymer Coacervates. *Macromolecules* **2020**, *53* (14), 6078–6086. https://doi.org/10.1021/ACS.MACROMOL.0C00979/SUPPL_FILE/MA0C00979_SI_004.MP4.

(245) Vailonis, K. M.; Gnanasekaran, K.; Powers, X. B.; Gianneschi, N. C.; Jenkins, D. M. Elucidating the Growth of Metal-Organic Nanotubes Combining Isoreticular Synthesis with Liquid-Cell Transmission Electron Microscopy. *J Am Chem Soc* **2019**, *141* (26), 10177–10182. https://doi.org/10.1021/jacs.9b04586.

(246) Wang, M.; Leff, A. C.; Li, Y.; Woehl, T. J. Visualizing Ligand-Mediated Bimetallic Nanocrystal Formation Pathways with *in Situ* Liquid-Phase Transmission Electron

Microscopy Synthesis. *ACS Nano* **2021**, acsnano.0c07131. https://doi.org/10.1021/acsnano.0c07131.

(247) Nulati Yesibolati, M.; Mortensen, K. I.; Sun, H.; Brostrøm, A.; Tidemand-Lichtenberg, S.; Mølhave, K. Unhindered Brownian Motion of Individual Nanoparticles in Liquid Phase Scanning Transmission Electron Microscopy. **2020**. https://doi.org/10.1021/acs.nanolett.0c02352.

(248) Ring, E. A.; de Jonge, N. Video-Frequency Scanning Transmission Electron Microscopy of Moving Gold Nanoparticles in Liquid. *Micron* **2012**, *43* (11), 1078–1084. https://doi.org/10.1016/j.micron.2012.01.010.

(249) Woehl, T. J.; Prozorov, T. The Mechanisms for Nanoparticle Surface Diffusion and Chain Self-Assembly Determined from Real-Time Nanoscale Kinetics in Liquid. *Journal of Physical Chemistry C* **2015**, *119* (36), 21261–21269. https://doi.org/10.1021/acs.jpcc.5b07164.

(250) Ring, E.; De Jonge, N.; Lu, ; J Y. Hopping Diffusion of Gold Nanoparticles Observed with Liquid Cell TEM. *Microsc. Microanal* **2020**, *9* (3), 2016. https://doi.org/10.1017/S1431927616004608.

(251) Chee, S. W.; Baraissov, Z.; Loh, N. D.; Matsudaira, P. T.; Mirsaidov, U. Desorption-Mediated Motion of Nanoparticles at the Liquid-Solid Interface. *Journal of Physical Chemistry C* **2016**, *120* (36), 20462–20470. https://doi.org/10.1021/acs.jpcc.6b07983.

(252) Chee, S. W.; Anand, U.; Bisht, G.; Tan, S. F.; Mirsaidov, U. Direct Observations of the Rotation and Translation of Anisotropic Nanoparticles Adsorbed at a Liquid–Solid

Interface. *Nano Lett* **2019**, *19* (5), 2871–2878. https://doi.org/10.1021/acs.nanolett.8b04962.

(253) de Jonge, N.; Houben, L.; Dunin-Borkowski, R. E.; Ross, F. M. Resolution and Aberration Correction in Liquid Cell Transmission Electron Microscopy. *Nature Reviews Materials 2018 4:1* **2018**, *4* (1), 61–78. https://doi.org/10.1038/s41578-018-0071-2.

(254) Woehl, T. J.; Jungjohann, K. L.; Evans, J. E.; Arslan, I.; Ristenpart, W. D.; Browning, N. D. Experimental Procedures to Mitigate Electron Beam Induced Artifacts during in Situ Fluid Imaging of Nanomaterials. *Ultramicroscopy* **2013**, *127*, 53–63. https://doi.org/10.1016/j.ultramic.2012.07.018.

(255) Chen, Q.; Smith, J. M.; Park, J.; Kim, K.; Ho, D.; Rasool, H. I.; Zettl, A.; Alivisatos, A. P. 3D Motion of DNA-Au Nanoconjugates in Graphene Liquid Cell Electron Microscopy. *Nano Lett* **2013**, *13* (9), 4556–4561. https://doi.org/10.1021/nl402694n.

(256) Jamali, V.; Hargus, C.; Ben-Moshe, A.; Aghazadeh, A.; Ha, H. D.; Mandadapu, K. K.; Alivisatos, A. P. *Anomalous Nanoparticle Surface Diusion in Liquid Cell TEM Is Revealed by Deep Learning-Assisted Analysis*; ChemRxiv, 2020. https://doi.org/10.26434/CHEMRXIV.12894050.V2.

(257) Faucheux, L. P.; Libchaber, A. J. Confined Brownian Motion. *Phys Rev E* **1994**, *49* (6), 5158–5163. https://doi.org/10.1103/PhysRevE.49.5158.

(258) Einsten, A. On the Motion of Small Particles Suspended in Liquids at Rest Required by the Molecular-Kinetic Theory of Heat. *Ann Phys* **1905**, *17*, 549–560. https://doi.org/10.1016/0306-4549(80)90076-6.

(259) Burada, P. S.; Hänggi, P.; Marchesoni, F.; Schmid, G.; Talkner, P. *Diffusion in Confined Geometries*; 2009; Vol. 10. https://doi.org/10.1002/cphc.200800526.

(260) Bezrukov, S. M.; Schimansky-Geier, L.; Schmid, G. Brownian Motion in Confined Geometries. *Eur. Phys. J. Special Topics* **2014**, *223*, 3021–3025. https://doi.org/10.1140/epjst/e2014-02316-6.

(261) Borodin, A. N.; Salminen, P. *Handbook of Brownian Motion — Facts and Formulae*; Birkhäuser Basel, 1996. https://doi.org/10.1007/978-3-0348-7652-0.

(262) Faucheux, L. P.; Libchaber, A. J. Confined Brownian Motion. *Phys Rev E* **1994**, *49* (6), 5158–5163. https://doi.org/10.1103/PhysRevE.49.5158.

(263) Saxton, M. J. Single-Particle Tracking: The Distribution of Diffusion Coefficients. *Biophys J* **1997**, *72* (4), 1744–1753. https://doi.org/10.1016/S0006-3495(97)78820-9.

(264) Zhang, K.; Zuo, W.; Chen, Y.; Meng, D.; Zhang, L. Beyond a Gaussian Denoiser: Residual Learning of Deep CNN for Image Denoising. **2016**. https://doi.org/10.1109/TIP.2017.2662206.

(265) de Jonge, N. Theory of the Spatial Resolution of (Scanning) Transmission Electron Microscopy in Liquid Water or Ice Layers. *Ultramicroscopy* **2018**, *187*, 113–125. https://doi.org/10.1016/J.ULTRAMIC.2018.01.007.

(266) Vo, G. D.; Park, C. Robust Regression for Image Binarization under Heavy Noise and Nonuniform Background. *Pattern Recognit* **2018**, *81*, 224–239. https://doi.org/10.1016/J.PATCOG.2018.04.005.

(267) Tinevez, J. Y.; Perry, N.; Schindelin, J.; Hoopes, G. M.; Reynolds, G. D.; Laplantine, E.; Bednarek, S. Y.; Shorte, S. L.; Eliceiri, K. W. TrackMate: An Open and Extensible Platform for Single-Particle Tracking. *Methods* **2017**, *115*, 80–90. https://doi.org/10.1016/J.YMETH.2016.09.016.

(268) Ershov, D.; Phan, M. S.; Pylvänäinen, J. W.; Rigaud, S. U.; Le Blanc, L.; Charles-Orszag, A.; Conway, J. R. W.; Laine, R. F.; Roy, N. H.; Bonazzi, D.; Duménil, G.; Jacquemet, G.; Tinevez, J. Y. TrackMate 7: Integrating State-of-the-Art Segmentation Algorithms into Tracking Pipelines. *Nature Methods 2022 19:7* **2022**, *19* (7), 829–832. https://doi.org/10.1038/s41592-022-01507-1.

(269) Lançon, P.; Batrouni, G.; Lobry, L.; Ostrowsky, N. Brownian Walker in a Confined Geometry Leading to a Space-Dependent Diffusion Coefficient. In *Physica A: Statistical Mechanics and its Applications*; North-Holland, 2002; Vol. 304, pp 65–76. https://doi.org/10.1016/S0378-4371(01)00510-6.

(270) *Trackpy: Fast, Flexible Particle-Tracking Toolkit — trackpy 0.5.0 documentation*. http://soft-matter.github.io/trackpy/v0.5.0/ (accessed 2021-05-09).

(271) Allan, D. B.; Caswell, T.; Keim, N. C.; van der Wel, C. M.; Verweij, R. W. Soft-Matter/Trackpy: Trackpy v0.5.0. **2021**. https://doi.org/10.5281/ZENODO.4682814.

(272) Park, C.; Woehl, T. J.; Evans, J. E.; Browning, N. D. Minimum Cost Multi-Way Data Association for Optimizing Multitarget Tracking of Interacting Objects. *IEEE Trans Pattern Anal Mach Intell* **2015**, *37* (3), 611–624. https://doi.org/10.1109/TPAMI.2014.2346202.

(273) Bakalis, E.; Höfinger, S.; Venturini, A.; Zerbetto, F. Crossover of Two Power Laws in the Anomalous Diffusion of a Two Lipid Membrane. *Journal of Chemical Physics* **2015**, *142* (21). https://doi.org/10.1063/1.4921891.

(274) Meroz, Y.; Sokolov, I. M.; Klafter, J. Test for Determining a Subdiffusive Model in Ergodic Systems from Single Trajectories. *Phys Rev Lett* **2013**, *110* (9). https://doi.org/10.1103/PHYSREVLETT.110.090601.

(275) Dasgupta, R.; Ballabh, T. K.; Tarafdar, S. Scaling Exponents for Random Walks on Sierpinski Carpets and Number of Distinct Sites Visited: A New Algorithm for Infinite Fractal Lattices. *J Phys A Math Gen* **1999**, *32* (37), 6503. https://doi.org/10.1088/0305-4470/32/37/302.

(276) Satin, S.; Gangal, A. D. Random Walk and Broad Distributions on Fractal Curves. *Chaos Solitons Fractals* **2019**, *127*. https://doi.org/10.1016/j.chaos.2019.06.019.

(277) Meroz, Y.; Sokolov, I. M.; Klafter, J. Test for Determining a Subdiffusive Model in Ergodic Systems from Single Trajectories. *Phys Rev Lett* **2013**, *110* (9). https://doi.org/10.1103/PhysRevLett.110.090601.

(278) Mackenzie, D. A Tisket, a Tasket, an Apollonian Gasket. *Am Sci* **2010**, *98* (1), 10–14. https://doi.org/10.1511/2010.82.10.

(279) Zheng, H.; Claridge, S. A.; Minor, A. M.; Alivisatos, A. P.; Dahmen, U. Nanocrystal Diffusion in a Liquid Thin Film Observed by in Situ Transmission Electron Microscopy. *Nano Lett* **2009**, *9* (6), 2460–2465. https://doi.org/10.1021/NL9012369/SUPPL_FILE/NL9012369_SI_004.AVI.

(280) Chaoi, Y.; Zhao-yuanzf, N.; Yu-hua, G.; Xiang-yingElf, W.; Yu, X.; Yuan-changE, W.; Ming-rong, S.; HaoEE, W. Fractal Aggregation Behavior in Amorphous Silicon Nitride Films. *Chinese Physics Letters* **1997**, *14* (6), 446. https://doi.org/10.1088/0256-307X/14/6/013.

(281) Mkrtchyan, M.; Gasparyan, A.; Mkhoyan, K.; Liddle, A.; Novembre, A.; Muller, D. SCALPEL Mask-Membrane Charging. *Microelectron Eng* **1999**, *46* (1–4), 223–226. https://doi.org/10.1016/S0167-9317(99)00067-2.

(282) Mkrtchyan, M. M.; Gasparyan, A. S.; Mkhoyan, K. A.; Gasparyan,) A S; Liddle, J. A.; Novembre, A. E. Determination of the Possible Magnitude of the Charging Effect in a SCALPEL Mask Membrane. *Journal of Vacuum Science & Technology B: Microelectronics and Nanometer Structures Processing, Measurement, and Phenomena* **1999**, *17* (6), 2888. https://doi.org/10.1116/1.591090.

(283) Liddle, J.; Blakey, M.; Gallatin, G.; Knurek, C.; Mkrtchyan, M.; James Alexander Liddle, al; Blakey, M. I.; Gallatin, G. M.; Knurek, C. S.; Mkrtchyan, M. M.; Novembre, A. E.; Waskiewicz, W. K.; Liddle, J.; Blakey, M.; Gallatin, G.; Knurek, C.; Mkrtchyan, M.; Novembre, A.; Waskiewicz, W. Space-Charge Results from the SCALPEL Proof-of-Concept System. *https://doi.org/10.1117/12.351090* **1999**, *3676* (25), 180–193. https://doi.org/10.1117/12.351090.

(284) Lee, Y.; Lee, W.; Chun, K. Calculation of Surface Potential and Beam Deflection Due to Charging Effects in Electron Beam Lithography. *Journal of Vacuum Science & Technology B: Microelectronics and Nanometer Structures Processing, Measurement, and Phenomena* **2000**, *18* (6), 3095. https://doi.org/10.1116/1.1319822.

(285) Schork, F. J.; Luo, Y.; Smulders, W.; Russum, J. P.; Butté, A.; Fontenot, K. Miniemulsion Polymerization. *Advances in Polymer Science* **2005**, *175*, 129–255. https://doi.org/10.1007/B100115/COVER.

(286) Capek, I.; Chern, C. S. Radical Polymerization in Direct Mini-Emulsion Systems. *Advances in Polymer Science* **2001**, *155*, 101–165. https://doi.org/10.1007/3-540-44473-4_2/COVER.

(287) Chern, C. S. Emulsion Polymerization Mechanisms and Kinetics. *Prog Polym Sci* **2006**, *31* (5), 443–486. https://doi.org/10.1016/J.PROGPOLYMSCI.2006.02.001.

(288) Fonseca, G. E.; McKenna, T. F.; Dubé, M. A. Miniemulsion vs. Conventional Emulsion Polymerization for Pressure-Sensitive Adhesives Production. *Chem Eng Sci* **2010**, *65* (9), 2797–2810. https://doi.org/10.1016/J.CES.2010.01.017.

(289) Rao, J. P.; Geckeler, K. E. Polymer Nanoparticles: Preparation Techniques and Size-Control Parameters. *Prog Polym Sci* **2011**, *36* (7), 887–913. https://doi.org/10.1016/J.PROGPOLYMSCI.2011.01.001.

(290) Asua, J. M. Miniemulsion Polymerization. *Prog Polym Sci* **2002**, *27* (7), 1283–1346. https://doi.org/10.1016/S0079-6700(02)00010-2.

(291) Carmean, R. N.; Becker, T. E.; Sims, M. B.; Sumerlin, B. S. Ultra-High Molecular Weights via Aqueous Reversible-Deactivation Radical Polymerization. *Chem* **2017**, *2* (1), 93–101. https://doi.org/10.1016/J.CHEMPR.2016.12.007.

(292) Carmean, R. N.; Sims, M. B.; Figg, C. A.; Hurst, P. J.; Patterson, J. P.; Sumerlin, B. S. Ultrahigh Molecular Weight Hydrophobic Acrylic and Styrenic Polymers through

Organic-Phase Photoiniferter-Mediated Polymerization. *ACS Macro Lett* **2020**, *9* (4), 613–618. https://doi.org/10.1021/ACSMACROLETT.0C00203/ASSET/IMAGES/LARGE/MZ0C00203_0004.JPEG.

(293) McCracken, J. R.; Datyner, A. The Preparation of Uniform Polystyrene Latices by True Emulsion Polymerization. *J Appl Polym Sci* **1974**, *18* (11), 3365–3372. https://doi.org/10.1002/app.1974.070181115.

(294) Eastoe, J. Microemulsions. *Colloid Science: Principles, Methods and Applications* **2009**, 77–97. https://doi.org/10.1002/9781444305395.CH5.

(295) Lawrence, M. J.; Rees, G. D. Microemulsion-Based Media as Novel Drug Delivery Systems. *Adv Drug Deliv Rev* **2000**, *45* (1), 89–121. https://doi.org/10.1016/S0169-409X(00)00103-4.

(296) Zhang, Y.; Chen, X.; Liu, X. Temperature-Induced Reversible-Phase Transition in a Surfactant-Free Microemulsion. *Langmuir* **2019**, *35* (44), 14358–14363. https://doi.org/10.1021/ACS.LANGMUIR.9B02842/ASSET/IMAGES/LARGE/LA9B02842_0006.JPEG.

(297) *VA -044 - Wako Chemicals*. https://polymer-additives.specialchem.com/product/a-wako-chemicals-va-044 (accessed 2023-05-06).

(298) Chen, S.; Sun, H.; Liu, J.; Wang, J.; Lu, H.; Hao, J.; Xu, L.; Liu, W. A Microemulsion Superlubricant with Largely Switchable Friction. **2023**. https://doi.org/10.21203/RS.3.RS-2368500/V1.

(299) Mukherjee, S.; Kushnick, A. P. Effect of Demulsifiers on Interfacial Properties Governing Crude Oil Demulsification. In *Oil-Field Chemistry: Enhanced Recovery and Production Stimulation* ; Borchardt, J. K., Yen, T. F., Eds.; American Chemical Society, 1989; pp 364–374. https://doi.org/10.1021/bk-1989-0396.ch019.

(300) Clausse, D.; Gomez, F.; Dalmazzone, C.; Noik, C. A Method for the Characterization of Emulsions, Thermogranulometry: Application to Water-in-Crude Oil Emulsion. *J Colloid Interface Sci* **2005**, *287* (2), 694–703. https://doi.org/10.1016/J.JCIS.2005.02.042.

(301) Perini, N.; Prado, A. R.; Sad, C. M. S.; Castro, E. V. R.; Freitas, M. B. J. G. Electrochemical Impedance Spectroscopy for in Situ Petroleum Analysis and Water-in-Oil Emulsion Characterization. *Fuel* **2012**, *91* (1), 224–228. https://doi.org/10.1016/J.FUEL.2011.06.057.